

THESE

PRESENTEE A

L'UNIVERSITE DE PAU ET DES PAYS DE L'ADOUR

ECOLE DOCTORALE DES SCIENCES EXACTES ET LEURS
APPLICATIONS

PAR

RONZANI Filippo

POUR OBTENIR LE GRADE DE

DOCTEUR

Specialité : CHIMIE-PHYSIQUE

Photosensitized oxidation reactions: transient reactive species and mechanisms at interfaces

Soutenue le 11 Décembre 2013, devant la commission d'examen formée de :

M. Xavier Allonas	Professeur à l'Université de Haute Alsace	<i>Rapporteur</i>
M ^{me} Sylvie Blanc	Chargé de recherches au CNRS	<i>co-Encadrant</i>
M ^{me} Sylvie Lacombe	Directeur de recherches au CNRS	<i>Encadrant</i>
M. Thierry Pigot	Professeur à l'U.P.P.A	<i>Président</i>
M ^{me} Claire Richard	Directeur de recherches au CNRS	<i>Examineur</i>
M ^{me} Elena Selli	Professur à l'Université de Milan, Italie	<i>Rapporteur</i>

Université de Pau et des Pays de l'Adour

Ecole Doctorale des Sciences Exactes et leurs applications

Spécialité

Chimie Physique

Filippo Ronzani

**Photosensitized oxidation reactions:
transient reactive species and mechanisms at interfaces**

Advisers Sylvie LACOMBE

Sylvie BLANC

Institut des Sciences Analytiques et de Physico-Chimie pour l'Environnement et les Matériaux,
UMR CNRS 5254, Equipe Chimie-Physique – IPREM, ECP

ABSTRACT

The main aim of the work carried out during this PhD project was to develop, characterize and analyze original materials for photosensitized oxidation reactions. Particular attention was paid to the determination of the photophysical properties of the selected photosensitizers (PSs) and the effect induced by the immobilization on an inert support (silica). The reactive species formed upon irradiation were identified and analyzed. Singlet oxygen production was monitored by two complementary methods. The solid-supported sensitizers were employed, in the form of either monoliths or powders, for the photooxidation of dimethyl sulfide at the gas-solid interface and of α -terpinene at the liquid-solid interface. Singlet oxygen was the main reactive oxygen species formed by the selected PSs; nonetheless, the reaction products were analyzed and other possible mechanistic scenarios investigated.

Keywords: Photochemistry - Photooxidation – Photosensitization – Singlet oxygen – ROS – Electron transfer – Transient species – Electronic spectroscopy – Fluorescence – Silica – Cyanoanthracenes – Phenothiazines – Anthraquinone – Reaction mechanisms

Réactions d'oxydation photosensibilisée :
espèces transitoires réactives et mécanismes aux interfaces

RÉSUMÉ

L'objectif principal du travail effectué au cours de cette thèse était de développer, caractériser et analyser des matériaux originaux pour des réactions d'oxydation photosensibilisée. Une attention particulière a été accordée à la détermination des propriétés photophysiques des sensibilisateurs (PSs) et à l'effet induit par l'immobilisation sur un support inerte (silice). Les espèces réactives formées lors de l'irradiation ont été identifiées et analysées. La production d'oxygène singulet a été suivie par deux méthodes complémentaires. Les sensibilisateurs supportés ont été employés, sous la forme de monolithes ou de poudres, pour la photo-oxydation du diméthyl sulfure à l'interface gaz-solide et de l' α -terpinène à l'interface liquide-solide. L'oxygène singulet est la principale espèce réactive de l'oxygène formée par les PSs sélectionnés; néanmoins, les produits de réaction ont été analysés afin de mettre en évidence d'autres mécanismes.

Mots clés: Photochimie - Photooxydation – Photosensibilisation – Oxygène singulet – ROS – Transfert d'électron – Espèces transitoires – Spectroscopie électronique – Fluorescence – Silice – Cyanoanthracènes – Phénothiazines – Anthraquinone – Mécanismes réactionnels

RÉSUMÉ SUBSTANTIEL

La molécule d'oxygène, si elle est activée par une quantité d'énergie suffisante, peut atteindre un état excité, dans lequel sa réactivité est totalement différente par rapport à son état fondamental : il s'agit des « espèces réactives de l'oxygène ». Parmi ces espèces réactives, l'oxygène singulet ($^1\text{O}_2$) est l'objet d'une thématique de recherche toujours d'actualité, notamment grâce aux applications potentielles dans lesquelles il peut jouer un rôle important : les applications liés à cette espèce activée deviennent de plus en plus significatifs. L'oxygène singulet peut être utilisé pour des réactions de synthèse organique en tant que réactif stéréosélectif, mais aussi comme oxydant pour la dépollution ; en outre, pendant les deux dernières décennies son rôle dans les domaines de la thérapie photodynamique contre les cellules cancéreuses et des phototraitements contre bactéries et virus a été étudié, compris et appréhendé de manière détaillé.

La photosensibilisation représente une des voies les plus utilisées et efficaces pour la génération de $^1\text{O}_2$ à température ambiante avec seulement la lumière visible et l'oxygène comme réactifs. Un grand nombre de photosensibilisateurs organiques est utilisé pour la production d'oxygène singulet en solution homogène. Cependant, pour la plupart des applications, la conception de matériaux photoactivables dans le visible, préparés en liant le sensibilisateur à un support inerte, est plus intéressante. Cela implique des étapes de développement très importantes : la synthèse de photosensibilisateurs performants et résistants à l'exposition à la lumière et aux réactifs chimiques, la préparation de supports stables et adaptés à l'application prévue (en termes de configuration, forme etc.), l'analyse détaillée de l'effet de la matrice sur les propriétés photophysiques et photochimiques du catalyseur organique. Des matériaux ainsi conçus peuvent trouver des applications pour la chimie fine, la dépollution et les traitements médicaux ou biologiques.

Le travail qui est présenté dans ce texte a comme objectif l'analyse détaillée des propriétés photophysiques de certains photosensibilisateurs, commerciaux ou synthétisés au sein du laboratoire, et à leur insertion ou greffage sur des supports inertes. La silice a été choisie comme support pour sa disponibilité, son inertie chimique et mécanique, la possibilité de fonctionnalisation et sa transparence en lumière visible. Des matériaux photosensibilisateurs ont été préparés sous forme de monolithes transparents ou de poudres. Les espèces transitoires et l'oxygène singulet produit en irradiant les sensibilisateurs en solution et en phase supportée ont été quantifiés et les effets de la matrice solide ont pu être mis en évidence. La transparence des monolithes de silice et leur forme ont permis à la fois la détection des espèces réactives par analyse directe sur les matériaux, et leur utilisation comme microréacteurs pour un procédé de photooxydation à l'interface gaz-solide.

L'analyse photophysique des sensibilisateurs a permis la compréhension des mécanismes impliqués dans les réactions d'oxydation photoinduite. Les matériaux préparés ont été testés pour deux réactions modèles de la chimie de $^1\text{O}_2$: l'oxydation du diméthylsulfure à l'interface gaz-solide (monolithes) et l'oxygénation de l' α -terpinène à l'interface liquide-solide (poudres en suspension). L'identification et la quantification des produits de réaction ont permis de compléter la compréhension des mécanismes. Nous avons pu remarquer que, selon le sensibilisateur utilisé et le substrat à oxyder, des mécanismes différents peuvent se produire. Dans la plupart des cas, l'espèce réactive principale générée est l'oxygène singulet; dans certains cas, cependant, des réactions de transfert d'électron favorisent des produits d'oxydation (déhydrogénation) plutôt que d'oxygénation.

Grâce à ce travail de recherche, nous avons démontré que des matériaux photosensibilisateurs à base de silice, facilement préparés dans des conditions douces, peuvent être efficacement utilisés pour des réactions d'oxydation et/ou d'oxygénation. En développant des matériaux avec des caractéristiques précises en termes de forme, configuration macroscopique et insertion du sensibilisateur, différentes applications peuvent être visées. En outre, les propriétés photophysiques du catalyseur organique peuvent aussi être modulées. Le choix du sensibilisateur et du support représente l'étape clés pour le développement de matériaux efficaces et résistants pour des applications en photooxydation.

And if in a distant future the supply of coal becomes
completely exhausted, civilization will not be
checked by that, for life and civilization will
continue as long as the sun shines!

Table of contents

FIGURES, SCHEMES, TABLES, CHARTS	15
---	-----------

1 INTRODUCTION	25
-----------------------	-----------

1.0. PHOTOCHEMISTRY IN ACTION	25
2.0. PHOTOOXIDATION REACTIONS	26
3.0. PHOTSENSITIZATION	27
3.1. GENERAL ASPECTS	27
3.2. LIGHT ABSORPTION AND PHOTOPHYSICAL PATHWAYS	28
3.3. OXIDATION MECHANISMS	29
3.3.1. Type I reactions	30
3.3.2. Type II reactions	33
3.3.3. Type I-II reactions	36
3.4. PHOTSENSITIZERS	37
3.4.1. Classes of photosensitizers	39
3.4.1.1. Polyaromatics	39
3.4.1.2. Aromatic ketones	39
3.4.1.3. Phenazine/phenothiazine derivatives	40
3.4.1.4. Xanthene derivatives	41
3.4.1.5. Acridine derivatives	42
3.4.1.6. Porphyrins and phthalocyanines	42
3.4.1.7. Miscellaneous	43
3.5. IMMOBILIZED ORGANIC PHOTOCATALYSTS	44
3.6. APPLICATIONS	46
3.6.1. Photodynamic processes	46
3.6.1.1. PDT	46
3.6.1.2. PDI	47
3.6.2. Water/air treatment	48
3.6.3. Fine chemistry	49
4.0. IMPROVEMENTS AND PERSPECTIVES FOR IMMOBILIZED ORGANIC PHOTOCATALYSTS	51

2 AIMS	55
---------------	-----------

1.0 PHOTSENSITIZERS	55
2.0 SUPPORTS	61
3.0 PHOTOPHYSICS	62
4.0 SINGLET OXYGEN	62

5.0	PHOTOREACTIVITY	63
5.1.	GAS PHASE REACTIONS	63
5.2.	LIQUID PHASE REACTIONS	63
3	MATERIALS AND METHODS	65
1.0	SYNTHESES	65
1.1	DEVELOPMENT OF CYANOANTHRACENE DERIVATIVES (COMPOUNDS 1-4)	65
1.2	TRANSPARENT SILICA MONOLITHS	67
1.2.1	Sol-gel technique	67
1.2.2	Procedure for the synthesis of silica monoliths	68
1.3	GRAFTING	71
1.3.1	Grafting on silica monoliths	71
1.3.2	Grafting on commercial silica gels	72
1.4	SUMMARY OF THE SYNTHESIZED MATERIALS	73
2.0	STRUCTURAL CHARACTERIZATION: B.E.T. TECHNIQUE	74
3.0	SPECTROSCOPIC CHARACTERIZATION	75
3.1	UV-VIS SPECTROSCOPY	75
3.2	FLUORESCENCE SPECTROSCOPY	76
3.3	DETECTION OF THE TRANSIENT SPECIES: LASER FLASH PHOTOLYSIS	78
4.0	SINGLET OXYGEN DETECTION	81
4.1	DIRECT METHOD: DETECTION OF $^1\text{O}_2$ PHOSPHORESCENCE AT 1270 NM	81
4.1.1	Steady-state measurements	81
4.1.2	Time-resolved measurements	83
4.2	INDIRECT METHOD: $^1\text{O}_2$ TRAPPING BY A MOLECULAR PROBE	84
4.2.1	Rubrene: a selective probe for $^1\text{O}_2$	85
4.3	EQUIPMENT FOR SINGLET OXYGEN DETECTION	86
5.0	PHOTOACTIVITY	89
5.1	MV: PHOTBLEACHING AND PHOTOOXIDATION OF DIBUTYL SULFIDE IN HOMOGENEOUS SOLUTIONS	89
5.2	MONOLITHS: PHOTOOXIDATION OF DIMETHYL SULFIDE AT THE GAS-SOLID INTERFACE	90
5.3	POWDERS: PHOTOOXIDATION OF α -TERPINENE AT THE LIQUID-SOLID INTERFACE	93
6.0	MEASUREMENTS OF IRRADIANT POWER	94
6.1	SPECTRORADIOMETRY	94
6.2	CHEMICAL ACTINOMETRY	97
4	CYANOANTHRACENES: SYNTHESIS AND CHARACTERIZATION IN SOLUTION	99
1.0	SYNTHESES	100
2.0	SPECTROSCOPIC CHARACTERIZATION	102
2.1	UV-VIS SPECTROSCOPY	103
2.2	FLUORESCENCE SPECTROSCOPY	105
3.0	ANALYSIS OF THE TRANSIENT SPECIES	107
4.0	SINGLET OXYGEN DETECTION	113
4.1	DIRECT $^1\text{O}_2$ PHOSPHORESCENCE DETECTION	113

4.2	DETECTION BY REACTION WITH A CHEMICAL PROBE	116
4.3	MECHANISMS OF $^1\text{O}_2$ GENERATION BY DCA AND DBTP DERIVATIVES	118
5.0	ELECTRON TRANSFER REACTIONS	123
6.0	CONCLUSIONS	125

5 PHENOTHIAZINES: PHOTOPHYSICAL CHARACTERIZATION IN SOLUTION **127**

1.0	UV-VIS AND FLUORESCENCE SPECTROSCOPY	128
1.1	NMB ⁺ AND MV	128
1.2	MV SOLVATOCHROMISM	133
1.2.1	UV-Vis spectroscopy in different solvents	133
1.2.2	Effect of acidity	139
1.2.3	Quantum chemical calculations	142
2.0	DETECTION OF THE TRANSIENT SPECIES	145
3.0	SINGLET OXYGEN PRODUCTION	149
4.0	REACTIVITY OF MV IN SOLUTION	152
5.0	CONCLUSIONS	158

6 ORGANIC PHOTOCATALYSTS IMMOBILIZED ON TRANSPARENT SILICA MONOLITHS: REACTIVITY AT THE GAS-SOLID INTERFACE **159**

1.0	SYNTHESES	160
1.1	SYNTHESIS OF COMPOUND 6	160
1.2	SYNTHESIS OF SILICA MONOLITH AND STRUCTURAL CHARACTERIZATION	161
1.2.1	Monoliths' shortcomings	165
2.0	SPECTROSCOPIC CHARACTERIZATION	166
2.1	UV-VIS AND DRUV-VIS SPECTROSCOPY	166
2.2	FLUORESCENCE SPECTROSCOPY	168
2.3	SPECTROSCOPIC BEHAVIOR OF SILICA-EMBEDDED MV	171
3.0	ANALYSIS OF THE TRANSIENT SPECIES	173
4.0	SINGLET OXYGEN DETECTION	179
4.1	SINGLET OXYGEN LIFETIME	179
4.2	SINGLET OXYGEN PRODUCTION AND QUANTUM YIELDS	180
5.0	PHOTOOXIDATION OF DMS AT THE GAS-SOLID INTERFACE	185
6.0	CONCLUSIONS	192

7 ORGANIC PHOTOCATALYSTS IMMOBILIZED ON SILICA POWDERS: THE PHOTOOXIDATION OF α -TERPINENE AT THE GAS-LIQUID INTERFACE **193**

1.0	SYNTHESIS AND CHARACTERIZATION	194
1.1	SYNTHESIS	194
1.2	SPECTROSCOPIC CHARACTERIZATION	196
2.0	DETERMINATION OF Φ_{Δ}	199
3.0	PHOTOOXIDATION REACTIONS	200

3.1	PHOTOSENSITIZED OXIDATION OF α -TERPINENE (α -T)	201
3.2	PHOTOSENSITIZED OXIDATION OF <i>P</i> -CYMENE (<i>P</i> -C)	206
3.3	DETECTION OF THE MAIN PRODUCTS AND BY-PRODUCTS BY ^1H NMR AND MS SPECTROSCOPY	207
4.0	DISCUSSION OF THE MECHANISMS	211
5.0	KINETIC STUDIES	214
6.0	CONCLUSIONS	215
GENERAL CONCLUSIONS		217
ACKNOWLEDGEMENTS		221
BIBLIOGRAPHY		227

Figures, schemes, tables, charts

- Figure 1** Main reactions involving superoxide radical anion. 31
- Figure 2** Main reactions involving singlet oxygen: formation of endoperoxides, allylic hydroperoxides and dioxetanes. 35
- Figure 3** Examples of photosensitized oxygenation reactions: a) formation of *p*-toluyl aldehyde from *p*-xylene, using acridinium ions as ELT PSs; b) oxygenation of 1,5-dihydroxynaphthalene to juglone by singlet oxygen addition; c) singlet oxygen addition to α -terpinene to form ascaridole; d) singlet oxygen induced hydroperoxidation of citronellol. 50
- Figure 4** Picture representing some silica-embedded PSs. Top: **SGO-PN**, **SGO-ACN-MV**, **SGO-MV**, **SGO-MB⁺**, **SGO-RB** (series 1). Bottom: **DCA**, **NMB⁺**, blank, **DBTP** and **RB** (all **SGO**) (series 2). See paragraph 1.4 and Chapter 6 for definitions. 69
- Figure 5** Pictures of the photosensitizing materials prepared by grafting chromophores on functionalized silica gels. a) Commercial **RB-ps** (rose bengal on polystyrene beads), b) **RB-Si**, c) **DBTP-Si**, d) **AQ-Si**. 73
- Figure 6** Fluorescence emission (visible light) of **DCA** (left) in ACN and in silica monolith (both excited at 385 nm) and of **MV** (right) in ACN (irradiated at 585 nm). The color of the emitted radiation is clearly detectable at the naked eye. 78
- Figure 7** Left: experimental apparatus for laser flash photolysis; the laser beam path is represented by the yellow arrow: from the laser source (a) the beam passes through optic elements to reach the sample (c); the transient detection is carried out by means of a pulsed Xe lamp (b). Right: schematic representation of the same apparatus. 81
- Figure 8** Absorption spectra of a solution containing rubrene (4.0×10^{-5} M) and **1** (6.0×10^{-5} M), following 385 nm photolysis in air-equilibrated ACN at 25 °C. The spectra were monitored over 10 min period and they were recorded every 60 s interrupting 385 irradiation (1.5×10^{-4} W cm⁻²). Reaction between rubrene and ¹O₂ selectively yields an endoperoxide. 86
- Figure 9** Set-up for the indirect detection of singlet oxygen. Left: Xe-Hg light source (a), irradiation monochromator (b) and spectrophotometer (c). Right, bottom: optical path of the light beam irradiating the cell containing the PS and the probe; right, top: fluorescence emission of **DCA** irradiated at 385 nm (top view). 88
- Figure 10** Profile of the variation of [DMS] during the photooxidation test. DMS conversion is calculated as the ratio of the filled area and the rectangular total area (dashed-line). 92
- Figure 11** Photochemical reactor (picture on the left: the orange polycarbonate filter is applied on the glass reactor for the analysis of **RB**, **MV**, **MB⁺**, **NMB⁺**) used for the DMS photooxidation tests. 92
- Figure 12** Rayonet® photoreactor setup: (left) schematic side view with inserted Pyrex flask (1: sintered glass frit, 2: oxygen inlet tube, 3: oxygen outlet tube, 4: septum port for sampling, 5: fluorescent tubes); (right) top view of actual setup with 16 × 8 W lamps. 94
- Figure 13** Irradiance spectra of the lamps used for the photooxidation of DMS; lamps with λ_{max} 420 nm (blue line) and lamps with λ_{max} at 575 nm (secondary axis; solid red line: filtered at 544 nm; dotted red line: non-filtered lamps). 95
- Figure 14** Irradiance spectra of the lamps used for the photooxidation of α -terpinene; lamps with λ_{max} at 420 nm (blue line) and lamps with λ_{max} at 575 nm (secondary axis; red line). 96
- Figure 15** Irradiance spectrum of the 200 W Xe-Hg lamp used for the photobleaching studies on **MV**, in the absence and in the presence of DBS. 96

- Figure 16** UV-Vis absorption spectra of compounds **1** (black dashed line), **2** (green line), **3** (red line) and **4** (grey line). The main absorption maxima are pointed out. **103**
- Figure 17** Comparison of the absorption spectra in ACN of **DCA** (green line) and **1** (red line). Inset: detail of the structured bands in the near-UV/ visible range. **104**
- Figure 18** Fluorescence excitation ($\lambda_{em} = 500$ nm) and emission ($\lambda_{ex} = 400$ nm) spectra of compounds **1** (black), **2** (green), **3** (bleu) and **4** (red) in ACN at room temperature. **105**
- Figure 19** Fluorescence excitation ($\lambda_{em} = 460$ nm) and emission ($\lambda_{ex} = 350$ nm) spectra of **DCA** in air-equilibrated ACN. **107**
- Figure 20** Time evolution of the transient absorption observed by laser flash photolysis of **1** in air-equilibrated (top) and Ar-saturated (bottom) ACN at room temperature. **108**
- Figure 21** Plot of the end of pulse transient absorption as a function of the laser pulse intensity. The absorption was monitored at 460 nm for **1** and at 470 nm for **2-4**. Diamonds (**1**, 2.7×10^{-5} M, $A_{355} = 0.17$), squares (**2**, 2.3×10^{-5} M, $A_{355} = 0.13$), triangles (**1**, 3.3×10^{-5} M, $A_{355} = 0.13$), circles (**1**, 7.2×10^{-5} M, $A_{355} = 0.35$) at room temperature in aerated ACN. **108**
- Figure 22** Time evolution of the transient absorption observed by laser flash photolysis of **2**, **3** and **4** in Ar-saturated ACN at room temperature. **109**
- Figure 23** Decay of the transient absorption of **1** observed by laser flash photolysis in argon- (red line), air- (blue line) and oxygen- (green line) saturated ACN solutions at room temperature. Inset: variation of the monomolecular rate constant of transient decay (k_d) as a function of $[O_2]$. **110**
- Figure 24** Decay of the transient absorption of **1-4** observed by laser flash photolysis in argon- (red line), air- (blue line) and oxygen- (green line) saturated ACN solutions at room temperature. **111**
- Figure 25** Transient absorption decay at 495 nm (top) and 530 nm (bottom) as a function of time in Ar-saturated ACN solutions at room temperature. Blue line: **1** (1.5×10^{-5} M); red line: **1** (1.5×10^{-5} M) and rubrene (2.0×10^{-4} M) as an energy acceptor. The increase of intensity due to the triplet state of rubrene formed by ET (top) and the decrease of intensity due to faster triplet quenching of **1** by ET to rubrene (bottom) are evident. **112**
- Figure 26** Variation of the ratio of the 1O_2 emission signals for reference (**PN**) and PS as a function of the PS concentration in ACN at room temperature: **DCA** (stars), **1** (circles), **3** (squares) and **4** (triangles). Errors: approx. 10%. **115**
- Figure 27** Variation of the ratio of the 1O_2 emission signals for **PN** and **2** as a function of the concentration of PS in ACN at room temperature. Errors: approx. 10%. **116**
- Figure 28** Absorption spectra of rubrene (red) and of the endoperoxide formed by singlet oxygen addition to rubrene (bleu). 1O_2 was produced by photosensitization using **PN**; the spectrum of the endoperoxide was obtained after complete conversion of rubrene and the subtraction of the photosensitizer absorption. Solvent: air-equilibrated ACN at 25 °C. **117**
- Figure 29** Energy levels of the S_1 and T_1 states of **DCA** and of the S_1 , T_3 and T_1 states of **1** in vacuum, heptane and ethanol. **122**
- Figure 30** Complete representation of the energy levels of the ground and excited states of **DCA** and **1** in heptane. The difference between the S_1 and T_1 states is higher than 94.2 kJ mol^{-1} only for **DCA**. **123**
- Figure 31** UV-Vis absorption spectra of **MV** (red) and **NMB⁺** (black) in ACN (solid lines) and MeOH (dashed lines). **129**
- Figure 32** UV-Vis absorption spectra of **RB** (black) and **MB⁺** (grey) in ACN (solid lines) and MeOH (dashed lines). **130**
- Figure 33** Fluorescence emission ($\lambda_{ex} = 550$ nm) spectra of **MB⁺** (a), **RB** (b), **NMB⁺** (c) and **MV** (d) in ACN (black solid lines) and MeOH (red dashed lines). Air-equilibrated solutions at room temperature. **130**
- Figure 34** Fluorescence excitation ($\lambda_{em} = 670$ nm) and emission ($\lambda_{ex} = 600$ nm) spectra of **NMB⁺** in MeOH (red) and ACN (black). **131**
- Figure 35** Fluorescence excitation ($\lambda_{em} = 650$ nm) and emission ($\lambda_{ex} = 550$ nm) spectra of **MV** in MeOH (red) and ACN (black). **131**

- Figure 36** Normalized absorption spectra of **MV** in various solvents: *n*-heptane (blue line), dioxane (red line), acetonitrile (green line), methanol (purple line) and water (orange line). Air-equilibrated solutions at room temperature. **133**
- Figure 37** Normalized absorption spectra (400-700 nm range) of **MV** in various solvents: *n*-heptane (black dashed line), triethylamine (green line), dioxane (red line), ACN (grey line), dimethylformamide (blue line) and water (black dotted line). Air-equilibrated solutions at room temperature. **134**
- Figure 38** Variation of the absorption maximum wavelength of **MV** as a function of the polarity/polarizability parameter (π^*) of the solvent; different correlations were found for aprotic (grey solid line, grey empty circles) and protic (black dashed line, black diamonds) solvents. **136**
- Figure 39** Variation of the absorption maximum wavelength of **MV** as a function of the hydrogen bond donation ability (α) of the solvent. **137**
- Figure 40** Variation of the absorption maximum wavelength of **MV** as a function of the hydrogen bond acceptance (β) of the solvent. **138**
- Figure 41** Variation of the absorption maximum wavelength of **MV** as a function of the normalized Dimroth-Reichardt's polarity (ETN) of the solvent; a unique correlation was found for aprotic (grey empty circles) and protic (black diamonds) solvents. **138**
- Figure 42** Variation of the absorption maximum wavelength of **MV** as a function of the global parameter (XYZ) of the solvent; a unique correlation was found for aprotic (grey empty circles) and protic (black diamonds) solvents. **139**
- Figure 43** Evolution of the absorption spectrum of **MV** in CHCl_3 for subsequent additions of $\text{CH}_3\text{SO}_3\text{H}$ (2.0×10^{-6} to 5.0×10^{-4} M). Inset: evolution of the absorption spectrum at higher concentrations of $\text{CH}_3\text{SO}_3\text{H}$ (1.0×10^{-3} to 2.0×10^{-2} M). **140**
- Figure 44** Evolution of the absorption spectrum of **MV** in ACN for subsequent additions of $\text{CH}_3\text{SO}_3\text{H}$ (1.3×10^{-8} to 1.4×10^{-5} M). **141**
- Figure 45** Evolution of the fluorescence emission spectrum ($\lambda_{\text{ex}} = 550$ nm) of **MV** in ACN for subsequent additions of $\text{CH}_3\text{SO}_3\text{H}$ (1.3×10^{-8} to 1.4×10^{-5} M). The decrease of fluorescence intensity (a) is pointed out by the arrow; black dashed line: spectrum recorded after addition of Et_3N to neutralize the acid. (b): normalized fluorescence emission spectra at different concentration of $\text{CH}_3\text{SO}_3\text{H}$: the arrow points out the red-shift provoked by acidification of the medium; the black dashed line (addition of Et_3N) shows the reversibility of the process. **142**
- Figure 46** Relative energy levels of the three protonated forms of **MV** in vacuum and DMSO; the numbers refer to the position of the protonation, as indicated in the chemical structures reported. **143**
- Figure 47** Relative strain energy as a function of the torsion angle of the C-N bond in position 3, for **MV** in vacuum (red), in vacuum considering nuclei's relaxation (black) and in MeOH (blue). **145**
- Figure 48** Transient absorption spectrum obtained by laser flash photolysis of MB^+ in ACN (2×10^{-5} M). Time-evolution (50 ns, diamonds, 250 ns, squares, and 1 μs , triangles, after the laser pulse end) of the transient spectrum in air-equilibrated ACN (a); detail of the spectrum obtained 1 μs (empty triangles, grey line, secondary axis) after the laser pulse in air-equilibrated ACN, compared to the one obtained at the laser pulse end (b). **145**
- Figure 49** Transient absorption spectrum obtained by laser flash photolysis of NMB^+ in ACN (1.3×10^{-4} M). Time-evolution (50 ns, diamonds, 250 ns, squares, and 1 μs , triangles, after the laser pulse end) of the transient spectrum in air-equilibrated ACN (a); spectrum obtained 6 μs (diamonds, black dashed line, secondary axis) after the laser pulse in Ar-saturated ACN, compared to those obtained 140 ns (empty grey circles), 1 μs (empty grey squares) and 2 μs (empty grey triangles) after the laser pulse (b). **146**
- Figure 50** Time-evolution (50 ns, diamonds, 250 ns, squares, and 1 μs , triangles, after the laser pulse end) of the transient spectrum obtained by laser flash photolysis of **MV** in air-equilibrated ACN (a, 5×10^{-6} M) and MeOH (c, 2.5×10^{-5} M). Spectra obtained 50 ns (diamonds, solid lines) and 1 μs (empty triangles, dashed lines, secondary axis) after the laser pulse in air-equilibrated ACN (b) and MeOH (d). **147**

- Figure 51** Decays of the transient absorption of MB^+ in ACN (a), NMB^+ in MeOH (b), MV in ACN (c) and MeOH (d) in Ar-saturated (red), air-equilibrated (blue) and oxygen-saturated (green) solutions. **149**
- Figure 52** Variation of the emission signals (normalized to the reference $^1\text{O}_2$ signal (PN, top and RB, bottom) and corrected for different photon flux absorbed by the PSs) for NMB^+ as a function of $[\text{NMB}^+]$ (triangles); variation of the apparent Φ_Δ of NMB^+ as a function of its concentration (diamonds). Air-equilibrated ACN (full symbols) and CD_3OD (empty symbols), at room temperature. **151**
- Figure 53** Absorption spectra of MV in ACN before (black lines) and after irradiation (red lines), in the absence (left) and in the presence (right) of DBS. Initial MV concentration: 7.5×10^{-6} M. Irradiation: 90 minutes (left) and 60 minutes (right), white light, $P_a = 5.1 \times 10^{-6}$ Einsteins $\text{L}^{-1} \text{s}^{-1}$. The spectrum recorded after addition of DBS in the dark (green line) is totally superimposed to the one recorded before the addition. **153**
- Figure 54** Absorption spectra of MV in MeOH before (black lines) and after irradiation (red lines), in the absence (left) and in the presence (right) of DBS. Initial MV concentration: 1.8×10^{-5} M. Irradiation: 200 minutes, white light, $P_a = 4.2 \times 10^{-6}$ Einsteins $\text{L}^{-1} \text{s}^{-1}$. **153**
- Figure 55** Absorption spectra of MV in dioxane before (black lines) and after irradiation (red lines), in the absence (left) and in the presence (right) of DBS. Initial MV concentration: 6.0×10^{-6} M. Irradiation: 40 minutes (left) and 20 minutes (right), white light, $P_a = 4.6 \times 10^{-6}$ Einsteins $\text{L}^{-1} \text{s}^{-1}$. **154**
- Figure 56** Variation of the quantum yield of photobleaching of MV in dioxane, acetonitrile and methanol in the absence (secondary axis, empty grey squares, grey dashed lines) and in the presence (black diamonds, black solid lines) of DBS as a function of the normalized Dimroth-Reichardt's polarity of the solvent. **155**
- Figure 57** Evolution of the absorption spectrum of MV in dioxane as a function of irradiation time, in the presence of DBS. Initial MV concentration: 2.6×10^{-5} M. Irradiation: white light, 170 minutes. The decrease of absorbance is pointed out by the arrow from $t = 0$ (black line) to $t = 170$ min (black dashed line). **157**
- Figure 58** Evolution of the absorption spectrum of MV in ACN, irradiated in the presence of rubrene; MV spectrum before adding rubrene (green line), spectrum of MV +rubrene before irradiation (red line), MV spectrum after complete rubrene consumption (12 minutes irradiation, dashed black line). Initial MV concentration: 6.0×10^{-6} M. Irradiation: white light, 12 minutes. Inset: variation of absorbance at 550 nm during irradiation. **157**
- Figure 59** Some silica monoliths (series 2). From the left top: **SG0-ACN-DBTP**, **SG0-OC 2.5% OC**, **SG0**, **SG0-MV**, **SG0-MB⁺**, **SG0-DBTP**, **SG0-PN**, **SG0-OC-DBTP 1% OC**, **SG0-NMB⁺**, **SG0-RB**, **SG0-ACN**, **SG0-DCA**. **161**
- Figure 60** a): **SG2-ACN-DBTP** (left) vs **SG0-ACN-DBTP** (right); b): **SG1** monoliths at various concentrations of NCO and **5**; c): **SG0-NCO** monoliths at different amounts of NCO. **163**
- Figure 61** Drag off effect for **RB** in a diluted sample (**SG0**, a); dye expulsion from the matrix in concentrated **SG0** samples: the case of **DCA** (b, agglomerates at the monolith's external surface), and **DBTP** (c, agglomerates on the cuvette's surface). **166**
- Figure 62** Transmission UV-Vis spectra of some PSs in silica monoliths. **SG0-NMB⁺** (dashed-dotted line), **SG0-MV** (long dashed line), **SG0-ACN-DBTP** (black solid line), **SG0-OC-DBTP** (dashed line), **SG0-PN** (grey solid line) and blank silica sample (dotted line). Inset: region between 330 and 500 nm. **167**
- Figure 63** DRUV-Vis spectra of **DBTP**-derived silica materials. **SG0-ACN-DBTP** (solid line), **SG0-OC-DBTP** (dashed line), **SG2-ACN-DBTP** (dotted line). **167**
- Figure 64** Fluorescence excitation ($\lambda_{\text{em}} = 470$ nm, solid lines) and emission ($\lambda_{\text{ex}} = 385$ nm, dashed lines) spectra of **DBTP**-derived silica materials: **SG0-ACN-DBTP** (grey) and **SG2-ACN-DBTP** (black). **169**
- Figure 65** Fluorescence excitation ($\lambda_{\text{em}} = 460$ nm, dashed line) and emission ($\lambda_{\text{ex}} = 400$ nm, solid line) spectra of **SG0-DCA**. **169**
- Figure 66** Fluorescence excitation ($\lambda_{\text{em}} = 690$ nm, solid lines) and emission ($\lambda_{\text{ex}} = 590$ nm, dotted lines) spectra of differently concentrated **SG0-NMB⁺** monoliths: the intensity of the fluorescence signals increases linearly with the PS concentration. **170**
- Figure 67** UV-Vis spectra of **SG0-ACN-MV** (blue, left in the picture) and **SG0-MV** (red, right in the picture). **171**

- Figure 68** Fluorescence excitation ($\lambda_{em} = 675$ nm, solid lines) and emission ($\lambda_{ex} = 555$ nm, dashed lines) spectra of **MV**-derived silica materials: **SGO-MV** (red) and **SGO-ACN-MV** (black). **172**
- Figure 69** Time-evolution of the transient spectrum obtained by laser flash photolysis of a) **SGO-PN** (80 ns, diamonds, and 1 μ s, circles, after the laser pulse) and b) **SGO-DCA** (60 ns, diamonds, and 100 ns, squares, after the laser pulse). **174**
- Figure 70** Time-evolution (50 ns, black squares, and 250 ns, grey triangles, after the laser pulse end) of the transient spectrum obtained by laser flash photolysis of **SGO-DBTP**. Inset: transient decays after irradiation of **SGO-DBTP** (grey) and **SGO-ACN-DBTP** (black); signals monitored at 470 nm. **174**
- Figure 71** a) time-evolution of the transient spectrum obtained by laser flash photolysis of **SGO-MB⁺** (monitored at 70 ns, diamonds, 1 μ s, squares, and 7 μ s, triangles, after the laser pulse end) and b) transient absorption spectrum of **SGO-RB** recorded at the laser pulse end. **175**
- Figure 72** Time-evolution (65 ns, diamonds, 250 ns, squares, and 1 μ s, triangles, after the laser pulse end) of the transient spectrum obtained by laser flash photolysis of **SGO-NMB⁺**. Inset: transient decays at different wavelengths: 340 nm (red), 420 nm (green), 680 nm (black), 740 nm (grey) and 840 nm (blue). **176**
- Figure 73** Time-evolution (65 ns, diamonds, 250 ns, squares, and 1 μ s, triangles, after the laser pulse end) of the transient spectrum obtained by laser flash photolysis of **SGO-MV**. Inset: transient decays at different wavelengths: 340 nm (red), 400 nm (green), 680 nm (black), 720 nm (grey) and 800 nm (blue). **177**
- Figure 74** Variation of the 1O_2 phosphorescence signal as a function of the photon flux absorbed by the PS for **SGO-ACN-DBTP** (squares), **SG2-ACN-DBTP** (triangles), **SGO-PN** (diamonds), **SGO-MV** (stars), **SGO-NMB⁺** (crosses) and **SGO-RB** (circles). Point zero is taken into account for all the linear fits. **181**
- Figure 75** Intensity of the 1O_2 emission signal as a function of time for an **SGO-PN** monolith with an absorbance $\gg 2$ at 367 nm: (a) in ambient air; (b) after injection of O_2 in a flow cell during 60 min. **182**
- Figure 76** Intensity of the 1O_2 signal as a function of time recorded for **SGO-PN** after: (a) Ar introduced *in-situ* above the monolith for approx. 30 minutes (the arrow shows the start of Ar injection); (b) injection of Ar in a flow cell during 30 min before the measurement. **183**
- Figure 77** Singlet oxygen emission signals as a function of the added gas in the flow cell during 30 minutes prior to the measurement of the phosphorescence signal (successive experiments on a **SGO-PN** material). **183**
- Figure 78** Intensity of the 1O_2 emission signal as a function of OC % in **DBTP** monoliths of the same absorbance ($A \approx 0.3$ at 367 nm) in ambient air. Inset: linear plot of the intensity of 1O_2 phosphorescence signal (diamonds, black) and singlet oxygen lifetime (empty squares, red, secondary axis) versus OC %. **184**
- Figure 79** DMS concentration variation during photooxidation (PO) tests. (a) Saturation step in the dark: comparison between water-saturated **SGO-ACN-DBTP** (black, triangles), **SGO-ACN-DBTP** (grey line) and **SGO-RB** (dotted black line). (b) Profile throughout the PO test for a water-saturated **SGO-ACN-DBTP** monolith. Reaction conditions: 100 mL min⁻¹ (air flow), 200 ppmv (DMS concentration), 420 nm (irradiation wavelength), room temperature. **187**
- Figure 80** GC profiles obtained after thermodesorption of the PO products from a **SGO-NMB⁺** monolith (two subsequent desorptions); retention times of the products: MMTS (12.68 min), DMSO₂ (10.43 min), DMSO (8.95 min), DMDS (7.23 min). **188**
- Figure 81** DRUV spectra of **SGO-ACN-DBTP** (black) and **SG2-ACN-DBTP** (grey) before (solid lines) and after (dashed lines) the PO tests for the evaluation the photobleaching extent. **191**
- Figure 82** Picture of the photosensitizing materials used: **RB-ps** (a), **RB-Si** (b), **DBTP-Si** (c), **AQ-Si** (d). **194**
- Figure 83** DRIFT spectra of the prepared materials: a) **RB-Si**, b) **DBTP-Si** and c) **AQ-Si**. The spectra are compared to those of the starting functionalized silica gels (dashed line for NH₂-Si and dotted line for Cl-Si). **197**
- Figure 84** DRUV spectra of solid **RB** (solid line), **RB-ps** (dashed-dotted line) and **RB-Si** (dotted line) vs irradiance of 575 nm fluorescent tubes (grey, secondary axis). **198**
- Figure 85** DRUV spectra of solid **DBTP-COOH** (solid line), **DBTP-Si** (dashed line), solid **AQ-COOH** (dotted line) and **AQ-Si** (dashed dotted line) vs irradiance of 419 nm fluorescent tubes (grey, secondary axis). **198**

Figure 86 Absorption spectra of RB (solid line), DBTP-COOH (dotted line) and AQ-COOH (dashed-dotted line, secondary axis) in methanol at room temperature.	199
Figure 87 (left) GC monitoring of α-t , asc , p-c and others during the photooxidation of α-t in the presence of RB (entry 2). (right) UV monitoring: intervals of 10 minutes, until disappearance of the signal of α-t at 267 nm.	202
Figure 88 Evolution of the absorption spectrum of RB as a function of the irradiation time during the photooxidation of α-t (entry 2). The arrow shows the decrease of absorbance and slight bathochromic shift occurred during the two hours of irradiation.	203
Figure 89 GC monitoring of α-t , asc , p-c and others during the photooxygenation of α-t in the presence of DBTP-COOH (entry 7).	204
Figure 90 (left) GC monitoring of α-t , p-c , ald and others during the photooxygenation of α-t in the presence of AQ-COOH (entry 11). (right) UV monitoring: measuring intervals of 10 minutes (0→150 minutes), until disappearance of the signal of α-t at 267 nm (grey) and the formation of ald , absorbing with a maximum at 250 nm.	205
Figure 91 GC monitoring of p-c and ald (main axis), ac , 7-ol , 8-ol and others (secondary axis) during the photosensitized oxidation of p-c in the presence of AQ-COOH (homogeneous ACN solution, standard conditions).	207
Figure 92 Chromatogram of the crude reaction mixture: the main product has a retention time of 14.71 minutes (a); SIFI analysis of the main product's peak, selecting the main m/z peaks of asc (c) and ald (b) to obtain the corresponding chromatographic signals.	208
Figure 93 MS spectra of asc and i-asc .	209
Figure 94 GC evolution of the crude reaction mixture resulting from the photooxidation of α-t with AQ -sensitizers; from top to bottom: t = 0, 50, 80, 110 and 150 minutes of irradiation.	210
Figure 95 MS spectra and chemical structures of the main products of photooxygenation of p-c . ald) cuminaldehyde, ac) 4-isopropylbenzoic acid, 7-ol) <i>p</i> -cymene-7-ol, 8-ol) <i>p</i> -cymene-8-ol.	211
Scheme 1 Schematic representation of the photophysical and photochemical pathways occurring after light absorption by the PS.	28
Scheme 2 Jablonski diagram representing schematically the photosensitized production of singlet oxygen; the energetic levels corresponding to the different spin states of molecular oxygen are reported.	33
Scheme 3 Schematic representation of the molecular orbitals diagram for O ₂ . The different spin orientations in the π^* antibonding orbitals are underlined in red.	34
Scheme 4 Schematic description of electron motion in electron transfer (ELT) reactions.	36
Scheme 5 Schematic description of electron motion in energy transfer (ET) reactions. a) electron exchange mechanism and b) dipole-dipole mechanism.	37
Scheme 6 Synthesis of compound 1 .	65
Scheme 7 Synthesis of compound 2 .	66
Scheme 8 Synthesis of compound 3 .	67
Scheme 9 Synthesis of compound 4 .	67
Scheme 10 Synthesis of graftable compounds 5 and 6 .	72
Scheme 11 Grafting of 2 (DBTP-COOH), AQ-COOH , RB on functionalized silica gels.	72
Scheme 12 Schematic representation of the equipment for steady-state detection of singlet oxygen phosphorescence at 1270 nm.	87
Scheme 13 Schematic representation of the equipment for time-resolved detection of singlet oxygen phosphorescence at 1270 nm.	88
Scheme 14 Representation of the set-up for DMS photooxidation at the gas-solid interface.	91

Scheme 15 Carbodiimide/NHS-mediated peptide coupling reaction applied to the nucleophilic attack to carboxylic acids.	101
Scheme 16 Schematic representation of the addition of <i>N</i> -Boc-1,6-hexanediamine to DBTP . The chemical structure of the Boc group is described.	102
Scheme 17 Protonation of the carbonyl group of MV in the presence of acids yielding MV-OH .	136
Scheme 18 Photosensitized oxidation of α-t .	201
Scheme 19 Photosensitized oxidation of <i>p</i>-c in the presence of AQ -sensitizers	206
Scheme 20 Thermally/photochemically induced isomerization of ascaridole (asc) to isoascaridole (<i>i</i>-asc).	208
Scheme 21 H-abstraction and radical formation on α-t : photosensitized dehydrogenation yields <i>p</i>-c .	213
Table 1 Maximum absorption wavelengths (0-0 transition), corresponding molar extinction coefficients and quantum yields of singlet oxygen production of the PSs used in this work; possibility of grafting and number of corresponding reference (SciFinder: research "substance identifier", June 28 th 2013). Data relative to already published studies.	60
Table 2 Molar absorption coefficients (ϵ) at the absorption maxima, relative band intensities and singlet excited state energy of 1-4 in ACN. Errors: approx. 10% for the ϵ values.	104
Table 3 Wavelengths of the fluorescence emission maxima, fluorescence lifetimes, quantum yields of fluorescence of compounds 1-4 and DCA in air-equilibrated ACN. Values in brackets are relative to Ar-saturated ACN solutions.	106
Table 4 Rate constants of transient decay (k_dT) in oxygen-, air- and argon- saturated solutions, rate constants of transient quenching by O ₂ (k_q, O_2T), $\epsilon_T\Phi_T$ values for compounds 1-4 . Solvent: ACN at room temperature.	110
Table 5 Quantum yields of formation of the tripled excited state of rubrene and anthracene as energy acceptors; rate constants of quenching of the triplet excited state of the PSs by energy transfer to anthracene ($k_{q, Ant}$).	112
Table 6 Values of ¹ O ₂ emission signals SeR and SePS in ACN at room temperature, at different absorbances (A^R , A^{PS}) and of SeRSePS corrected for small differences in absorption factors (α) between PS (DCA , 1 , 2 , 3 and 4) and PN ; wavelength of irradiation: 367 nm.	114
Table 7 Quantum yields of singlet oxygen production (Φ_Δ) and rate constants of ¹ O ₂ quenching by the PS for DCA and compounds 1-4 determined by direct singlet oxygen luminescence detection. Solvent: air-equilibrated ACN.	115
Table 8 Quantum yields of singlet oxygen production (Φ_Δ) for DCA and compounds 1-4 determined by detection using rubrene as a chemical probe; comparison with the results obtained by direct detection. Solvent: air-equilibrated ACN at 25 °C.	116
Table 9 Apparent quantum yields of singlet oxygen production of 2 in ACN at room temperature, measured by direct ¹ O ₂ detection and by trapping by rubrene at different concentrations of PS.	117
Table 10 Measured quantum yields of ¹ O ₂ production (Φ_Δ , direct method), rate constants of fluorescence emission (k_f , Ar-saturated solutions), rate constant of S ₁ quenching by O ₂ (kO_2S), fractions of S ₁ states quenched by O ₂ (PO_2S), fractions of T ₁ states quenched by O ₂ (PO_2T), quantum yields of triplet (T ₁) formation (Φ_T) and fractions of T ₁ states quenched by O ₂ yielding ¹ O ₂ ($f\Delta T$) for 1-4 and DCA in ACN. Values from Tables 3, 4 and 7.	119
Table 11 Reduction potentials ($E(PS/PS^{\bullet-})$) of DCA , 1 , 3 , 4 and free energy changes (ΔG) involved in the ELT reaction from Et ₃ N as an electron donor to the S ₁ state of the PSs; Stern-Volmer constants (K_{SV, Et_3NS}) and rate constants of fluorescence quenching by Et ₃ N (k_q, Et_3NS); free energy changes ($\Delta G_{O_2^{\bullet-}}$) involved in the formation of superoxide radical anion by ELT from PS ^{•-} as an electron donor. Solvent: ACN at room temperature.	124

- Table 12** Wavelengths of absorption maximum (λ_{max}), molar extinction coefficients at the absorption maximum (ϵ_{max}), wavelengths of fluorescence emission maximum ($\lambda_{\text{max,em}}$), fluorescence quantum yields (Φ_{F}) and fluorescence lifetimes (τ_{F}) in MeOH, ACN and the ratio of the values measured in MeOH and in ACN (only for Φ_{F} and τ_{F}) for the four PSs under study. Air-equilibrated solutions at room temperature. **132**
- Table 13** Wavelengths of absorption maximum (λ_{max}) and corresponding energy of the singlet excited state (E_{S}) for **MV** in several solvents; properties of the solvents: hydrogen bond donation ability (α), hydrogen bond acceptance (β), polarity/polarizability coefficient (π^*), Dimroth-Reichardt's polarity ($E_{\text{T}}(30)$), Dimroth-Reichardt's normalized polarity (ETN, see equation 5.02) and sum of all the mentioned parameters (XYZ, see equation 5.01). Values taken from:³⁰¹. **135**
- Table 14** Wavelengths of the first allowed electronic transition (absorption, *abs* and fluorescence emission, *em*) calculated for **MV** and **MV-OH** in vacuum, ACN, acidified ACN and MeOH; Values are compared to those experimentally measured (*exp*). **143**
- Table 15** Rate constants of triplet decay (k_{d}) in Ar-saturated, air-equilibrated and O₂-saturated solutions, rate constants of triplet quenching by O₂ ($k_{\text{q,O2T}}$), triplet lifetimes (τ_{T}) in Ar-saturated solutions. Data for **MB⁺**, **NMB⁺** and **MV** in ACN and MeOH. **148**
- Table 16** Quantum yields of singlet oxygen production (Φ_{Δ}) and rate constant of ¹O₂ total quenching by the PS (*ktPS*) for **RB**, **MB⁺**, **NMB⁺** and **MV** in ACN and CD₃OD. **RB** and **PN** were used as reference PSs in CD₃OD and ACN, respectively. In brackets the Φ_{Δ} values measured by detection with a probe (rubrene). **150**
- Table 17** Variation of the apparent quantum yields of singlet oxygen production with the concentration of **NMB⁺** in air-equilibrated CD₃OD and ACN at room temperature. **151**
- Table 18** Quantum yields of bleaching ($\phi_{\text{bleaching}}$) of **MV** in MeOH, ACN, dioxane, both in the absence and in the presence of DBS; ratio of the quantum yields of bleaching calculated in the presence and in the absence of dibutyl sulfide. **154**
- Table 19** Structural analysis of silica monoliths. Surface area (B.E.T. method), percentage, area, volume and diameter of mesopores (calculated by B.J.H. method), water percentage measured by sample weighing before and after drying under vacuum at 80 °C (in brackets values relative to TG-MS analyses). PO = after photooxidation tests. **164**
- Table 20** Spectroscopic characterization of dye-doped **SG**-materials: maximum absorption wavelengths for the 0-0 transition (λ_{max}), molar extinction coefficients at λ_{max} (ϵ_{max}), maximum wavelengths of fluorescence emission ($\lambda_{\text{max,em}}$) and fluorescence lifetimes (τ_{F}); in brackets the corresponding values for PSs in MeOH (or in other solvents if specified). **168**
- Table 21** Spectroscopic parameters of **MV** in various solvents and silica monoliths: absorption, fluorescence excitation-emission maximum wavelengths (λ_{max}), absorption extinction coefficients (ϵ_{max}) and fluorescence lifetimes (τ_{F}). **173**
- Table 22** Rate constants of transient decay (k_{d}) at different monitoring wavelengths, triplet excited state lifetimes measured for several silica monoliths and triplet excited state lifetimes in ACN (air-equilibrated and Ar-saturated solutions) and MeOH. **178**
- Table 23** Values of ¹O₂ lifetimes (τ_{Δ}) derived from monoexponential decays in the case of **PN**, **DCA**, **DBTP** and **RB** monoliths (a) and from biexponential decays in the case of **SGO-MV** and **SGO-NMB⁺** (b). **179**
- Table 24** Slopes (*b*) of the variation of the ¹O₂ emission intensity (S_{e}) as a function of the photon flux absorbed by the PS (α_{PS}) (equation 6.01), quantum yields of ¹O₂ production relative to **PN** ($\Phi_{\Delta,\text{rel}}$). **180**
- Table 25** PO activity of some **SGO** materials (series 3) for the sensitized oxidation of DMS: conversions (%) and initial rates are reported for both the first and the second cycles. The conversion values normalized by the absorbed photon flux are reported in brackets. Bleaching percentage (after 2 × 24 h irradiation) was estimated from DRUV spectra recorded before and after the two irradiation cycles. **189**
- Table 26** PO properties of some **DBTP** derived monoliths for the photooxidation of DMS, two series corresponding to as many synthesis batches. Initial conversion rate (v_0), conversion % and, in brackets, percentage conversion normalized by the photon flux absorbed by the PS, bleaching % (estimated from DRUV-Vis spectra). Specific surface areas and mesoporous percentage: see Table 20. **190**

Table 27 Experimental details for the synthesis of PS-Si and characteristic IR bands.	195
Table 28 Quantum yields of singlet oxygen production of RB , DBTP-COOH , AQ and AQ-COOH determined by chemical probing with rubrene (Reference PS: PN . Solvent: air-equilibrated ACN at room temperature).	200
Table 29 Experimental results for the photooxidation of α -t.	202
Table 30 Reuse experiment: experimental results for photooxygenations of α -t with DBTP-Si (irradiation times: 30 min). Initial loading: 50 mg of DBTP-Si . Approximately 5 mg lost for each recovery.	205
Table 31 Calculated free energy for the electron transfer reactions from α -terpinene to the singlet or triplet excited states of the studied photosensitizers; free energy of the photosensitized ELT reaction from the PS radical anion to oxygen, yielding superoxide radical anion. Redox potentials are expressed vs SCE in ACN. ΔG values obtained from equation 1.15. Redox potential of α -t: $E(\alpha\text{-t}/\alpha\text{-t}^{\bullet+})_0 = 1.60 \text{ V vs SCE}$. ³⁶³	214
Table 32 Kinetic constants for photosensitized conversion of α -t (k = kinetic constant directly calculated from the evolution of UV absorption signals; k_p = approximate values of kinetic constants normalized by the estimated photon flux absorbed by the PS (equation 3.37); ϕ_{conv} = approximate values of quantum yields of conversion of α -t).	215
Chart 1 Polyaromatic PSs: anthracene and 9,10-dicyanoanthracene.	39
Chart 2 Aromatic ketones as PSs: 9,10-anthraquinone and perinaphthenone (1 <i>H</i> -phenalen-1-one).	40
Chart 3 Phenazine (top) and phenothiazine (bottom) PSs.	40
Chart 4 Xanthene dyes as PSs; rose bengal is one of the most commonly used derivative of xanthene.	41
Chart 5 Acridine.	42
Chart 6 Porphine and phthalocyanine: mother compounds of the large chemical families of porphyrins and phthalocyanines.	43
Chart 7 Miscellaneous PSs: triphenylpyrylium ion (left), fullerene C60 (middle) and tris(bipyridine) Ruthenium(II) ion.	44
Chart 8 Commercial PSs selected for this work: 9,10-dicyanoanthracene (DCA), perinaphthenone (PN), anthraquinone-carboxylic acid (AQ-COOH), methylene blue (MB ⁺), rose bengal B (RB), methylene violet (MV), new methylene blue (NMB ⁺).	56
Chart 9 Chemical structure of DBTP and substituents (R) corresponding to 2-6 DBTP derivatives.	60
Chart 10 Structure of the cyanoanthracene derivatives synthesized: DBTP (1), DBTP-COOH (2), DBTP-CONH-(CH ₂) ₃ -OH (3) and DBTP-CONH-(CH ₂) ₆ -NH-Boc (4).	100
Chart 11 Chemical structure of methylene blue (MB ⁺), rose bengal (RB), methylene violet (MV) and new methylene blue (NMB ⁺).	128
Chart 12 PSs encapsulated in silica monoliths.	160
Chart 13 Compound 6, the DBTP derivative grafted onto silica monoliths.	160
Chart 14 The three PSs grafted to silica.	194
Chart 15 Schematic representation of the reference (RB-ps) and synthesized materials.	195
Chart 16 Identified secondary products obtained during the photooxidation of α -t in the presence of AQ photosensitizers: 4-isopropylbenzaldehyde (cuminaldehyde, ald), 4-isopropylbenzoic acid (ac), (4-isopropylbenzyl)methanol (<i>p</i> -cymene-7-ol, 7-ol), 2-(4-methylphenyl)-2-propanol (<i>p</i> -cymene-8-ol, 8-ol), 1,3,3-trimethyl-2-oxabicyclo[2.2.2]octane (eucalyptol, euc), 1-isopropyl-4-methyl-7-oxabicyclo[2.2.1]heptane (isocineole, <i>i</i> -cin), and possible open chain aldehydes (3,7-dimethyl-2-octenal-6-on, op1) and (3-isopropyl-2-heptenal-6-on, op2).	206

1 Introduction

1.0. PHOTOCHEMISTRY IN ACTION

Photochemistry studies chemical reactions induced by the interaction between light and matter. Sunlight represents an immense energy source: the amount of solar radiation arriving to Earth has been calculated at approx. 1366 W m^{-2} (solar constant) and even after passing through our atmosphere and taking into account the geometrical parameters of the case (Earth is a rotating sphere), the average solar energy power touching Earth surface is 250 W m^{-2} daily. Taking into account the whole surface irradiated by sunlight, the total power “generated” by the solar radiation reaching Earth’s surface approaches 50 million GW per day, while the daily total power generated by a power station can reach some GW. It is not difficult thus to imagine the impacts and the interests connected to these immense amount of available energy.

For ages photochemical reactions have been responsible for the formation of the atmosphere as it is nowadays. Furthermore, thanks to the photosynthesis carried out by cyanobacteria, free oxygen began to accumulate in the atmosphere, approx. 2.4 billion years ago. The presence of free O_2 in the atmosphere reduced the amount of methane and other compounds responsible of the greenhouse effect and allowed the development of life outside water. Photosynthesis controls the delicate oxygen equilibrium of the atmosphere: light and its interactions with matter are responsible for life on Earth. Vision and the production of vitamin D (“sunshine vitamin”) are other examples of the fundamental impacts of photochemistry on our lives. Mankind has been capable to apprehend this power to develop techniques that are really important in our daily life: photography, photochromic materials, photopolymerization and imaging are just some examples.¹

Increasing demands of energy supplies, as well as impelling demands for techniques to restrain pollution, immensely amplified the global resonance of photochemistry: the presence of such an amount of freely available and renewable energy made photochemistry really attractive from both economical end environmental points of view. In addition, photons can be considered as traceless reagents: no waste is produced upon light absorption. Researches on solar energy storage and photochemical oxidation techniques have been greatly stimulated over the past few decades: the age of green chemistry has officially begun. Solar energy mediated synthesis, photovoltaics and photoinduced pollutant degradation or mineralization are some subjects whose development is strictly related to the energetic-environmental demands of nowadays society; photomedical and photobiological techniques for health and disinfection are not appealing less attention. Among all the branches of photochemistry, photoinduced oxidation reactions, which make the object of this work, will be treated and described in more detail.

2.0. PHOTOOXIDATION REACTIONS

Photochemical reactions usually follow mechanistic pathways that cannot be easily gained by conventional thermal processes: reaction products, their distribution and their stereochemical structures can be tuned by choosing the synthetic route corresponding to the suitable mechanism for the desired products. In general, light absorption excites one electron from the highest occupied molecular orbital (HOMO) to the lowest unoccupied molecular orbital (LUMO): such a variation in the electronic configuration can change the fate of a chemical reaction, yielding products that cannot be formed in the dark. For example, according to the Woodward-Hoffmann rules,² a given pericyclic reaction can follow disrotation or conrotation rearrangements depending on the choice of thermal or photoinduced activation, with different final stereochemical configurations. Similarly, photoinduced oxidation reactions can follow different mechanisms than conventional thermal oxidations, yielding different products.³ Following the definitions recommended by IUPAC, photooxidation reactions can be classed in two categories: a substrate can lose one or more electrons after being promoted to its excited state upon light absorption, or oxygen can directly add to a given substrate by means of light absorption. The latter process is commonly defined as photooxygenation.^{4,5} The advantages of photooxidation reactions lie in the possibility to obtain high energy reactive species upon light absorption, *via* either the formation of radicals or the generation of excited species, much more reactive than ground state oxygen and that can add to several substrates. In both cases the activity of the oxidation process can be strongly improved and depending on the mechanism the products distribution can be tuned. Depending on the absorbing system different Reactive Oxygen Species (ROS) can be formed: singlet oxygen ($^1\text{O}_2$), hydrogen peroxide (H_2O_2), ozone (O_3) or radicals such as hydroxyl (OH^\bullet) or superoxide anion ($\text{O}_2^{\bullet-}$).^{6,7} These species have high oxidation capability and can react with many substrates. ROS can thus find applications as reactants in many oxygenation/oxidation processes, the mechanisms and the products depending both on the substrate and on the reactive oxygen species formed. The photochemical approach for ROS production needs just light (solar light when possible) and oxygen (air) to initiate the oxidation reaction: starting from freely available and renewable ingredients it is possible to develop oxidation reactions for many applications.

Photooxidation reactions can be induced either by direct light absorption by the substrate or by means of another species that absorbs light and consequently initiates the oxidation of the substrate. In the latter case, two approaches for initiating oxidation processes are mainly employed:

- Photocatalysis is defined as a “change in chemical reaction or its initiation under the action of ultraviolet, visible or infrared radiation in the presence of a substance—the photocatalyst—that absorbs light and is involved in the chemical transformation of the reaction partners”. Photocatalysts are narrow band-gap semiconductors like titanium dioxide that can absorb light and produce, in the presence of water, OH^\bullet as main reactive oxygen species; hydroxyl radical can non-selectively oxidize organic substrate until total mineralization (CO_2 and H_2O).⁵
- Photosensitization refers to a “photophysical or photochemical alteration occurring in one molecular entity as a result of initial absorption of radiation by another molecular entity called photosensitizer”; photosensitizers (PS) are not consumed during the chemical transformations. PSs are organic or inorganic compounds that can produce ROS such as

singlet oxygen and superoxide radical anion upon light absorption; oxidation reactions are usually only partial, allowing selective formation of high-added value compounds.⁵

3.0. PHOTSENSITIZATION

3.1. General aspects

In photosensitized reactions light quanta are absorbed by a molecular species, the photosensitizer (PS, usually organic compounds or metal complexes), and then transferred either directly to the substrate or to molecular oxygen. This energy conveyance can take place either by energy or electron transfer. In the case of direct interaction between the PS and the substrate, reactive radicals may be formed; in the case of interaction between the sensitizer and oxygen, singlet oxygen and superoxide radical anion are usually formed. After transferring the energy excess, the PS is regenerated in its ground state, ready to restart the cycle.⁶⁻⁸

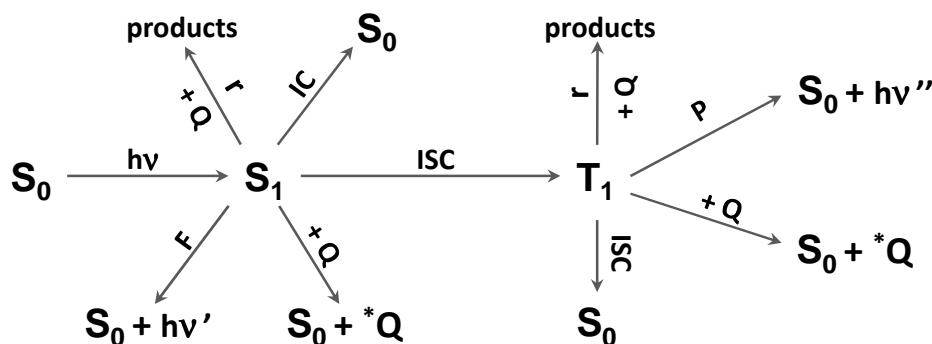
Since photosensitizers absorb light inducing chemical transformations of the reaction participants without being consumed in the chemical process, they can be also defined as *organic photocatalysts* (to distinguish from semiconducting materials for photocatalysis). The use of photosensitizers to induce oxidation reactions presents many advantages:

- Only light (in the visible range) and oxygen (air) are needed as reactants; thus, photosensitization totally fulfills environmental restrictions and the definition of *green* processes: the use of renewable energetic sources and eco-compatible reactants (photons are traceless reagents)
- Many visible-light absorbing chromophores can be used as PSs: not only solar radiation can be directly used to initiate the process, but by choosing suitable compounds as photosensitizers the light absorption range can be tuned and adapted to the foreseen application
- By modifying the PS structure it is possible to tune its photophysical and redox properties, adapting thus the photochemical system to the desired products
- Thanks to the formation of $^1\text{O}_2$ and $\text{O}_2^{\bullet-}$ as main reactive oxygen species, it is possible to select the degree of substrate oxidation: partial oxidation is truly obtained and high-added value compounds can be produced. The spectrum of possible applications is thus very large.

Semiconductor and organic photocatalysts, despite the common definition, present two important differences: the mostly used semiconductors (TiO_2 , ZnO) absorb light mainly in the UV region and yield total mineralization (oxidation) of the organic substrate, while photosensitizers are able to absorb light in all the spectral regions between UV and near-IR and the selectivity of the oxidation reaction can be controlled. It emerges here that the applications in the general field of photoinduced oxidation reactions are different: while semiconductors are mainly utilized for water and air depollution and disinfection, PSs can find applications also in organic synthesis and biological-medicinal treatments.^{6,8} The potential applications of photosensitization will be discussed in detail later.

3.2. Light absorption and photophysical pathways

The photosensitization mechanism has been described in a general way, without taking into account the various physical aspects deriving from the interaction between light and the PS. In Scheme 1 the possible photophysical pathways that can occur after light absorption are described.³



Scheme 1 Schematic representation of the photophysical and photochemical pathways occurring after light absorption by the PS.

Upon absorption of a quantum of energy (a photon, $h\nu$), a generic singlet excited state of the PS (S_n) is populated by the excited electron; the S_n state is rapidly deactivated by non-radiative vibrational relaxation to yield the first more stable singlet excited state (S_1). The S_1 state can be deactivated following several pathways:

- by physical interaction with a generic quencher (Q), the quencher itself can be excited to a generic state Q^* and the PS comes back to its ground state (S_0)
- by interaction with a quencher (the PS itself can act as a quencher for other PS molecules) a chemical reaction (r) can occur, yielding products depending on the structures of PS and Q
- by internal conversion (IC) the ground state S_0 can be obtained without any emission
- by fluorescence emission the S_1 state can be deactivated to the ground state S_0 with emission of a quantum of energy ($h\nu'$)
- by intersystem crossing (ISC), a generic triplet excited state (T_n) can be obtained

ISC is a spin-forbidden transition that becomes more probable in organic compounds for which spin-orbit coupling is non-negligible. Simplifying the situation without going into quantum mechanical details, spin-orbit coupling could be described as the coupling of the spin and the orbital motions of the excited electron. The main consequence of spin-orbit coupling is to blur the distinction between two states characterized by different spin multiplicity (S_1 and T_n in this case). The states that should be separated become partially mixed: the triplet state takes on some singlet state character and *vice versa*. Thanks to this quantum mixing, the forbidden singlet-triplet transition somehow steals some intensity from the allowed singlet-singlet transition: ISC can take place and the triplet excited state (T_n) of the PS can be populated. As for the $S_n \rightarrow S_1$ transition, by vibrational relaxation the first triplet excited state (T_1) is formed; such a state can be deactivated in several ways:

- by physical interaction with a generic quencher (Q), the quencher itself can be excited to a generic state Q^* and the PS comes back to its ground state (S_0)
- by interaction with a quencher a chemical reaction can occur, yielding products depending on the PS and Q structures
- by intersystem crossing (ISC), the ground state S_0 can be re-gained without any emission
- by phosphorescence emission the T_1 state can be deactivated to the ground state S_0 with emission of a quantum of energy ($h\nu''$)

In order for photosensitized reactions to take place, the energy absorbed by the PS has to be transferred to either the substrate or oxygen, to create more reactive species: molecular oxygen and the substrate act as quenchers (Q).

Since O_2 is exceptionally characterized by a triplet ground state and since selection rules tell us that transitions between states with the same spin multiplicity are spin-allowed (*i.e.* more probable), it emerges that the production of singlet oxygen passes through the formation of the PS triplet excited state (T_1) and the following interaction with ground state oxygen (T_0 , 3O_2). The transfer of the exceeding energy will be discussed in paragraph 3.3 with the oxidation reaction mechanisms. For now thus, the most important species to be considered is the PS triplet excited state. Once light absorbed, intersystem crossing represents the key-pathway for obtaining T_1 (vibrational relaxation $T_n \rightarrow T_1$ is much more rapid and becomes negligible): the efficiency of the photosensitized oxidation reaction will be strictly conditioned by the formation of the T_1 state, in turn related to the intrinsic efficiency of intersystem crossing and to the efficiency of the competitive photophysical pathways. The less dissipation mechanisms (of S_1 state) other than ISC are favored, the more likely triplet formation will occur. In this analysis the fact that, as a consequence of the spin-forbidden character of the transition, the photophysical pathways involving two excited states with different spin multiplicities are slower than in the case of spin-allowed transitions should be also taken into account. For this reason, the triplet excited state lifetimes are usually much longer than those of the singlet excited states.

A very useful concept for the determination of the efficiency of all photophysical processes is that of quantum yield, defined by equation 1.01.

$$\Phi = \frac{n^\circ \text{ moles (molecules) product}}{n^\circ \text{ einstein (photons) absorbed}} \quad 1.01$$

For example, if a PS has quantum yield of triplet formation (Φ_T) equal to 0.6, it means that the 60% of the PS molecules that absorb light subsequently yield the triplet excited state. More detailed analytical formulas for the determination of quantum yields will be given later in the text.

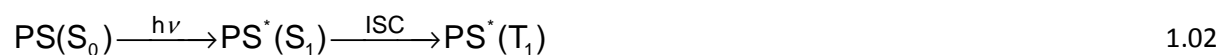
3.3. Oxidation mechanisms

Until now, the absorption of light and its first consequences on the photophysics of the photosensitizer have been discussed. Once the excited state of the PS is formed, its interaction with O_2 can yield one of the ROS cited above and the sensitizer in its initial S_0 ground state. This interaction represents the very heart of photosensitization: light quanta are absorbed by molecular

oxygen by means of the intermediation of an efficient chromophore, the photocatalyst.⁶⁻⁸ Alternatively, the excited PS can interact with the substrate to yield radicals:⁹ in such a situation, oxygen doesn't represent a key intermediate, but it can participate to the overall mechanism. It is important to take into account that, even if not described here, other dissipation pathways can undesirably occur from the interaction PS-O₂. The PS excited state usually involved in photosensitized oxidation reactions is the triplet state; nonetheless, photosensitization from the singlet excited state can also occur.

Conventionally, two general mechanisms can be identified for the transfer of quanta between the involved species: electron transfer (**ELT**, type I reactions) and energy transfer (**ET**, type II reactions). The mechanisms are detailed below.

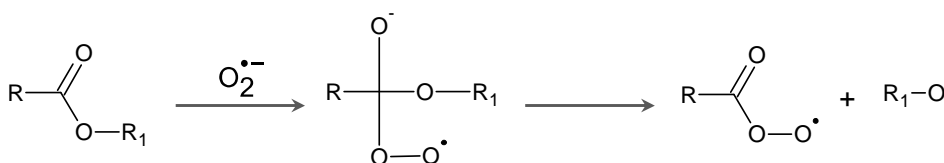
3.3.1. Type I reactions



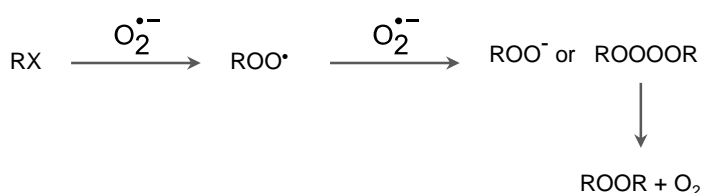
Equations 1.02 to 1.12 represent the main reactions that can occur through ELT mechanisms.^{6-8,10-14} Other reactions are possible (especially in water) but this scheme summarizes the general mechanism and the species involved. After initial PS excitation (equation 1.02), the transfer of one electron from the sensitizer to the quencher Q (the organic substrate to oxidize) yields a radical pair (equation 1.03): starting from this radical pair an electron transfer cascade reaction can take place, according to the equations above. Superoxide radical anion (O₂^{•-}) can then be formed by ELT between the radical anion of the PS and oxygen (equation 1.04). This is the main ROS formed by ELT, from which other reactive species can be formed: hydroperoxyl (HOO[•]) and hydroxyl (HO[•]) radicals,

hydrogen peroxide (H_2O_2). Direct reaction between $\text{O}_2^{\bullet-}$ and Q^{*+} can yield oxygenation products (equation 1.06). Alternatively hydrogen abstraction from Q^{*+} can yield hydroperoxy-radicals and partially dehydrogenated Q radicals (equations 1.05 and 1.07); the latter can then react with ground state oxygen giving either dehydrogenation ($\text{Q}(-\text{H}\cdot)$) or oxygenation products (equations 1.08 and 1.09). The ROS produced during the first steps ($\text{O}_2^{\bullet-}$ and HOO^{\bullet}) can then rearrange to yield other reactive species, as indicated in equations 1.10-1.12, mainly implying H_2O_2 participation to the reaction and the formation of the highly reactive HO^{\bullet} radical (equation 1.12). The reactivity between the substrate and superoxide radical anion in aprotic solvents can follow different possible routes, mainly depending on the substrate itself. $\text{O}_2^{\bullet-}$ can act as a strong nucleophile towards carboxylic derivatives like esters, acyl halides and halogenated hydrocarbons, yielding peroxides; it can act as either an oxidizing or a reducing agent toward substrates with coupled hetero atoms (ascorbic acid, catechols and α -tocopherol *e.g.*) and quinone-like compounds, respectively; it can reduce or oxidize metal ions like Fe^{+3} in its complexed forms. Some of these reactions are presented in Figure 1.^{12,14}

Nucleophilic addition to carbonyl



S_N2 reaction with halogenated hydrocarbons



One-electron reduction

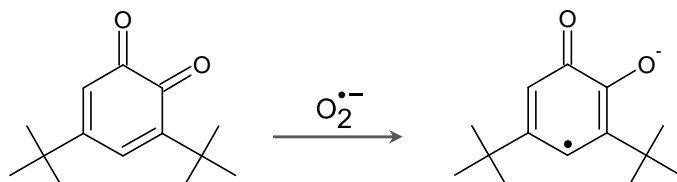


Figure 1 Main reactions involving superoxide radical anion.

In water and protic solvents the superoxide radical anion can be formed, but it has a limited reactivity: as a strong Brønsted base it rapidly attacks water to yield the hydroperoxyl radical HO_2^\bullet which is responsible of the radical reactivity in these media, through its disproportionation to yield hydrogen peroxide (equations 1.13, 1.14).¹²



The feasibility of ELT processes depends on the first electron exchange between the excited PS and Q (equation 1.03); the excited state of the sensitizer must be a good electron acceptor to oxidize the substrate and create the radical pair ($\text{PS}^{\bullet-} - \text{Q}^{\bullet+}$). The thermodynamic feasibility of such an electron transfer is described by the Rehm-Weller equation (equation 1.15),¹⁵

$$\Delta G = 96.39 \left[E_{(\text{D}/\text{D}^{\bullet+})} - E_{(\text{PS}/\text{PS}^{\bullet-})} - \frac{e_0^2}{a\epsilon_r} - \Delta E_{00} \right] \quad 1.15$$

where $E_{(\text{D}/\text{D}^{\bullet+})}$ (V) is the oxidation potential of the donor (a generic Q), $E_{(\text{PS}/\text{PS}^{\bullet-})}$ (V) the reduction potential of the acceptor (PS), e_0^2 is the energy gained by bringing the two radical ions to the encounter distance ($a = 7 \text{ \AA}$) in a solvent of dielectric constant ϵ_r (approx. 0.06 V in ACN) and ΔE_{00} (eV) is the electronic excitation energy of the PS. ΔG represents the free energy change (kJ mol^{-1}) of the ELT reaction between a substrate and the excited PS. For the formation of superoxide radical anion (equation 1.04), since no excited states are directly concerned, the thermodynamic feasibility is simply expressed by equation 1.16, as for a common redox couples.

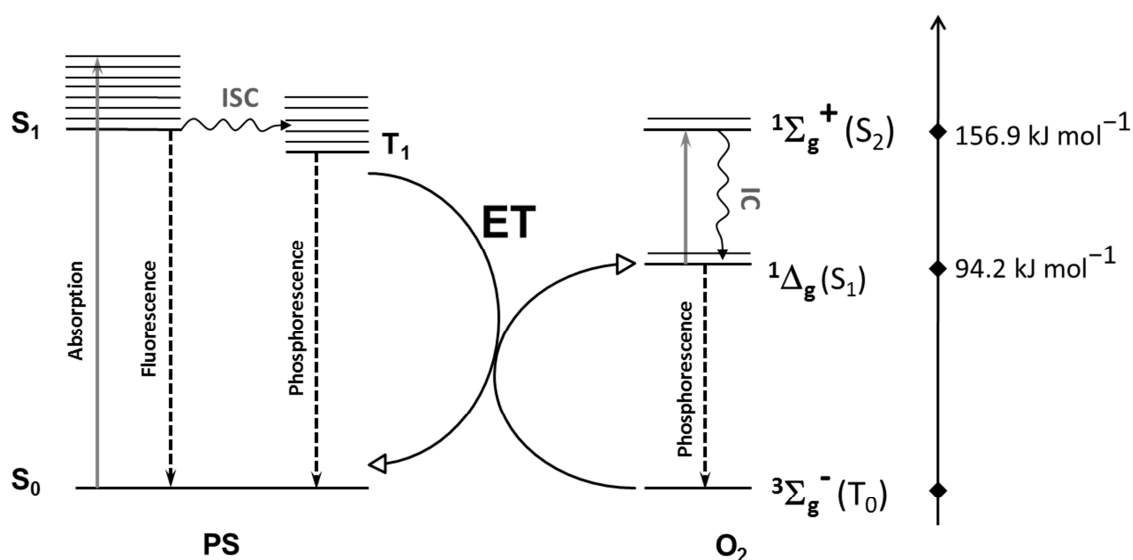
$$\Delta G = -nF(E_{(\text{A}/\text{A}^{\bullet-})} - E_{(\text{D}/\text{D}^{\bullet+})}) \quad 1.16$$

where n is the number of electrons involved in the redox process, F is the Faraday constant ($96.48 \times 10^3 \text{ J V}^{-1} \text{ mol}^{-1}$), $E_{(\text{A}/\text{A}^{\bullet-})}$ and $E_{(\text{D}/\text{D}^{\bullet+})}$ (V) the redox potential of the acceptor (O_2) and the donor ($\text{PS}^{\bullet-}$), respectively. Since $E_{(\text{O}_2/\text{O}_2^{\bullet-})}$ is -0.58 V vs SCE ,^{16,17} the redox potential of the sensitizer (*i.e.* for the $\text{PS}/\text{PS}^{\bullet-}$ couple) must be more negative than this value to make the reduction of oxygen to the superoxide radical anion possible.

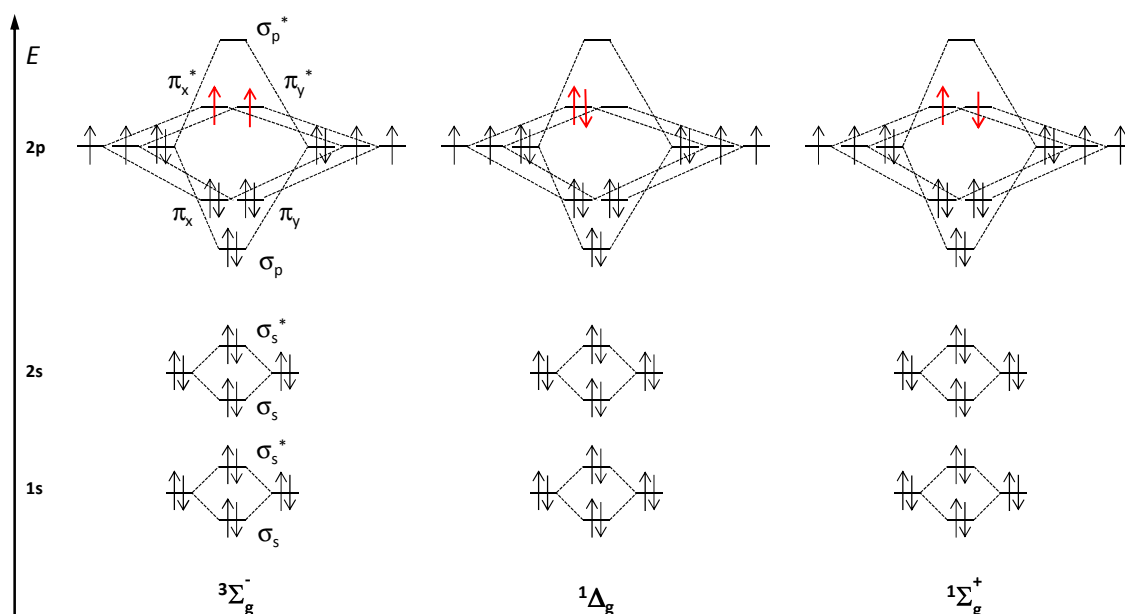
As recently detailed by Fukuzumi and Ohkubo,⁹ many multi-step syntheses commonly conducted under severe conditions and producing several by-products can be carried out employing organic photocatalysts whose activity is related to ELT mechanisms: even if yields can be poor, the use of recyclable photosensitizers, the presence of oxygen and light as only reactants and the single-step mechanisms make the photosensitized processes very attractive. Even if the primary ROS produced by electron transfer is superoxide radical anion, the reaction mechanisms can follow other pathways among those described above. Consequently, through ELT reactions both photooxidation and photooxygenation reactions can occur. Applications of photosensitized processes will be detailed below.

3.3.2. Type II reactions

The PS in its T_1 state can alternatively be subjected to energy transfer by collision with oxygen (Scheme 2), yielding singlet oxygen (S_1 state): the higher-energy singlet oxygen configuration $^1\Sigma_g^+$ can be initially reached but it is rapidly deactivated by internal conversion (IC) to $^1\Delta_g$. The energy gap between the ground state ($^3\Sigma_g^-$) and the lowest of the singlet states of oxygen is 94.2 kJ mol^{-1} . This is the amount of energy necessary to change the spin configuration of one electron in the antibonding π molecular orbitals (MO) of oxygen. $^3\Sigma_g^-$ has two electrons with the same spin orientation in the two π^* orbitals, whereas $^1\Delta_g$ has two unpaired electrons in the π_x^* MO.^{18–22} Singlet oxygen is not an excited state in the common sense that considers electron excitation from the HOMO to the LUMO: only a reorganization of the electrons in the HOMO takes place (Scheme 3). Nonetheless, in the text we will refer to singlet oxygen as an excited state. The formation of singlet oxygen is highly endothermic: even though chemical methods are available to generate it, the photochemical pathway is the most convenient and efficient one.



Scheme 2 Jablonski diagram representing schematically the photosensitized production of singlet oxygen; the energetic levels corresponding to the different spin states of molecular oxygen are reported.



Scheme 3 Schematic representation of the molecular orbitals diagram for O_2 . The different spin orientations in the π^* antibonding orbitals are underlined in red.

Conditio sine qua non for energy transfer between $PS(T_1)$ and $O_2(T_0)$ to take place is the energy level of the sensitizer triplet excited state: the triplet energy level of the PS must be higher than the energy gap between $^3\Sigma_g^-$ and $^1\Delta_g$, 94.2 kJ mol^{-1} . If the triplet excited state ($E_T / \text{kJ mol}^{-1}$) of the sensitizer has not enough energy to promote the variation of the electronic configuration in the antibonding π orbitals of O_2 (Schemes 2 and 3), no energy transfer is possible and no singlet oxygen is formed. PSs have usually relatively high triplet energy but the dissipation mechanisms that can occur before that energy transfer takes place can diminish or impede singlet oxygen production: quantitative ET is needed to efficiently produce 1O_2 .

Contrary to ELT reactions, singlet oxygen is the sole ROS formed through type II mechanism. This molecule is a good oxygenation agent, as well as a good electrophile.^{22,23} It efficiently reacts with electron-rich unsaturated compounds,^{24,25} as well as with nucleophiles such as amines,²⁶ sulfides^{23,27} and anions. 1O_2 is highly reactive towards dienes: [4+2] cycloaddition produces endo- and hydroperoxides (Figure 2).²⁶ In the presence of olefins with two or more allylic substituents, double bond shift with formation of an allylic hydroperoxide can occur: this reactivity is very important in biological systems for the oxidation of tryptophan, histidine and fatty acids.^{24–26} Dioxetanes can be formed by singlet oxygen addition to π -electron rich alkenes; dioxetanes undergo decomposition to yield two carbonyl groups.^{28,29} 1O_2 can also oxidize polymers *via* radical pathways.³⁰ It can be responsible of the formation of dioxetanes and peroxides which can jeopardize the stability and the properties of polymers. Similar is the case of paper: singlet oxygen addition to lignin yellows paper under light exposure.³⁰

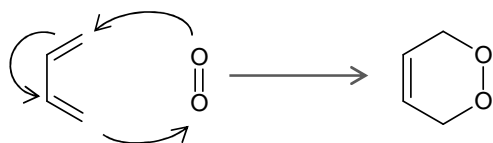
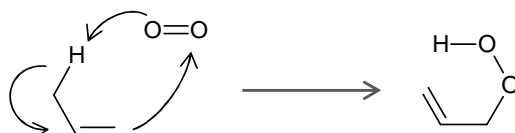
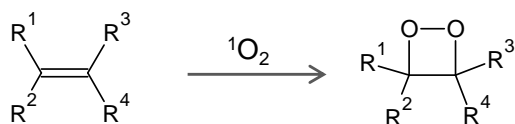
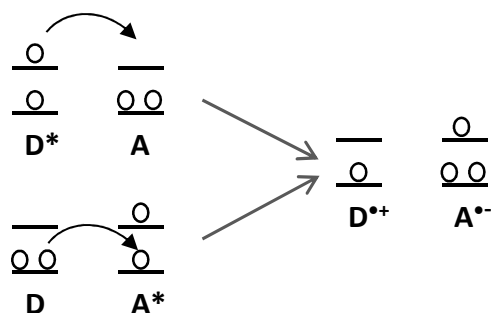
Diels-Alder [4+2] cycloadditionAlder-ene reactionDioxetane reaction

Figure 2 Main reactions involving singlet oxygen: formation of endoperoxides, allylic hydroperoxides and dioxetanes.

Once formed, singlet oxygen can be deactivated following several pathways: it can occur by either luminescence emission (phosphorescence at approx. 1270 nm), chemical reaction with a substrate or physical quenching (*e.g.* collisions with solvent and/or quencher molecules). Excited states lifetimes depend on the efficiency of the corresponding deactivation routes. Considering the different spin multiplicity between the singlet (S_1) and the triplet (T_0) states, the photophysical transition between these energetic configurations is rather disfavored (as discussed for the photophysics conducting to the PS triplet excited state). Thus, luminescence emission is less probable than chemical reaction or quenching by the solvent and can be neglected.³¹⁻³³ Consequently, the interaction between 1O_2 and the solvent must be seriously taken into account. In terms of singlet oxygen lifetime (τ_Δ) the differences can be extremely important: 3-4 μ s in water, 71 μ s in acetonitrile, 160-410 μ s in chloroform, 26-87 ms in perhalogenated solvents (CCl_4), 54 ms in air.³⁴ Clearly, the reaction rate of 1O_2 addition (for a given substrate or quencher) varies extremely from a solvent to another: quantifications on singlet oxygen production have to be done very carefully and for the applications the best reaction conditions must be selected. 1O_2 dependence on the environment is more important than in case of superoxide radical anion, whose lifetime is in the order of seconds.

3.3.3. Type I-II reactions

ELT takes place through the shift of one single electron: this can occur either from the LUMO of the excited donor to the LUMO of the acceptor or from the HOMO of the donor to the HOMO of the excited acceptor (Scheme 4). This mechanism needs orbital overlap between the two species: electron transfer can take place if donor and acceptor are closer than 10 Å.³⁵

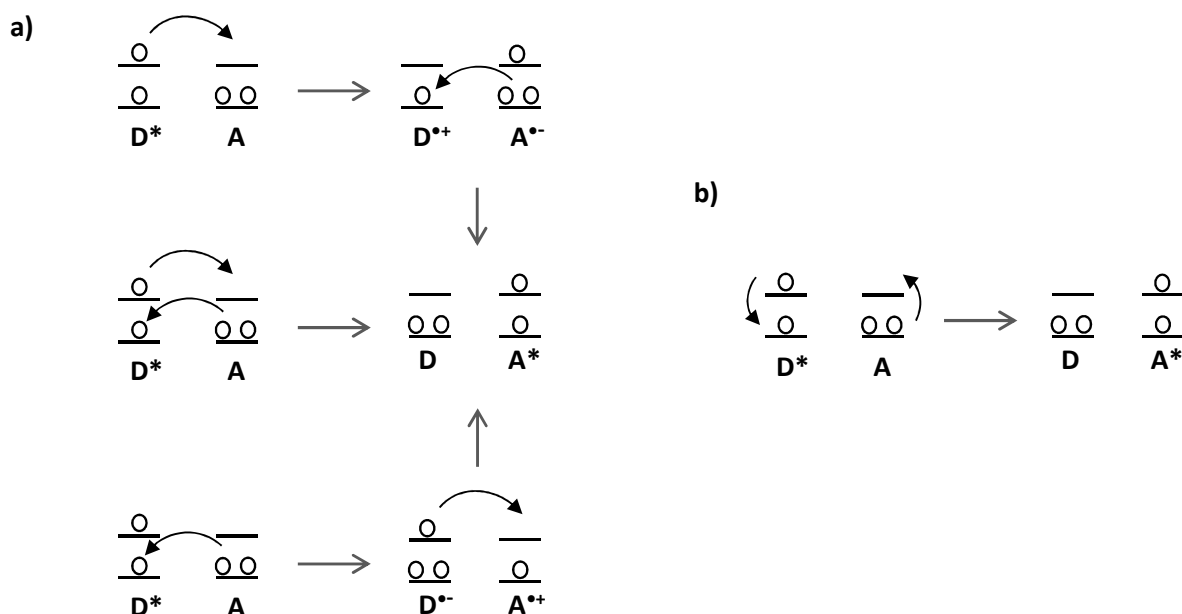


Scheme 4 Schematic description of electron motion in electron transfer (ELT) reactions.

As far as the ET mechanisms are concerned, two possible scenarios can be proposed according to a simplified molecular orbital scheme (Scheme 5):

- one electron moves from the LUMO of the donor to that of the acceptor and another electron moves from the HOMO of the acceptor to the HOMO of the donor (*electron exchange mechanism*). Similarly to what observed for ELT with the difference of the number of electrons involved, the orbital overlap between donor and acceptor is needed, so that the distance required is less than 10 Å. The two movements can occur simultaneously or successively (Scheme 5a)
- the electrons of the excited PS are coupled to those of the energy acceptor by dipole-dipole interactions (*dipole-dipole* or *coulombic mechanism*); while the electron of the excited PS falls back to the HOMO, an electron of the acceptor is promoted to the corresponding higher energy level. The result is gained without any orbital overlap: the distance scale of coulombic electronic interactions is in the limits of 100 Å, decreasing the distance requirements for the energy transfer (Scheme 5b).

Despite the two possibilities, triplet-triplet energy transfer by dipole-dipole mechanism is forbidden: sensitized ¹O₂ production occurs through electron exchange mechanism. Both ELT and ET are thus triggered by the same starting mechanism: electron transfer; the different number of electrons involved changes the reactive oxygen species produced and thus the overall oxidation mechanism.³⁵



Scheme 5 Schematic description of electron motion in energy transfer (ET) reactions. a) electron exchange mechanism and b) dipole-dipole mechanism.

It is common that a PS has both a redox potential suitable for reacting by electron transfer and a triplet energy high enough to react by energy transfer: which of the competitive mechanisms will thus be favored? It is difficult to predict. Generally it hinges on the medium (the substrate and the solvent) and it often occurs that a PS is able to give either ELT or ET reactions depending on the reaction conditions. The case of 9,10-dicyanoanthracene, which will be treated in more detail in the following chapters, is significant: for a given substrate, both mechanisms can occur, according to the solvent. Since triplet-triplet energy transfer takes place through electron-exchange mechanism, comparable to a “double” electron transfer, general trends are difficult to set. In cases where both superoxide radical anion and singlet oxygen are produced, the photooxidation products will depend on the substrate reactivity in the presence of either of the ROSs.

3.4. Photosensitizers

Considering the several aspects raised in the paragraphs above about the photosensitized production of reactive oxygen species it is possible now to make an overview of the characteristics a compound must meet to be a good PS.

- I. Light absorption. For applications in an environmentally-friendly perspective, PSs should be used in the near-UV/visible/near-IR range: chromophores absorbing light in the visible and characterized by high molar extinction coefficients will be good candidates. Depending on the application foreseen, absorption in a particular part of the visible spectrum can be appropriate: this parameter can be tuned by choosing the most adapted compound. Compounds that absorb visible light are usually highly conjugated: functional groups that usually increase the absorption wavelength can be identified following the Woodward-Fieser

- rules: double bonds extending conjugation (aromatics), thioethers and secondary amines are often present on good chromophores.^{3,36}
- II. Photophysics. The most of the photosensitized activity is related to the triplet excited state and the deactivation of the excited states of the sensitizer. The ideal situation corresponds to 100% intersystem crossing (ISC) efficiency, long triplet lifetime and totally disfavored dissipation pathways: no emission, no quenching by the solvent or other species, no chemical reaction, no radiationless deactivation, for both the singlet and the triplet excited states. Back to reality, good sensitizers present high quantum yields of triplet formation and relatively long triplet lifetimes: upon irradiation the T_1 state is efficiently populated and lasts enough to give ELT or ET reactions. For an optimal efficiency of triplet formation, spin-orbit coupling must be high; the extent of spin-orbit coupling depends on the principal and orbital quantum numbers and on the fourth power of the atomic number (Z^4).³ With increasing atomic numbers the spin-orbit coupling is more important, and ISC more efficient: heavy atoms increase thus the probability of obtaining the triplet excited states.
 - III. Energy/electron transfer. The energy of the triplet excited state (E_T) must be higher than 94.2 kJ mol⁻¹ ($T_0 \rightarrow S_1$ gap for oxygen) to make the production of singlet oxygen possible; similarly, the PS redox potential must be more negative than -0.58 V vs SCE ($E_{(O_2/O_2^{\cdot-})}$) to form superoxide radical anion by electron transfer. Photophysical and electrochemical characterizations are useful to determine the energy levels of the PS transient reactive species. The choice of a given PS depends on the desired photosensitized reaction. Since many PSs are able to induce both ET and ELT, preliminary tests are often necessary to determine the PS reactivity towards a particular reaction.
 - IV. Photostability. PSs, as organic compounds characterized by high conjugation, can be sensitive to reactive oxygen species. The reaction between the photocatalyst and the ROS produced has two deleterious consequences: the activated oxygen species is quenched by the sensitizer itself and does not react with the substrate and the PS can be deteriorated and lose its capability of absorbing light. Singlet oxygen and other ROS can attack double bonds: endo- and hydro-peroxides are formed as photodegradation products, the PS loses the π -conjugation responsible of its chromophore character and light absorption becomes impossible. Photobleaching thus prevents further use of the PS for photooxidation reactions and if the PS stability under irradiation is too limited in time its use as a photocatalyst loses interest.^{6,26} As it will be shown below, for some applications a certain degree of photobleaching is desired: in such cases a good compromise between photoactivity and photobleaching is searched.
 - V. Supports. For photocatalytic applications, the use of supported sensitizers is more convenient: for this reason it is useful to develop PSs that can be grafted (bound through covalent bonds) to various solid and inert supports. Possibility of chemical modification, in order to attach functional groups to the sensitizer without jeopardizing the chromophore structure, is an important feature to be considered for the development of organic photocatalytic materials. The ideal situation occurs when the immobilization onto supports has no influences in the photophysical and photochemical behavior of the PS.

3.4.1. Classes of photosensitizers

Many PSs belonging to several different chemical families are known and have been studied until now. The division in classes is convenient to analyze the photophysical/sensitizing properties of the PSs. A summarizing overview of the main classes of PSs is reported below.

3.4.1.1. Polyaromatics

Polycyclic aromatic compounds such as naphthalenes, anthracenes, naphthalenes have been used for their photosensitizing properties.³¹

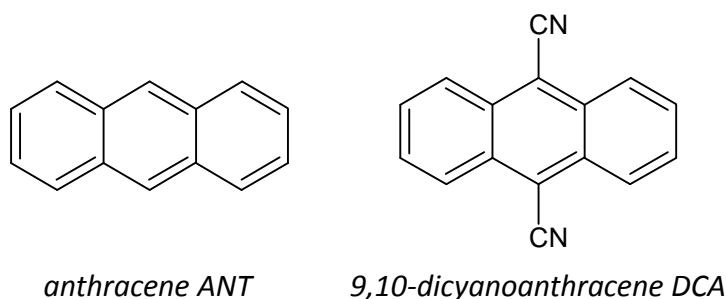


Chart 1 Polyaromatic PSs: anthracene and 9,10-dicyanoanthracene.

Thanks to their triplet excited state energies and redox potentials these compounds have good photosensitizing properties: both ELT and ET can be possible for many aromatic PSs.^{31,37} In the presence of DCA, for example, for a given substrate both type I and type II oxidations can take place, depending on the solvent; for the photosensitized oxidation of sulfides for example, in polar solvents the ELT route is favored relative to ET, which is likely to occur in non-polar media.^{7,8,38-41} With polyaromatic sensitizers, drawbacks are related to their inactivity in the visible region. The case of anthracene (ANT) and its 9,10-dicyano- derivative (DCA, Chart 1) is significant: the insertion of the two nitriles on the anthracene moiety makes the absorption maximum increase from 380 nm to 420 nm, in the visible.^{32,42,43} Many anthracenes are not stable under irradiation as very sensitive to ¹O₂: dimethyl- and diphenylanthracene for example are commonly used as singlet oxygen probes.⁴⁴ On the contrary, the insertion of the two cyano groups on ANT prevents singlet oxygen addition on the aromatic skeleton. Chemical derivatization influences the properties of these compounds also as far as grafting is concerned: it is very difficult to modify polyaromatic compounds and many of them cannot be grafted.

3.4.1.2. Aromatic ketones

Aromatic ketones (Chart 2) are good photosensitizers, for both type I and type II reactions. These compounds are very stable under irradiation and their properties are poorly influenced by the chemical environment; aromatic ketones are often considered as references for the determination of the sensitizing properties of other molecules.⁴⁵ Perinaphthenone (PN) is commonly adopted as the reference for the determination of quantum yields of singlet oxygen production: its quantum yield is rather insensitive to the chemical environment and close to unity in most solvents.⁴⁵⁻⁴⁸ Such a high quantum yield of singlet oxygen production derives from the fact that the triplet excited state

formation is strongly favored relative to other dissipation routes and that ET to oxygen is very efficient.^{46,49–52} The main drawback of this class of compounds is related to their absorption properties: the weak $n \rightarrow \pi^*$ band often lies in the UV-A region. Nevertheless, some PSs display an absorption band slightly extended to the visible, usually between 400 and 425 nm. Though weakly, anthraquinone (AQ) derivatives can absorb visible light and efficiently induce both ELT and ET reactions.^{10,17,53–55} Graftable and commercially available derivatives of 9,10-anthraquinone (e.g. carboxylic and sulfonic acids) have good photosensitizing properties.^{56,57} AQ derivatives can thus act as excellent photosensitizers.

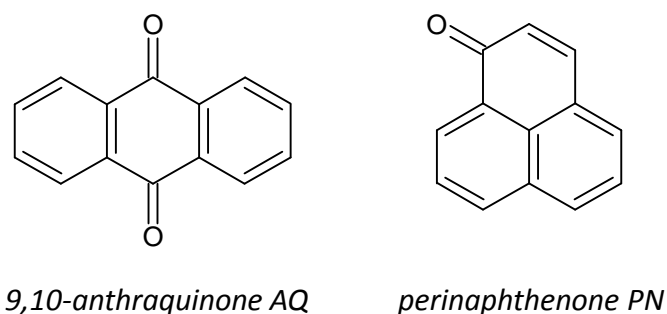


Chart 2 Aromatic ketones as PSs: 9,10-anthraquinone and perinaphthenone (1*H*-phenalen-1-one).

3.4.1.3. Phenazine/phenothiazine derivatives

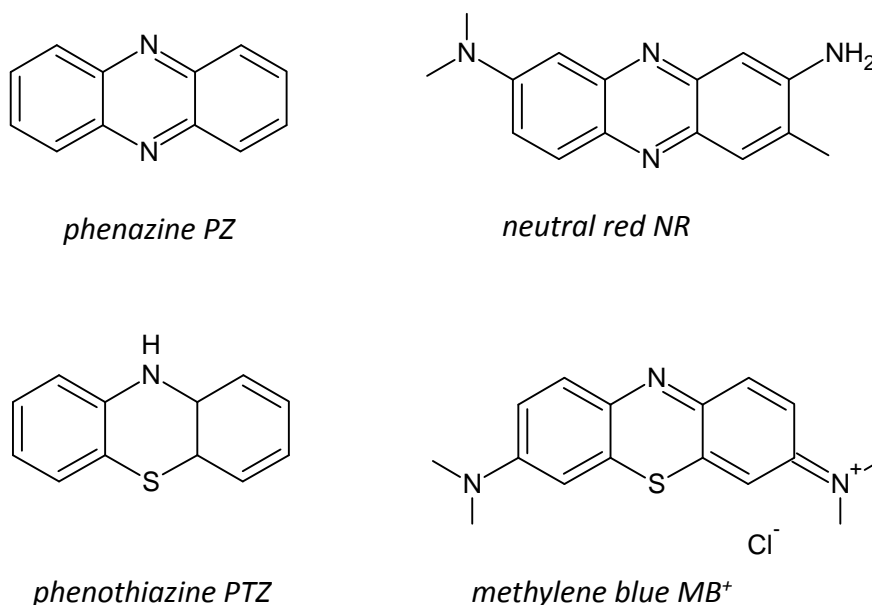


Chart 3 Phenazine (top) and phenothiazine (bottom) PSs.

Phenazines (PZs, Chart 3) represent an important class of dyes that can be used as PSs; such chromophores are already used as dyestuffs and drugs. Phenazine absorbs at approx. 425 nm, its triplet excited state energy is 186 kJ mol^{-1} , its redox potential $-1.23 \text{ V versus SCE}$:³⁷ PZ can thus promote energy and electron transfer upon visible light irradiation.⁵⁸ Chemical functionalization can be readily carried out, in order to obtain either neutral PZ derivatives or charged phenazinium salts: the absorption properties can be tuned depending on the substituents. Some derivatives are red-colored and others are blue-colored, depending on the chemical formula; neutral red changes its color from red to yellow depending on the pH.

Phenothiazines (PTZs, Chart 3) have properties close to those of PZs. These compounds are used as neuroleptic drugs and dyestuffs. Phenothiazine can induce ET and ELT reactions but does not absorb in the visible.^{37,59} Nonetheless, a large variety of visible-light absorbing, both neutral and positively charged (phenothiazinium salts, water soluble), derivatives can be easily produced: methylene blue (λ_{max} 650 nm), and thionine (3,7-diaminophenothiazinium, λ_{max} 640 nm) are just two examples of well-known and commercially available PZT photosensitizers.^{60,61} Methylene blue (MB^+) has been known since 1876 and used for many applications: drug for malaria treatment and sensitizer for oxidative stress in cancers, peroxide generator, sensor for sulfides, stain dye, and many others. Many MB^+ derivatives are commonly used as PSs as they efficiently produce singlet oxygen and promote electron transfer reactions, they are less toxic than many other dyes and they absorb light at wavelengths higher than 550 nm: these chromophores are good PSs, above all concerning biological and medical applications.⁶²⁻⁶⁵ Photobleaching of PZs and PTZs is relatively important.

3.4.1.4. Xanthene derivatives

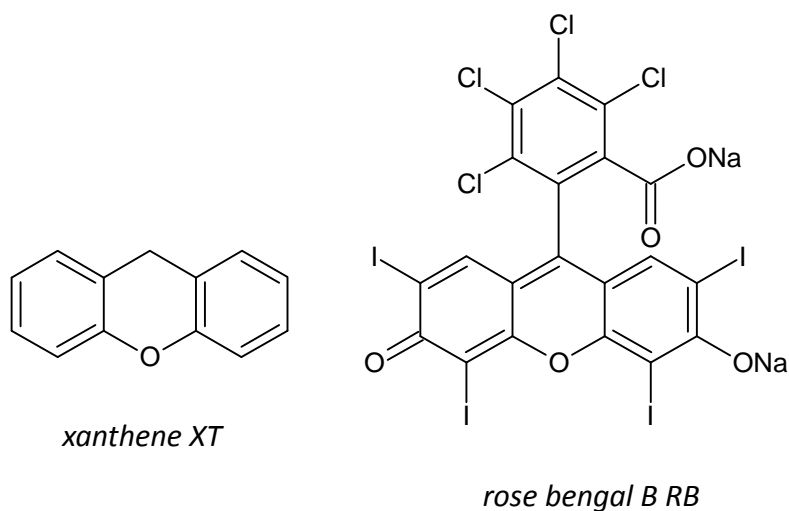
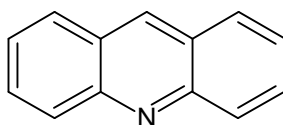


Chart 4 Xanthene dyes as PSs; rose bengal is one of the most commonly used XT derivative.

Xanthene (XT) is a UV absorbing compound from which several important photosensitizers derive (Chart 4).^{6-8,37} Among them, fluoresceins (*i.e.* rose bengal, RB),⁶⁶ eosins and rhodamines⁶⁷ are the most common. XT dyes are yellow to pink/red colored, usually very fluorescent. Most of them are salts (and water soluble) and grafting groups allow their covalent immobilization on supports. Heavy atoms can be easily attached to the xanthene skeleton: their doubly positive effect corresponds to a

bathochromic shift of the absorption spectra and to an increase of the spin-orbit coupling, which consequently increases the quantum yield of triplet excited state formation. Photobleaching, like in the case of RB, can be important;⁶ nonetheless, they present excellent photosensitizing properties, particularly for yielding singlet oxygen, and they are studied for several potential biological applications.

3.4.1.5. Acridine derivatives



acridine AC

Chart 5 Acridine.

As reported by Wainwright,⁶⁸ acridine (Chart 5) chromophores show important antibacterial and antiseptic activities and many derivatives have been studied since 1912. Together with the development of antibiotics, studies on acridine dyes for biological applications have been neglected. Their importance can increase nowadays with the development of drug-resistant bacteria, notably for the possibility of local light-induced activation of the dye-derived drug. AC and many of its derivatives can perform both types of photosensitized reactions.

3.4.1.6. Porphyrins and phthalocyanines

Porphyrins (PFs, porphine derivatives, Chart 6) can be considered ideal candidates for photosensitization, since their natural presence in biological systems make them not toxic in the absence of light. Another advantage is represented by their extended visible light absorption: these compounds usually present an absorption band in the blue (Soret band) and a more red-shifted Q-band; moreover, their triplet excited state lifetimes are very long. Many derivatives can be synthesized, mostly through symmetric tetra-substitution, and grafted to various supports; in addition, these compounds can be metallated through complexation of several metal cations.^{6-8,69}

Phthalocyanines (PCs, Chart 6) derive from the same structure as PFs, with the difference of having nitrogen atoms for the linkage between the pyrrole units. Due to the presence of the additional benzene rings, relative to PFs, these compounds absorb light deeper in the visible, around 700 nm; their triplet lifetimes can be very long (> 100 μ s), but usually shorter than for metallated PFs. As for porphyrins, many substituted derivatives can be produced and grafted, and metal cations can be complexed by the macrocyclic structure.^{6-8,69}

Both types of compounds are mostly used for singlet oxygen production, even though they can also produce hydrogen peroxide and superoxide radical anion. The main drawback of porphyrins is their sensitivity to singlet oxygen: the ROS can provoke a fast photobleaching of PFs, preventing their photoactivity. Nonetheless, recent results seem to indicate that a decrease of photobleaching can be reached by preventing aggregation phenomena, which can be very important for these classes of PSs.

Grafting seems to hinder aggregation, and the dyes are more stable during their use under irradiation.⁶⁻⁸

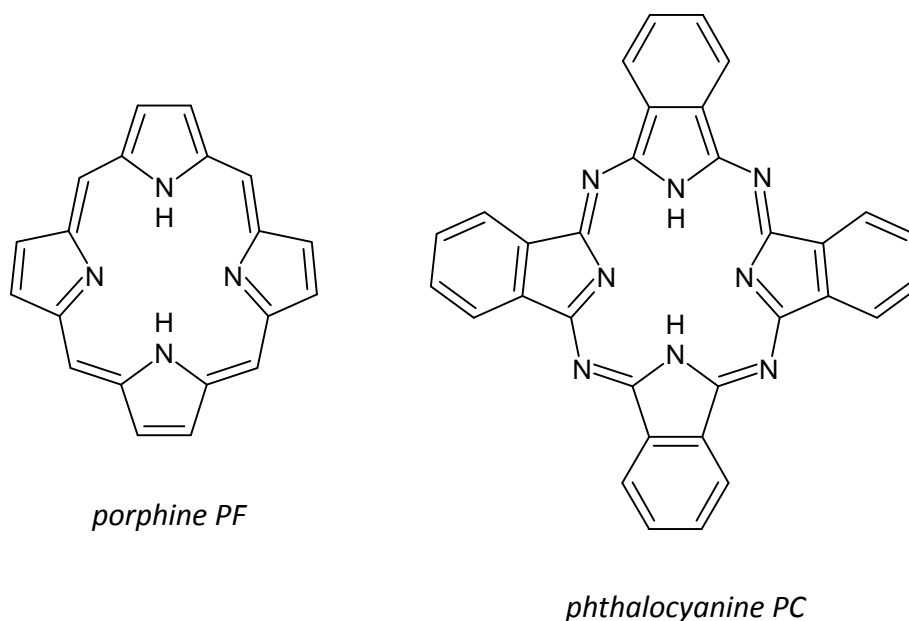


Chart 6 Porphine and phthalocyanine: mother compounds of the large chemical families of porphyrins and phthalocyanines.

3.4.1.7. Miscellaneous

Many other classes of PSs exist and are used. We will report some examples (Chart 7). Triphenylpyrylium salts (TPPs) can efficiently induce electron transfer reactions upon irradiation in the 300-450 nm region; also, the formation of HO^\bullet and $^1\text{O}_2$ has been reported for TPP salts included in zeolites.^{7,8,70-73} Modified TPP compounds can be easily achieved and grafted. Fullerenes showed good photosensitization activities, both for type I and type II reactions; they absorb light throughout the visible region and they can be grafted through their chemical derivatization; nonetheless, their low solubility in many solvents makes fullerenes much more interesting immobilized on various supports than in solutions.^{7,74,75} Transition metal complexes can be also used for photosensitization; Ruthenium complexes like tris(bipyridine)Ru(II) (RTBP) are the most studied examples, but also complexes of Osmium, Iridium, Platinum and Palladium have been reported to have good sensitizing properties.^{6,7} These compounds can relatively efficiently absorb visible light and the change of the organic ligands makes the tuning of their properties possible; the main drawback is the cost (economical and environmental) of using transition metals.

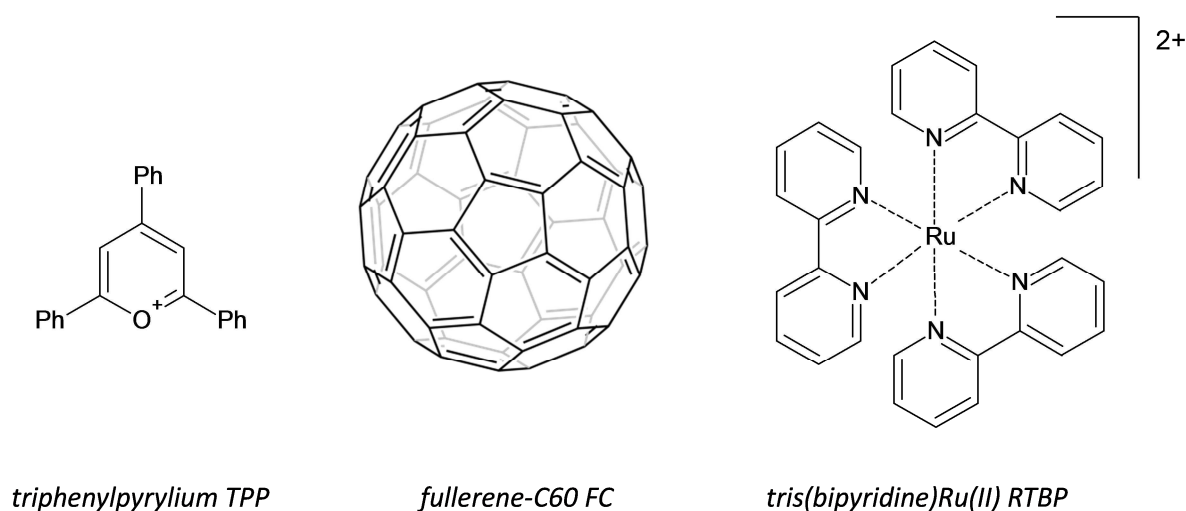


Chart 7 Miscellaneous PSs: triphenylpyrylium ion (left), fullerene C60 (middle) and tris(bipyridine) Ruthenium(II) ion.

3.5. Immobilized organic photocatalysts

Fundamental advantages are gained when the photosensitizers are immobilized on inert supports.⁷ According to common logic, for most catalytic applications the use of supported photosensitizers allows to recover and reuse the photocatalyst, to separate the products from the reaction medium, to carry out solvent-free processes, to control the PS photostability and its aggregation. TPP, for example, undergoes photobleaching by hydrolytic ring-opening under irradiation in water; relative to solutions, the geometry of the excited state of grafted TPP is different, which prevents any ring opening: TPP is not photobleached thanks to the covalent interaction with the support.^{8,76} Nonetheless, disadvantages can arise: quantum yields of ROS production decrease and reactants diffusion can be limited. The decrease of quantum yields of ROS production is due to a more effective physical quenching in the solid matrix than in solution but can be considered negligible taking into account the better reusability and recovery of the photocatalyst.

We will report below a general overview of the characteristics that supports and immobilized photosensitizers can have; a more detailed description would enter in the field of chemistry of materials and is out of the scope of this work.

Photosensitizing materials can be divided in categories depending on the parameters considered:

- I. Chemical structure. PSs can be immobilized onto organic or inorganic materials. Organic supports are essentially polymers and textiles:
 - a. Many polymers have been used for supports. RB has been supported, among others, on polyamides, polymethacrylate, polyethylene glycol;^{77,78} rose bengal grafted on chloromethylated polystyrene-co-vinylbenzene is commercially available and widely used. Methylene blue has been immobilized on polysiloxanes,⁷⁹ polyurethanes,⁸⁰ poly-*N*-isopropylacrylamide⁸¹ and on Nafion® membranes.⁸² Other examples of polymers used for PS immobilization are polystyrene fibers, water-soluble poly-methacrylic acid,⁸⁴ nanofibrous polyethylene-co-methacrylic acid membranes⁸³ and PVC.⁸⁵ In these cases,

the chemical stability of the supports has to be considered attentively: polymers can be unstable in some solvents.

- b. Natural and artificial textiles can also be used for this purpose. Anthraquinone-carboxylic acid has been grafted on cotton fabrics,^{10,86} rose bengal and methylene blue on nylon fabrics,⁸⁷ porphyrins have been studied grafted on nylon, chitosan and cellulose.⁸⁸⁻⁹⁰ Seaweed-derived Ca²⁺-alginate beads have also been used as *green* supports for RB.⁹¹

Several inorganic materials have been exploited for immobilizing PSs. Silica is an easily available and functionalizable inert support: many dyes such as methylene blue,⁹² rose bengal,⁹³ TPP salts,^{94,95} dicyanoanthracene,⁹⁶⁻⁹⁸ anthraquinone,^{58,98} acridines,⁵⁸ phthalocyanines and porphyrins^{99,100} have been supported on silica. Several PSs (rose bengal, porphyrins and metal complexes) have been immobilized through ionic interactions in silica aerogels.^{85,101} Zeolites also showed good characteristics for supporting photosensitizers, which were embedded or intercalated in the aluminosilicate structure.^{71,102,103} Fullerenes C₆₀ have been deposited on commercially available molecular sieves;¹⁰⁴ clays such as bentonite and layered double hydroxides (LDH) have been used as supports.¹⁰⁵⁻¹⁰⁷ Ruthenium salts have been immobilized on porous silicones through hydrophobic interactions.^{108,109} Interesting approaches have been developed to graft photosensitizers on titanium dioxide or to couple titania and PSs grafted on various materials.¹¹⁰⁻¹¹²

- II. Macroscopic configuration. Different macroscopic forms of the photocatalyst can be appropriate depending on the final process envisaged. Supports in the form of films,^{85,113} powders,¹⁰⁰ fibers,^{83,88} beads,^{91,115} nanoparticles¹¹⁴ have been widely adopted, to immobilize several PSs; cast materials such as monoliths can also be used.^{85,116,117} Films and bulk materials are adapted to gas phase configurations, while particles find applications in suspension as solid-liquid interface photocatalysts. Microemulsions,¹¹⁸ gels^{119,120} and micellar systems¹⁰¹ have also been adopted for supporting PSs in green chemistry applications. Interestingly, micellar systems have been created by suitable functionalization of porphyrins, forming mono-molecular core-shell structures.¹²¹
- III. Immobilization. PSs can be immobilized through the creation of physical interactions with the support. Some examples have already been shown: intercalation and impregnation in layered or organized aluminosilicates,^{104,106,122} hydrophobic interactions between metal complexes and silicone,^{108,109} ionic interactions between many PSs and silica or ion exchange resins,^{85,95,123-125} trapping in cast inorganic or organic polymers (silica and PVC for example),⁸⁵ adsorption.¹²⁶ Physical immobilization, either by adsorption, intercalation or insertion, is more easily achieved. Drawbacks can occur when the interaction between the dye and the solid support is not strong enough: the chromophore can be washed out by a solvent or migrate inside the solid. In the latter case aggregation and difficult accessibility by light and reactants can occur. The alternative is represented by the creation of covalent bonds between the PS and the support. Grafting completely prevents any migration of the photocatalyst in the material, with no risk of PS loss during the use. The grafting procedure must change neither the photophysical properties of the sensitizer nor the mechanical characteristics of the support. The fundamental condition to make grafting possible is the presence of functional groups that can react and create a chemical bond: this can make the modification of both the PS and the support necessary. Grafting can be carried out on several host materials, belonging to the above-mentioned families. Porphyrins and phthalocyanines have been grafted on silica⁹⁹ as well as on organic polymers, such as polystyrene¹¹⁵ or poly

ethylene-co-methacrylic acid nanofibres,⁸³ nanofibrous membranes^{83,85,88} or films: the distance between the support and the macrocyclic PSs can be tuned by the insertion of suitable spacers.⁸³ Porphyrins have also been grafted on amino-derived PVC.⁸⁵ Metal complexes have been grafted on water-soluble poly-methacrylic acid.⁸⁴

More generally, many parameters should be taken into account in the choice of the support for a determinate process:

- Inertness: the support must be chemically stable in the reaction medium; this aspect interests more organic polymers than inorganic materials. In the case of grafted PSs, the dye-host covalent linking must be stable in the reaction medium
- Mechanical stability: the photocatalysts must bear the physical strains to which they are subjected during the process; materials should not crack and maintain their shape throughout the process
- Porosity and specific area: for the adsorption-desorption of reactants and products, as well as for their migration inside the material, the specific surface area and the porosity of the support play an important role. These parameters should be controlled, in order to favor the contact between ROS and reactants and the products desorption
- Oxygen diffusion: the materials configuration should be selected in order to allow good oxygen diffusion inside its structure. For example, swelling of polystyrene backbone in suspension seems to increase the efficiency of O₂ diffusion inside the polymer beads, usually disfavored⁷⁷
- Functionalization: supports that can be chemically and/or physically modified are surely more versatile than others. PSs which can be functionalized to form covalent bonds or to maximize the physical interaction PS-support are more convenient than others. Functionalization can be done either during the support preparation or in a post-synthesis phase, depending on the material¹¹³
- Shape: it is convenient to work with supports that can be prepared in various forms. In this sense, silica is really versatile: many functionalized silica precursors are available and materials can be prepared in the form of powder, films or bulk materials.

3.6. Applications

3.6.1. *Photodynamic processes*

The photodynamic effect describes the damage provoked on living tissues by photoinduced oxidation reactions. Singlet oxygen plays the major role, even though superoxide radical anion can intervene for complementary reactions.^{6,62,65,127-129} The applications involving photodynamic reactions are mainly photodynamic therapy on cancers (PDT) and photodynamic bactericidal treatments (photodynamic inactivation, PDI).

3.6.1.1. PDT

This photomedical technique is based on the cytotoxic effect of singlet oxygen on tumor cells. It has already been showed that ¹O₂ reacts with nucleophiles: in biological systems it can attack heterocycles such as tryptophan and histidine, as well as fatty acids, yielding endoperoxides and

hydroperoxides.^{24,25} The degradation of essential amino-acids and of the cell membrane's components can lead to cell death (apoptosis). The corresponding reaction mechanisms are out of the scope of this work, but they are now well understood and deeply resumed in the literature.²⁶ In addition to singlet oxygen, superoxide radical anion can play a complementary role in PDT. Tumor cells have reduced amounts of the superoxide dismutase enzyme (responsible of the deactivation of the corresponding ROS): in the presence of $O_2^{\bullet-}$ the cell defensive response can be not sufficient and lead to cell apoptosis.¹²⁷ Advantages coming from PDT are bound to the possibility of confining the PS in the tumor region, as well as irradiation: the effects on healthy tissues are thus limited.

Photosensitizers for PDT should fulfill several criteria: low toxicity in the absence of light, selective accumulation in cancer tissues, limited in-vivo stability to favor removal from tissues, high absorption in the red region ($\lambda > 620$ nm, $\epsilon \geq 50000$ M⁻¹ cm⁻¹) to maximize light penetration depth in skin, high quantum yield of singlet oxygen production. PSs should also be water soluble, possessing at the same time a hydrophobic moiety to facilitate the penetration in membranes. Several classes of compounds have been studied to reach the good compromise between the desired properties. For their photophysical properties, porphyrins and other macrocyclic photosensitizers (phthalocyanines, chlorins and bacteriochlorins) have been identified as good candidates for PDT.⁶ For maximizing the solubility of these PSs in biological media, different kinds of delivery models are being studied to control both the PSs transport and their selective localization on tumor tissues. For example, lysosomes,¹³⁰ micelles,¹³¹ polymeric hydrogels,^{85,132} oligomeric nanocomposites¹³³ and diphenylalanine micro/nanotubes¹²⁶ have been reported for delivery and targeting in PDT. These carriers must not negatively influence the photophysics of the PSs. Thanks to the advances reached in the latter years, PDT can now be selected as an efficient procedure for superficial non-metastatic tumors; problems with light penetration in living tissues prevent the use of PDT for largely developed internal tumors, even though the use of optical fibers let envisage future deeper applications.

Several examples of supported photocatalysts for photodynamic therapy have been reported: methylene blue has been inserted in nanoparticles, oligomeric nanocomposites and microgels,¹³²⁻¹³⁵ porphyrin-derivatives have been grafted on silica nanoparticles.¹¹⁴ Jia and coworkers¹⁰⁰ reported an overview of phthalocyanines grafted on several kinds of nanoparticles: quantum dots, colloidal gold, silica and polymeric nanoparticles enhanced the photodynamic effect of the corresponding PSs. Mamaeva *et al.* recently published a complete overview about mesoporous silica nanoparticles for medical purposes.¹³⁶

3.6.1.2. PDI

The general concepts described for PDT can be extended to photosensitized microbial inactivation. Methylene blue and many of its derivatives can be efficient for plasma sterilization, even though their activity is limited in time because of enzymatic deactivation.¹³⁷ Phenothiazines, porphyrins and phthalocyanines showed good PDI properties.^{62,65,128,129,138,139} Drawbacks related to PDI on other blood fractions concern the sensitivity of platelets and red blood cells towards singlet oxygen: selective photomicrobial activity is hardly attained. PDI for blood purification is used complementarily to other procedures, such as nanofiltration, direct photolysis and pasteurization.^{62,65}

Photosensitizers can be also used as insecticides and herbicides.¹⁴⁰⁻¹⁴² Singlet oxygen photodynamic effect can kill undesirable plants but the accumulation of PSs in plants can provoke PD-induced

damages also on the desired ones. Insecticides based on photosensitizers are quite effective and, relative to commonly used chemical pesticides, avoid the disadvantage of persistence in the environment. Xanthenes, acridines, phenothiazines and porphyrins are good PDI agents.¹⁴²

Many bactericidal photosensitizing materials have been developed in the last decade, for applications in solution and in the gas phase. Functionalized porphyrins have been grafted on cotton fabrics and several kinds of polymeric nanofibers;^{88,89} MB⁺ has been efficiently used embedded on polyurethane films;⁸⁰ Ruthenium complexes have been immobilized on porous silicones and hydrophobic polymers;^{109,143} phthalocyanines have been supported on polystyrene nanofibers;¹⁴⁴ cyanoanthracene derivatives and anthraquinone were used for water disinfection both inserted and grafted on silica powders.⁹⁸

3.6.2. *Water/air treatment*

Waste-water treatment and air remediation are important and current issues, both because of the increase of pollutants release and of the increase of legislations and regulation demanding lower pollutants levels. Semiconductor photocatalysis, mainly with TiO₂, is certainly the most important technique for water and air decontamination: materials are cheap and efficient and the contaminants are completely mineralized to H₂O and CO₂. Nonetheless, most semiconductors absorb light in the UV region; in cases where visible light absorption is demanded photosensitizing materials are possible alternatives. A large variety of pollutants can be oxidized by photosensitization: sulfur derivatives,^{97,106} phenols,^{94,145,146} aromatic aldehydes and acids, carbamates, heteroaromatics.⁸ The choice of the PS must be attentively pondered: since mineralization is not reached, photooxidation products can differ from a sensitizer to another, depending on the reaction mechanisms. Thus, for a given pollutant, the oxidation products obtained using a given PS have to be identified and analyzed: the formation of more toxic and dangerous photoproducts must be totally avoided. The analysis of the mechanisms involved is far from being useless: depending on the more desirable products, PSs favoring either ELT or ET mechanisms can be selected. Photooxidation of sulfides is an example: by electron transfer the main photoproducts are disulfides, whereas by forming singlet oxygen sulfoxides and sulfones are mainly obtained.^{41,55,71,147,148} In addition to the favored mechanism, the photostability of the PS must be taken into account. For decontamination applications the organic photocatalysts must be as much resistant as possible under irradiation. On the one hand, PS degradation can cause the formation of other pollutants, on the other hand the more stable the PS is, the more sustainable the depollution process will be. Another important parameter for this application field is the support. Its structure and configuration can significantly influence the diffusion of both the pollutant and oxygen in the support itself. In addition, some solids can have cooperating activities: zeolites based-photocatalysts for example can present enhanced degradation activity due to the strong adsorption properties of the support which facilitate the contact between the catalyst and the substrate.^{71,103} Generally, photosensitized depollution techniques may be appropriate if coupled with subsequent biological steps to reach the desired decontamination level.

Immobilized photocatalysts demonstrated to act as efficient materials for air and water treatment and many examples have been reported in the literature, in particular for the photooxidation of sulfides^{71,96,97,105,106,148} and phenols.^{94,107,119,145,146} Efficient oxidation of organic sulfides has been reached using layered double hydroxides-intercalated 4-benzoylbenzoate,¹⁰⁶ silica-supported

cyanoaromatics,^{58,97,116,117} TPP on zeolites,⁷¹ MB⁺ inserted on clays¹⁰⁵ and RB supported on Wang resins.¹⁴⁸ Phenols and chlorophenols can be oxidized in the presence of phthalocyanines and porphyrins supported on bentonite, silica and ion exchange resins;^{107,145} rose bengal and methylene blue immobilized on silane gels,¹¹⁹ as well as TPP on carbon nanotubes,¹⁴⁹ have been successfully applied to the degradation of chlorophenols. The combined effect of TiO₂ and cotton-grafted porphyrins showed promising results for the visible-light photooxidation of dyes.¹¹¹

3.6.3. Fine chemistry

Photosensitized oxygenation reactions can be used for synthetic purposes, to produce whether fine chemicals or building blocks and intermediates for other synthesis. Even though singlet oxygen is the most interesting reactant due to its stereoselectivity,^{23,26} ELT reactions can also be used in this field.⁹ Some examples are presented below and in Figure 3; the detailed mechanisms are rather out of the scope of this brief general presentation and will be ignored for now.

Oxygenations of aromatic compounds to yield aromatic aldehydes are important pathways for the synthesis of pharmaceutical drugs, dyestuffs, perfumes and pesticides; the use of photocatalytic one-step ELT reactions can increase both selectivity and yield, relative to conventional oxidations. For example, for the acridinium-catalyzed oxidation of *p*-xylene to *p*-tolualdehyde high yield (75-100% depending on the reaction conditions) and selectivity have been achieved; H₂O₂ is the only by-product of this reaction. Acridinium salts (Ac⁺) have been used for other reactions, such as the oxidation of anthracene to anthraquinone, the oxygenation of cyclohexane *via* the decomposition of peroxide intermediates and the bromination of aromatic hydrocarbons and thiophenes using aqueous HBr instead of other toxic Br sources. For the latter reaction, high-yields (close to 100%) and selectivity can be obtained. Phenol and alkoxybenzenes can be obtained by heteroaromatic-photosensitized ELT oxygenation of benzene, in the presence of water or alcohols, respectively; oxygenation of substituted toluenes and styrenes can be also carried out. Photocatalytic oligomerization of fullerenes and other compounds can be carried out by C-C bond formation via radical coupling.⁹

Reactions involving singlet oxygen addition to various substrates have been reported. As described above, ¹O₂ is a highly stereoselective reactant (Figure 2). The main reactions occurring in the presence of ¹O₂ are described in paragraph 3.3.2.^{6,26} Significant examples of ¹O₂ reactivity are the formation of ascaridole from α -terpinene, the production of juglone from 1,5-dihydroxynaphtalene and the peroxidation of citronellol (Figure 3). Ascaridole is produced very efficiently using different PSs; it finds applications as an anthelmintic drug (vermicide) and, as a relative unstable compound and similarly to other endoperoxides, can be used to initiate radical reactions. Juglone (5-hydroxynaphtoquinone) is very efficiently produced with many sensitizers. Juglone is used for dyestuffs, cosmetics, as an herbicide and a pesticide; in addition, as other naphtoquinones, it represents an important building block for biologically-active products.^{91,118,123} It is conventionally synthesized oxidizing 2,3-dichloro-5,6-dicyano-1,4-benzoquinone (using oxidation agents such as MnO₂ or Ag₂O), which is obtained from cyanation and chlorination of 1,4-benzoquinone; the latter is itself obtained from the oxidation of hydroquinone, benzene or aniline. At least three steps are necessary, whereas using photosensitization it is synthesized by a one-step reaction, starting from a more easily available compound (1,5-dihydroxynaphtalene).⁹¹ The advantages of utilizing

photocatalytic synthetic procedures are evident in this case. The photoinduced oxygenation of citronellol is another example of industrially interesting application of photosensitized processes. It is a natural monoterpene used in perfumery and as insect repellent; $^1\text{O}_2$ addition to citronellol yields a mixture of isomeric hydroperoxides which are further reduced and cyclized to obtain rose oxide, a commonly used fragrance, already industrially produced by this photochemical method.^{85,124}

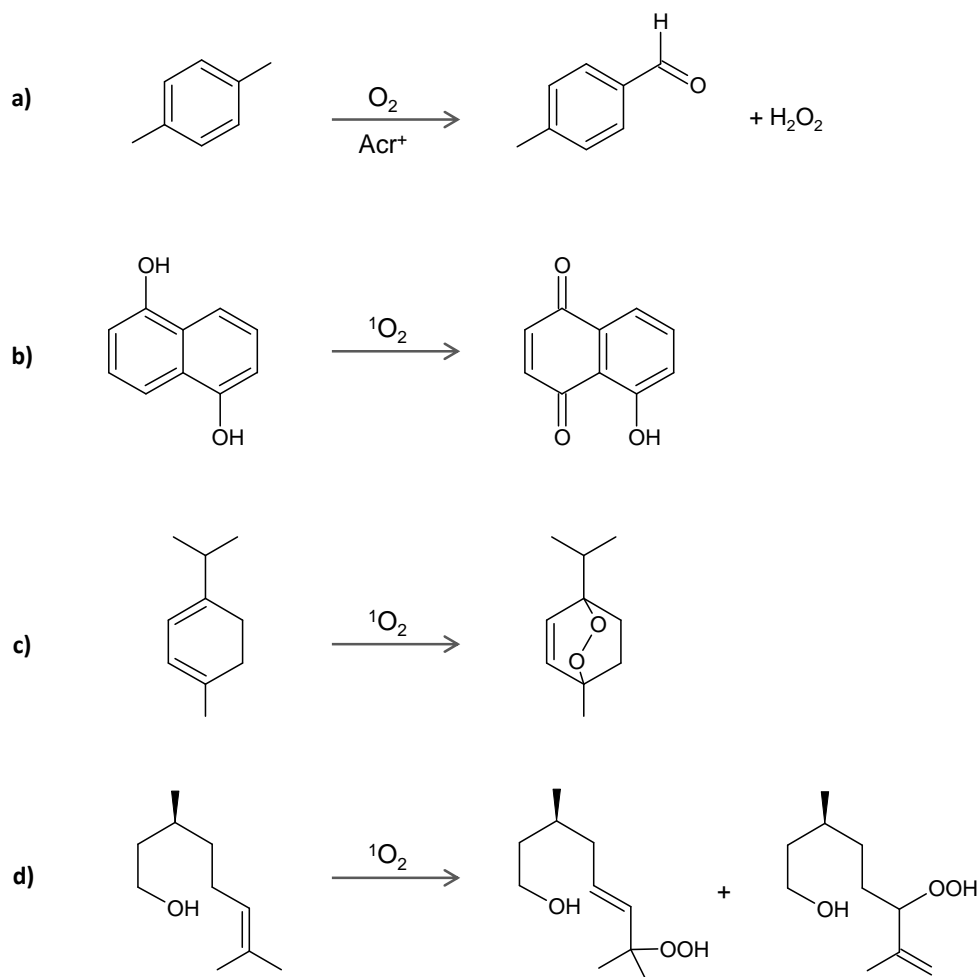


Figure 3 Examples of photosensitized oxygenation reactions: a) formation of p -tolyl aldehyde from p -xylene, using acridinium ions as ELT PSs; b) oxygenation of 1,5-dihydroxynaphthalene to juglone by singlet oxygen addition; c) singlet oxygen addition to α -terpinene to form ascaridole; d) singlet oxygen induced hydroperoxidation of citronellol.

Many examples of immobilized photocatalysts for the photooxygenation reactions reported above are described in the literature. Functionalized porphyrins supported on silica or polystyrene beads,^{99,115} as well as perylene diimides grafted on silica and PVC thin films,^{150,151} have been recently used for the photooxygenation of α -terpinene to ascaridole. The same reaction was conducted in supercritical carbon dioxide with several immobilized photosensitizers by Han *et al.*⁸⁵ RB, RTBP and tetradi(2,6)chloro-phenylporphyrin were trapped in PVC films, inserted through ionic interactions in SiO_2 aerogels or grafted onto amino-derived PVC. These latter materials were also efficiently applied to the photooxygenation of citronellol.⁸⁵ The photooxygenation of dihydroxynaphthalene has been

used as a model reaction for testing several supported organic photocatalysts. Rose bengal, methylene blue and porphyrins have been the mostly used. MB⁺ was used in microemulsion systems and supported on ion exchange resins;^{118,123} porphyrins have been tested in microemulsions¹¹⁸ and immobilized on polyethylene-co-methacrylic acid nanofibrous membranes.⁸³ RB was used in microemulsions,¹¹⁸ grafted on polystyrene¹²³ and intercalated in Ca²⁺-alginate beads.⁹¹ The latter is an interesting example of green approach to the development of immobilized photosensitizers: alginate polymer, extracted from seaweeds, is totally compatible with food and biochemical industrial processes. Ca²⁺ is used as a gelation agent that replaces Na⁺ cations in the copolymer: increasing amounts of Ca²⁺ diminish RB leaching during the photochemical reaction.

4.0. IMPROVEMENTS AND PERSPECTIVES FOR IMMOBILIZED ORGANIC PHOTOCATALYSTS

Supported photosensitizers represent thus suitable alternatives to conventional synthetic methods for oxidation and oxygenation reactions. The development of photosensitizing materials for fine chemistry represents one of the key pathways towards the development of green chemical processes. Efficient materials for photodynamic therapy stand for an advance towards the set-up of less invasive procedures for medicinal treatments. Organic photocatalysts for depollution can be considered as alternatives to inorganic photocatalysts for visible-light applications. Many materials are available and used for lab-scale set-ups. These advances are deeply connected to the technological progresses in the field of reactor engineering and solar chemistry. Some examples of the most important technological progresses directly related to photooxidation processes are listed below. It is not a complete list but the fields we considered as priorities are reported.

- I. Microreactors. These recently developed devices have unique characteristics that make them very interesting for carrying out operations on small scales. The main advantages deriving from the use of microreactors are: large surface/volume ratio, fast and efficient heat dissipation, diffusion dominated mass transfer and easy control of reagents and products. For these reasons they are employed to improve selective reactions with unstable intermediates, heterogeneous catalysis, multi-step synthesis, photochemical processes and, in general, reactions at the gas-liquid interface.¹⁵² Microreactors and microflow reactors applied to photooxidation processes offer several advantages: extensive light penetration in the narrow channels and product removal from the irradiation area. It is thus possible to work at high concentration of PS and to prevent product decomposition under irradiation. In addition, the proximity of the channels maximize the liquid-gas interface which occurs through the channels walls.^{153,154} Different photochemical reactions have been tested in microflow reactors: α -photodecarboxylations, photodecarboxylative cyclizations and additions, photoadditions of alcohols to furanones are some examples.^{153,155,156} Soluble RB has been efficiently used for microflow reactor and bubble microreactor photooxygenation of dihydroxynaphthalene, citronellol and α -terpinene.¹⁵⁷ The combination of microflow technology and supported organic photocatalysts would further improve the green perspective of photooxidation processes, removing the step of product/photosensitizer separation. Unfortunately, the immobilization of organic photocatalysts in the narrow channels designed for microreactors may be difficult. Notwithstanding this difficulty, important and stimulating developments can emerge from

joining micro- and photosensitized chemistry. The developments of microflow chemistry would have a direct impact on the field of photosensitized synthesis of fine chemicals.

- II. Solar chemistry. The use of direct sunlight for chemical processes is the basic concept of photochemistry,¹⁵⁸ nevertheless, in laboratories the use of solar light instead of lamps can be rather difficult. In many cases solar simulator are used: this allows the study of photocatalysts in conditions similar to those of sunlight irradiation.^{72,159} Nonetheless, several examples of the use of solar reactors for photosensitized reactions have been reported. Different devices have been designed to receive, collect and concentrate solar radiation.^{160–163} Thanks to the solar power concentration strategy it is possible to carry out photochemical processes even on a large scale: important examples concern the Plataforma Solar de Almeria, Spain, and the Chemical research plant at DLR (Deutsches Zentrum für Luft und Raumfahrt, German Aerospace Center), Cologne, Germany. Oelgemöller *et al.*¹²⁴ used the last-mentioned infrastructures to carry out photooxygenation and photoacylation reactions with solid-supported organic photocatalysts: in their study, dihydroxynaphthalene and citronellol were efficiently oxygenated at the kg-scale using concentrated sunlight and RB on polystyrene or MB⁺ on ion exchange resins as photocatalysts. Pohlmann and coworkers¹⁶⁴ had already worked in the above-mentioned solar plant for fine chemicals production. At the solar plants in southern Spain, most of applications are pointed towards photocatalytic applications to water treatment (using different kinds of inorganic materials).¹⁶⁰ Some examples of lab-scale photochemical reactions conducted under sunlight have been reported: Sanjuán *et al.*⁷⁰ (Valencia, 39° 28' N, Spain) reported in 1998 of the efficient photodegradation of 4-chlorophenoxyacetic acid with zeolite-supported TPP; Gryglik *et al.*¹¹⁹ (Łódź, 51° 47' N, Poland) used RB, MB⁺ and a porphyrin derivative immobilized in silane gel thin films for the photooxidation of 2-chlorophenol; Suchard *et al.*¹²³ (Dublin, 53° 20' N, Ireland) carried out the photooxygenation of dihydroxynaphthalene with supported methylene blue and rose bengal under direct and concentrated sunlight, obtaining quantitative yields. The experiments locations are reported in brackets to underline the possibility of carrying out solar photochemistry even at “non-suitable” latitudes. Evidently, the possibility to perform outdoor photochemistry using direct sunlight represents a fundamental improvement to the sustainability of this field: freely available renewable energy with no dependence to energy carriers. Nevertheless, atmospheric changes impede continuous processes: for large-scale photochemistry the need of energy storage emerges. Despite such a drawback, solar chemistry can be considered a progress toward sustainability and can be much further improved.^{124,165,166}
- III. LEDs sources. Light-emitting diodes (LEDs) have been developed during the last few decades, and have been used for many daily life applications (as far as the illumination of electronic devices is concerned, *e.g.*). One of the main drawbacks of LEDs was the price, much higher than that of incandescent or fluorescent lamps. Nonetheless, thanks to the continuous fast development of this technology, LEDs are becoming economically competitive relative to standard irradiation sources for photochemistry. Many advantages arise from the use of LEDs in small/micro-scale photochemical processes: luminous efficiency, color selection without filters, small size (→2 mm), quick light up ($\approx \mu\text{s}$), resistance to on-off cycles, cool light (little heat radiated in the form of IR), lifetime (50000 hours, against 15000 and 2000 hours for fluorescent and incandescent bulbs, respectively), shock resistance, light focus. In addition, thanks to their size, LEDs can be combined in flexible arrays which can be adapted to the form of photochemical reactors. Considering the size and the possibility to focus light, LEDs can have a

special influence on photodynamic therapy, for the treatment of confined areas without photosensitization on healthy tissues. Many examples of photosensitizing materials for PDT activated by means of LEDs have been reported in the last years.^{89,90,167-169} LEDs have also been used for illuminating photochemical reactors and microreactors for photosensitized oxidation reactions such as citronellol and α -terpinene peroxidation.^{85,152,170} For applications in water and air treatment, LEDs have been adopted for lab-scale irradiation of both semiconductors and organic photocatalysts,¹⁷¹⁻¹⁷⁵ but the use of sunlight still represents the main potential development for the scale-up in the field of environmental remediation.

Twelve principles are considered for the development of green chemistry:¹⁷⁶

1. It is better to prevent waste than to treat or clean up waste after it is formed.
2. Synthetic methods should be designed to maximize the incorporation of all materials used in the process into the final product.
3. Wherever practicable, synthetic methodologies should be designed to use and generate substances that possess little or no toxicity to human health and the environment.
4. Chemical products should be designed to preserve efficacy of function while reducing toxicity.
5. The use of auxiliary substances (*e.g.* solvents, separation agents, etc.) should be made unnecessary wherever possible and innocuous when used.
6. Energy requirements should be recognized for their environmental and economic impacts and should be minimized. Synthetic methods should be conducted at ambient temperature and pressure.
7. A raw material or feedstock should be renewable rather than depleting wherever technically and economically practicable.
8. Reduce derivatives - Unnecessary derivatization (blocking group, protection/ deprotection, temporary modification) should be avoided whenever possible.
9. Catalytic reagents (as selective as possible) are superior to stoichiometric reagents.
10. Chemical products should be designed so that at the end of their function they do not persist in the environment and break down into innocuous degradation products.
11. Analytical methodologies need to be further developed to allow for real-time, in-process monitoring and control prior to the formation of hazardous substances.
12. Substances and the form of a substance used in a chemical process should be chosen to minimize potential for chemical accidents, including releases, explosions, and fires.

It is thus evident that from the use of immobilized organic photocatalysts, combined to the development of new technologies (such as those described above), represents and will represent an important advance towards the set-up of green chemical processes.

2 Aims

The main aim of the work carried out during this PhD project was to develop, characterize and analyze original materials for photosensitized oxidation reactions. Particular attention was paid to the determination of the photophysical properties of the selected PSs and the effect induced by the immobilization on an inert support (silica). The detection of the reactive species was of primary importance: the excited states of the sensitizers formed upon irradiation were identified and analyzed. Singlet oxygen production was monitored by two complementary methods. The supported photosensitizers were employed, in the form of either monoliths or powders, for the photooxidation of two substrates commonly adopted as models to study singlet oxygen reactivity: dimethyl sulfide at the gas-solid interface and α -terpinene at the liquid-solid interface. Singlet oxygen was the main ROS expected to be formed by the selected PSs; nonetheless, the reaction products were analyzed and other possible mechanistic scenarios investigated.

1.0 PHOTSENSITIZERS

In Chart 8, the commercial PSs selected for this study are presented.

9,10-dicyanoanthracene (DCA) is a cyanoaromatic whose photophysical properties have been investigated in detail: it can be considered as a reference for this class of compounds. As mentioned in the Introduction, it absorbs in the visible region (approx. 425 nm), it has a versatile reactivity but can be hardly functionalized.¹⁷⁷ **DCA** is able to react via both electron and energy transfer; in acetonitrile, its reduction potential is -0.97 vs SCE and its triplet state energy is 175 kJ mol^{-1} .^{32,37,41,42} the production of both superoxide radical anion and singlet oxygen is possible. Its reactivity strongly depends on the substrate (and its corresponding oxidation potential). In the presence of particular substrates, such as thioanisoles, sulfides and arylalkanols, the ELT route can be enhanced or decreased: electron donating compounds, for example, favor the formation of a complex with **DCA** in the excited states, which efficiently evolves towards the formation of a radical pair.^{41,43,147} One of the main peculiarities of **DCA** is its excellent quantum yield of fluorescence, which is around 0.9 in most solvents. For this reason intersystem crossing is strongly disfavored (quantum yields of triplet formation between 0.02 and 0.04, depending on the solvent).^{42,43} Nonetheless, singlet oxygen production by **DCA** can be very efficient, even though the quantum yields reported in the literature are highly variable: Wilkinson *et al.*³¹ reported in 1993 values between 0.09 (CHCl_3 , air) and 2 (CCl_4 , oxygen saturation), while Cantau *et al.*¹¹⁶ reported values > 1 for silica-embedded **DCA**. The energy of the excited states of **DCA**, approx. 280 and 175 kJ mol^{-1} , respectively for the singlet and the triplet states, can help better understand this particular behavior.^{32,37,42} Considering the high energy difference between the two excited states (105 kJ mol^{-1} , *i.e.* $> 94.2 \text{ kJ mol}^{-1}$) and the rate constant of fluorescence quenching by ground state oxygen ($1.0 \times 10^{10} \text{ M}^{-1} \text{ s}^{-1}$), it emerges that **DCA** singlet excited state is efficiently deactivated by oxygen and can yield singlet oxygen.¹⁷⁸ Afterwards, either

the triplet excited state or the ground state of the PS can be obtained. Subsequently, from the triplet excited state of **DCA**, further singlet oxygen may be produced. Such a particular behavior explains why it is possible to measure quantum yields of $^1\text{O}_2$ production > 1 , notably under oxygen saturation.⁴⁰ Quantum yields of singlet oxygen production higher than 1 and its production from the singlet excited state of the PS are very uncommon. Its photophysical behavior being striking, **DCA** has been studied in detail over the past three decades and many of its spectroscopic and photophysical insights are known. The absorption spectra of the radical anion¹⁷⁹ and the triplet excited state^{42,43} have been recorded in solution (the latter only in the presence of heavy atoms to enhance the amount of populated triplet states), its fluorescence properties have been determined in extreme detail,^{32,40,42,43,178} its reactivity studied in the presence of several substrates, such as sulfides,^{55,116,147} alkanols, alkenes, aromatics, cyclopropanes and anisyl ethers.⁴¹

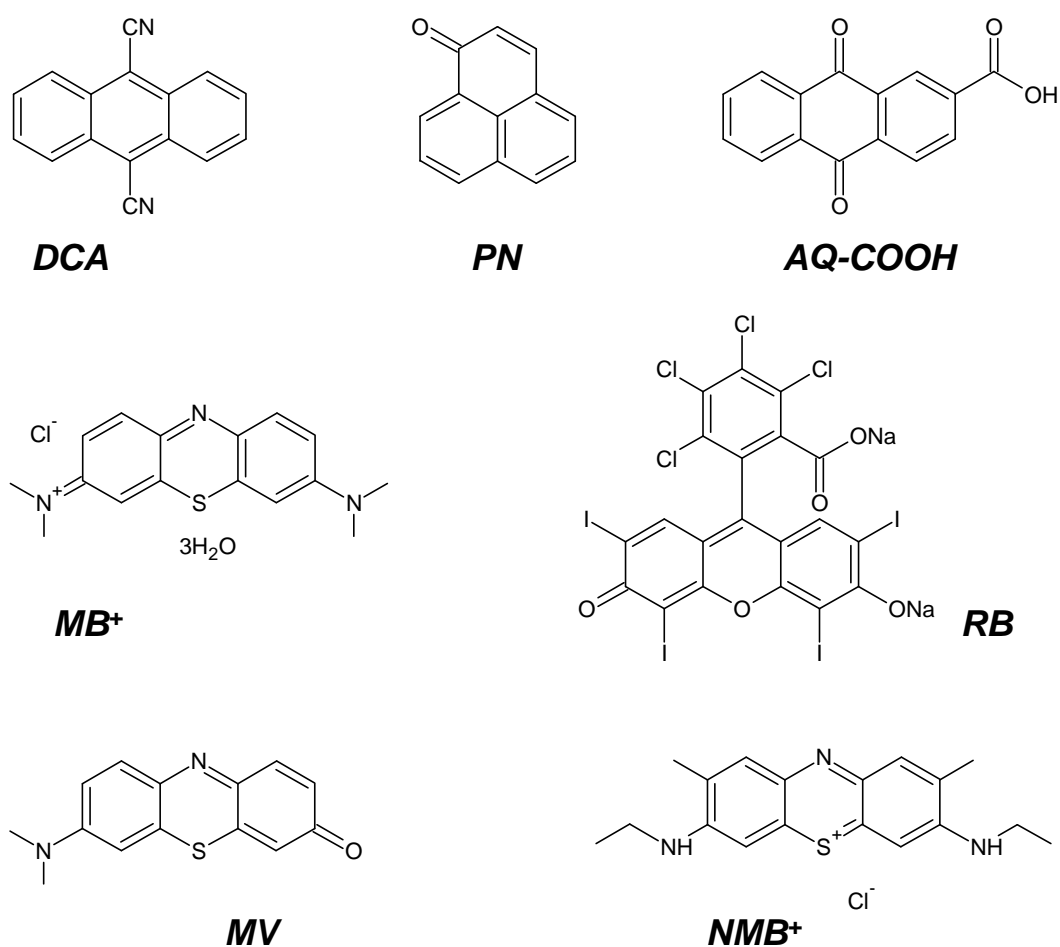


Chart 8 Commercial PSs selected for this work: 9,10-dicyanoanthracene (**DCA**), perinaphthenone (**PN**), anthraquinone-carboxylic acid (**AQ-COOH**), methylene blue (**MB⁺**), rose bengal B (**RB**), methylene violet (**MV**), new methylene blue (**NMB⁺**).

Perinaphthenone (PN) is an aromatic ketone usually selected as a reference for the determination of the quantum yield of singlet oxygen production: its photophysical behavior is well known and doesn't vary with the chemical environment.^{45,47} Its absorption band is predominantly positioned in the UV-A

region, even though it extends till the visible range (**PN** is yellow). It efficiently gives the triplet excited state with quantum yields of intersystem crossing close to unity. ET is very efficient and the quantum yield of singlet oxygen production has been calculated to be approx. 1 in most solvents (cyclohexane, toluene, acetonitrile, ethanol, dichloromethane).^{45–48} The energy of its triplet excited state is between 174 (cyclohexane) and 183 (dichloromethane) kJ mol^{-1} .⁴⁵ The absorption spectrum of the triplet excited state, as well as that of the radical anion, have been measured.^{46,51} *Ab initio* calculations have been carried out to precisely determine the photophysics of **PN** evolving to singlet oxygen production. After the initial population of the S_2 excited state with $(\pi-\pi^*)$ character, the system undergoes internal conversion to the $^1(n-\pi^*)$ state. After reaching the S_1 minimum, the system rapidly evolves to the T_1 ($\pi-\pi^*$) state by intersystem crossing ($k_{ISC} \approx 10^{10} \text{ s}^{-1}$, vs $k_F \approx 0.6 \text{ s}^{-1}$).^{49,50} From the T_1 state, ET to molecular oxygen is very efficient. The main drawbacks of **PN** are its non-solubility in water and the impossibility of grafting. To overcome these negative aspects, functionalization can be carried out. A water-soluble sulfonate derivative which is as efficient as **PN** can be prepared in very extreme conditions (H_2SO_4 96%, 170 °C for 36 hours);¹⁸⁰ a methoxy derivative (no Φ_Δ available) can be obtained after 4 synthetic steps, in quite low yields;¹⁸¹ an amino-derivative is commercially available but the reported quantum yield of singlet oxygen production is very low (0.04 in ethanol).¹⁸² Good results have been obtained for the insertion of heteroatoms (Mg, Br) on the **PN** structure: the derivatives were obtained in quite high yields and they showed good results in antiprotozoal applications.¹⁸³ **PN** is quite stable under irradiation and compatible with many solvents and environments.

Anthraquinone (AQ), an aromatic ketone, has been chosen, together with its graftable derivative **anthraquinone-2-carboxylic acid (AQ-COOH)**, for its particular reactivity as a PS for both singlet oxygen production and electron transfer reactions. As for **PN**, the weak $n \rightarrow \pi^*$ absorption band of **AQ** is only slightly extended in the visible region; nevertheless, its excellent sensitizing properties and its photostability counterbalance the limited absorption in the visible. **AQ** has a high quantum yield of intersystem crossing (0.90)³³ and the values of quantum yield of singlet oxygen production (Φ_Δ) reported in the literature are comprised between 0.62 and 0.70.^{33,56} Similarly to **DCA**, the energy of the singlet excited state is very high, 284 kJ mol^{-1} ,^{37,54} nevertheless, the energy of the triplet excited state also being high (approx. 260 kJ mol^{-1}),^{37,54} contrary to dicyanoanthracene, it cannot form singlet oxygen from the singlet excited state. **AQ** can however act as an ELT sensitizer (reduction potential = -0.86 V vs SCE in ACN):³⁷ radical mechanisms have been described for the oxidation of isopropanol,¹⁸⁴ dichlorophenol⁵⁷ and cyclopropanes.¹⁷ Studies have been carried out on the sulfonic acid derivative of **AQ**: electron transfer is still possible and the quantum yields of singlet oxygen production do not seem modified by the functionalization (Φ_Δ 0.69 in acetonitrile).^{33,56} Few studies have been carried out on the carboxylic derivative **AQ-COOH**: it showed a good photosensitizing activity once grafted on cotton for the degradation of pesticides and for bactericidal applications.⁸⁶ Since the properties of anthraquinones do not seem highly dependent on the functionalization and considering the possibility of grafting the PS through the carboxylic moiety, it was interesting to focus on the carboxylic derivative **AQ-COOH**.

Methylene blue (MB⁺) is a water-soluble and very well-known phenothiazine dye. It has been known and used for many purposes for more than a century. It has been used as medicinal and textile stain, ISO test pollutant for photocatalysis, antioxidant and antiseptic, singlet oxygen sensitizer, diagnostic agent, antidote for cyanide and nitrate, as a drug for malaria, Alzheimer and other

neurodegenerative diseases.⁶⁰ It is a good candidate for photodynamic therapy applications: it efficiently produces singlet oxygen (quantum yields of $^1\text{O}_2$ production between 0.37 and 0.70),³¹ it is non-toxic in the dark, it strongly absorbs at $\lambda > 600$ nm and it photobleaches quite rapidly.^{62–65} In addition it can be easily supported on several materials,¹³² at relatively high loadings: Gut *et al.*¹²⁵ adsorbed MB^+ in ion exchange resins, reaching concentrations higher than $2 \text{ g}_{\text{dye}}/\text{g}_{\text{resin}}$. Its photophysical behavior has been studied in detail: the singlet excited state is very short-living and relaxes very efficiently by ISC to the triplet excited state ($k_{\text{ISC}} = 3 \times 10^9 \text{ s}^{-1}$).⁵⁹ As reported in the Introduction, many MB^+ -based materials have already been developed, particularly for photomedical and photobiological applications. It can difficultly be grafted as it is, but many derivatives can be readily prepared to remedy this drawback.

New methylene blue N (NMB^+) is a phenothiazine dye characterized by properties which recall those of MB^+ . Several studies have been carried out by biologists for potential applications in photodynamic-techniques. Nonetheless, a rigorous study from a photophysical point of view was missing and thus worth being carried out. From the data reported in the literature, NMB^+ presents two main advantages relative to MB^+ : it has a higher quantum yield of singlet oxygen production (1.35 taking MB^+ as a reference) and it is much more lipophilic.^{63,134,185,186} This latter parameter is fundamental for photobiological applications: a higher affinity to membranes allows an easier penetration in cells, increasing the possibility of intracellular PDT activity. NMB^+ has been localized in higher amounts in the intracellular space, in particular at ribosomal sites,^{62,187,188} it seems that a part of its biological activity is bound to the attack of fatty acids in cellular membranes.¹⁸⁹ NMB^+ is non-toxic in the dark and it presents a good activity against highly drug-resistant organisms.¹⁹⁰ It has been embedded in various polymeric matrices: the production of singlet oxygen in those materials was found to be lower than in solution and dependent on the polymer (polystyrene better than polyacrylate).⁶⁴ To our knowledge electron transfer reactions have not been checked with NMB^+ . Any grafting reaction would be difficultly carried out because secondary amines in benzylic position, which represent the only attacking point in NMB^+ , are barely reactive.

Methylene violet (MV) is the only neutral MB^+ derivative. The absence of a positive charge is far from being unimportant: this PS presents a higher activity than MB^+ for killing intracellular viruses thanks to the much easier penetration in cells. Nonetheless, MV is more easily trapped by lipoproteins than MB^+ , which can limit its activity in biological media.^{128,191} No information has been reported on the possibility of type I reactions, but it can form singlet oxygen by energy transfer with relatively high efficiency (in buffered solutions the quantum yield of $^1\text{O}_2$ production is 0.7 relative to MB^+).¹²⁸ Despite the lower $^1\text{O}_2$ production relative to other phenothiazines, it has a particular affinity towards DNA which makes it a good PS for photodynamic therapy: it seems that it is able to covalently bind to DNA under visible irradiation, and that this interaction is not necessarily correlated to the presence of oxygen.^{192,193} As it is in the form reported in Chart 8 it cannot be grafted but it would be interesting to determine what kind of interaction is created between MV and DNA to analyze further grafting possibilities. Some MV derivatives have been prepared, in order to enhance the production of singlet oxygen: by adding iodine atoms (3 steps synthesis) on the structure the photosensitizing properties were improved; unfortunately, the yields were not as high as expected.^{128,194} MV is rather unstable under irradiation, as all phenothiazine derivatives. Its spectroscopic properties strongly depend on the solvent (see Table 1) and on the chemical environment in general.¹⁹⁵

The last commercial PS chosen for this study is a xanthene dye, **rose bengal B** (4,5,6,7-tetrachloro-2',4',5',7'-tetraiodofluoroscein sodium salt, **RB**), selected as a reference for the other red-absorbing dyes (strong absorption maximum at 555 nm). This compound is well-known and its properties have been deeply investigated: it is used as stain for eye damages and liver cancer, as an insecticide, as an antiseptic and it has recently been inserted in formulations against melanoma and psoriasis/eczema. The latter pharmaceuticals are being subjected to clinical tests (Provectus Pharmaceuticals INC.). Its reactivity is probably limited to type II mechanisms and it produces singlet oxygen rather efficiently (quantum yields of $^1\text{O}_2$ production reported in the literature between 0.54 and 0.95).^{31,67,196} It presents two available grafting groups, which make it very interesting for the development of photosensitizing materials. **RB** is commercially available grafted on both Merrifield resin (Sensitox) and polystyrene. Even though it is rather unstable under irradiation, its high activity makes him a good PS for many applications. Several examples of **RB**-based materials for various application fields are reported in the literature. It has been successfully bound to several polymers, since the first results of Schaap *et al.*^{197,198} and Nilsson and Kearns.¹⁹⁹ Yan *et al.*²⁰⁰ reported the grafting of **RB** on wool for high-yields photooxygenation reactions in fine chemistry, Brewer *et al.*⁸⁷ described the activity of cotton- and nylon- supported **RB** for the oxidation of aromatic sulfides, Burguete *et al.*^{201,202} detected $^1\text{O}_2$ production by **RB** supported in cast polymeric monoliths, Shiraishi *et al.*²⁰³ prepared colored photostable polymers including **RB** and chlorophenols as sacrificial groups, Moczek *et al.*²⁰⁴ described the preparation of water-soluble photodegradable polymers based on chitosan and **RB**. It can be grafted on other supports such as silica, as reported by Tamagaki *et al.*⁹³

Other photosensitizers have been developed within our laboratory: considering the preliminary promising results (on compound **1**, Chart 9), in this work several efforts have been carried out to study in detail the photophysical properties of what we could define as an original class of cyanoaromatic dyes. **Benzo[b]triphenylene-9,14-dicarbonitrile (DBTP, 1)** and its derivatives are reported in Chart 9. Since **1** cannot be grafted, it was functionalized to yield compounds **2-6**; notably, compound **6** has been prepared to be grafted on isocyanate groups by one-pot procedure without the formation of by-products. **DBTP** presents a medium-strong absorption band positioned at approx. 420 nm and it showed to be a good singlet oxygen producer; its photophysics is highly dependent on the environment.^{117,205} It is characterized by a redox potential (-0.92 V vs SCE) negative enough to allow the formation of superoxide radical anion by ELT.²⁰⁵ Compounds **2-6** have been synthesized, in addition to grafting purposes, to analyze in detail the effect of functionalization on the photophysics of **DBTP**.

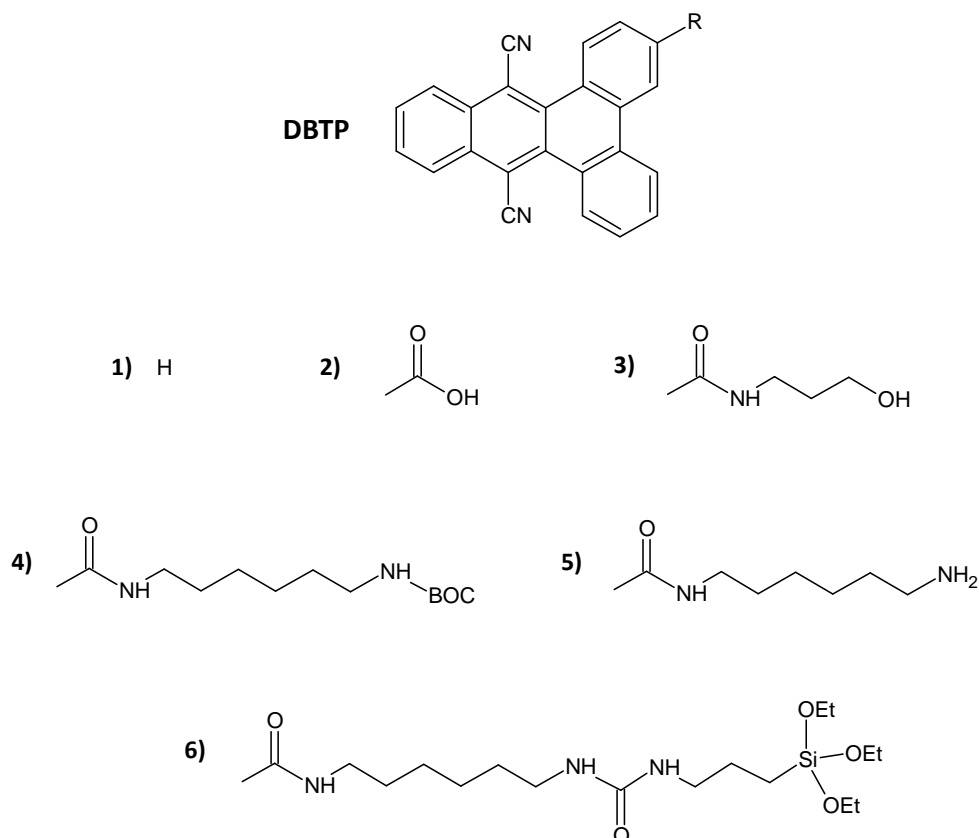


Chart 9 Chemical structure of DBTP (1) and substituents (R) corresponding to compounds 2-6.

Table 1 Maximum absorption wavelengths (θ - θ transition), corresponding molar extinction coefficients and quantum yields of singlet oxygen production of the PSs used in this work; possibility of grafting and number of corresponding reference (SciFinder: research “substance identifier”, June 28th 2013). Data relative to already published studies.

PS	λ_{\max} / nm	ϵ_{\max} / $M^{-1}cm^{-1}$	$\Phi_{\Delta}^{31,33}$	graftable	n° references
DCA ^{32,40,42,116}	425	9500 \rightarrow 13000	0.09 \rightarrow 2.00	no	749
PN ⁴⁵⁻⁴⁸	370	8000 \rightarrow 11000	0.97 \rightarrow 1.00	no	483
AQ-COOH	-	-	-	yes	459
AQ ⁵⁴⁻⁵⁶	416	1000 \rightarrow 3000	0.01 \rightarrow 0.74	no	13484
DBTP-R ^{117,205}	415	11000 \rightarrow 20000	0.89	if R \neq H	7
MB ^{+59,60,63,206}	655	70000 \rightarrow 101000	0.37 \rightarrow 0.70	no	21570
NMB ^{+63,134}	630	-	1.35 (vs MB ⁺)	yes	257
MV ^{61,63,128,194,195}	520 \rightarrow 620	-	0.70 (vs MB ⁺)	no	167
RB ^{67,201,207,208}	555	36000 \rightarrow 106000	0.68 \rightarrow 0.95	yes	3449

2.0 SUPPORTS

Silica (SiO_2) was chosen as support for the photosensitizing materials developed for this work. Silica presents several advantages:

- I. Inertness: it is stable in various chemical media and it should not significantly affect the photophysical characteristics of the chromophores. It is compatible with most grafting techniques and it can be used for applications in various media
- II. Availability: functionalized silica gels and silanes (silica precursors) are not expensive and commercially available
- III. Functionalization: PSs grafting is relatively easily carried out thanks to the differently functionalized silica gels or silica precursors available
- IV. Preparation: silica materials can be prepared by soft-chemistry procedures. Sol-gel methods are very useful and easily put to use
- V. Shape and conformation: silica materials can be prepared, by sol-gel or other techniques, in various forms, depending on the characteristics desired for given applications or analyses. Particles (powders), films, monoliths, foams, fibers can be prepared and functionalized
- VI. Structure: by choosing the suitable preparation technique and the use of templates, determined structures can be obtained. Specific surface area and porosity (structure, size, surface area, volume) can be tuned by choosing the precursors and the synthetic route. Microporous silica can be transparent, a useful characteristic for spectroscopic analyses and photooxidation tests. High surface areas favor adsorption/desorption phenomena, important for photochemical reactions.

This work focused on two kinds of silica supports: transparent monoliths and powders.

Monoliths were synthesized starting from commercially available silanes by a sol-gel method developed within the group which allows the formation of transparent porous structures.^{55,116,117} Several PSs were encapsulated in the monoliths: the transparency of the supports allowed the spectroscopic characterization of the supported sensitizers and their macroscopic shape enabled their use as photochemical microreactors for gas-solid processes. All monoliths were characterized by B.E.T. to determine their structural properties (surface area and porosity). Different chemical modifications were attempted in order to study the effect on both the material structure and the PS photophysical behavior; in particular we tried to modify the hydrophobicity of the materials to investigate the role of water on photophysical and photochemical phenomena. Moreover, monoliths preparation was modified to graft **DBTP**-derived photosensitizers. It was thus possible to study the influence of grafting on the photosensitizing properties of **DBTP**.

DBTP- **AQ**- and **RB**- derived powders were prepared by grafting the corresponding chromophores on commercially available functionalized silica gels. The effect of the grafting on the PSs properties was determined and the light-induced oxidation of α -terpinene in the liquid phase was used to investigate the photosensitizing properties of these materials in suspension.

3.0 PHOTOPHYSICS

The PSs were characterized in detail from a spectroscopic point of view, both in solution (mainly acetonitrile) and in the supported-phase (monoliths).

Absorption and excitation/emission fluorescence spectra were recorded, as well as the fluorescence quantum yields and lifetimes. **DCA** and **MB⁺** were used as reference PSs for the fluorescence analyses. Such a characterization was carried out in solutions and in monoliths to study the effect induced by the matrix. Powders were analyzed by diffuse reflectance UV-Vis spectroscopy (DRUV).

Laser flash photolysis was used to detect and analyze the transient species produced upon irradiation in both solutions and silica monoliths. The transient species were identified, their absorption spectra recorded, the corresponding lifetimes, deactivation rate constants and quenching rate constants in the presence of oxygen determined. The direct characterization of the transient species produced by irradiating the supported PSs was remarkable and innovative: such a study on solid-supported dyes is usually carried out in suspension. This detailed analysis of the photophysics of the selected PSs allowed a deeper understanding of the mechanisms involved in photosensitized oxidation reactions.

4.0 SINGLET OXYGEN

A method for the indirect detection of singlet oxygen was developed. The procedure, which will be detailed in the next chapter, consisted in quantifying the singlet oxygen produced by means of the consumption of a suitable selective probe. In our case, the probe absorbed in the visible region, while the product formed by ¹O₂ addition was uncolored; it was thus possible to follow the degradation reaction by spectrophotometry and to consequently determine the efficiency of singlet oxygen production. With our set-up it was possible to follow the reaction of the probe while the irradiation took place. The apparatus was set up, the probe chosen and its reaction with singlet oxygen analyzed in detail; the quantum yield of ¹O₂ production (Φ_{Δ}) in ACN was determined for all the PSs selected for this work.

In parallel, singlet oxygen production was analyzed by detecting its phosphorescence centered at 1270 nm. This technique offers a proper method for singlet oxygen quantification: the system under measurement is only composed by the PS (in solution or in silica monolith) and thus no artefacts can be provoked by the presence of another compound in the medium. The intensities of ¹O₂ emission upon continuous irradiation of the samples were determined at different PS concentrations to determine whether ¹O₂ quenching by the sensitizer itself occurred or not. For both the indirect and direct singlet oxygen detection methods, perinaphthenone was used as the reference PS. The results obtained with the two methods were compared: the goal was to determine the possibility of using the selected indirect technique as an alternative effective singlet oxygen detection method. Singlet oxygen emission was also used for measuring its lifetime in silica monoliths; for this purpose a time-resolved set up was necessary.

5.0 PHOTOREACTIVITY

5.1. Gas phase reactions

Silica monoliths can be considered as self-supported porous microreactors; their transparency makes them suitable for uses at the gas-solid interface: since light is transmitted throughout the support, it can be absorbed by the PS in the whole bulk. The photosensitized oxidation of volatile dimethyl sulfide was adopted as a model reaction. It represents an environmentally interesting reaction: sulfides are produced as by-products in many industrial processes and they cause an important olfactory pollution. Singlet oxygen attacks very efficiently sulfides, yielding sulfoxides and sulfones, predominantly; electron transfer reactions can also occur, yielding mainly disulfides. By analyzing the distribution of the products we could determine the main mechanism.

5.2. Liquid phase reactions

Powders were prepared for applications in the field of fine-chemicals production; silica particles were uniformly suspended in acetonitrile and the photosensitized oxidation of α -terpinene was used as a model process. As for the gas-phase reactivity, by analyzing the distribution of the reaction products, we could study the mechanisms involved in the oxygenation reaction and their dependence on the photocatalyst.

In the following chapters, the results will be reported in detail. This study gave rise to the following publications and oral presentations:

- F. Ronzani, N. Costarramone, S. Blanc, A. K. Benabbou, M. Le Behec, T. Pigot, M. Oelgmöller, S. Lacombe, *J. Catal.*, **2013**, *303*, 164-174. Visible-light photosensitized oxidation of α -terpinene using novel silica-supported sensitizers: photooxygenation vs photodehydrogenation
- F. Ronzani, E. Arzoumanian, S. Blanc, P. Bordat, T. Pigot, C. Cugnet, E. Oliveros, M. Sarakha, C. Richard, S. Lacombe, *PhysChemChemPhys*, **2013**, *15*, 17219-17232. Efficient cyanoaromatic photosensitizers for singlet oxygen production: synthesis and characterization of the transient reactive species
- F. Ronzani, P. Saint-Cricq, E. Arzoumanian, T. Pigot, S. Blanc, M. Oelgmöller, E. Oliveros, C. Richard, S. Lacombe, *Photochem. Photobiol.*, accepted. Immobilized organic photosensitizers with versatile activity for various visible light applications

- F. Ronzani, A. Trivella, E. Arzoumanian, P. Bordat, S. Blanc, M. Sarakha, C. Richard, E. Oliveros, S. Lacombe, *Photochem. Photobiol. Sci.*, accepted. Comparison of the photophysical properties of three phenothiazine derivatives: transient detection and singlet oxygen production
- F. Ronzani, P. Bordat, S. Blanc, S. Lacombe, *draft*. Methylene violet as a sensitive protons probe: photophysical and photochemical insights
- F. Ronzani, E. Arzoumanian, E. Oliveros, M. Sarakha, C. Richard, S. Blanc, T. Pigot, S. Lacombe, submitted. Transparent organo-silica photocatalysts activated by visible-light: photophysical and oxidative properties at the gas-solid interface

- **ICP 2013** (The International Conference on Photochemistry), Leuven, Belgium – July 2013

Oral presentation: *Visible-light photosensitized oxidation of α -terpinene using original supported sensitizers: photooxygenation vs photodehydrogenation*

- **XXIV IUPAC Symposium on Photochemistry**, Coimbra, Portugal – July 2012

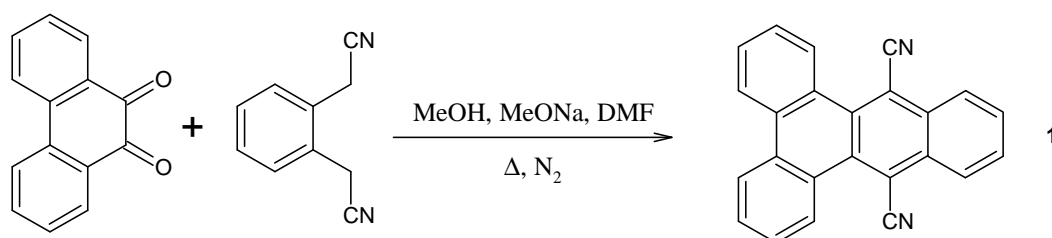
Oral presentation: *Photosensitizing materials for oxidation reactions: detection of reactive species in a complex environment*

3 Materials and Methods

1.0 SYNTHESSES

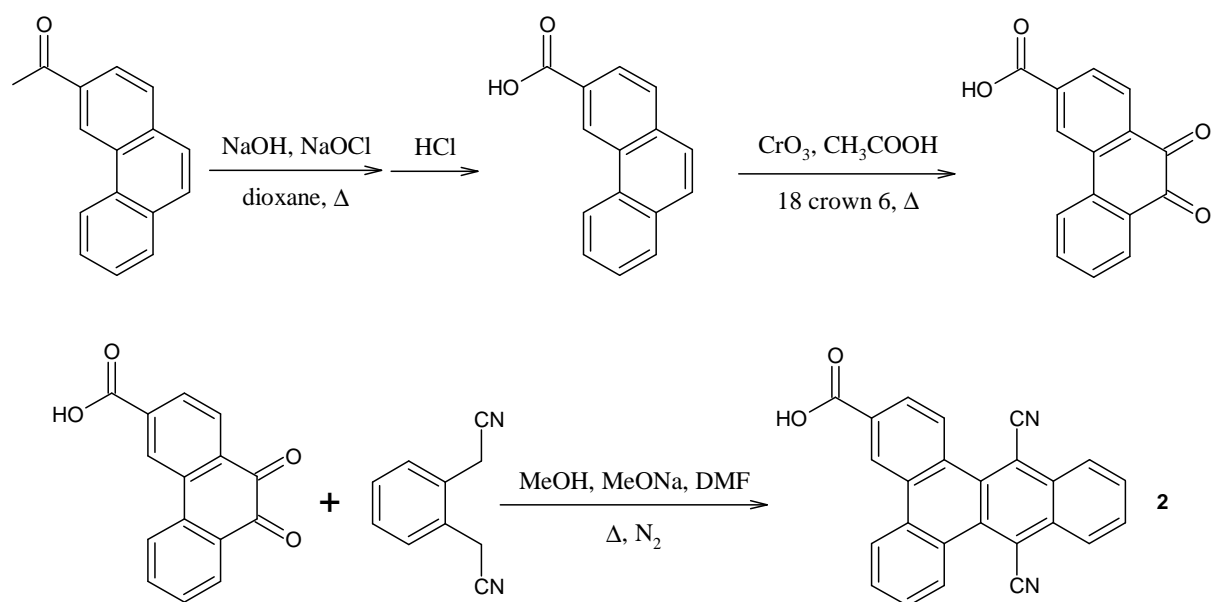
1.1 Development of cyanoanthracene derivatives (compounds 1-4)

Compounds **1** and **2** were prepared under classical conditions by the condensation reaction of phenylenediacetonitrile and a phenanthrenequinone derivative, following the procedure reported by Albano *et al.*²⁰⁹ In Schemes 6 and 7 the reaction routes for the synthesis of compounds **1** and **2** are reported. **1** was obtained by a single-step reaction in a 75% yield starting from commercially available 9,10-phenanthrenequinone and phenylenediacetonitrile (Scheme 6).²¹⁰ For preparing the graftable carboxylic derivative **2** it was necessary to synthesize the suitable phenanthrenequinone derivative (Scheme 7, first two steps). The last step for obtaining **2** did not change from the one described for **DBTP**. The first step of the synthesis of **2** has been slightly modified (addition of NaOH to keep basic pH during the reaction) relative to the procedure already published by Lacombe *et al.* in 2009:¹¹⁷ this was necessary to adapt the synthesis to higher amounts of reactants.



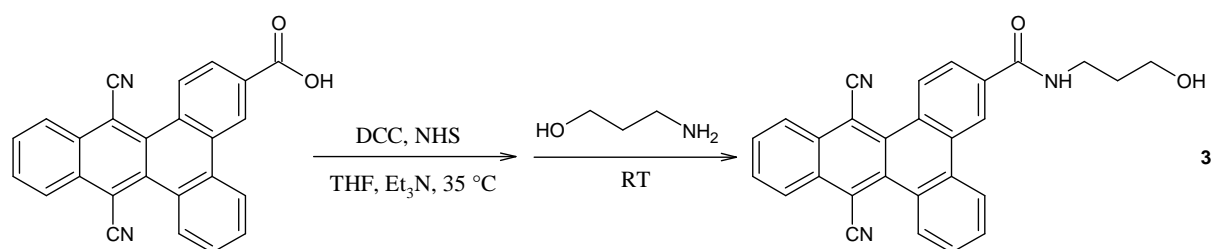
Scheme 6 Synthesis of compound **1**.

Compounds **3** and **4** were originally conceived for this work. Grafting carboxylic acids on silica can be achieved only by previous derivatization (*e.g.* to yield acyl halides), or by creating a more reactive **DBTP**-adduct by adding peptide-coupling reagents (see below); in both cases, by-products that can pollute the final material are formed. On the contrary, the reaction between isocyanates (NCO) and amines or alcohol can form stable adducts (ureas and carbamates, respectively) without the formation of any by-product.²¹¹ The goal was thus the preparation of hydroxy or amino derivatives of **DBTP**, to be efficiently bound to NCO-functionalized silanes or silica powders by one-step procedures and without by-products.

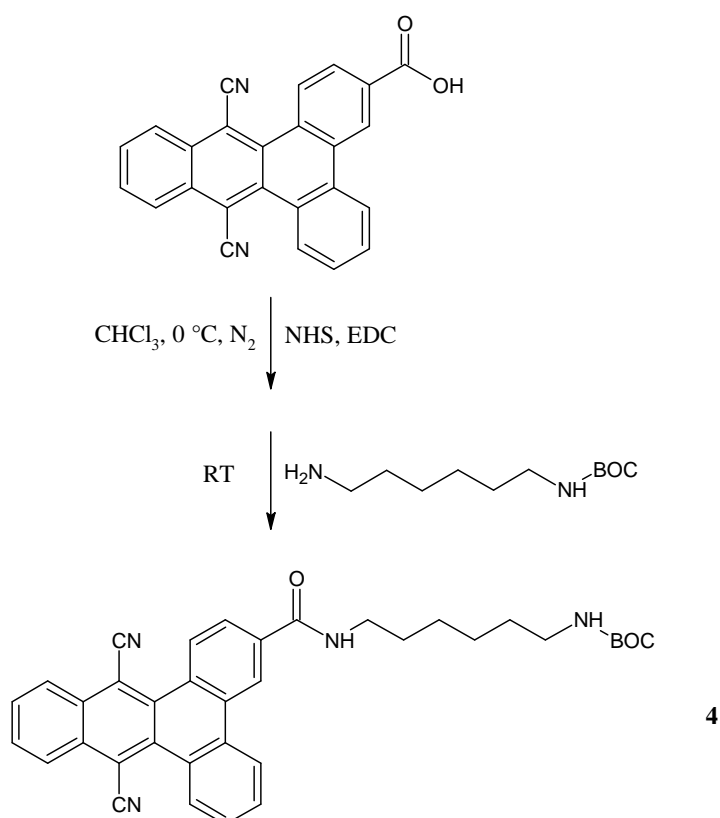


Scheme 7 Synthesis of compound 2.

Compounds **3** and **4** were prepared under usual conditions for solid-phase peptide synthesis (Schemes 8 and 9).^{212,213} For **3** we followed the procedure described by Choitani *et al.*²¹⁴ The carboxylic group of compound **2** was activated by DCC (*N,N'*-dicyclohexylcarbodiimide) to form an *O*-acylurea intermediate, which subsequently reacted with NHS (*N*-hydroxysuccinimide). The resulting activated carboxylic group is very sensitive to electron donor groups, especially amines: the reaction with 3-amino-1-propanol is ten times faster on the NH_2 group than on OH.^{215,216} The addition of the aminoalcohol forms selectively an amide (compound **3**) with a free hydroxyl group at the end of the aliphatic chain. The main drawback of such a synthetic method is related to the by-products arising from the decomposition of the *O*-acylurea intermediate: the *N,N'*-cyclohexylurea formed is rather insoluble in all solvents and difficultly removed. The choice of a *t*-butyloxycarbonyl (Boc)^{217,218} mono-protected hexanediamine as a coupling agent for obtaining compound **4** was made considering that the protection on one of the NH_2 groups avoids any side-reaction and that the Boc deprotection step is compatible with the entire molecule. Other advantages are gained for the further coupling step between compound **5** (Scheme 10) and 3-(isocyanato)propyl-functionalized silica to prepare **DBTP**-grafted materials (see below). Compound **4** was synthesized following the same pathway as **3** with slight modifications. DCC was replaced by water soluble EDC (1-ethyl-3-(3-dimethylaminopropyl)carbodiimide)^{219,220} since it is easily washed away once the reaction is completed; tetrahydrofuran (THF)²¹¹ was replaced by chloroform (CHCl_3) as a solvent.



Scheme 8 Synthesis of compound 3.



Scheme 9 Synthesis of compound 4.

1.2 Transparent silica monoliths

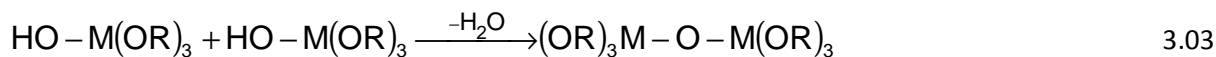
1.2.1 Sol-gel technique

The sol-gel method represents a versatile tool for the synthesis of materials, based on soft-chemistry conditions: room temperature and standard pressure.²²¹ The polymerization of molecular precursors yields the formation of an oxide structure. Typical precursors are easily hydrolysable alkoxides of the form $M(OR)_x$ where M represents a transition metal or a semi-metal. The name sol-gel derives from the colloidal form of the reaction medium: the initially formed *sol* turns into a *gel* which subsequently turns into the solid structure of the final material. A sol is generally defined as a

colloidal suspension of large molecules (1-100 nm) in a solvent (water or alcohol in most sol-gel syntheses); a gel is a solid colloidal system where the dispersed particles form a ramified structure.^{222,223} The only reactants used in the sol-gel process are the alkoxide and water; since the metal precursor is usually insoluble in water a common solvent, usually the alcohol corresponding to the alkoxide, ROH, is added. The first step occurring in a sol-gel synthesis is the *hydrolysis* of the alkoxide, which partially or completely replaces the OR groups with OH groups (equations 3.01 and 3.02).



In a second time the *polymerization* (or condensation) takes place: the hydrolyzed alkoxides react to create oxygen-bridge groups eliminating molecules of water or solvent (equations 3.03-3.05).



At the end of the process a tridimensional network composed by the metal oxide is formed. Several parameters, some of which were considered in detail for this work, can play a role in these two steps: the alkoxide and its concentration, the water/precursor molar ratio, the solvent, the temperature, the pH.

When the rigid 3D-network of the oxide is formed and mixed to the liquid phase (*alkogel*) and no runoff of the solvent occurs, *gelation* is completed: before reaching this stage it is possible to pour the sol in a mold, whose form will be conserved in the final material (monoliths). The alkogel undergoes then an *aging* step, during which the polymerization keeps being underway, the gel volume contracts, the liquid phase is thrown out and the links between the solid particles of the colloid grow. The system becomes rigid. For densifying the oxide network, a drying step is needed:²²⁴ the evaporation of the water/solvent phase produces a capillary pressure inducing a further contraction of the solid: the resulting *xerogel* is 5→10 times smaller than the humid alkogel.

The sol-gel method presents many advantages: highly pure materials can be prepared at low temperature,²²⁵ their characteristics can be controlled and tuned, the form of the final xerogels can be controlled, catalysts or other compounds can be inserted in the structure.^{226,227}

1.2.2 Procedure for the synthesis of silica monoliths

For spectroscopic characterizations and photochemical applications, cast silica materials should respect some criteria: transparency to visible light to allow light penetration into the bulk to excite the PS inside the material; high porosity to optimize the contact between the reagents; inertness

towards the PS; ease in synthesis and functionalization for the grafting of photocatalysts; geometrical form appropriate for spectroscopy (self-standing parallelepiped). Silica positively responded to all these parameters and by a sol-gel procedure developed within the laboratory transparent silica monoliths could be prepared.⁵⁵

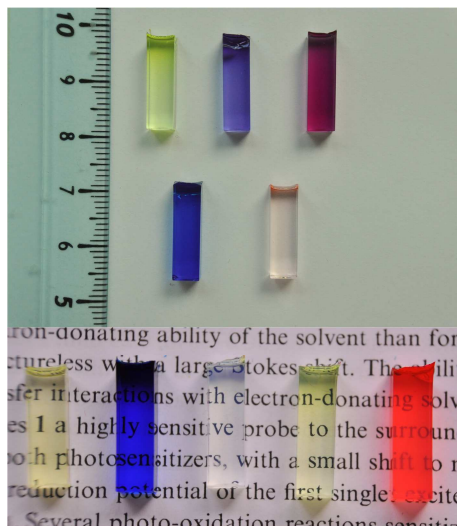


Figure 4 Picture representing some silica-embedded PSs. Top: **SG0-PN**, **SG0-ACN-MV**, **SG0-MV**, **SG0-MB⁺**, **SG0-RB** (series 1). Bottom: **DCA**, **NMB⁺**, blank, **DBTP** and **RB** (all **SG0**) (series 2). See paragraph 1.4 and Chapter 6 for definitions.

The synthesis of silica monoliths was conducted *via* the conventional hydrolysis and condensation of TMOS (tetramethyl orthosilicate) in the presence of MeOH (methanol) and water (**SG0** material if no additional reactant was added). Attempts were carried out using other Si precursors in addition to TMOS (in order to functionalize silica) or MeOH/ACN mixtures as a solvent. Specific area and porosity depend on the alkoxide/alcohol/water molar ratio: in this work a 1/5/4 molar ratio was chosen. Following the procedure, the alkoxide was dissolved in the reaction solvent and the sol was stirred for 2 minutes; after the addition of water and other 2 minutes stirring, the sol was poured into disposable Plastibrand® UV-cuvettes (12.5×12.5×45 mm, 3.5 mL each). The cuvettes were firmly closed (with their lids and parafilm®) and stored 3 weeks at 55 °C (gelation). Afterwards the cuvettes were opened and stored 4 weeks at 30 °C (aging). Finally, the temperature was raised to 50 °C for the drying step (2 days). For the monoliths bearing sulfonic acid groups (**SG0-SO₃H**), the cuvettes filled with the freshly prepared gels were firstly put in a water-ice bath for 3 hours and then stored at room temperature for several weeks; to dry the gels, the opened cuvettes were stored 7 weeks at 35 °C. PSs were usually encapsulated in silica matrices (**SG0** materials). Solutions of the photosensitizers in MeOH (or MeOH+ACN, in the case of **DBTP** and **MV** as PSs for **SG0-ACN** materials) were prepared and suitable volumes were added to the starting sols: volumes were calculated in order to obtain monoliths at different PSs concentrations and absorbances. This way of including PSs in the matrix was followed for all the **SG0** synthesis.⁵⁵

Monoliths bearing octyl groups (**SG0-OC**) were synthesized in order to decrease the hydrophilic character of the materials;^{228–230} to obtain 1→5% molar percentages, small volumes of TMOS-OC

(trimethoxy(octyl)-silane) were added to the starting sols. In addition to the higher hydrophobicity of the final xerogel, the presence of an alkyl substituent (electron donating) on the alkoxide has the effect of accelerating the rate of hydrolysis by stabilizing the positive charge formed on the Si atom. As a consequence of the fast hydrolysis, the final materials were supposed to be essentially microporous.

Some monoliths were prepared with a methanol/acetonitrile (MeOH/ACN)²²¹ mixture as solvent (1/1 molar ratio, **SGO-ACN**): it was done to study the effects on porosity and to increase the amount of inserted **DBTP** (more soluble in the mixture ACN+MeOH). The synthetic procedure did not change and TMOS was used as the only alkoxide. ACN is a polar non-protic solvent: if a mixture of ACN and MeOH is used, the initial hydrolysis rate is mainly controlled by MeOH and its possibility to create H-bonds with the alkoxide. In contrast, ACN makes the polymerization rate slightly slower relative to methanol. For these reasons, the structures of **SGO** and **SGO-ACN** monoliths were not expected to be very different. In addition, the two solvents have similar polarities (in terms of relative static permittivity, ϵ_r):²³¹ the migration of the dye during the synthesis and its final distribution inside the monolith should not strongly vary using MeOH or MeOH+ACN.

Silica monoliths bearing sulfonic acids groups (**SGO-SO₃H**)^{232–234} were prepared adding TMOS-SH ((3-mercaptopropyl)trimethoxysilane) to the initial sol and hydrogen peroxide to start hydrolysis. TMOS-SH molar amount was calculated to be the 1% (0.01 eq.) of the starting TMOS amount (1 eq.); H₂O₂ (0.035 eq.) was added in excess relative to TMOS-SH, to oxidize the precursor SH to the corresponding sulfonic acid SO₃H. This type of functionalized silica is known to be highly transparent: the final structure is essentially microporous.²³⁴ The main drawback of the one-pot synthetic approach developed by Margolese *et al.*²³² for obtaining sulfonic acids by silyl-thiol H₂O₂ mediated oxidation is its high exothermicity: the raise of temperature (approx. 50 °C) during the initial step can trigger too fast hydrolysis and condensation reactions, making the porous structure collapse. To avoid this disadvantage, the sol was prepared in an ice bath and the gels were kept at room temperature for several weeks. Relative to the usual procedure, the formation of acid sites makes the alkoxide protonation faster and consequently the more electrophilic Si atom is much more rapidly attacked by water. This acceleration can be harmful for the matrix structural organization if temperature is not controlled. To our knowledge sulfonic acid functionalized porous silica are always obtained by means of template mediated sol-gel synthesis. Nonetheless, the surfactant can contaminate the materials and its extraction could have made the monoliths fragile; for this reason no attempt has been made.

The preparation of NCO-functionalized silica monoliths was carried out to investigate the possibility to post-graft compound **5** (see below) on the finished monolith bearing NCO groups (**SGO-NCO** and eventually **SGO-NCO-DBTP**). The dye, through its amino moiety, can add to free NCO groups present in the monolith. Several attempts were carried out to insert free isocyanate functions in the silica matrix (**SGO-NCO**), at different NCO loadings (0.5→5 mol%), by adding various amounts of TEOS-NCO (3-(triethoxysilyl)propylisocyanate). In normal conditions, the reaction between NCO and water or alcohols is rather disfavored; in the case of alcohols, basic or metal catalysts are necessary. Nevertheless, in the conditions adopted for the preparation of silica monoliths, all the reagents were very concentrated (MeOH and water were at least 10³ times more concentrated than TEOS-NCO) and let reacting for several weeks: such conditions probably favored the hydrolysis of the NCO groups,

preventing the formation of well-structured materials. Due to their fragility, the monoliths could not be used and no attempt of **DBTP** post-grafting (**SG0-NCO-DBTP**) has been done.

1.3 Grafting

1.3.1 Grafting on silica monoliths

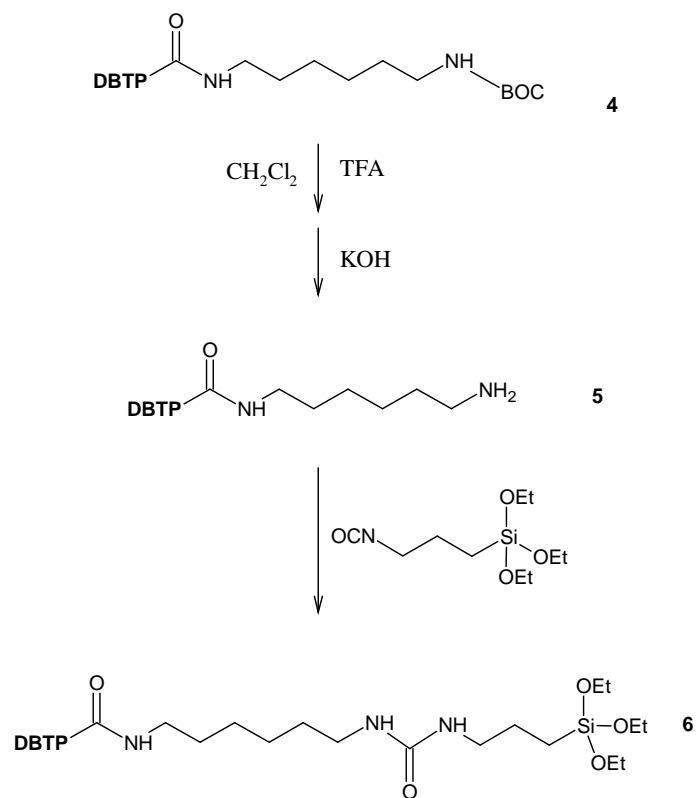
Compounds **5** and **6** were synthesized in order to graft **DBTP** to NCO functionalized silica by a one-pot pathway, without the formation of by-products.^{235–239}

In Scheme 10 the synthesis of compounds **5** and **6** is reported. Compound **5** was prepared from **4** following usual conditions for Boc-deprotection reactions.²¹⁷ The addition of trifluoroacetic acid (TFA) breaks the carbamate linker, forming an ammonium salt between the amino-derivative of **DBTP** and TFA. The **4**-TFA salt is neutralized by the addition of a strong base such as KOH. The reaction was easily followed by TLC (R_f (ethyl acetate/cyclohexane:75/25 vol%): 0.69 and 0 for **4** and **4**-TFA, respectively; R_f (ethyl acetate/methanol:75/25 vol%): 0.52 and 0 for **4**-TFA and **5**, respectively).

Compound **6** was obtained by a one-pot condensation reaction between the amino moiety of **5** and 3-(triethoxysilyl)propylisocyanate (TEOS-NCO). Very dry conditions were necessary to avoid premature polycondensation reactions of the triethoxysilyl-derivative. The reaction between primary amines and isocyanates to yield urea adducts is very fast: completion was reached after some hours under stirring at room temperature (checking by TLC (ethyl acetate): R_f of 0.87 and 0 for **6** and **5**, respectively). The freshly prepared ACN solution containing **6** was directly added to the sols for monoliths synthesis.

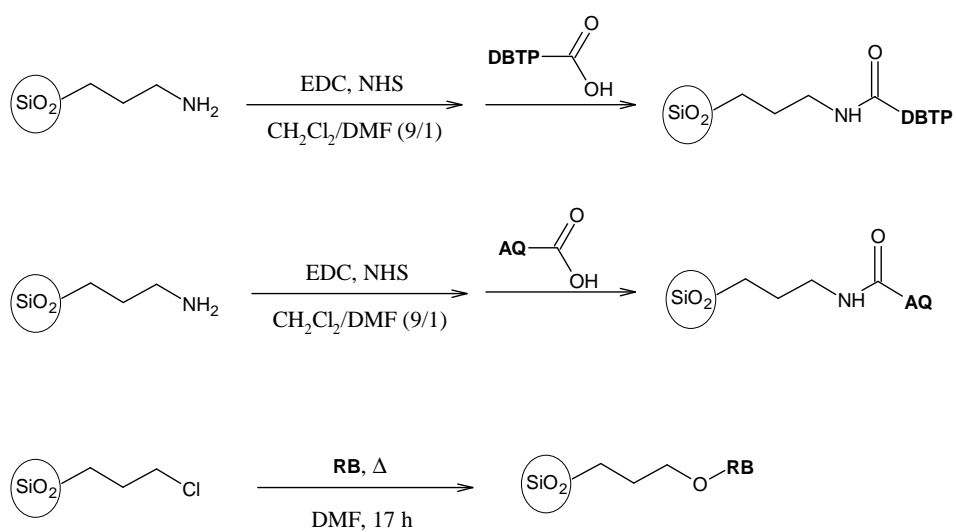
The PS-silyl derivative **6** was introduced in the sol and it participated to the polycondensation process (**SG2** materials): the PS is covalently bound to the matrix. Since the synthesis of **6** was carried out in ACN, a mixture of MeOH and ACN (molar ratio 1/1) was selected for the preparation of the monoliths (**SG2-ACN**); TMOS was used as the main alkoxide and the molar ratio was maintained as for the **SG0** synthesis. Different volumes of the freshly prepared solution containing **6** were added to the sol. **SG2-ACN** materials were fragile but transparent.

An attempt was made to create *in-situ* the isocyanate-**DBTP** adduct participating to the polymerization reaction (**SG1-NCO-DBTP**), by adding to the initial sols (before adding water) variable amounts of **5** and TEOS-NCO (0.5-5%). The reaction between NCO and NH_2 should be more favored than NCO hydrolysis but these monoliths had the same aspect as **SG0-NCO** materials: opaque and fragile. For this reason no characterization was carried out on these monoliths.



Scheme 10 Synthesis of graftable compounds 5 and 6.

1.3.2 Grafting on commercial silica gels



Scheme 11 Grafting of 2 (DBTP-COOH), AQ-COOH, RB on functionalized silica gels.

DBTP- AQ- and **RB-** derived powders were prepared by grafting the corresponding chromophores on commercially available functionalized silica gels. The syntheses are reported in Scheme 11.

DBTP-Si and **AQ-Si** were prepared by reacting **DBTP-COOH** and **AQ-COOH** with $\text{NH}_2\text{-Si}$ (aminopropyl functionalized silica gel). A common peptide coupling method using NHS and EDC was followed.^{211,214,240} Given amounts of dried **2** or **AQ-COOH** were dissolved in a mixture (90/10 vol%) of anhydrous dichloromethane and *N,N'*-dimethylformamide (DMF) under argon. Once the solid was dissolved, NHS and EDC were added and the reaction mixture was stirred at room temperature until thin layer chromatography indicated complete conversion of free sensitizer. $\text{NH}_2\text{-Si}$ was added and the reaction mixture was sonicated for 1 hour and then filtered. The solids were washed by Soxhlet extractions with tetrahydrofuran (THF) until no absorbance was detected by UV-Vis spectrophotometry. When strictly excluding moisture from the reaction medium, the desired coupling is readily achieved and by-products as well as unreacted sensitizer are easily removed by washing. **RB-Si** was prepared according to the one-pot procedure reported by Tamagaki *et al.*,⁹³ starting from commercially available 3-chloropropyl-functionalized silica gel (Cl-Si) and rose bengal sodium salt (**RB**). The reactants were let in DMF under reflux for several hours. After filtration and washing of the colored silica with water, methanol, acetone and chloroform, several Soxhlet extractions with methanol and chloroform were carried out until no visible color appeared in the effluent.

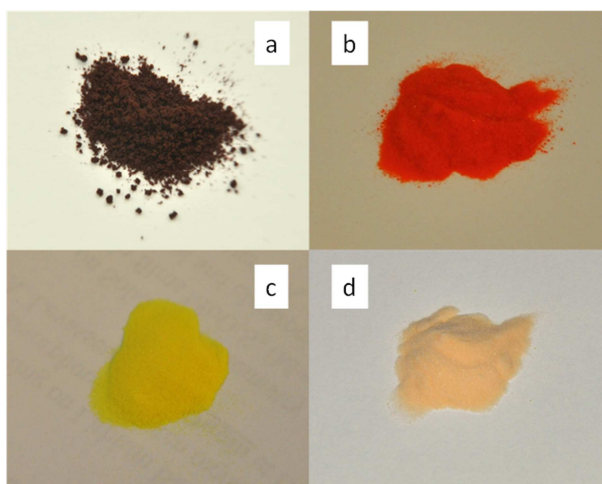


Figure 5 Pictures of the photosensitizing materials prepared by grafting chromophores on functionalized silica gels. a) Commercial **RB-ps** (rose bengal on polystyrene beads), b) **RB-Si**, c) **DBTP-Si**, d) **AQ-Si**.

1.4 Summary of the synthesized materials

All the prepared materials and their labels are listed below:

- **SGO** monoliths: transparent silica monoliths prepared under conventional hydrolysis of TMOS (tetramethyl orthosilicate) in MeOH (methanol). Molar ratio: TMOS/MeOH/H₂O:1/5/4. PSs included: **DBTP**, **DCA**, **PN**, **RB**, **MB⁺**, **NMB⁺**, **MV**.

- **SG0-OC** monoliths: transparent silica monoliths prepared under conventional hydrolysis of TMOS in MeOH containing various molar percentages of octyl groups (deriving from the silica precursor: trimethoxy(octyl)-silane, TMOS-OC). Molar ratio: TMOS/TMOS-OC/MeOH/H₂O:1-x/x/5/4, with x = 0.01→0.05. PS included: **DBTP**.
- **SG0-ACN** monoliths: transparent silica monoliths prepared under conventional hydrolysis of TMOS in MeOH/ACN mixture as a solvent. Molar ratio: TMOS/MeOH/ACN/H₂O:1/2.5/2.5/4. PSs included: **DBTP, MV**.
- **SG0-NCO** monoliths: transparent silica monoliths prepared under conventional hydrolysis of TMOS in MeOH containing various molar percentages of isocyanate groups (deriving from the silica precursor: 3-(triethoxysilyl)propylisocyanate, TMOS-NCO). Molar ratio: TMOS/TMOS-NCO/MeOH/H₂O:1-x/x/5/4, with x = 0.005→0.05.
- **SG0-SO₃H** monoliths: transparent silica monoliths prepared under conventional hydrolysis of TMOS in MeOH containing various molar percentages of sulfonic acid groups (deriving from the oxidation of the silica precursor: (3-mercaptopropyl)trimethoxysilane, TMOS-SH). Molar ratio: TMOS/TMOS-SH/MeOH/H₂O/H₂O₂:1-x/x/5/4-y/y, with x = 0.01, y = 0.035. PSs included: **MV, NMB⁺**.
- **SG1-NCO-DBTP** monoliths: transparent silica monoliths prepared under conventional hydrolysis of TMOS in MeOH containing various molar percentages of isocyanate groups (deriving from the silica precursor: 3-(triethoxysilyl)propylisocyanate, TMOS-NCO). Molar ratio: TMOS/TMOS-NCO/MeOH/H₂O:1-x/x/5/4, with x = 0.01→0.05. Various amounts of compound **5** were added to the initial sol to stoichiometrically react with TMOS-NCO.
- **SG2-ACN-DBTP** monoliths: transparent silica monoliths prepared under conventional hydrolysis of TMOS in MeOH/ACN mixture. Molar ratio: TMOS/MeOH/ACN/H₂O:1/2.5/2.5/4. Various amounts of compound **6** were added to the initial sol (grafting).
- **PS-Si** powders: **2 (DBTP-COOH), AQ-COOH** and **RB** grafted on commercial silica gels.

2.0 STRUCTURAL CHARACTERIZATION: B.E.T. TECHNIQUE

The structure of porous materials is usually characterized by B.E.T. method. Developed since 1938, this technique provides the possibility of a complete structural characterization analyzing the adsorption-desorption of inert gases (notably N₂) on porous samples. By studying the adsorption-desorption isotherms profiles it is possible to determine features such as specific surface area, pore size distribution, pore shape and pore volume. Starting from the work of Brunauer, Emmet and Teller who described a model based on an evolution of the Langmuir theory of monolayer molecular adsorption, the method has been enlarged by applying finer models to the interpretation of adsorption-desorption phenomena. Thanks to the models developed by Barret, Joiner and Halenda (BJH, 1951), Lippens, Linsen and De Boer (t-plot, 1964) and Horvath and Kavazoe (HK, 1983), finer and finer analysis could be carried out on all sort of porous materials, reaching high levels of precision. The main advantage of this technique is that starting from the same N₂ adsorption-desorption isotherms, many models can be applied to the data. Every model corresponds to a precise type of porous material and by the fitting between the model and the experimental data information about the structure is found.

Practically, the inert gas at its boiling point (77 K with N₂) passes through the sample and is adsorbed; the system measures the variation of pressure deriving from the adsorption and calculates the volume of gas adsorbed. Isotherms are traced as curves of adsorbed volume (V_{ads}) as a function of relative gas pressure (p/p_0 , where p_0 is atmospheric pressure); desorption isotherms are measured in the same way, decreasing the gas pressure instead of increasing it.

In this work we were interested in the definition of the specific surface area (S_a , m² g⁻¹) and the pores characteristics of our materials (size distribution, diameter, volume). The B.E.T. and B.J.H. models were used for determining S_a and the characterization of mesopores, respectively. A more detailed structural characterization was out of the scope of this work. The B.E.T. model allows the determination of the volume of gas adsorbed in form of a monolayer from the adsorption isotherm; the calculation of S_a is thus carried out taking into account the number of moles adsorbed and the surface covered by a single adsorbate molecule. This model is valid in a range of p/p_0 between 0.05 and 0.35. The B.J.H. method relates the profile of the desorption isotherm (in the range $0.4 < p/p_0 < 1$) to the pore diameter, independently of the surface area of the sample. Data about the pores volume and surface can be obtained from the pores size distribution. This method is particularly adapted to the pores comprised in a diameter range of 2-50 nm (mesopores). Although models particularly applied to the characterization of microporous materials exist (the monoliths prepared for this study were supposed to be essentially microporous and partially mesoporous), we focused on the characterization of mesopores by the B.J.H. method; the relative percentage of micropores was calculated by the ratio of mesopores and the total pores volumes.

For this work the B.E.T. analyses were carried out employing an ASAP 2010 Micropore Micromeritics. The samples were first dried under vacuum (approx. 1.3×10^{-5} bar) at 150 °C for 24 hours. Once the pressure constant (samples completely “vacuumed”) the N₂ adsorption-desorption isotherm was recorded at 77 K and the data analyzed and fitted by the software.

3.0 SPECTROSCOPIC CHARACTERIZATION

3.1 UV-Vis spectroscopy

UV-Vis spectroscopy is a common tool for the determination of the electronic transitions occurring in molecules upon light absorption. The measurements are usually carried out in transmission: for this study we analyzed the PSs in both solutions and transparent silica monoliths, conceiving for the latter a special self-made sample holder. Alternatively, in the presence of solid samples, it is possible to record and analyze the light reflected by the sample (DRUV). Electronic spectra give preliminary information about the photophysical behavior of the dye and the influences of the environment on its electronic transitions. The Beer-Lambert equation relates the concentration and the absorbance of the chromophore, allowing the quantitative interpretation of the spectra:

$$A_\lambda = \varepsilon_\lambda c \ell \quad 3.06$$

Where A is the absorbance at a given wavelength, ε (M⁻¹ cm⁻¹) the molar extinction coefficient at that given wavelength, c (M) is the concentration of the PS, ℓ (cm) the optical path of light through the sample. The molar extinction coefficient is a key parameter for the determination of the capability of

a dye to absorb light in a given medium. It is an intrinsic property of the chromophore and it strongly depends on the solvent.

The DRUV (Diffuse Reflectance UV-Vis spectroscopy) is an electronic spectroscopy technique used for the analysis of solids by detecting the light reflected by the sample. Diffuse reflectance (R) can be expressed as the ratio of the intensity of the reflected beam to the intensity of the incident beam. The diffuse reflectance can be considered as the sum of several phenomena (reflection, refraction, diffraction) induced by the interaction of the incident radiation on randomly-oriented solid particles. The Kubelka-Munk model^{241,242} is the most commonly used for studying absorption and diffusion of light in inhomogeneous media. The model is based on the assumption that the layer of solid interacting with light is homogeneous in depth: hence, the absorption and the diffusion coefficients (respectively K and S), defined as the fraction of photons absorbed per unity of depth and as the fraction of light diffused per unity of depth (depending on the particle size), are constant in the considered layer. Considering R_{∞} as the diffuse reflectance of a layer of infinite depth, the Kubelka-Munk formula for the correlation between the dye concentration and the reflectance of the sample is:

$$F(R_{\lambda}) = \frac{(1 - R_{\lambda, \infty})^2}{2R_{\lambda, \infty}} = \frac{K_{\lambda}}{S_{\lambda}} \quad 3.07$$

which becomes

$$F(R_{\lambda}) = \frac{(1 - R_{\lambda, \infty})^2}{2R_{\lambda, \infty}} = \frac{\epsilon_{\lambda} c}{S_{\lambda}} \quad 3.08$$

since S can be considered constant and K is given by the product of the molar extinction coefficient of the chromophore and its concentration. DRUV analyses are often only qualitative. To obtain quantitative data it is necessary to measure spectra relative to a certified reference.

In this work UV-visible absorption spectra were recorded with a double beam Cary 5000 spectrophotometer in steps of 0.5 nm using a 1 cm quartz optical cell (Hellma). With this set-up the light coming from the source is doubled: one beam passes through the sample, the other is used as a reference. A photomultiplier records the light which passes through the sample as a function of the wavelength. The diffuse reflectance UV-Vis spectra (DRUV) of monolithic or powder samples were measured with a Perkin-Elmer 860 Spectrophotometer equipped with a 15 cm diameter integrating sphere bearing the holder in the bottom horizontal position. They were recorded at room temperature in steps of 1 nm, in the range 300-800 nm with a bandwidth of 2 nm. The instrument was calibrated with a certified Spectralon white standard (Labsphere, North Sutton, USA).

3.2 Fluorescence spectroscopy

Steady-state and time-resolved fluorescence spectroscopy allows the analysis and characterization of the singlet excited states of chromophores; intrinsic photophysical parameters as well as kinetic characteristics of the excited state can be determined. Fluorescence spectroscopy is a very sensitive technique, with detection limits in the 10^{-9} - 10^{-12} M range (depending on the studied compound).³

In a fluorescence spectrometer a near-continuum source of UV-Vis radiation passes through a monochromator which selects an excitation wavelength. The dye (fluorophore), which can be dissolved in a solvent or supported on silica, absorbs the radiation and emits fluorescence. Fluorescence emission is collected at right angle relative to the excitation beam and focused on the entrance of a second monochromator; fluorescence radiation is transmitted to a photomultiplier for acquisition. Emission is collected at right angle to the optical axis of the incident light beam to reduce the interference of the scattered excitation radiation. Two types of spectra can be recorded: i) by setting the excitation wavelength with the first monochromator and by scanning the second monochromator over the emission region of the sample, *emission spectra* are recorded; ii) *excitation spectra* are recorded by setting the second monochromator to a wavelength emitted by the sample, while the first one is scanned to discover the wavelengths absorbed by the sample which can give fluorescence emission. Theoretically, the first transitions of the excitation and the emission spectra should occur at the same wavelength. Nonetheless, in most organic compounds, the electronic excitation induces large nuclear geometry changes (following the Franck-Condon principle), which results in a significant red-shift of the fluorescence emission relative to the absorption spectrum (Stokes shift). To avoid artefacts due to re-absorption phenomena, it is important to analyze diluted samples: the absorbance corresponding to the 0-0 transition is usually ≤ 0.1 . In more concentrated samples the emitted fluorescence could be reabsorbed by the sample itself, inducing errors in the results.

By analyzing fluorescence spectra, it is possible to determine the fluorescence quantum yields (the ratio of the emitted and the absorbed photons) of a chromophore in a given medium (solvent). For these calculations equation 3.09 was used.

$$\Phi_{PS} = \Phi_R \frac{1 - 10^{-A_R}}{1 - 10^{-A_{PS}}} \frac{S_{PS}}{S_R} \left(\frac{n_{PS}}{n_R} \right)^2 \quad 3.09$$

The absorption spectra of the PS under study and a reference (R) are recorded, their absorbance (A_R and A_{PS} , respectively for the reference and the PS) at the wavelength of irradiation (excitation) are precisely determined. The emission spectra of both reference and PS are recorded, corrected by the solvent emission, without any change in the experimental parameters. By numeric integration, the areas of the emission spectra are determined (S_{PS} and S_R , respectively for PS and reference). It is thus possible to calculate the fluorescence quantum yield of a chromophore by comparison with a reference; in the case of analysis in different solvents, a correction taking into account the different refractive indexes (n) is necessary. For **DBTP** derivatives, **DCA** was selected as a reference fluorophore ($\Phi_F = 0.87$ in ACN),¹⁷⁸ while for the dyes absorbing at higher wavelength, the quantum yield of methylene blue in methanol (0.03) has been chosen as a reference.²⁴³

For the determination of the fluorescence lifetime it is necessary to analyze the variation of the emitted radiation as a function of time. It is thus necessary to obtain, through an intense burst of light, an initial high concentration of excited molecules and to measure the corresponding decay rate. The concentration of molecules in the singlet excited state exponentially decreases as a function of time, by means of a rate constant, k_f , which takes into account all the possible dissipation pathways (fluorescence, internal conversion, intersystem crossing).

$$[\text{PS}^*] = [\text{PS}^*]_0 e^{-k_F t} \quad 3.10$$

$$\tau_F = 1/k_F \quad 3.11$$

The software analyzes the decay traces and calculates the corresponding lifetimes. Fluorescence lifetimes are usually comprised in the range of 10^{-10} - 10^{-7} s: nano- and pico-seconds radiation pulses are necessary. To increase the signal/noise ratio, time-correlated single photon counting (TCSPC) is very useful. The set-up briefly consists of two photomultipliers (PM) and a device called time-to-amplitude converter. The first PM detects the excitation light pulse and triggers the time-to-amplitude converter, which subsequently initiates a voltage ramp (the ramp rate is selected by the operator). The second PM detects the emitted photons and sends a signal to the converter which stops the voltage ramp; the second PM is extremely sensitive, capable of responding to a single photon. Hence, the time occurred between the excitation pulse and the detection of the emitted photon is converted into an electric signal. Such a cycle (extremely fast) is repeated thousands or millions of times per second, amplifying the final signal.

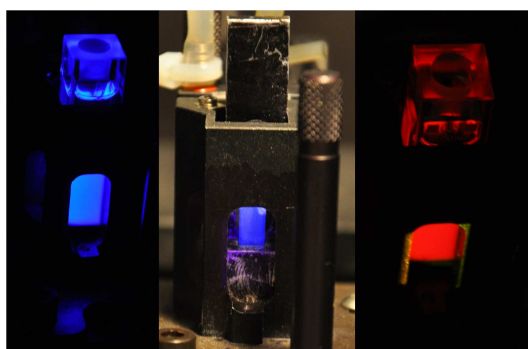


Figure 6 Fluorescence emission (visible light) of **DCA** (left) in ACN and in silica monolith (both excited at 385 nm) and of **MV** (right) in ACN (irradiated at 585 nm). The color of the emitted radiation is clearly detectable at the naked eye.

In this work, corrected steady-state emission and excitation spectra were measured using a photon counting Edinburgh FLS920 fluorescence spectrometer equipped with a Xe lamp. Time-resolved fluorescence experiments were carried out by using a nano-second flash-lamp (nF900) and a time-correlated single photon counting. The lifetime data were analyzed with the re-convolution fit (including instrument response) of the Edinburgh software. The concentrations of all compounds were adjusted to give an absorbance around 0.1 at the absorption maximum (I_1) in a 1 cm fluorescence quartz optical cell (Hellma).

3.3 Detection of the transient species: laser flash photolysis

The detection of transient species is usually carried out by laser flash photolysis. This time-resolved spectrophotometric technique, developed in 1949 by Eigen, Norrish and Porter, allows the detection of short-lifetime (> 50 ns) intermediates and transient species. The system under analysis is

perturbed by a short and intense radiation (a laser beam) and the evolution of the perturbation is analyzed as a function of time. The measurements after the laser pulse are carried out in a way similar to the one described for time-resolved fluorescence. The analytical radiation which passes through the sample is directed at right angle relative to the perturbation beam in order to avoid any interference. After passing through the sample (a solution in a quartz cell or a monolith) the light is filtered by a monochromator and analyzed by a PM (photomultiplier). The analysis of the transient species is done by measuring the absorbance of the chromophore before and after the laser pulse, in order to put in evidence the perturbation occurred in the system in terms of ΔA (difference of absorbance). The absorbance variation as a function of time is calculated with the following formula:

$$\Delta A = \log \frac{S_{100} - S_0}{S_t - S_0} \quad 3.12$$

Where S_0 is the signal intensity in the absence of the analytical radiation, S_{100} the signal intensity recorded after the passage of light through the non-perturbed sample, S_t the signal intensity at a given time after the laser irradiation. If the absorption is due to a unique transient species, the decay trace (ΔA vs t) gives the variation of the transient concentration as a function of time, which can be easily exploited to determine the lifetime of the concerned species. If the ground-state absorbance of the species under study doesn't vary during the experiment (*i.e.* no photobleaching), it is possible to determine the absorption spectrum of the transient species and its evolution as a function of time after the laser pulse. This is done by measuring the transient decay at different wavelengths and building the absorption spectrum point-by-point.

From the mathematical analysis of the exponential decays it is possible to determine the lifetime of the concerned species, considered as the inverse of the rate constant of deactivation (k_d). Moreover, studying the decays at different concentration of a quencher, if the irradiated quencher doesn't produce a transient species absorbing in the same wavelength range of the compound under analysis, it is possible to study the reaction between the chromophore transient and the quencher. Considering for instance oxygen as a quencher, by measuring the rate constants of transient deactivation (from the decay profiles) at different O_2 concentration, the bi-molecular rate constant of the transient quenching by oxygen is obtained. Such a parameter was carefully considered in this work for studying singlet oxygen formation by energy transfer from the triplet excited state of the PS.

It is possible to carry out quantitative analyses for the determination of the product $\epsilon\Phi$, where ϵ ($M^{-1} \text{ cm}^{-1}$) is the molar absorption coefficient of the transient species and Φ its quantum yield of formation. The calculation is done by comparison to a chemical actinometer (Ac), for which the product $\epsilon\Phi$ is known and which must have the same ground-state absorbance at the irradiation wavelength as the probe compound. For both species, the transient absorption (A) is monitored at different laser pulse energy (P). The absorbance should linearly increase with P and the slope ($A/P = b\epsilon\Phi$) is related to the product $\epsilon\Phi$ by a constant b . The latter constant only depends on the experimental conditions and can be used to relate the data obtained with the chemical actinometer and the PS under study:

$$\epsilon_\lambda \Phi = (\epsilon_\lambda \Phi)_{Ac} \frac{A/P}{(A/P)_{Ac}} \quad 3.13$$

Further analyses are necessary for the identification of the transient species formed upon irradiation. For the detection of triplet excited states, in addition to experiments of quenching by O₂, energy transfer tests from the PS to a suitable energy acceptor can be carried out: the PS is excited and the triplet excited state of the acceptor, formed by energy transfer, is monitored. By comparison to a chemical actinometer, it is possible to measure $\epsilon_T\Phi_T$ of the triplet produced by ET (which must be distinguished from the triplet produced upon direct irradiation). Supposing that energy transfer is quantitative, the quantum yield of triplet formation by ET can be considered equal to the quantum yield of PS triplet formation. In this way, knowing the ϵ_T of the triplet excited state of the energy acceptor, even if the uncertainty can be high, it is possible to determine the quantum yield of triplet formation of the PS under study. The acceptor must have a triplet energy lower than the PS to make the ET process possible; moreover, if it is not possible to selectively irradiate the PS to avoid any direct formation of the acceptor transient, this latter component must be subtracted to the overall triplet production.

The detection of transient species was carried out on all the PSs studied in acetonitrile or methanol solutions. The analysis of silica-embedded PSs (irradiated in a custom-built sample holder) was limited to the determination of the transient lifetimes and the transient absorption spectra. For all measurements a Nd-YAG laser (GCR 130-1, pulse width 9 ns, 355 nm or 266 nm) was used for sample irradiation. The monitoring system consisted of a 150 W pulsed Xe arc lamp, a R928 photomultiplier and a 05-109 Spectra Kinetics Applied Photophysics monochromator. Signals were digitized by a HP54522A oscilloscope. The laser pulse energy (P) was measured using a joulemeter Ophir Optronics Ltd. Each data was the average of 5 measurements. The absorbance at pulse end was measured for various P values to check the linearity of the dependence of A on P and the monophotonic formation of the transient. For measurements at 355 and 266 nm benzophenone (BP, $\epsilon_T\Phi_T = 6500 \text{ M}^{-1} \text{ cm}^{-1}$, monitored at 520 nm)²⁴⁴ and potassium peroxydisulfate (K₂S₂O₈, $\epsilon\Phi = 1900 \text{ M}^{-1} \text{ cm}^{-1}$, monitored at 450 nm)²⁴⁵⁻²⁴⁷ were respectively selected as actinometers for the determination of $\epsilon_T\Phi_T$ products. Energy transfer experiments were carried out by using rubrene^{37,248} as an acceptor: the energy of the triplet excited state of this compound ($E_T = 109 \text{ kJ mol}^{-1}$) is quite low and ground state rubrene does not absorb significantly at the wavelength of excitation (355 nm), allowing in most cases the selective excitation of the photosensitizer. Rubrene triplet-triplet absorption spectrum is known (λ_{max} 490 nm), as well as its ϵ_T ($26000 \text{ M}^{-1} \text{ cm}^{-1}$). To avoid problems of solubility in ACN, a highly concentrated solution of rubrene in toluene was prepared. To check for any solvent effect, control tests were carried out by adding the same volume of pure toluene in the ACN solution under analysis. Upon laser excitation of oxygen-free solutions of photosensitizers ($1.5 \times 10^{-5} \text{ M}$) and rubrene ($2 \times 10^{-4} \text{ M}$) in ACN, a fast decay of the triplet was observed (monitoring at 470 or 575 nm), as well as an increase of the absorbance at 495 nm attributed to the formation of the rubrene triplet excited state *via* energy transfer (Figure 25). The quantum yield of formation of the triplet state of rubrene was estimated using absorbances measured at the maximum of the triplet formation (approximately 2.5 μs after the laser pulse) for a range of P . Anthracene was also used as an energy acceptor. Solutions were excited at 266 nm, and it was necessary to make a correction for the anthracene triplet formation through direct excitation. The absorbance of triplet anthracene was monitored at 420 nm, and the T-T molar absorption coefficient was taken as $64700 \text{ M}^{-1} \text{ cm}^{-1}$.²⁴⁹

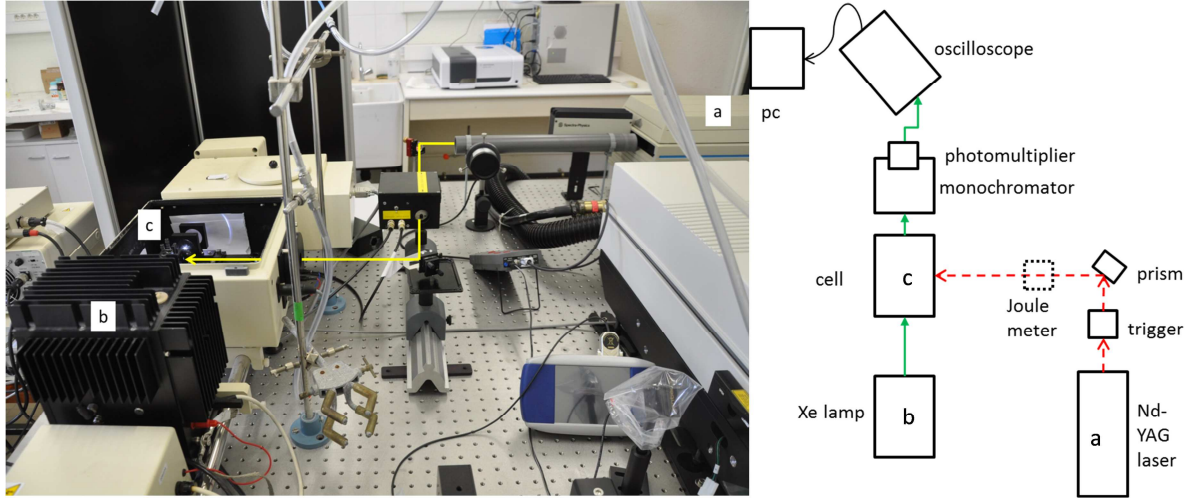


Figure 7 Left: experimental apparatus for laser flash photolysis; the laser beam path is represented by the yellow arrow: from the laser source (a) the beam passes through optic elements to reach the sample (c); the transient detection is carried out by means of a pulsed Xe lamp (b). Right: schematic representation of the same apparatus.

4.0 SINGLET OXYGEN DETECTION

4.1 Direct method: detection of $^1\text{O}_2$ phosphorescence at 1270 nm

4.1.1 Steady-state measurements

Detection of the singlet oxygen near-IR phosphorescence, albeit weak, provides a convenient method for the direct monitoring of this species under steady-state or time-resolved regimes.^{45,250}

The analysis and quantification of $^1\text{O}_2$ by recording its emission signal upon continuous monochromatic excitation of the sensitizer provides the means for determining quantum yields of $^1\text{O}_2$ production (Φ_Δ) and rate constants of $^1\text{O}_2$ total quenching by the PS, as described below.^{251–253} Under continuous irradiation of a sensitizer, the quantum yield of $^1\text{O}_2$ emission is given by:

$$\Phi_e = \frac{P_e}{P_a} = \frac{CS_e}{P_0\alpha} \quad 3.14$$

where C is a proportionality factor depending on geometric and electronic characteristics of the detection system and on specific parameters of the medium (refractive index, NIR absorbance), S_e is the $^1\text{O}_2$ signal intensity, P_0 and P_a are the incident photon flux and the photon flux absorbed by the sensitizer at the wavelength of excitation, P_e is the photon flux emitted by singlet oxygen (phosphorescence). α is the absorption factor, given by:

$$\alpha = 1 - 10^{-A} \quad 3.15$$

where A is the absorbance of the PS at the wavelength of excitation. Φ_e may be also expressed as:

$$\Phi_e = \Phi_\Delta k_e \tau_\Delta \quad 3.16$$

Where Φ_{Δ} is the quantum yield of singlet oxygen production, k_e is the rate constant of $^1\text{O}_2$ emission (s^{-1}) and τ_{Δ} the $^1\text{O}_2$ lifetime (s). Noticeably, the proportionality between the quantum yield of singlet oxygen production (and consequently the quantum yield of singlet oxygen phosphorescence emission) and its lifetime is a key concept of this technique. It is important now to analyze the deactivation pathways of singlet oxygen, which will determine the corresponding lifetime in a given medium.



$^1\text{O}_2$ is deactivated by physical quenching by the solvent (equation 3.17) and by phosphorescence emission at 1270 nm (equation 3.18); in the presence of a quencher (Q), which can be the photosensitizer itself, additional deactivation pathways can occur: chemical reaction with the quencher, yielding a stable oxygenation adduct (equation 3.19), or physical quenching by Q (equation 3.20). Since the phosphorescence emission is negligible relative to physical quenching by the solvent ($k_e \ll k_d$),^{34,254,255} in the absence of a quencher, singlet oxygen lifetime is defined by

$$\tau_{\Delta} = 1/k_d \quad 3.21$$

where k_d is the above-mentioned rate constant of physical quenching by the solvent (s^{-1}). In the presence of Q, the other deactivation pathways must be taken into account, and the corresponding expression of singlet oxygen lifetime is:

$$\tau_{\Delta} = 1/(k_d + k_t^{\text{Q}}[\text{Q}]) \quad 3.22$$

where k_t^{Q} ($\text{M}^{-1} \text{s}^{-1}$) indicates the rate constant of total quenching by Q, generically given by the sum of physical (k_d) and chemical quenching (k_r):

$$k_t = k_r + k_q \quad 3.23$$

Combining equations 3.14, 3.16 and 3.22, it is possible to correlate the $^1\text{O}_2$ phosphorescence emission signal in the presence of a PS to the signal recorded in the presence of a reference photosensitizer, with known Φ_{Δ} .

$$\frac{\Phi_e^{\text{PS}}}{\Phi_e^{\text{R}}} = \frac{C^{\text{PS}} S_e^{\text{PS}} P_0^{\text{R}} \alpha^{\text{R}}}{C^{\text{R}} S_e^{\text{R}} P_0^{\text{PS}} \alpha^{\text{PS}}} = \frac{\Phi_{\Delta}^{\text{PS}}}{\Phi_{\Delta}^{\text{R}}} \frac{k_d + k_t^{\text{R}}[\text{R}]}{k_d + k_t^{\text{PS}}[\text{PS}]} \quad 3.24$$

The proportionality factor C is usually constant for all measurements ($C^{\text{PS}} = C^{\text{R}}$) and singlet oxygen quenching by the reference sensitizer is usually negligible relative to the quenching by the solvent. Hence, equation 3.24 can be simplified to

$$\frac{S_e^{\text{R}} P_0^{\text{PS}} \alpha^{\text{PS}}}{S_e^{\text{PS}} P_0^{\text{R}} \alpha^{\text{R}}} = \frac{\Phi_{\Delta}^{\text{R}}}{\Phi_{\Delta}^{\text{PS}}} (1 + \tau_{\Delta} k_t^{\text{PS}} [\text{PS}]) \quad 3.25$$

where k_t^{PS} ($\text{M}^{-1} \text{s}^{-1}$) is the rate constant of total quenching by the PS. The plot of $(S_e^{\text{R}}/S_e^{\text{PS}})(\alpha^{\text{PS}}/\alpha^{\text{R}}) = f([\text{PS}])$ should be linear and values of k_t^{PS} and $\Phi_{\Delta}^{\text{R}}/\Phi_{\Delta}^{\text{PS}}$ may be obtained from the slope and the intercept of this plot if the value of τ_{Δ} in the solvent used is known. It should be noticed that the equation simplifies if the reference and the PS under study have the same absorbance at the (same) irradiation wavelength:

$$\frac{S_e^{\text{R}}}{S_e^{\text{PS}}} = \frac{\Phi_{\Delta}^{\text{R}}}{\Phi_{\Delta}^{\text{PS}}} (1 + \tau_{\Delta} k_t^{\text{PS}} [\text{PS}]) \quad 3.26$$

When $k_t^{\text{PS}}[\text{PS}] \ll k_d$ (negligible $^1\text{O}_2$ quenching by PS in the range of concentrations used), the quantum yield of singlet oxygen production of a PS in a given medium can be calculated using the following expression:

$$\Phi_{\Delta}^{\text{PS}} = \Phi_{\Delta}^{\text{R}} \frac{S_e^{\text{PS}} P_0^{\text{R}} \alpha^{\text{R}}}{S_e^{\text{R}} P_0^{\text{PS}} \alpha^{\text{PS}}} \quad 3.27$$

Again, if P_a for PS and R doesn't change, the expression simplifies to:

$$\Phi_{\Delta}^{\text{PS}} = \Phi_{\Delta}^{\text{R}} \frac{S_e^{\text{PS}}}{S_e^{\text{R}}} \quad 3.28$$

The quantum yield of singlet oxygen production is simply given by the ratio of the $^1\text{O}_2$ phosphorescence intensity measured in the presence of the sample and of the reference.

This method was used to determine quantum yields of singlet oxygen production for all the PSs chosen for this study in both solutions and silica monoliths. The $^1\text{O}_2$ emission signals were measured at various absorbances for the PSs investigated in order to determine the rate constants of $^1\text{O}_2$ total quenching by the PSs. The analysis was based on relative measurements comparing the experimental results for the PSs investigated to those obtained with a reference sensitizer of known Φ_{Δ} . The standard sensitizer 1*H*-phenalen-1-one (perinaphthenone, **PN**, Chart 2) was chosen for its high Φ_{Δ} value in a large variety of solvents and used as a reference throughout this study.

4.1.2 Time-resolved measurements

The same idea developed for time-resolved fluorescence and laser flash photolysis can be applied to time-resolved detection of singlet oxygen, where $^1\text{O}_2$ represents the transient to detect (lifetime $\approx \mu\text{s}$). A laser pulse is used to perturb the sample containing the PS, singlet oxygen is formed and its phosphorescence emission is detected as a function of time after the laser pulse. The measuring

system converts the intensity of the signal at 1270 nm in an exponential decay trace, which can be analyzed for both determining the singlet oxygen lifetime and quantifying the Φ_{Δ} of the PS in the medium under analysis.²⁵⁵⁻²⁵⁷ In this work time-resolved detection of $^1\text{O}_2$ phosphorescence was only used for the determination of τ_{Δ} in silica monoliths and to confirm the τ_{Δ} in ACN ($71 \pm 2 \mu\text{s}$).³⁴ Singlet oxygen phosphorescence decay traces are usually fitted with a single exponential function from which τ_{Δ} values could be derived.

$$S_t = S_0 e^{-t/\tau_{\Delta}} \quad 3.29$$

Where S_t and S_0 are the amplitudes of the $^1\text{O}_2$ luminescence signals at time t and extrapolated at zero time (laser pulse), respectively. In some cases decay traces can be only fitted to a biexponential function, giving two values of $^1\text{O}_2$ lifetimes, $\tau_{\Delta,1}$ and $\tau_{\Delta,2}$.

$$S_t = A_1 e^{-t/\tau_{\Delta,1}} + A_2 e^{-t/\tau_{\Delta,2}} \quad 3.30$$

4.2 Indirect method: $^1\text{O}_2$ trapping by a molecular probe

The rate of disappearance of a probe Q (quencher) by reaction with singlet oxygen is given by equation 3.31:

$$-\frac{d[Q]}{dt} = k_r [^1\text{O}_2][Q] \quad 3.31$$

where $[^1\text{O}_2]$ is given by equation 3.32 if it is produced by photosensitization:

$$[^1\text{O}_2] = P_a \Phi_{\Delta} \frac{1}{k_d + k_t^{\text{PS}}[\text{PS}] + k_t^{\text{Q}}[\text{Q}]} \quad 3.32$$

where P_a (Einsteins $\text{L}^{-1} \text{s}^{-1}$) is the photon flux absorbed by the PS, Φ_{Δ} its quantum yield of singlet oxygen production, k_d the rate constant of $^1\text{O}_2$ quenching by the solvent, k_t^{PS} and k_t^{Q} the rate constants of $^1\text{O}_2$ total quenching by the sensitizer (PS) and the probe (Q), [PS] and [Q] the sensitizer and probe concentrations, respectively. If there is no interference by the reaction products it is possible to combine equations 3.31 and 3.32:

$$-\frac{d[Q]}{dt} = P_a \Phi_{\Delta} \frac{k_r [Q]}{k_d + k_t^{\text{PS}}[\text{PS}] + k_t^{\text{Q}}[\text{Q}]} \quad 3.33$$

This equation was used to calculate the quantum yields of singlet oxygen production for our photosensitizers in acetonitrile using rubrene as chemical probe. k_t^{PS} data were obtained by luminescence experiments and applied to the calculations for indirect $^1\text{O}_2$ detection. If singlet oxygen total quenching by the sensitizer and the probe are negligible ($k_t^{\text{PS}}[\text{PS}] \ll k_d$ and $k_t^{\text{Q}}[\text{Q}] \ll k_d$), the kinetic analysis is simplified to a first-order model:

$$\ln([Q]/[Q]_0) = -P_a \Phi_{\Delta} (k_r/k_d)t \quad 3.34$$

The use of chemical probes for singlet oxygen detection and quantification requires a detailed knowledge of the kinetic parameters of the reaction between the ROS and the probe. Nevertheless, once the rate constants determined, the analysis of the data is fast and the experimental set-up is simpler than in the case of direct luminescence detection. This experimental method could not be applied to the detection of $^1\text{O}_2$ in monoliths.

4.2.1 Rubrene: a selective probe for $^1\text{O}_2$

As presented in the Introduction, many compounds are known to react with singlet oxygen. Their use as probes for $^1\text{O}_2$ is limited by various parameters:

- The compound must selectively react with singlet oxygen; if it can react with other ROS eventually produced by the PS, the formation of singlet oxygen can be overestimated.
- The product must be stable during the experiment and it must not interact with the other species in the reaction medium.
- The formation of the product (or, alternatively, the consumption of the reagent) must be easily detectable. Different analytical techniques can thus be considered, depending on the properties of the probe/product: UV-Vis spectroscopy, fluorescence spectroscopy and chromatography (HPLC for instance) are the most commonly adopted techniques.

Spectrophotometric probes were specifically considered for this work. Several compounds present absorption spectra which change after reaction with singlet oxygen: the addition of $^1\text{O}_2$ to such chemical probes usually breaks the π -conjugation responsible of the absorption spectrum (near UV and visible region) and the disappearance of the band typical of the compound can be easily followed by means of a spectrophotometer. For instance, substituted anthracenes (dimethyl- or diphenylanthracene, DMA and DPA) and diphenylisobenzofuran (DPBF) are commonly used as probes for $^1\text{O}_2$.^{44,258,259} Dealing with PSs absorbing in the 350-420 nm region, many probes couldn't be used: anthracenes absorb between 350 and 400 nm, DPBF has a maximum of absorption at approx. 415 nm. Some probes are highly expensive and not commercially available: for instance rare earth complexes, terrylene diimide derivatives or substituted xanthene-anthracene adducts.²⁶⁰⁻²⁶⁴ Among the possible probes, rubrene was chosen. This compound has been studied in detail for several applications and many data about it are available in the literature.^{248,265-269} It has been used as a probe for studying singlet oxygen reactivity towards conjugated dienes since the Sixties.²⁷⁰⁻²⁷⁴ Rubrene is a selective probe for singlet oxygen, yielding the formation of a thermally and photochemically stable endoperoxide; such an oxidation product doesn't absorb in the visible, while rubrene is characterized by a characteristic band around 500 nm (Figures 8 and 28).²⁷⁵⁻²⁷⁸ Rubrene consumption was followed by spectrophotometric analysis during irradiation, directly measuring the reaction rate ($-\text{d}[Q]/\text{dt}$). The value of k_t^Q , found in the literature, corresponds to $1.0 \times 10^8 \text{ M}^{-1} \text{ s}^{-1}$ (ACN).²⁶⁵ In the same publication, the reported value of k_r for rubrene photooxygenation in ACN was $3.8 \times 10^7 \text{ M}^{-1} \text{ s}^{-1}$; as it will be showed later, using these two constants it was impossible to have an agreement with our experimental results, and k_r was re-calculated (attempts for determining k_t have been unsuccessful). For the determination of k_r , perinaphthenone ($\Phi_\Delta = 1$) was used as a reference: the kinetics of rubrene oxidation was analyzed following equation 3.33. To optimize the accuracy of the measure, the key parameter P_a was determined by both spectroradiometry and chemical

actinometry using potassium ferrioxalate (see below): the average value was considered. The measured value of k_r ($(9.2 \pm 1) \times 10^7 \text{ M}^{-1}\text{s}^{-1}$) was much higher than the one reported by Günther *et al.* ($(3.8 \pm 0.2) \times 10^7$).²⁶⁵ Such a value means that the physical quenching by rubrene is negligible: singlet oxygen quenching by this probe is almost completely due to chemical reaction. Notwithstanding several efforts trying to understand the discrepancy between our result and that of Günther *et al.*,²⁶⁵ we could not find an explanation. Rubrene produces singlet oxygen itself, but its activity is negligible for short irradiation times (30-60 seconds) at the irradiation wavelengths selected for the experiments. This is the limit of its use as a chemical probe: the PS under study must significantly absorb in a region where rubrene absorption is low. Despite that, it has been used in several works, for determining quantum yields of singlet oxygen production in various media: solutions,²⁷⁸ micellar systems²⁷⁵ and at the liquid/solid interface (PS supported on films immersed in solutions).²⁷⁹

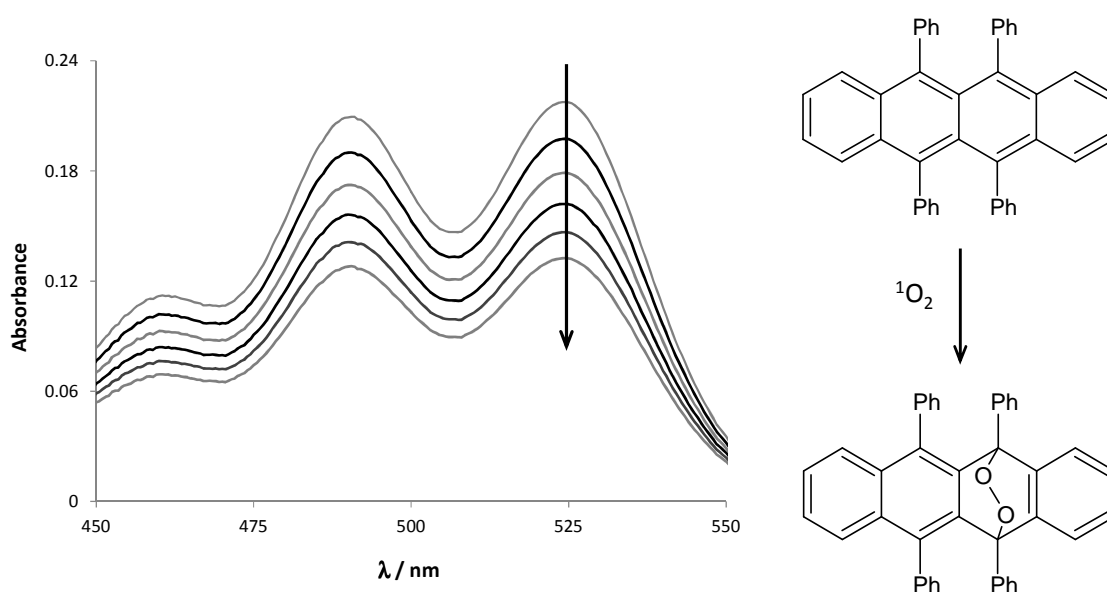


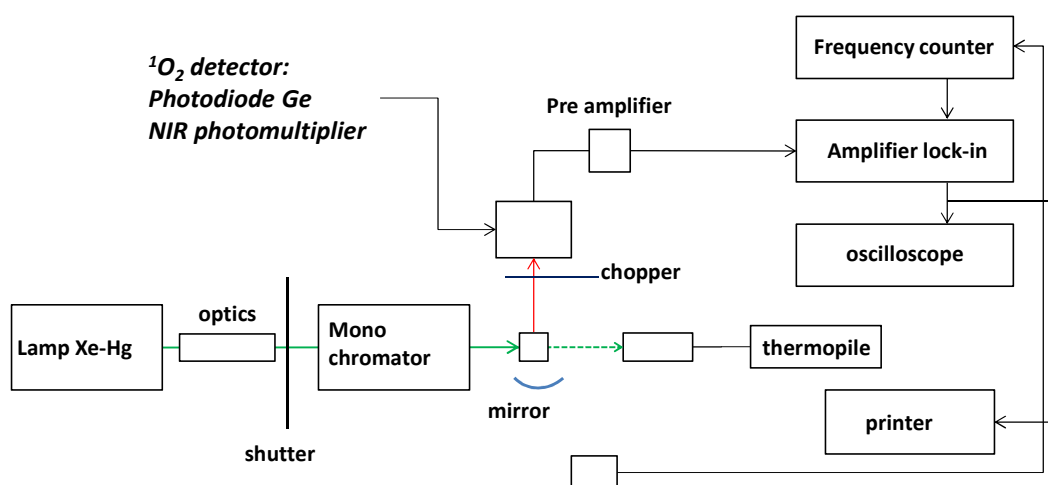
Figure 8 Absorption spectra of a solution containing rubrene ($4.0 \times 10^{-5} \text{ M}$) and **1** ($6.0 \times 10^{-5} \text{ M}$), following 385 nm photolysis in air-equilibrated ACN at 25 °C ($\ell = 1 \text{ cm}$). The spectra were monitored over 10 min period and they were recorded every 60 s interrupting 385 irradiation ($1.5 \times 10^{-4} \text{ W cm}^{-2}$). Reaction between rubrene and $^1\text{O}_2$ selectively yields an endoperoxide.

4.3 Equipment for singlet oxygen detection

The equipment used to monitor the $^1\text{O}_2$ luminescence at 1270 nm upon continuous monochromatic excitation of the PS has been custom-built.²⁵³ A cooled (-80 °C) NIR photomultiplier (Hamamatsu R5509 PMT) was used as a $^1\text{O}_2$ phosphorescence detector. The solutions or the monoliths containing the different PSs were irradiated at 367 nm and 547 nm with a Xe-Hg arc lamp (1 kW) through a water filter, focusing optics and a monochromator. $^1\text{O}_2$ luminescence was collected with a mirror, chopped (at 11 Hz) and, after passing through a focusing lens, a cut-off filter (1000 nm) and an interference filter (1271 nm). Phosphorescence signals were detected at 90° with respect to the incident beam using the NIR photomultiplier and a lock-in amplifier (Stanford Research Systems, Model SR830 DSP). Singlet oxygen luminescence signals were recorded as a function of irradiation

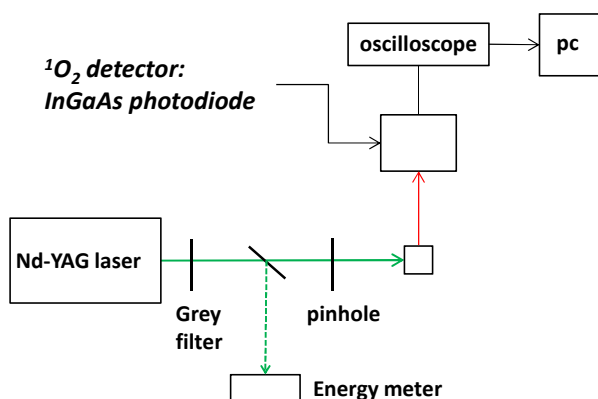
time during a minimum of three minutes. The experimental results were the average of two to three independent series of measurements; for the monoliths the measurements were repeated at least four times (one measurement per side). Mean values were retained for calculations. Absorption spectra were recorded before and after irradiation with a UV-Vis spectrophotometer (Agilent 8453) to detect any sensitizer bleaching during irradiation. The incident radiant powers (W / mW) at the wavelengths of irradiation (λ_{ex}) were measured using a thermopile (Laser Instrumentation, model 154): values of approx. 3.5 mW and 1.8 mW were measured at 367 nm and 547 nm, respectively. The relative incident photon fluxes were calculated as:

$$P_0 = W\lambda_{ex} \quad 3.35$$



Scheme 12 Schematic representation of the equipment for steady-state detection of singlet oxygen phosphorescence at 1270 nm.

The set-up used for the *time-resolved* 1O_2 phosphorescence detection (TRPD)²⁵⁶ consisted of a Nd-YAG laser (Continuum Minilite) equipped with a frequency doubler (532 nm) and a frequency tripler (355 nm) to irradiate the samples. The diameter of the excitation beam was reduced to approximately 0.3 cm. The energy of the laser pulse was varied between 350 and 1010 μJ . An energy meter (Gentec QE12) was employed to monitor the energy of the laser pulse. A sample holder adapted for supporting the monoliths was custom-built. The 1O_2 phosphorescence signal was detected at right-angle geometry with the help of a custom-built detector equipped with an InGaAs photodiode (IR Components) and working at room temperature.^{255,257} Besides appropriate lenses, the focusing optics included also a cutoff filter at 1098 nm and an interference filter at 1270 nm. The output of the detector was fed to an oscilloscope (DSOX3052A) and transferred to a computer. The laser was run at 5 Hz and 256 shots were averaged for each kinetic trace. Absorbance measurements were performed before and after irradiation in order to check for PS photobleaching.



Scheme 13 Schematic representation of the equipment for time-resolved detection of singlet oxygen phosphorescence at 1270 nm.

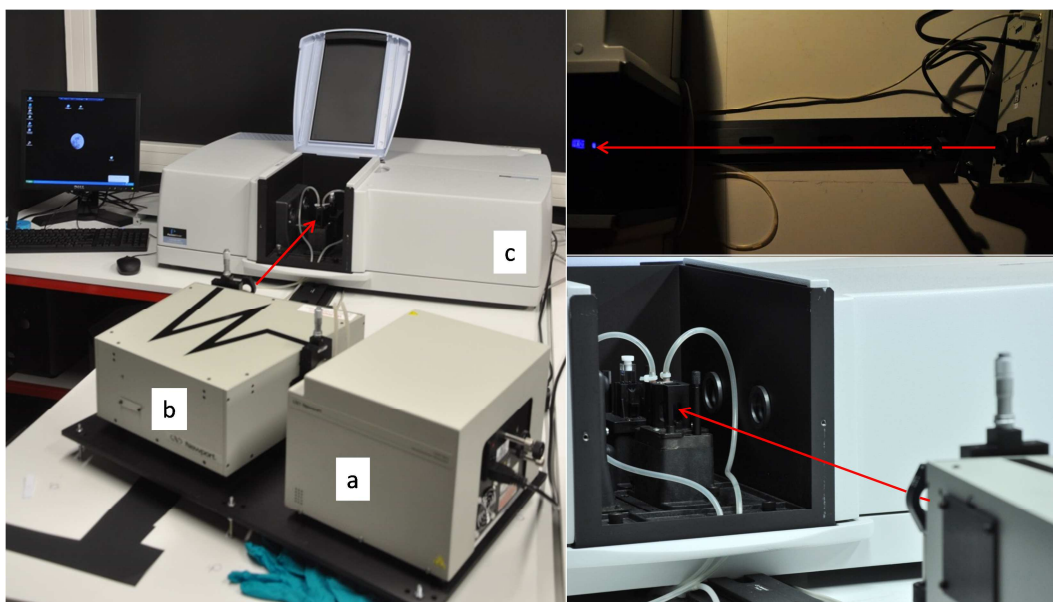


Figure 9 Set-up for the indirect detection of singlet oxygen. Left: Xe-Hg light source (a), irradiation monochromator (b) and spectrophotometer (c). Right, bottom: optical path of the light beam irradiating the cell containing the PS and the probe; right, top: fluorescence emission of DCA irradiated at 385 nm (top view).

For the indirect detection of singlet oxygen, an optical bench was set-up to irradiate samples while in the holder of a spectrophotometer: irradiation and analysis could be simultaneously carried out (Figure 9). An Apex Monochromator Illuminator with an off-axis F/4 corrected mirror was used as host for a 200W Xe-Hg Lamp; a Cornerston 260 motorized 1/4m monochromator with a USB communication interface was used to select the irradiation wavelength. Between the light source and the monochromator a CGA-375nm filter and an IR filter were put. An LH1 M4 lens was put between the monochromator and the analytical apparatus to collect and concentrate the light beam; a Perkin Elmer double beam, double monochromator Lambda850 UV-Vis spectrophotometer was used for the analysis. All optical elements were purchased from Newport.

A quartz fluorescence cuvette, filled with 3 mL of acetonitrile solution containing both a photosensitizer and rubrene, was magnetically stirred at controlled temperature (25°C) directly on the support of the spectrophotometer. The light source was put perpendicularly to the analytical beam in order to analyze the decrease of rubrene absorbance while irradiated. Thus, we could follow the kinetics of consumption of the probe during irradiation (looking at the decrease of the absorbance at 490 nm during irradiation) and control the solution by comparing the spectra recorded before and after irradiation. Irradiation wavelengths were chosen to excite the PSs near their absorption maxima in the visible and to avoid absorption of light by rubrene.

The values of the photon flux absorbed by the PS were calculated using equation 3.36: the absorbance at the emission maximum (A) was measured spectrophotometrically, P_0 with an International Light ILT900 spectroradiometer, giving the total emitted irradiance (thus taking into account the fluctuations of the emission source).

$$P_a = P_0 (1 - 10^{-A}) \quad 3.36$$

$$\sum_{\lambda} P_{a,\lambda} = \sum_{\lambda} P_{0,\lambda} (1 - 10^{-A_{\lambda}}) \quad 3.37$$

Equation 3.37²⁸⁰ had to be applied in the case of **DCA** due to the narrow absorption bands of this compound in the 20 nm wavelength range of irradiation.

5.0 PHOTOACTIVITY

5.1 MV: photobleaching and photooxidation of dibutyl sulfide in homogeneous solutions

For the determination of the photosensitizing properties of **MV**, the photooxidation of dibutyl sulfide (DBS) as a model reactant has been analyzed in various solvents (dioxane, acetonitrile and methanol). Since **MV** is quite unstable under irradiation, its photobleaching has been analyzed in presence and in absence of the model pollutant.

The reaction in the liquid phase was performed in two different set-ups:

- For studying the photobleaching of the dye, small volumes of solutions have been irradiated as for the indirect measurements of singlet oxygen production: quartz cells (optical path 1 cm) were filled with 3 mL of a solution containing the PS, between 0.8 and 1.2×10^{-5} M, depending on the solvent. These solutions were irradiated with white light (Xe-Hg lamp, Figure 15, monochromator set to $\lambda = 0$) for periods between 40 and 270 minutes, again depending on the solvent, in order to obtain a significant decrease of the PS's absorbance. As it will be presented below, the extent of photobleaching depended on the solvent, which explains the different exposure times. The amount of bleached PS was evaluated from the decrease of the absorption maximum, in terms of $\text{mol}_{\text{MV}} \text{L}^{-1} \text{s}^{-1}$ ($M_{\text{MV}} \text{s}^{-1}$). From the irradiance spectrum of the light source and the absorption spectra of **MV**, the amount of photons absorbed by the PS could be obtained ($P_a / \text{Einsteins} \text{L}^{-1} \text{s}^{-1}$, equation 3.37). By simply dividing

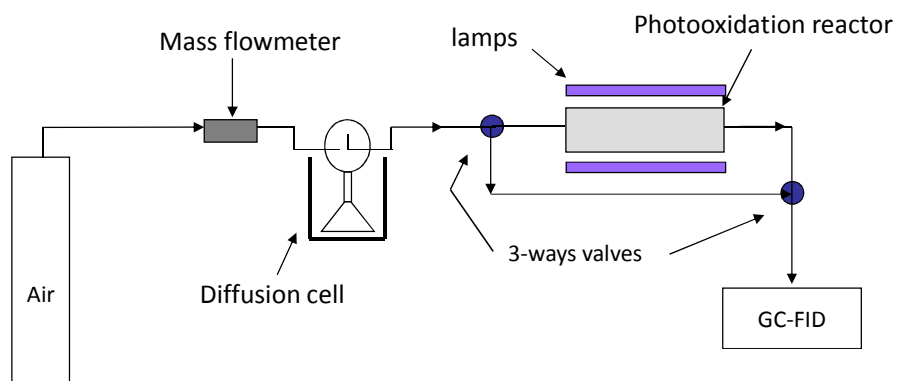
the decrease of PS concentration by the absorbed photon flux, the quantum yield of photobleaching ($\phi_{\text{bleaching}}$) could be obtained in $\text{mol}_{\text{MV}} \text{Einstein}^{-1}$. For measurements in the presence of DBS, 15 μL of pure sulfide were added to the PS solution, for a final DBS concentration of 0.028 M: the reactant was thus in large excess relative to the PS. Photobleaching in the presence and in the absence of DBS was then evaluated following the above-mentioned procedure, and the quantum yields compared by considering their ratio.

- For studying the photooxidation of DBS under irradiation of **MV**, preparative batch reactions were carried out. Air equilibrated ACN solutions (50 mL) containing **MV** (1.0×10^{-4} M) and DBS (5.0×10^{-3} M) were irradiated in a Rayonet® reactor equipped with 16×8 W lamps with $\lambda_{\text{max}} = 575$ nm (RPR-5750Å). The reaction was checked by measuring the solution absorbance (quartz cell, optical path 0.01 cm). The reactions were performed for approx. 20 minutes, until no more variations in the UV-Vis spectrum of **MV** were noticed. The reaction mixture was analyzed by ^1H NMR (CDCl_3) to put in evidence the main reaction products.

5.2 Monoliths: photooxidation of dimethyl sulfide at the gas-solid interface

The gas-phase photooxidation activity of the PSs supported on silica monoliths were studied analyzing the photosensitized degradation of dimethyl sulfide (DMS) in a pass-through reactor (Scheme 14, Figure 11). The pollutant concentration in the air flux entering the reactor was controlled using a system derived from the one developed by Benoit-Marquié *et al.*^{116,281–283} By means of a capillary (length: 12 cm; diameter: 0.2 cm) the reservoir containing the liquid pollutant is connected to a mixing flask where it is mixed to the air flux. Reservoir and capillary are immersed in the thermoregulated bath of a cryostat Julabo FP40 (temperature set to -14 °C in this work). The air stream (synthetic air, AirLiquide) is controlled by a mass flowmeter (Brooks Instruments 5850, 50 NL h^{-1} , air) and a flow controller (Brooks Instruments 0152) upstream of the diffusion cell. The air stream flows through a cylindrical pyrex reactor (internal diameter 1.2 cm, minimum dead volume) thermoregulated at 20 °C. To have a DMS concentration of 200 ppmv, the air flow was set to 100 mL min^{-1} ; the latter could be changed to vary the DMS mass flow but in any condition adopted in this study the DMS molar flow was 9.0×10^{-7} mol min^{-1} . Monoliths, previously dried under vacuum at approx. 80°C for 4 to 5 hours, were located in the central part of the reactor and were tested one at a time. After the adsorbing phase in the dark (DMS saturation) two irradiation-resaturation cycles followed; irradiations were carried out for 24 hours. The reactor was located inside a Rayonet®-like custom-built lamp support, equipped with 8 lamps. **DBTP**-, **DCA**- and **PN**-based materials were irradiated with Philips AQUACORAL ($\lambda_{\text{max}} = 420$ nm) lamps; the other PSs (**NMB**⁺, **MB**⁺, **MV**, **RB**) were irradiated with Philips F15W COOLWHITE ($\lambda_{\text{max}} = 575$ nm) lamps, filtered with Dolman orange-colored polycarbonate cylindrical filters (Sonepar 842464 orange, cut-off 544 nm) wrapped around the reactor (Figure 13). The irradiance of the light sources, measured with an Avaspec 2048L spectroradiometer (Avantes), was 4.90 mW cm^{-2} and 2.04 mW cm^{-2} for the lamps with a maximum at 420 nm and filtered 575 nm, respectively. The gas outlet was directly sampled by a pneumatic valve located in the injection port of a Variant GC-FID CP3900 (CPC column, 30m×0.25mm×1.00 μm ; gas vector: He 5.0; ZA-1500 FDBS zero air generator; Parker H2PEM-260 hydrogen generator). The gas flow was analyzed every 30 minutes and the reaction progress was checked in terms of DMS consumption. Conversion % was evaluated by the ratio between the total DMS consumed during

irradiation (not detected downstream of the reactor) and the total entering amount of DMS (Figure 10). The conversion values were then divided by the photon flux absorbed by the PS (equation 3.37) for obtaining the normalized conversions. The initial rates (v_0 , ppmv h⁻¹) were calculated taking into account the first points once the irradiation started: the decrease of the amount of DMS vs time is expressed.



Scheme 14 Representation of the set-up for DMS photooxidation at the gas-solid interface.

The reaction products were strongly adsorbed on the media and were analyzed with an ATD Turbomatrix 650-GC Clarus 680-MS Clarus 600S (PerkinElmer). The products were extracted by two subsequent desorption cycles (10 min at 180 °C, He 50 mL min⁻¹, then secondary desorption from the trap: from -30 °C to 250 °C, 40 °C s⁻¹, transfer line at 250 °C, outlet split He 20 mL min⁻¹, P = 26 psi), separated by gas chromatography (40 °C → 100 °C at 10 °C min⁻¹, then 100 °C → 260 °C at 20 °C min⁻¹) and analyzed by mass spectroscopy (EI = 70 eV, transfer line at 250 °C, source at 200 °C, mass between 20 and 250 m/z analyzed). DRUV spectra were recorded before and after the photooxidation tests to estimate the bleaching of the dyes under irradiation.

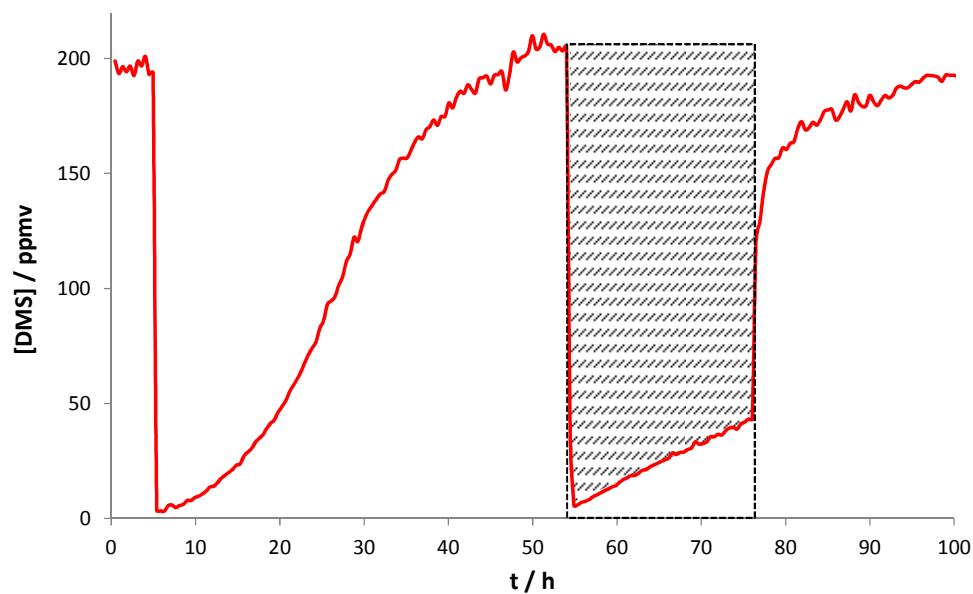


Figure 10 Profile of the variation of [DMS] during the photooxidation test. DMS conversion is calculated as the ratio of the filled area and the rectangular total area (dashed-line).

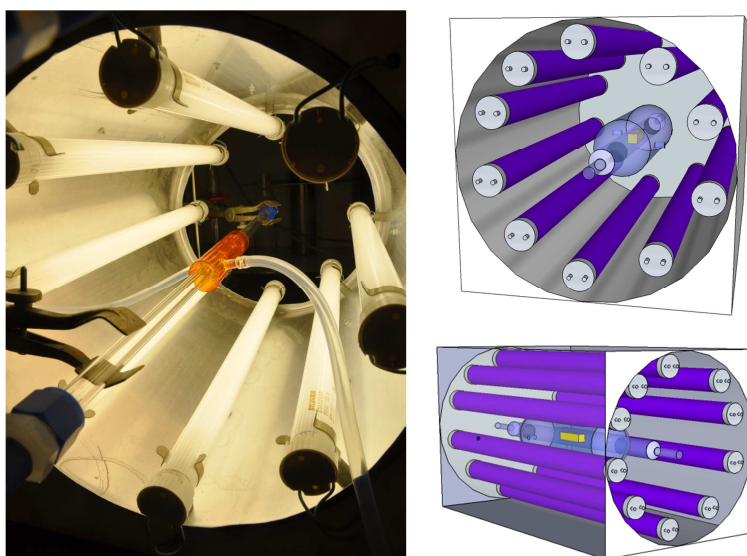


Figure 11 Photochemical reactor (picture on the left: the orange polycarbonate filter is applied on the glass reactor for the analysis of RB, MV, MB⁺, NMB⁺) used for the DMS photooxidation tests.

5.3 Powders: photooxidation of α -terpinene at the liquid-solid interface

The photooxidation of α -terpinene at the solid-liquid interface was used as a model reaction for the determination of the photosensitizing properties of **RB**, **AQ** and **DBTP** grafted on silica powders; their activities were compared to those of the corresponding soluble PSs and of the reference material, **RB** grafted on polystyrene (**RB-ps**). α -terpinene (267 mg, 1.75 mmol) and the soluble PS (various amounts) were dissolved in 50 mL of acetonitrile (ACN, 35 mM α -terpinene) and loaded into a Pyrex flask equipped on its bottom with a sintered glass frit and at its top with a gas outlet and a screw cap for sampling during irradiation (Figure 12). The reaction mixture was irradiated in a Rayonet[®] reactor while stirring and purging with a gentle stream of oxygen (16 mL min⁻¹) through the sintered frit. The reactor was equipped with 16 \times 8 W lamps with $\lambda_{\text{max}} = 419$ nm (RPR-4190Å) for **DBTP-Si** and **ANT-Si**, and $\lambda_{\text{max}} = 575$ nm (RPR-5750Å) for **RB-ps** and **RB-Si**, respectively. The reactor was cooled by an internal cooling fan (approx. 30 °C). For solid-supported photosensitizers, the same procedure was followed, the crude reaction mixture was finally filtered and the solid residue was washed with fresh ACN (10 mL). Reuse experiments were carried out following the same experimental conditions; in these cases the photocatalyst was recovered each time, washed with ACN and dried before reuse. Irradiations were performed for 30 min and were monitored by GC-MS analysis. Some control tests were carried out using *p*-cymene (usually formed as by-product during the photooxidation of α -terpinene) as a substrate; such reactions were conducted under the same experimental conditions, at the same substrate molar amount.

The crude reaction mixture was evaporated carefully (≤ 30 °C water bath to avoid decomposition)²⁸⁴ and the oily residue was analyzed by ¹H NMR spectroscopy. Noteworthy, *p*-cymene and unreacted α -terpinene were removed with the solvent during evaporation. NMR analysis could thus not be used to determine the composition of the crude product.²⁸⁵ Ascaridole was isolated by column chromatography on silica gel using a gradient 10 \rightarrow 15 \rightarrow 20 vol% ethyl acetate in cyclohexane as a mobile phase.

This reaction was analyzed by zero order kinetics with respect to α -terpinene. The corresponding integrated rate expression was used:

$$[\alpha - \text{terpinene}] = [\alpha - \text{terpinene}]_0 - kt \quad 3.38$$

A plot of $[\alpha\text{-terpinene}]$ vs time yielded a straight line of slope k . The concentrations were deduced from the absorbance measurements using the Beer-Lambert law ($\ell = 0.01$ cm) at the absorption maximum (267 nm) of α -terpinene in acetonitrile (ACN, $\epsilon_{267\text{nm}} = 8160$ M⁻¹ cm⁻¹). Rate constants (k , M min⁻¹) were adjusted to the data sets by linear regression and normalized by the PSs molar amount or by the photon flux absorbed by the photosensitizer, giving k_m (M min⁻¹ mmol_{PS}⁻¹) and k_p (M Einstein⁻¹), respectively. The estimated values of the absorbed photon flux were calculated using equation 3.37, taking into account that with the Pyrex reactor, only wavelengths higher than 300 nm could be absorbed by the PS. $P_{0,\lambda}$ (Einsteins s⁻¹ nm⁻¹) was estimated from spectroradiometric data (W m⁻² nm⁻¹) by taking into account the photon energy at a given wavelength and by normalizing to the Avogadro's number (N_A). The total irradiance (P_0) of the lamps emitting at 575 and 419 nm was 1.6 and 3.1 mW cm⁻², respectively (Figure 14). The values of irradiance were measured with an International Light ILT900 spectroradiometer. The absorbance of the supported sensitizers was

estimated from their molar absorption coefficients in ACN and their concentrations. The quantum yields of conversion of α -terpinene ($\phi_{\text{conv}} / \text{mol}_{\alpha\text{-terpinene}} \text{Einteins}^{-1}$) were approximated by calculating the ratio of the converted molar amount of α -terpinene and the photons absorbed by the sensitizer.

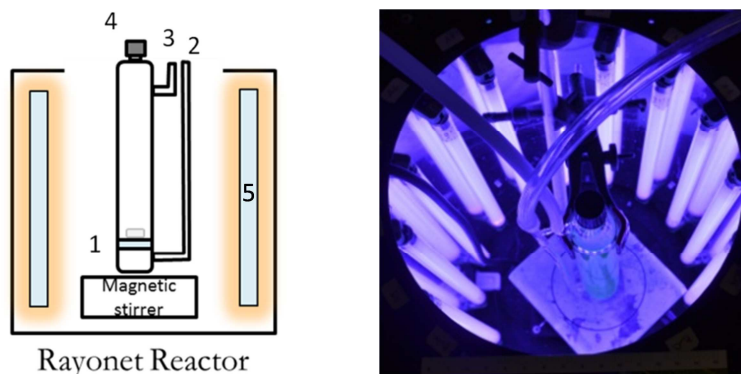


Figure 12 Rayonet® photoreactor setup: (left) schematic side view with inserted Pyrex flask (1: sintered glass frit, 2: oxygen inlet tube, 3: oxygen outlet tube, 4: septum port for sampling, 5: fluorescent tubes); (right) top view of actual setup with 16 x 8 W lamps.

6.0 MEASUREMENTS OF IRRADIANT POWER

For the steady-state $^1\text{O}_2$ phosphorescence detection experiments, the incident radiant powers (mW) at the wavelengths of irradiation were measured using a thermopile (Laser Instrumentation, model 154). For the time-resolved $^1\text{O}_2$ luminescence detection, an energy meter (Gentec QE12) was employed to monitor the energy of the laser pulse; for time-resolved transient detection the laser pulse energy was measured using a joulemeter Ophir Optronics Ltd. For the determination of the emitted radiant flux in photooxidation tests and in singlet oxygen detection by chemical probing with rubrene, spectroradiometric techniques were employed. Chemical actinometry was necessary for the precise determination of the kinetic parameters of rubrene photooxygenation by $^1\text{O}_2$.

6.1 Spectroradiometry

Radiometry is defined as a technique for measuring electronic radiation, characterizing the distribution of the radiation power in space (contrary to photometry which deals with the light interaction with the human eye).⁴ The light detector is usually sensitive to a quite large range of wavelengths, from the UV to the near-IR. For each wavelength the sensor gives a value of radiant power, which can be expressed in terms of radiant energy (J), radiant flux (W) or irradiance (W m^{-2}), depending on the instrument specifications. Using spectroradiometers it is possible to obtain a spectrum of the emitted radiation: this is particularly useful for polychromatic light sources (e.g. fluorescent tubes for photochemical tests).

An Avaspec 2048L spectroradiometer (Avantes) with an 1 m x 600 μm UV optic fiber and a 3900 μm 180° cosine sensor was used for irradiance measurements of the lamps used for the gas-phase photooxidation tests (Figure 13). This radiometer was previously calibrated from 200 to 1000 nm

with an AVALIGHT-DH-CAL calibration light (with deuterium and halogen lamps). For the gas phase oxidation tests the sensor was placed at a fixed distance from the light source, obtaining 4.90 and 2.04 mW cm^{-2} for the lamps with a maximum at 420 nm and 575 nm (filtered), respectively.

An International Light ILT900 spectroradiometer was used for the irradiance measurements of the lamps used for the liquid-solid photooxidation experiments (Figure 14). The total irradiances of the lamps emitting at 575 and 419 nm were 1.6 and 3.1 mW cm^{-2} , respectively. The values were measured placing the light sensor at a fixed distance of 3 cm from the source.

The photon flux emitted by the Xe-Hg lamp (Figure 15) used for indirect singlet oxygen detection and **MV** photobleaching was measured with the last-mentioned International Light ILT900 spectroradiometer. After each experiment several measurements were carried out, positioning the light sensor in correspondence to the sample holder, and the average values were considered for calculations. Repetitions were necessary to minimize the uncertainty induced by the fluctuations of the source. The irradiance data (W m^{-2}) were easily converted to photons per surface unit per time unit by means of Planck equation, considering the emission monochromatic. Using equation 3.36 and normalizing by the irradiated volume, the photon flux absorbed by the PS was obtained.

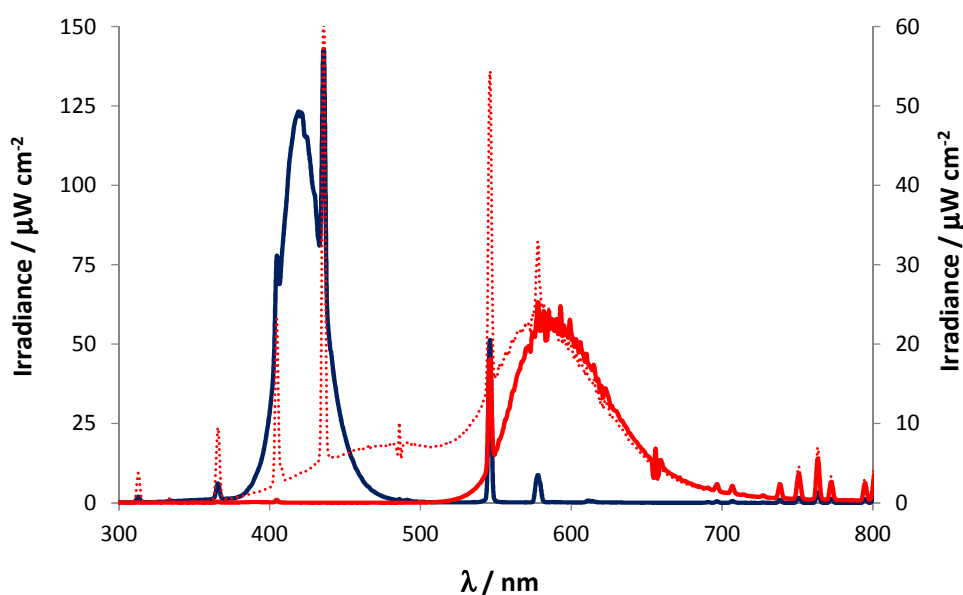


Figure 13 Irradiance spectra of the lamps used for the photooxidation of DMS; lamps with λ_{max} 420 nm (blue line) and lamps with λ_{max} at 575 nm (secondary axis; solid red line: filtered at 544 nm; dotted red line: non-filtered lamps).

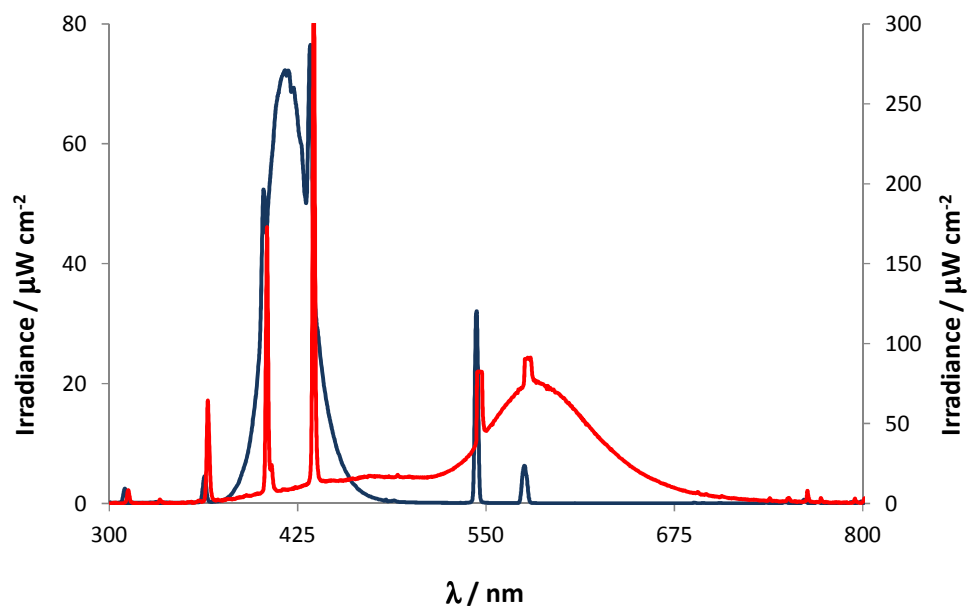


Figure 14 Irradiance spectra of the lamps used for the photooxidation of α -terpinene; lamps with λ_{\max} at 420 nm (blue line) and lamps with λ_{\max} at 575 nm (secondary axis; red line).

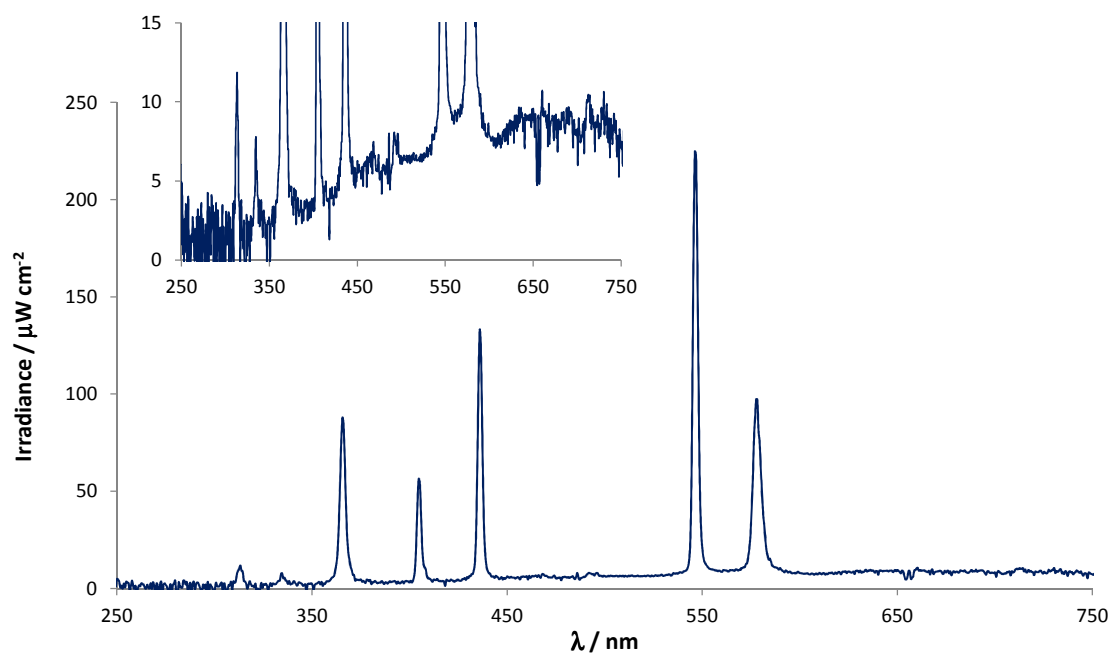


Figure 15 Irradiance spectrum of the 200 W Xe-Hg lamp used for the photobleaching studies on MV, in the absence and in the presence of DBS.

6.2 Chemical actinometry

Following the IUPAC definition, an actinometer is a chemical system which can be used for the determination of the number of photons absorbed into the defined space of the photochemical reactor.^{4,212,286} Photochemical reactions characterized by a known quantum yield at given wavelengths can be used: by the precise quantification of the products it is possible to determine the number of photons absorbed by the system. Many compounds are known and used for this purpose. Potassium ferrioxalate, $K_3Fe(C_2O_4)_3 \cdot 3H_2O$, is widespread employed as a chemical actinometer due to its wide wavelength range of applications (254-500 nm), its ease of handling and its availability/preparation (it can be easily prepared from iron(III) sulphate and potassium oxalate in the presence of barium oxalate). Upon irradiation, the salt is broken and the iron cation is complexed, yielding a product whose formation can be followed and quantified by UV-Vis spectroscopy. 1,10-Phenanthroline (Phen) is used as a complexing agent for the Fe^{2+} formed during the irradiation of the actinometer, and the absorbance of the complex is monitored at 510 nm. The incident photon flux P_0 , defined as the total number of photons entering the solution per unit of time and unit of volume, is calculated using the following equation:

$$P_{0,\lambda} = \frac{n_{Fe^{2+}}}{\Phi_{Ac,\lambda} t} \quad 3.39$$

where

$$n_{Fe^{2+}} = \frac{N_A \alpha \Delta A_{510}}{10^3 \ell \epsilon_{510}} \quad 3.40$$

N_A is Avogadro's number, α a dilution correction factor, ΔA_{510} the variation of the absorbance at 510 nm due to the formation of the complex between Phen and the photochemically produced Fe^{2+} ions, ℓ the optical path length of the spectrophotometric cell, ϵ_{510} the molar absorption coefficient of the complex at 510 nm, $n_{Fe^{2+}}$ the number of Fe^{2+} ions formed upon irradiation, $\Phi_{Ac,\lambda}$ the quantum yield of the production of Fe^{2+} from potassium ferrioxalate, t the irradiation time.

This method was used for the exact determination of the photon flux emitted by the Xe-Hg lamp used for the indirect detection of singlet oxygen (monochromatic wavelength, 385 nm). A 7.4×10^{-3} M solution of potassium ferrioxalate was used, the pH being controlled with H_2SO_4 . Solutions have been irradiated at 385 nm for variable irradiation times; from the absorbances at 510 nm and the value of $\Phi_{Ac,\lambda}$ (1.13 at 385 nm), the value of P_0 was calculated. We obtained a mean value of $(3.3 \pm 0.4) \times 10^{14}$ photons s^{-1} (*i.e.* $(1.8 \pm 0.5) \times 10^{-7}$ Einsteins $L^{-1} s^{-1}$) for the incident photon flux.

To check the value obtained by actinometry, we measured by spectroradiometry the irradiance of the light source at the selected wavelength of 385 nm. We measured a total irradiance of 9.9×10^{-5} $W cm^{-2}$, for a corresponding value of photon irradiance of $(1.92 \pm 0.4) \times 10^{14}$ photons $cm^{-2} s^{-1}$. This value is in good agreement with the photon irradiance ($(1.98 \pm 0.4) \times 10^{14}$ photons $cm^{-2} s^{-1}$) calculated from the photon flux obtained by actinometry, taking into account the irradiated surface on the spectrophotometric cell and the volume of solution used.

4 Cyanoanthracenes: synthesis and characterization in solution

DBTP (1), as reported in the previous chapters, has already shown good photosensitizing properties: silica-supported **1** is remarkably active under visible light irradiation for the photooxidation of sulfides at the gas-solid interface and singlet oxygen has been detected as the main ROS generated.^{116,117} A carboxylic derivative of **1**, **DBTP-COOH (2)**, has been synthesized and grafted to silica monoliths: its photooxidation properties seemed to be similar to those of **1**, with efficient singlet oxygen production.¹¹⁷ The carboxylic group inserted on the **DBTP** core represents the means for grafting the PS: the COOH moiety can be easily modified in order to create reactive intermediates, which can be subsequently grafted on various supports or further functionalized to yield different **DBTP**-derivatives. Compound **2** can be directly grafted on several functionalized silica or silanes only under previous conversion into more reactive intermediates. Grafting on amino-functionalized silica monoliths has been achieved by converting **2** into the corresponding acyl chloride and making the latter react with the amino group (Schotten-Baumann reaction); the synthesis of **DBTP**-silane adducts (and their subsequent participation to the materials preparation) has been carried out by activating the carboxylic acid with reagents used for peptide-coupling reactions (see below). Both methods are quite efficient but they imply the formation of by-products which can be difficultly removed and which can pollute the final material. For this reason we focused on the further functionalization of compound **2** in order to obtain more easily graftable PSs. Simultaneously, we focused on the use of isocyanate (NCO) silanes/silica as grafting groups for **DBTP**-derivatives. The main advantage of NCO groups is their reactivity towards amines and alcohols, which yields urea and carbamate adducts, respectively, without forming any by-product.²¹¹ Compound **2** was thus modified to synthesize the hydroxy and amino derivatives **3** and **4**. In the first step of this work, compounds **2-4** were fully characterized in solution (acetonitrile) to put in evidence the possible effects of the substituent on the photophysical properties and on $^1\text{O}_2$ production: they were compared in detail to compound **1**, considering **DCA** as a reference for the whole **DBTP** family. The synthesis of compounds **3** and **4**, as well as the detailed characterization in acetonitrile of the photophysical and photosensitizing properties of all **DBTP**-derivatives are treated in this chapter. We put in evidence important differences between **DBTP** and **DCA**: the photosensitization mechanisms involved with the two classes of cyanoanthracenic chromophores will be discussed in detail.

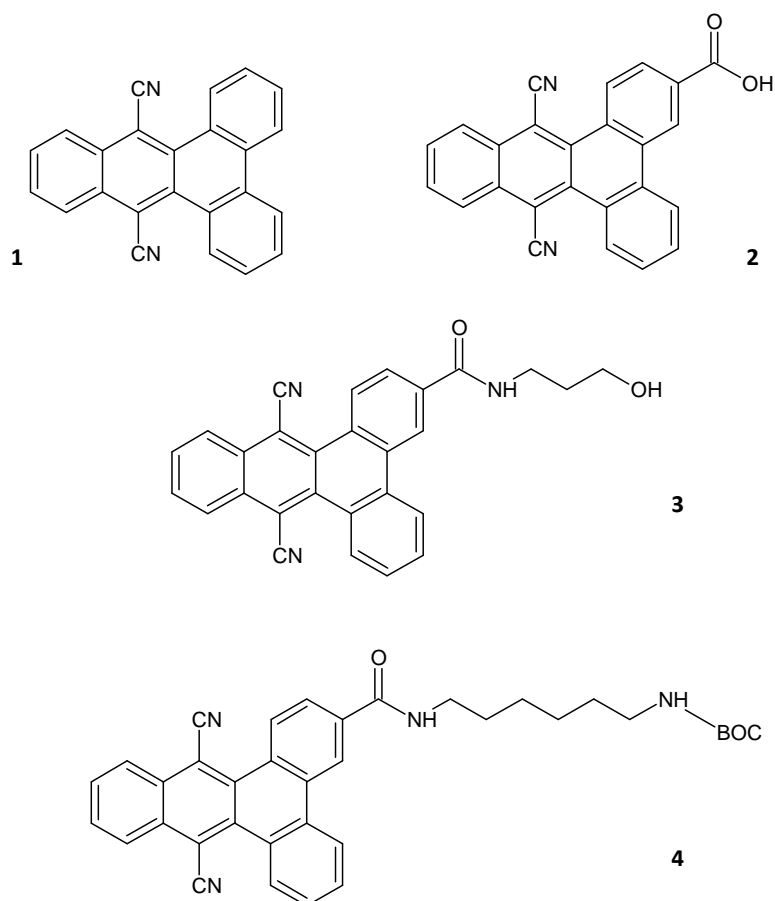


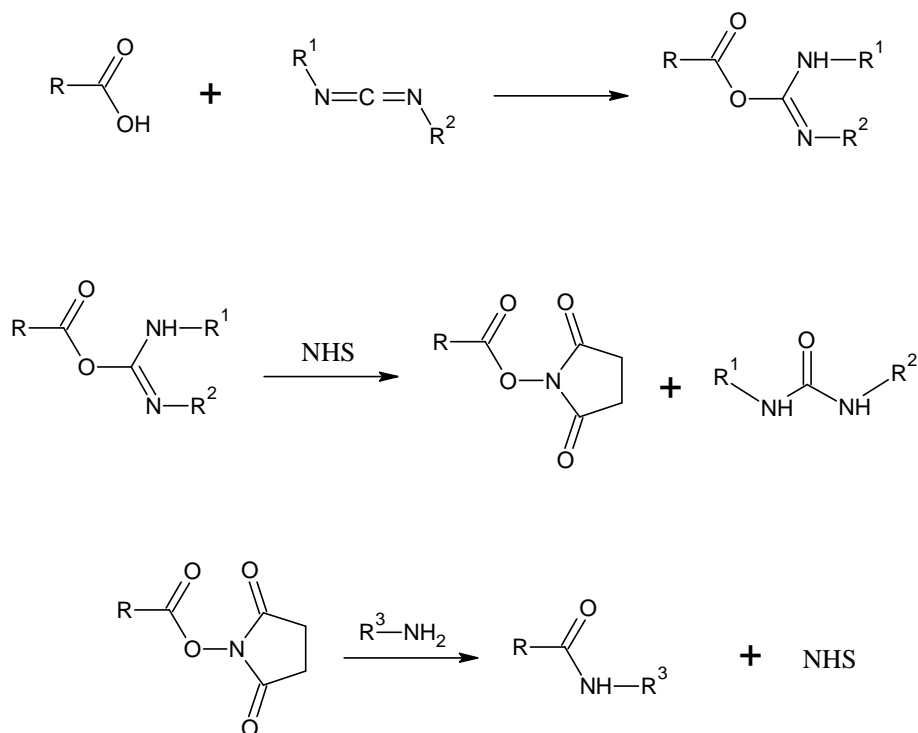
Chart 10 Structure of the cyanoanthracene derivatives synthesized: DBTP (**1**), DBTP-COOH (**2**), DBTP-CONH-(CH₂)₃-OH (**3**) and DBTP-CONH-(CH₂)₆-NH-Boc (**4**).

1.0 SYNTHESSES

Compounds **1** (9,14-dicyanobenzo[*b*]triphenylene) and **2** (9,14-dicyanobenzo[*b*]triphenylene-3-carboxylic acid) were synthesized following the procedure reported by Lacombe *et al.*¹¹⁷ and described in the previous chapter (Schemes 6 and 7). They were prepared by a high yield (> 70%) one-step condensation reaction between 1,2-phenylenediacetonitrile and 9,10-phenanthrene-9,10-dione (to yield **1**) or 3-phenanthrenecarboxylic acid, 9,10-dihydro-9,10-dioxo (to yield **2**).

Compounds **3** and **4** were prepared from **2** under usual conditions for solid-phase peptide coupling (Schemes 8, 9 and 15). The carboxylic acid is firstly activated by adding a carbodiimide, yielding an *O*-acylurea intermediate. Another reactive derivative is then formed by condensation of the activated carboxylic acid and *N*-hydroxysuccinimide (NHS); the carbodiimide is eliminated in the form of a urea side-product. The ester intermediate (formed by the addition of NHS on the carboxylic acid) can easily react with a primary amine to yield an amide. NHS is a good leaving group for a nucleophilic attack to the carbonyl group. This procedure for carboxylic acid activation prevents the neutralization of carboxylic acids in the presence of amines and allows the formation of amides in relatively mild conditions: it thus represents a good alternative to the use of acyl halides as activated intermediates for amide synthesis. Drawbacks can arise from the side-products, in particular those deriving from the decomposition of the *O*-acylurea intermediate: after the addition of NHS the carbodiimide is

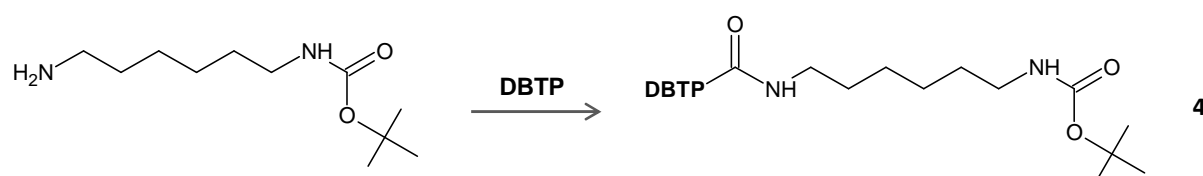
converted to a urea, which can be very difficultly removed. In common peptide-coupling such a drawback is negligible since the reaction is carried out in a two-phase system which allows the easy separation of the solid-grafted peptides. This way of applying the solid-phase peptide-coupling procedure is nonetheless really effective and easily achieved.



Scheme 15 Carbodiimide/NHS-mediated peptide coupling reaction applied to the nucleophilic attack to carboxylic acids.

For the synthesis of compound **3** (3-(*N*-hydroxypropyl)carboxamido-9,14-dicyanobenzo[*b*]triphenylene (**DBTP-CO-NH-(CH₂)₃-OH**), we followed the procedure described by Choitani *et al.*²¹⁴ The carboxylic group of compound **2** was activated by DCC (*N,N'*-dicyclohexylcarbodiimide) to form the *O*-acylurea. The ester intermediate formed by the subsequent addition of NHS reacted with 3-amino-1-propanol. The intermediate, very sensitive to many nucleophiles (*i.e.* both amines and alcohols), is supposed to react with amines approx. ten times more efficiently than with alcohols.^{216,225} Therefore, the use of a reactant bearing the two functional groups should not represent a problem: as confirmed by ¹H NMR, which showed just one aromatic species, the reaction with the aminoalcohol selectively formed an amide with a free hydroxyl group at the end of the aliphatic chain (compound **3**). The NMR spectrum put in evidence the presence of aliphatic impurities, arising from the main by-product of this reaction, *N,N'*-cyclohexylurea, poorly soluble and very difficult to remove. Due to the low solubility of both the by-product and compound **3**, the purification step was difficult and we could not obtain a really pure product. Due to these difficulties the reaction yield was very low (approx. 45%). Nevertheless, compound **3** was characterized in solution: as it will be detailed, the presence of impurities could not be considered negligible and for this reason it was not considered for grafting on silica.

Compound **4** (3-(*N-N'*-Boc-aminohexyl)carboxamido-9,14-dicyanobenzo[*b*]triphenylene (**DBTP-CO-NH-(CH₂)₆-NH-Boc**)) was synthesized following the same pathway as **3** with only slight modifications. DCC was replaced by water soluble EDC (1-ethyl-3-(3-dimethylaminopropyl)carbodiimide),^{219,220} which was easily washed away once the reaction completed, and tetrahydrofuran (THF)²¹¹ was replaced by chloroform (CHCl₃) as a solvent. A *t*-butyloxycarbonyl (Boc)^{217,218} mono-protected hexanediamine (*N*-Boc-1,6-hexanediamine, Scheme 16) was selected as a coupling agent. Such a choice was made considering several factors: from a synthetic point of view, the protection on one of the NH₂ groups avoids any side-reaction, the Boc protecting group increases product solubility and the Boc deprotection step is compatible with the entire molecule. Other advantages are gained when considering the further expected coupling step between Boc-deprotected **4** (**5**, see chapter dealing with grafting on monoliths) and 3-(isocyanato)propyl-functionalized silica to prepare **DBTP**-grafted materials: amines are more reactive than alcohols for grafting on isocyanate, longer aliphatic chains would excessively modify silica porosity during the sol-gel process, while shorter chains would not contribute enough to increase the solubility of the **DBTP** derivative. As it was expected, the aliphatic chain and the *t*-butyl group of **4** increased the product solubility, making the purification simpler. Actually, compound **4** was a higher purity, more soluble and more easily handled product than **3**. It thus represents a good candidate for grafting **DBTP** onto various supports, from both the points of view of derivative synthesis and subsequent material preparation. Considering the reaction yields (45% vs 65% for compounds **3** and **4**, respectively) it is evident that the synthesis of **4** was a noticeable improvement.



Scheme 16 Schematic representation of the addition of *N*-Boc-1,6-hexanediamine to **DBTP**. The chemical structure of the Boc group is described.

2.0 SPECTROSCOPIC CHARACTERIZATION

Blanc *et al.*²⁰⁵ reported in 2010 a detailed systematic comparison of the photophysical properties of **1** and **DCA**. Both compounds have been analyzed by UV-Vis and Fluorescence spectroscopy, in various solvents. In this work we focused on the comparison between several derivatives of **1**: acetonitrile (ACN) was selected as a solvent for the spectroscopic characterization. The above-cited article was considered as a reference, notably concerning **DCA**.

2.1 UV-Vis spectroscopy

The absorption spectra of **1** and its three derivatives in ACN are reported in Figure 16. Compounds **1**, **3** and **4** present a first absorption maximum (0-0 transition) at 415nm (I_1), corresponding to a singlet excited state energy (S_1) of 288 kJ mol⁻¹. For compound **2**, I_1 is shifted at 413 nm (S_1 energy: 290 kJ mol⁻¹). Compound **1** has three maxima at 394, 318 and 306 nm (I_2 to I_4) and the spectra of **2-4** show the same shape in this spectral range with a bathochromic shift of 2 to 4 nm. Finally, for compounds **2**, **3** and **4** the broad peak I_5 at 254 nm disappears, while the position of I_6 does not show any variation in the series.

From Table 2, it may be seen that there is an important decrease of the molar absorption coefficient (ϵ) of compounds **2-4** relative to compound **1**, with a maximum difference (about 50%) for I_1 and I_2 . Both the position of the absorption bands and the ratio I_1/I_2 are slightly different for **1** relative to those of its three derivatives. As expected, the effect of the substituent on the **DBTP** core clearly plays a minor role in the absorption properties: since no functionalization was carried out on the aromatic skeleton responsible of the near-UV and visible absorption. The main difference between **1** and **2-4** is about the intensity of the absorption band in the visible range, sign of a more efficient light harvest in the case of **1**. In Figure 17 the absorption spectra of **DCA** and **1** are compared: in the visible region the position of the absorption maxima doesn't change significantly (the energy of the singlet excited state S_1 is approx. 280 kJ mol⁻¹ for **DCA**⁴² and 288 kJ mol⁻¹ for **1**) and the molar extinction coefficient is in the same order of magnitude for both chromophores.

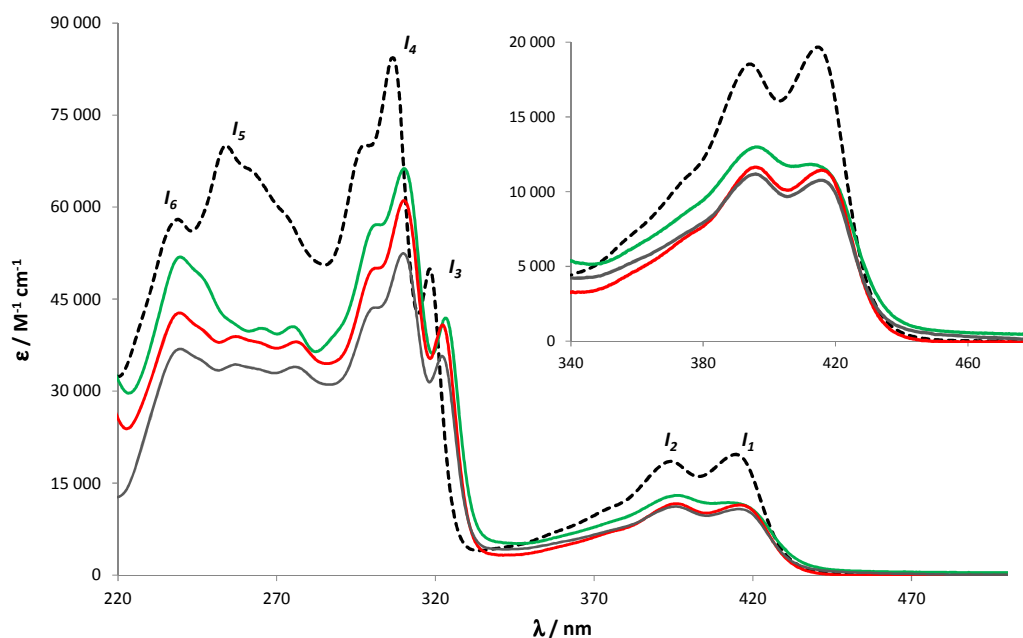


Figure 16 UV-Vis electronic spectra of compounds **1** (black dashed line), **2** (green line), **3** (red line) and **4** (grey line). The main absorption maxima are pointed out.

Table 2 Molar absorption coefficients (ϵ) at the absorption maxima, relative band intensities and singlet excited state energy of **1-4** in ACN. Errors: approx. 10% for the ϵ values.

PS	$\epsilon / \text{M}^{-1} \text{cm}^{-1} (\lambda / \text{nm})$						I_1/I_2	$E_s / \text{kJ mol}^{-1}$
	I_1	I_2	I_3	I_4	I_5	I_6		
1	19665 (415)	18535 (394)	49885 (318)	84335 (306)	70040 (254)	58005 (239)	1.06	288
2	11835 (413)	12985 (396)	41875 (323)	66270 (310)	-	51870 (239)	0.91	290
3	11445 (415)	11640 (396)	40740 (322)	61070 (310)	-	42750 (239)	0.98	288
4	10755 (415)	11175 (396)	35730 (322)	52465 (310)	-	36850 (240)	0.96	288

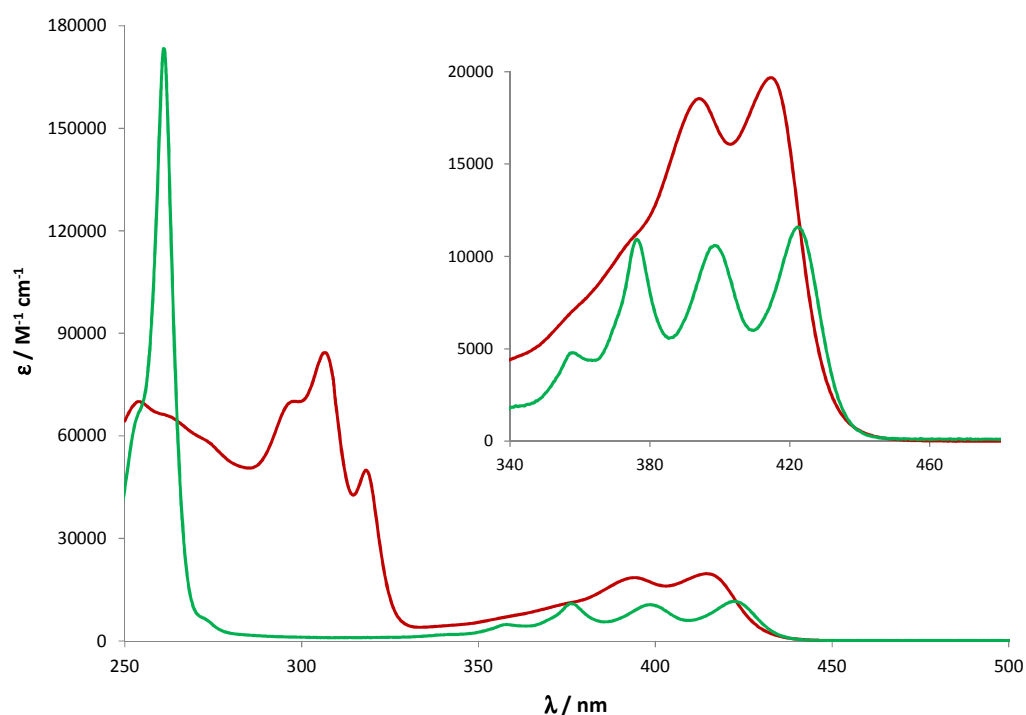


Figure 17 Comparison of the electronic spectra in ACN of **DCA** (green line) and **1** (red line). Inset: detail of the structured bands in the near-UV/ visible range.

2.2 Fluorescence spectroscopy

The excitation-emission spectra of compounds **1-4** in ACN are given in Figure 18. The excitation spectra coincide with the structured absorption spectra. The emission spectra of all compounds in ACN appear as a broad unstructured band, red-shifted relative to the excitation spectrum. This result is in contrast with the structured emission centered at shorter wavelength (420 nm) and observed up to now only for **1** in hexane.²⁰⁵ The utmost bathochromic shift is characteristic of compound **1** with an emission maximum at 490 nm, while for **2**, **3** and **4** the maxima are positioned at 469, 474 and 477 nm respectively. The extent of the bathochromic shift relative to the excitation spectrum (Table 3) is inversely proportional to the polarity of the substituent. The polarity of the substituent also affects the fluorescence lifetimes (Table 3): the largest value in ACN was observed for **1** (5.4 ns), whereas τ_f slightly decreased from 4.9 ns to 4.3 ns from **4** to **2**, respectively, approaching the value measured for **1** in hexane (3.6 ns).²⁰⁵ The fluorescence quantum yields are similar for the four molecules, only slightly lower for **2**, but significantly lower than the one calculated for **1** in hexane (0.29).²⁰⁵

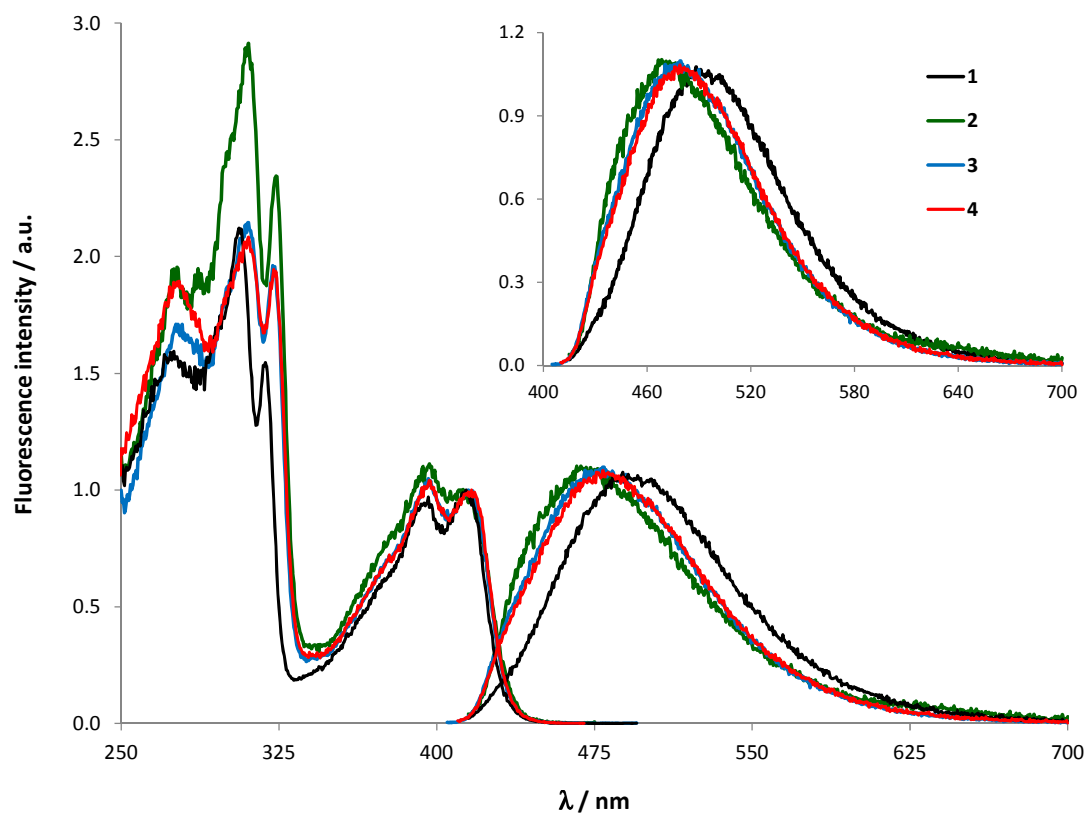


Figure 18 Fluorescence excitation ($\lambda_{em} = 500$ nm) and emission ($\lambda_{ex} = 400$ nm) spectra of compounds **1** (black), **2** (green), **3** (bleu) and **4** (red) in ACN at room temperature.

Table 3 Wavelengths of the fluorescence emission maxima, fluorescence lifetimes, quantum yields of fluorescence of compounds **1-4** and **DCA** in air-equilibrated ACN. Values in brackets are relative to Ar-saturated ACN solutions.

PS	$\lambda_{\text{max}} / \text{nm}$	$\tau_{\text{f}} / \text{ns}$	Φ_{f}
1	490	5.4 ± 0.1 (6.3 ± 0.1)	0.15 ± 0.02 (0.16 ± 0.02)
2	469	4.3 ± 0.1 (5.0 ± 0.1)	0.12 ± 0.01 (0.12 ± 0.02)
3	474	4.8 ± 0.1 (5.6 ± 0.1)	0.15 ± 0.02 (0.16 ± 0.02)
4	477	4.9 ± 0.1 (5.7 ± 0.1)	0.16 ± 0.02 (0.16 ± 0.02)
DCA ^{178,205}	435	12.7 ± 0.1 (16.5 ± 0.1)	0.87 ± 0.02

Considering the different emission spectra of **1** in polar and non-polar solvents, the presence of two different emitting species is evident, depending on the polarity of the medium. Since the emission spectrum in hexane is structured and slightly bathochromically shifted relative to the absorption spectrum (small Stokes shift), the fluorescent species formed in non-polar solvents was attributed to the monomeric form of **1**. The change in the emission spectra in polar media could be explained on the basis of the formation of an exciplex/excimer in the excited state. Such a species has not been identified yet: it can be assigned whether to an interaction between the excited solute and the solvent (exciplex) or to the formation of aggregates of the PS at the excited state (excimer).^{117,205} Since the formation of this species occurs in polar solvents and the extent of the bathochromic shift seems to depend on the solvent permittivity (ϵ_r), the first hypothesis (exciplex) seems clearly more probable. Nonetheless, it would be possible that the polarity of the solvent increases the stability of aggregates of **1** (excimers), favoring thus the emission of the non-monomeric species. Independently on the nature of the fluorescent species, it is evident that it is formed in polar solvents. In this work we focused on acetonitrile, a remarkably highly polar solvent: is the unstructured emission band recorded for compounds **1-4** completely due to the exci-species formed upon irradiation? Or does it arise from the superimposition of two distinct emission bands, that of the monomer and that of the exci-species? Unfortunately the experimental data collected until now do not allow a definitive conclusion on this subject. A higher polarity of the substituent (**2** > **3** > **4** > **1** from the height of the thin layer chromatography spots) seems to destabilize the excimer/exciplex species, resulting in an emission signal closer to the one of the monomer. Our experimental results on both the wavelength of the emission maximum (**1** > **4** > **3** > **2**) and the lifetime (**1** > **4** > **3** > **2**) of the excited state (which cannot be properly assigned to the S_1 state if a complex is formed) support this hypothesis. From an application point of view the discrimination between the monomeric form and the excimer/exciplex species is rather academic: what would be truly interesting is the identification of possible influences of these excited states on the photosensitizing properties of **DBTP**-derived dyes.

Relative to **DCA**^{32,178,205,287} compounds **1-4** have shorter lifetimes and lower quantum yields of fluorescence (Table 3; spectra of **DCA** in Figure 19). Evidently the more extended aromatic moiety of **1-4** compared to **DCA** induces much larger changes in the photophysical properties than substitution on the **DBTP** structure (**1** vs **2-4**).

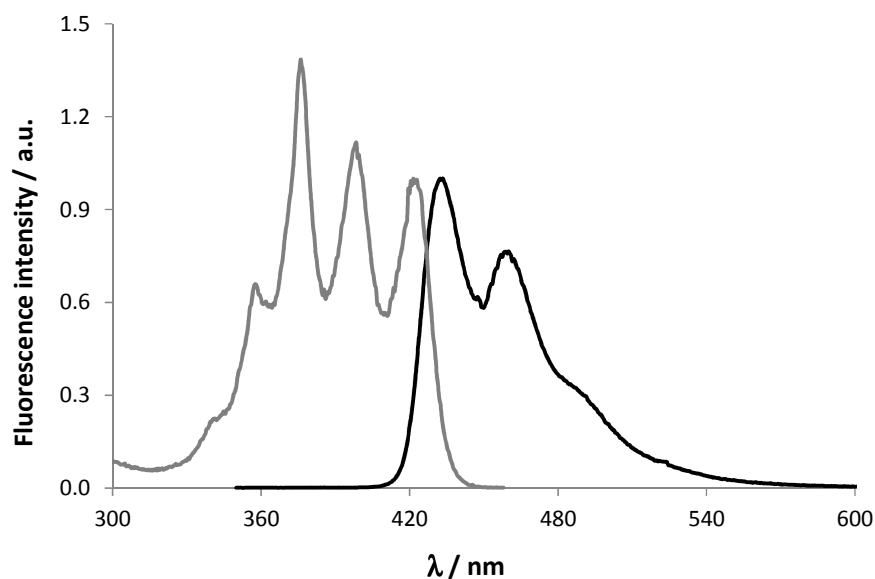


Figure 19 Fluorescence excitation ($\lambda_{em} = 460$ nm) and emission ($\lambda_{ex} = 350$ nm) spectra of DCA in air-equilibrated ACN.

3.0 ANALYSIS OF THE TRANSIENT SPECIES

For the four compounds, the transient species formed upon nanosecond time-resolved laser flash photolysis were investigated. The irradiation of **1** at 355 nm in Ar-saturated ACN (3×10^{-5} M) led to the transient spectrum shown in Figure 20 (bottom). As pointed out in Figure 20, the transient absorption spectrum of **1** is not influenced by the presence of oxygen dissolved in ACN. Moreover, the absorption band, broad extending between 320 nm and 600 nm, doesn't evolve as a function of time after the laser pulse, sign that a unique transient species is formed upon laser excitation. Photobleaching of the ground state prevents the precise determination of the absorption maximum, evidently positioned in the 380-480 nm range. The transient absorbance measured at 460-470 nm at the pulse end increases linearly with the flash intensity as expected for a monophotonic formation process (Figure 21). No significant differences were observed for the transient spectra of **2-4** (Figure 22): functionalization doesn't seem to significantly influence the transient states formed upon irradiation and their properties.

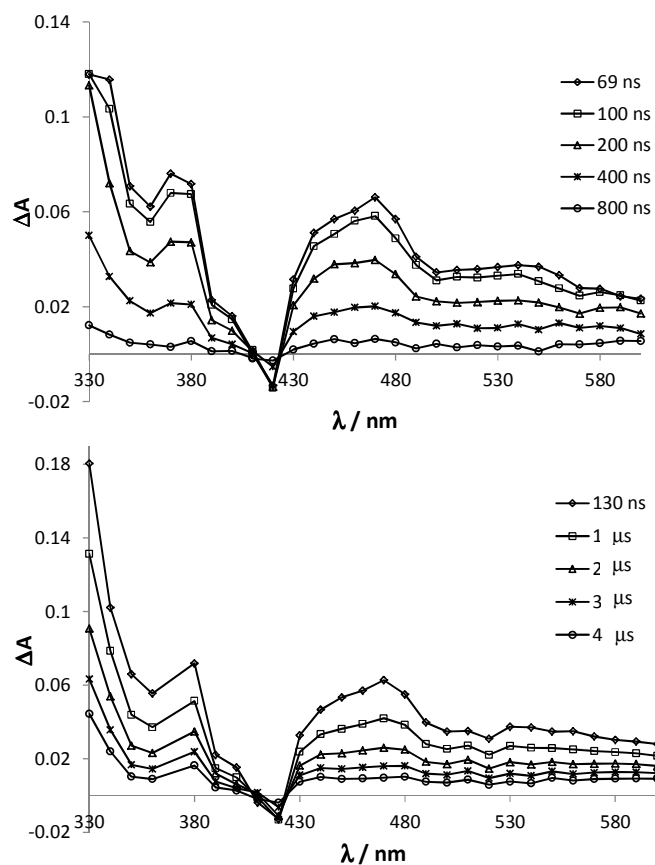


Figure 20 Time evolution of the transient absorption observed by laser flash photolysis of **1** in air-equilibrated (top) and Ar-saturated (bottom) ACN at room temperature.

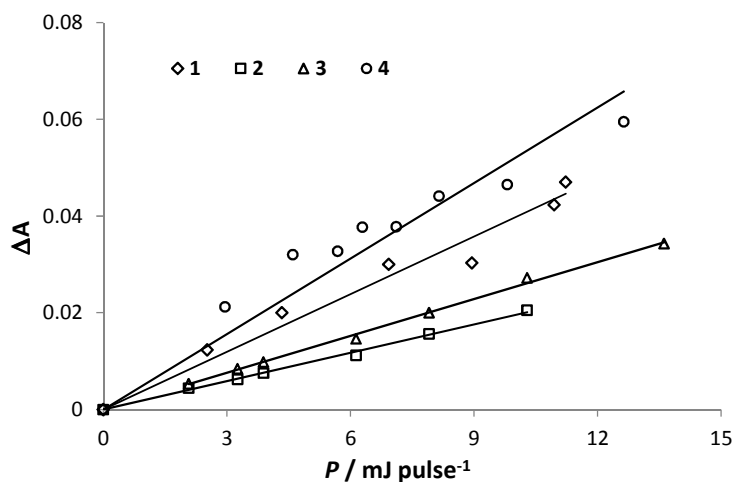


Figure 21 Plot of the end of pulse transient absorption as a function of the laser pulse intensity. The absorption was monitored at 460 nm for **1** and at 470 nm for **2-4**. Diamonds (**1**, 2.7×10^{-5} M, $A_{355} = 0.17$), squares (**2**, 2.3×10^{-5} M, $A_{355} = 0.13$), triangles (**3**, 3.3×10^{-5} M, $A_{355} = 0.13$), circles (**4**, 7.2×10^{-5} M, $A_{355} = 0.35$) at room temperature in aerated ACN.

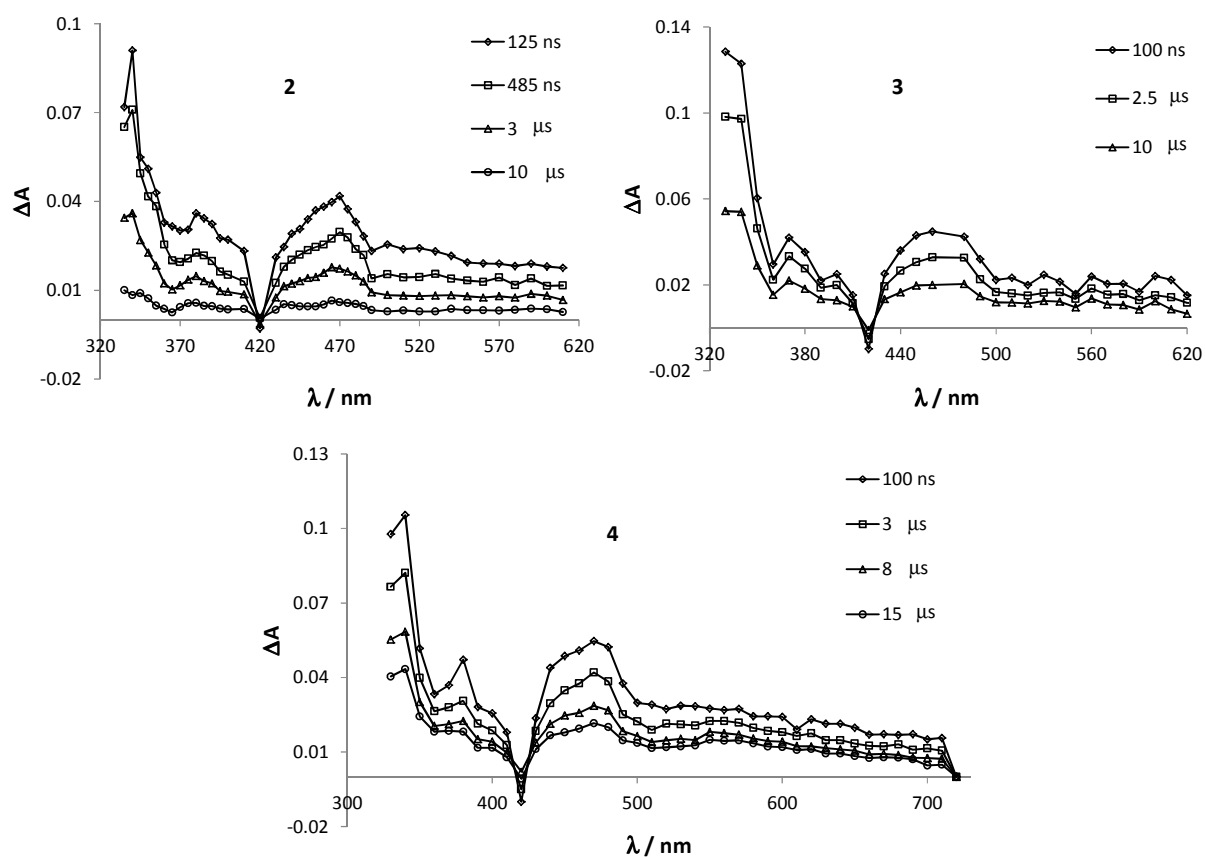


Figure 22 Time evolution of the transient absorption observed by laser flash photolysis of **2**, **3** and **4** in Ar-saturated ACN at room temperature.

In Ar-saturated ACN, the transient decays of **1-4** (Figures 23 and 24) follow first-order kinetics and lifetimes are found between 5.0 and 8.3 μs (Table 4). The transients are efficiently quenched by O_2 (Figures 23 and 24), as showed by the decay profiles of the transients of **1-4** at different oxygen concentrations (air-equilibrated, argon- and oxygen- saturated ACN). As an example, the variation of the monomolecular rate constant of transient decay as a function of $[\text{O}_2]$ is reported in Figure 23 (for compound **1**): from the corresponding slope the bimolecular (second order) rate constant of transient quenching by oxygen ($k_{q,\text{O}_2}^T / \text{M}^{-1} \text{s}^{-1}$) is obtained. The rate constants vary in a narrow range, between $(2.3 \pm 0.2) \times 10^9 \text{ M}^{-1} \text{ s}^{-1}$ for compound **4** and $(1.5 \pm 0.2) \times 10^9 \text{ M}^{-1} \text{ s}^{-1}$ for compound **3**: the transient species produced (probably the triplet excited state) are efficiently quenched by O_2 , with no significant influence of the substituent.

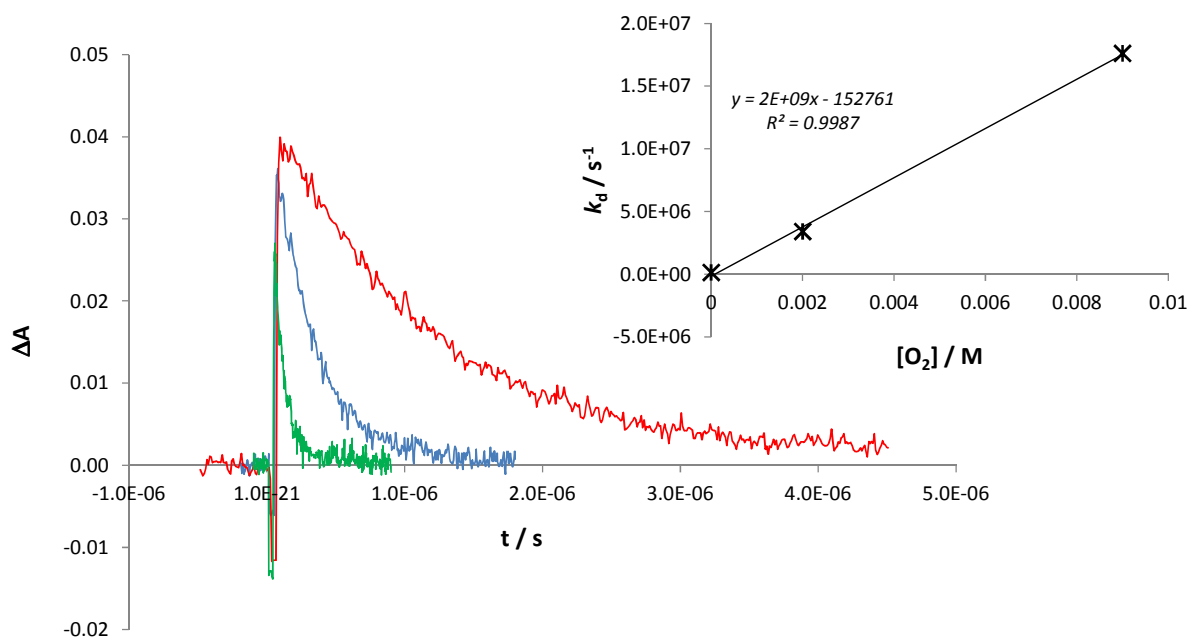


Figure 23 Decay of the transient absorption of **1** observed by laser flash photolysis in argon- (red line), air- (blue line) and oxygen- (green line) saturated ACN solutions at room temperature. Inset: variation of the monomolecular rate constant of transient decay (k_d) as a function of $[O_2]$.

Table 4 Rate constants of transient decay (k_d^T) in oxygen-, air- and argon- saturated solutions, rate constants of transient quenching by O_2 (k_{q,O_2}^T), $\epsilon_T\Phi_T$ values for compounds **1-4**. Solvent: ACN at room temperature.

PS	k_d^T			$\tau_T / \mu s$	$k_{q,O_2}^T / 10^9 M^{-1} s^{-1}$	$\epsilon_T\Phi_T / M^{-1} cm^{-1}$
	$O_2 / 10^7 s^{-1}$	air / $10^6 s^{-1}$	Ar / $10^5 s^{-1}$			
1	1.8 ± 0.3	3.4 ± 0.3	1.4 ± 0.2	7.1	2.0 ± 0.2	1680 ± 170 (460 nm) 2500 ± 250 (470 nm)
2	1.5 ± 0.5	3.8 ± 0.2	2.0 ± 0.2	5.0	1.7 ± 0.2	2550 ± 250 (470 nm)
3	1.4 ± 0.4	4.0 ± 0.3	1.4 ± 0.2	7.1	1.5 ± 0.2	3560 ± 350 (460 nm)
4	2.0 ± 0.4	3.7 ± 0.3	1.2 ± 0.1	8.3	2.3 ± 0.2	3760 ± 370 (470 nm)

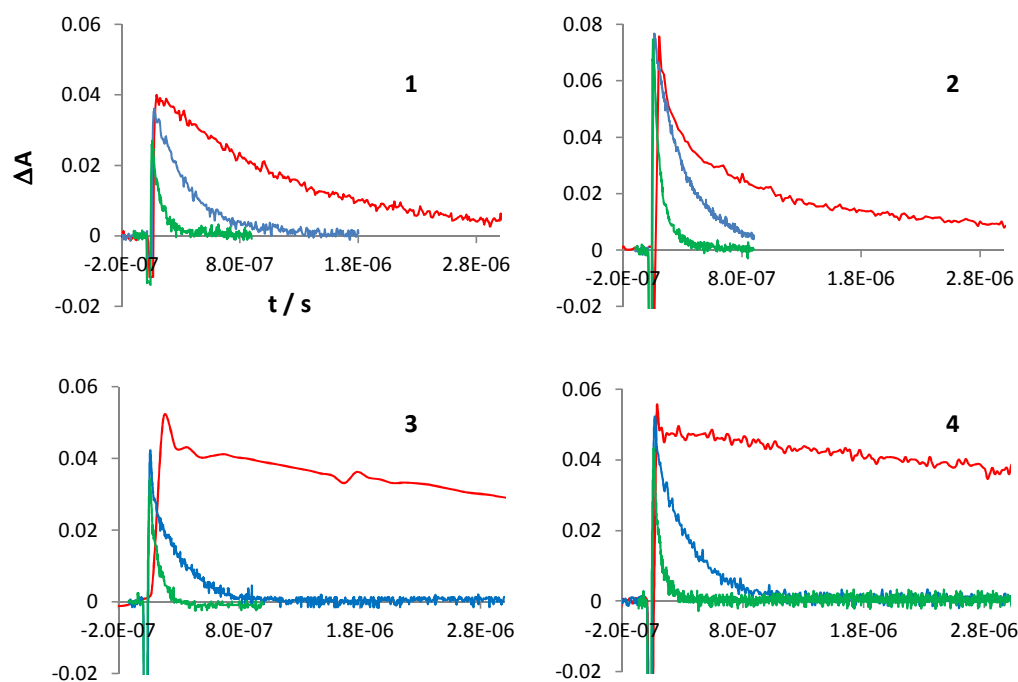


Figure 24 Decay of the transient absorption of **1-4** observed by laser flash photolysis in argon- (red line), air- (blue line) and oxygen- (green line) saturated ACN solutions at room temperature.

To confirm that the detected transients corresponded to the triplet excited states, energy transfer experiments using either anthracene ($E_T = 176 \text{ kJ mol}^{-1}$) or rubrene ($E_T = 109 \text{ kJ mol}^{-1}$)³⁷ as energy acceptors were carried out. The procedures described in the Chapter 3 were followed.

Laser excitation at 266 nm of **1** ($1.5 \times 10^{-5} \text{ M}$) in Ar-saturated ACN and in the presence of anthracene ($1.7 \times 10^{-4} \text{ M}$) led to a fast decay of the transient and to a simultaneous growing-up of the absorbance at 420 nm. This formation brings evidence that the anthracene triplet excited state is produced *via* energy transfer. Similar findings were obtained for compounds **2-4**. The second order rate constant for the energy transfer to anthracene was evaluated to be approximately $(5.7 \pm 0.5) \times 10^9 \text{ M}^{-1} \text{ s}^{-1}$ for all compounds. The quantum yield of triplet anthracene formation was estimated using absorbances measured at the maximum of the triplet formation (approximately 500 ns after the laser pulse) for a range of P . We evaluated the quantum yield of anthracene triplet formation through energy transfer ($\phi_{T, \text{Ant}}$) to be 0.17 in the case of **1**, and even lower for **2** and **3** (Table 5).

Similar experiments were carried out using rubrene as an energy acceptor. Solutions containing both the PS and rubrene were irradiated at 355 nm, wavelength which allowed the selective excitation of the PS. Upon laser excitation of oxygen-free solutions of PS ($1.5 \times 10^{-5} \text{ M}$) and rubrene ($2 \times 10^{-4} \text{ M}$) in ACN, a fast decay of the triplet was observed (monitoring at 470, 530 (Figure 25) or 575 nm), as well as an increase of the absorbance at 495 nm attributed to the formation of the rubrene triplet excited state *via* energy transfer (Figure 25). The quantum yield of triplet rubrene formation was estimated using absorbances measured at the maximum of the triplet formation (approximately 2.5 μs after the laser pulse) for a range of laser pulse energy. For the four compounds the results are close to those obtained using anthracene: the quantum yields of rubrene triplet formation vary between 0.05 and 0.10 (Table 5). These very low values compared to the quantum yields of singlet oxygen production

(see next paragraph) show that the energy transfer to anthracene or rubrene is only partial and therefore quantum yields of triplet formation (Φ_T) for **1-4** could not be obtained by this method.

Table 5 Quantum yields of formation of the tripled excited state of rubrene and anthracene as energy acceptors; rate constants of quenching of the triplet excited state of the PSs by energy transfer to anthracene ($k_{q, Ant}$).

PS	$\Phi_{T, Ru}$	$\Phi_{T, Ant}$	$k_{q, Ant} / 10^9 \text{ M}^{-1} \text{ s}^{-1}$
1	0.10 ± 0.1	0.17 ± 0.3	5.9 ± 0.6
2	0.05 ± 0.1	0.07 ± 0.1	5.5 ± 0.5
3	0.09 ± 0.1	0.08 ± 0.2	5.7 ± 0.6
4	0.09 ± 0.1	-	-

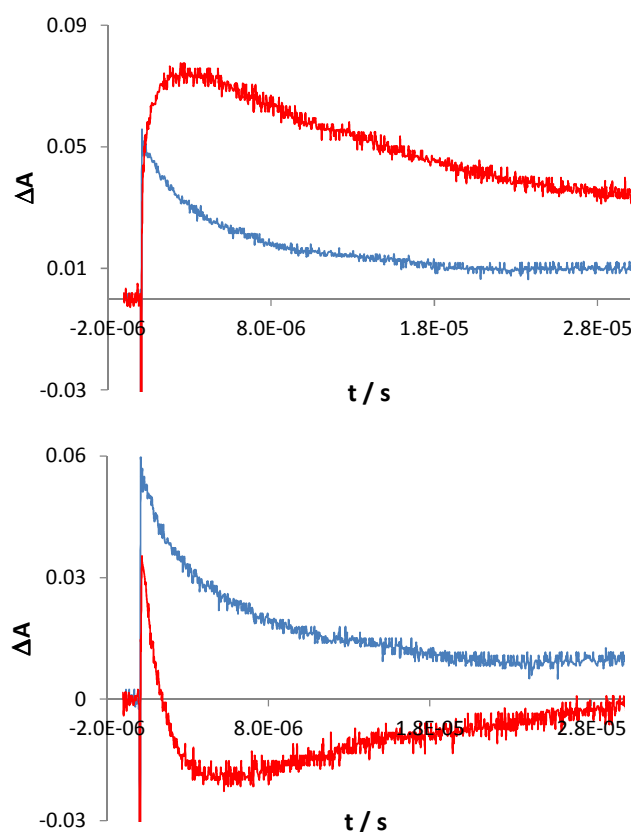


Figure 25 Transient absorption decay at 495 nm (top) and 530 nm (bottom) as a function of time in Ar-saturated ACN solutions at room temperature. Blue line: **1** ($1.5 \times 10^{-5} \text{ M}$); red line: **1** ($1.5 \times 10^{-5} \text{ M}$) and rubrene ($2.0 \times 10^{-4} \text{ M}$) as an energy acceptor. The increase of intensity due to the triplet state of rubrene formed by ET (top) and the decrease of intensity due to faster triplet quenching of **1** by ET to rubrene (bottom) are evident.

An attempt was made to evaluate Φ_T using the partial saturation method.^{288,289} A value comprised between 0.4 and 0.5 was obtained for **1**. However, the partial saturation method, based on the two-state model (ground state and T_1), gives good results only under the condition that the rate constant of light absorption is negligible compared to the rate constant of S_1 decay. Unfortunately, this requirement is not fulfilled for **1** and the Φ_T value obtained was not fully reliable.

From the energy transfer experiments, taking into account the transient decay profiles and the transient absorption spectra which pointed out the presence of only one transient species for compounds **1-4**, it is possible to conclude that all **DBTP** derivatives efficiently populate the triplet excited state (T_1) to subsequently generate singlet oxygen via energy transfer. Contrary to **DCA**, for which the T-T absorption spectrum (λ_{\max} 440 nm) could be recorded only in the presence of heavy atoms to enhance intersystem crossing,^{32,42,43} the formation of the triplet excited state in the case of derivatives **1-4** could be easily observed.

4.0 SINGLET OXYGEN DETECTION

4.1 Direct 1O_2 phosphorescence detection

Quantum yields of 1O_2 production (Φ_Δ) and rate constants of 1O_2 total quenching (k_t^{PS}) of the investigated PSs in ACN were determined by monitoring the 1O_2 near-IR phosphorescence emission, upon continuous irradiation, using perinaphthenone (**PN**) as a reference (R), following the procedure previously described.^{46,47}

The 1O_2 emission signals (S_e) were measured at various PS concentrations for all **DBTP** derivatives, for **DCA** and **PN**. All solutions were irradiated at 367 nm, corresponding to one of the emission peaks of the Xe-Hg lamp. The ratio of 1O_2 signals for R and PS was analyzed as a function of the PS concentration, in order to determine the rate constants of total quenching by the PS itself (k_t^{PS}) in the range of concentrations used for this work. In all cases, except for **2**, such a ratio, eventually corrected for small differences in absorption factors ($(S_e^R/S_e^{PS})(\alpha^{PS}/\alpha^R)$, equations 3.25 and 3.26), did not vary significantly with the PS concentration (Figure 26 and Table 6). It can therefore be concluded that, in our experimental conditions, 1O_2 quenching by the PS was negligible compared to quenching by the solvent ($k_t^{PS}[PS] \ll k_d$). Under these conditions, values of Φ_Δ could be directly calculated from the mean values of the ratios of (S_e^R/S_e^{PS}) and (α^R/α^{PS}), following equation 3.27 (equation 3.28 if R and PS have the same absorbance at the irradiation wavelength), with Φ_Δ^{PN} close to 1.⁴⁵⁻⁴⁷

Table 6 Values of $^1\text{O}_2$ emission signals S_e^R and S_e^{PS} in ACN at room temperature, at different absorbances (A^R , A^{PS}) and of S_e^R/S_e^{PS} corrected for small differences in absorption factors (α) between PS (**DCA**, **1**, **2**, **3** and **4**) and PN; wavelength of irradiation: 367 nm.

PS	A^R (367 nm)	S_e^R / a.u.	A^{PS} (367 nm)	S_e^{PS} / a.u.	$\frac{S_e^R \alpha^{PS}}{S_e^{PS} \alpha^R}$
DCA	0.71	11.6	0.72	3.5	3.38
	0.59	10.2	0.57	3.1	3.30
	0.49	9.1	0.49	2.7	3.37
	0.37	7.9	0.38	2.3	3.46
	0.28	6.0	0.27	1.8	3.31
1	0.12	3.2	0.13	3.2	1.16
	0.17	3.6	0.20	4.1	0.97
	0.25	6.0	0.25	5.4	1.10
	0.39	7.6	0.40	7.1	1.09
	0.56	9.8	0.53	8.9	1.08
	0.63	12.2	0.63	11.0	1.11
2	0.12	3.2	0.12	2.6	1.29
	0.17	3.6	0.18	2.5	1.42
	0.28	5.4	0.31	3.0	1.85
	0.28	5.4	0.29	3.0	1.78
	0.39	7.6	0.38	3.7	2.02
	0.56	9.8	0.55	4.2	2.33
3	0.12	3.2	0.12	2.2	1.44
	0.17	3.6	0.2	2.7	1.45
	0.25	6.1	0.25	3.5	1.69
	0.28	5.4	0.28	3.6	1.50
4	1.03	16.4	1.02	13.9	1.18
	0.81	13.6	0.81	11.1	1.18
	0.62	11.3	0.61	9.4	1.17
	0.51	9.8	0.51	8.2	1.18
	0.41	8.1	0.41	6.3	1.18

Values of Φ_Δ for **1**, **2** and **4** (Table 7) under our experimental conditions (air-equilibrated ACN solutions) are all much higher (0.82-0.91) than for **DCA** (0.30). The lower value for compound **3** may possibly be assigned to traces of *N,N'*-cyclohexylurea that could quench singlet oxygen.

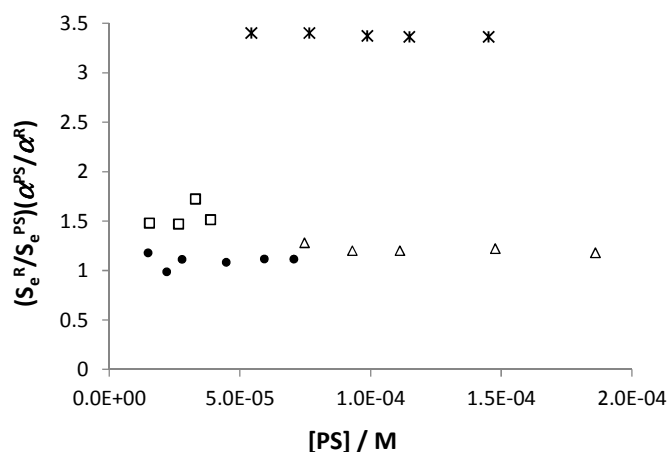


Figure 26 Variation of the ratio of the $^1\text{O}_2$ emission signals for reference (PN) and PS as a function of the PS concentration in ACN at room temperature: **DCA** (stars), **1** (circles), **3** (squares) and **4** (triangles). Errors: approx. 10%.

Table 7 Quantum yields of singlet oxygen production (Φ_Δ) and rate constants of $^1\text{O}_2$ quenching by the PS for **DCA** and compounds **1-4** determined by direct singlet oxygen luminescence detection. Solvent: air-equilibrated ACN.

PS	Φ_Δ	$k_t^{\text{PS}} / \text{M}^{-1} \text{s}^{-1}$
DCA	0.30 ± 0.03	$\leq 9.7 \times 10^6$
1	0.91 ± 0.04	$\leq 2.0 \times 10^7$
2	0.95 ± 0.03	$2.9 \pm 0.5 \times 10^8$
3	0.65 ± 0.04	$\leq 2.8 \times 10^7$
4	0.82 ± 0.04	$\leq 8.9 \times 10^6$

Taking into account the highest concentrations of **DCA**, **1**, **3** and **4** used in this work (Table 7) and a $^1\text{O}_2$ lifetime ($\tau_\Delta = 1/k_d$) of 71 μs , limiting values for k_t^{PS} could be estimated (under the assumption that $k_t^{\text{PS}}[\text{PS}]_{\text{max}} \leq 0.1k_d$, Table 7). These values are lower than $2.8 \times 10^7 \text{M}^{-1} \text{s}^{-1}$ for all the tested PSs. In the case of **2**, a significant variation of the signal intensity as a function of the PS concentration was observed: singlet oxygen quenching by the PS is in this case not negligible and the use of equation 3.27 yields only an apparent Φ_Δ value ($\Phi_{\Delta,\text{app}}$, Table 9) for each concentration of PS, not corrected for $^1\text{O}_2$ quenching. Values of Φ_Δ and k_t^{PS} were thus estimated from the intercept and the slope of the linear plot of $[(S_e^R/S_e^{\text{PS}})(\alpha^{\text{PS}}/\alpha^R)]$ vs [PS] (Figure 27, equation 3.26). The value of k_t^{PS} for **2** ($(2.9 \pm 0.5) \times 10^8 \text{M}^{-1} \text{s}^{-1}$) is at least 10 times larger than for the other PSs investigated (Table 7).

Therefore, the carboxylic substituent on the **DBTP** moiety of **2** induces a much more efficient $^1\text{O}_2$ deactivation, most probably by increasing the charge transfer character in the collision complex formed between $^1\text{O}_2$ and the PS ground state.^{287,290–292} Most probably, the higher polarity of this derivative explains this result.

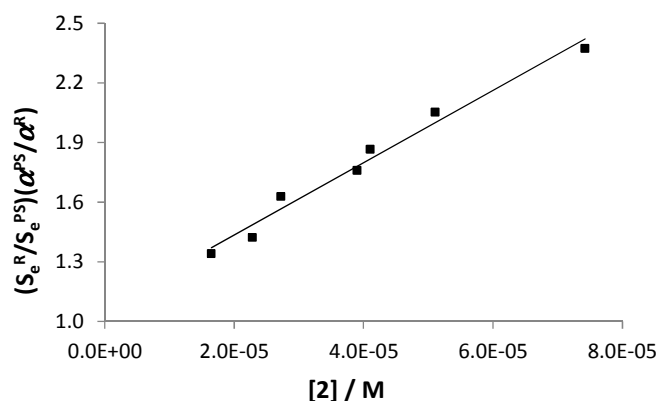


Figure 27 Variation of the ratio of the $^1\text{O}_2$ emission signals for PN and **2** as a function of the concentration of PS in ACN at room temperature. Errors: approx. 10%.

4.2 Detection by reaction with a chemical probe

Determination of Φ_{Δ} was also carried out using rubrene as a chemical probe (Figures 8 and 9). The reaction between rubrene and singlet oxygen selectively yields a thermally and photochemically stable endoperoxide,^{269,278} which does not absorb in the visible, whereas rubrene is characterized by a band centered at approx. 500 nm (Figure 28). The kinetics of the reaction and the experimental set-up, are described in Chapter 3. For the determination of the quantum yields of singlet oxygen production we used equation 3.33; as shown by $^1\text{O}_2$ phosphorescence detection, quenching by the PS itself was negligible compared to $^1\text{O}_2$ deactivation by the solvent for **DCA**, **1**, **3** and **4** and was taken into account only for compound **2**. The resulting values of Φ_{Δ} for all the PSs are in good agreement with those measured by $^1\text{O}_2$ luminescence detection (Table 8).

Table 8 Quantum yields of singlet oxygen production (Φ_{Δ}) for **DCA** and compounds **1-4** determined by detection using rubrene as a chemical probe; comparison with the results obtained by direct detection. Solvent: air-equilibrated ACN at 25 °C.

PS	Φ_{Δ}	Φ_{Δ} (direct method)
DCA	0.31 ± 0.05	0.30 ± 0.03
1	1.00 ± 0.05	0.91 ± 0.04
2	1.03 ± 0.05	0.95 ± 0.03
3	0.67 ± 0.05	0.65 ± 0.04
4	0.89 ± 0.03	0.82 ± 0.04

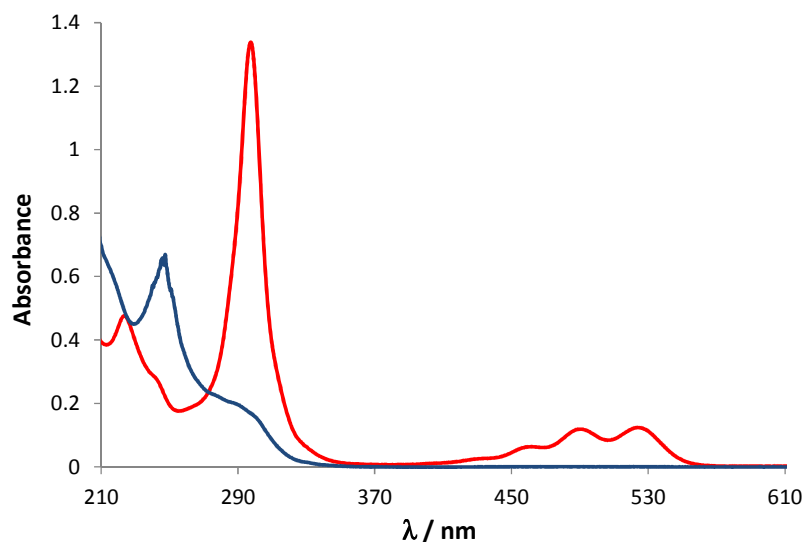


Figure 28 Absorption spectra of rubrene (red) and of the endoperoxide formed by singlet oxygen addition to rubrene (bleu). $^1\text{O}_2$ was produced by photosensitization using PN; the spectrum of the endoperoxide was obtained after complete conversion of rubrene and the subtraction of the photosensitizer absorption. Solvent: air-equilibrated ACN at 25 °C ($\ell = 1$ cm, quartz cells).

In the case of **2**, taking into account the rate constant of singlet oxygen total quenching obtained by $^1\text{O}_2$ luminescence detection ($k_t^{\text{PS}} = 2.9 \times 10^8 \text{ M}^{-1} \text{ s}^{-1}$), we measured the apparent Φ_{Δ} at three different concentrations of **2**. By using both the direct and the indirect methods, the values of apparent quantum yield of $^1\text{O}_2$ production had the same dependence on the PS concentration, as showed in Table 9.

Table 9 Apparent quantum yields of singlet oxygen production of **2** in ACN at room temperature, measured by direct $^1\text{O}_2$ detection and by trapping by rubrene at different concentrations of PS.

$[\mathbf{2}] / 10^{-5} \text{ M}$	$\Phi_{\Delta, \text{app}}$	$\Phi_{\Delta, \text{app}}$ (direct method)
3.0	0.62 ± 0.05	0.65 ± 0.03
1.5	0.68 ± 0.05	0.73 ± 0.05
0.75	0.75 ± 0.05	0.78 ± 0.05

It is evident from the results reported in Tables 8 and 9 that the method for singlet oxygen detection by chemical trapping by rubrene developed during this project is really reliable and represents a good alternative to the direct detection method. By directly detecting singlet oxygen phosphorescence no interferences can be caused by the addition of chemical species other than the PS and no artefacts can derive from the kinetic analysis of the reaction between the probe and $^1\text{O}_2$. Nevertheless, this method requires very sensitive detectors which cannot be used unless at very low temperature (liquid N_2); in addition, several components of the set-up are very fragile. For the

indirect method it is necessary to carefully apprehend all the kinetic parameters concerning the selected probe but once all parameters determined, measurements are very easily carried out, working at room temperature, using only a spectrophotometer as an analytical tool.

4.3 Mechanisms of $^1\text{O}_2$ generation by DCA and DBTP derivatives

Although **DCA** and compounds **1-4** share the same cyanoanthracenic structure, important differences were observed in their photophysical properties and quantum yields of $^1\text{O}_2$ production (0.30 for **DCA** and 0.65-0.95 for the other PSs). These large differences between the two classes of chromophores were striking and led to a detailed analysis of the mechanisms of photosensitization, which took into account all the photophysical properties already described in this chapter. The discussion below is mainly based on a comparison between **DCA** and **1**, since it was demonstrated that substitution on the **DBTP (1)** moiety does not affect these properties to a significant extent.

The fluorescence lifetime of **1** ($\tau_F = 6.3$ ns) in Ar-saturated ACN is more than twice shorter than that of **DCA** (14.9-16.5 ns), whereas the Φ_F value is more than five times smaller for **1** (0.16) than for **DCA** (0.87) (Table 3).^{32,42,178,205,287,293} On the other hand, the triplet excited state (T_1) of **DCA** is hardly detectable, with values of quantum yield of triplet formation (Φ_T) reported in the literature lower than 0.04.^{42,43} In contrast, the triplet excited states of **1** and its derivatives were easily observed by laser flash photolysis and were efficiently quenched by oxygen (Figures 23 and 24). It should be also noted here that, as outlined in the Introduction, although **DCA** has been intensively studied, the values of its Φ_Δ reported in the literature vary depending on the authors, the techniques used for its determination, the solvent, the concentration of O_2 .^{31,39,40,287} The Φ_Δ measured in this work for **DCA** (0.30), under conditions identical to those for **1-4**, is three times lower than Φ_Δ of **1** (0.91).

Taking into account the various photophysical pathways involved in the production of $^1\text{O}_2$, Φ_Δ may be expressed as the sum of the fractions of singlet oxygen generated starting from the singlet and the triplet excited states of a PS:^{32,291,294}

$$\Phi_\Delta = \Phi_\Delta^S + \Phi_\Delta^T = P_{\text{O}_2}^S f_\Delta^S + \Phi_T P_{\text{O}_2}^T f_\Delta^T \quad 4.01$$

where P_{O_2} is the fraction of excited state (S_1 or T_1) quenched by ground state O_2 and f_Δ is the fraction of excited state quenched by O_2 yielding $^1\text{O}_2$. The fraction of $^1\text{O}_2$ produced from the singlet excited state of the PS is in most cases negligible; however, exceptions may occur. P_{O_2} can be determined from the kinetic parameters of the deactivation of the corresponding excited state, according to equation 4.02:

$$P_{\text{O}_2} = \frac{k_{q,\text{O}_2} [\text{O}_2]}{k_{q,\text{O}_2} [\text{O}_2] + k_{\text{Md}}} \quad 4.02$$

where k_{q,O_2} is the rate constant of the excited state quenching by O_2 , $[\text{O}_2]$ is the concentration of oxygen in air-equilibrated ACN (≈ 2.42 mM)³⁷ and k_{Md} is the rate constant of the monomolecular decay of the excited state (due to radiative and radiationless pathways); in the case of S_1 it is the sum of the rate constants of fluorescence emission (F), internal conversion to the ground state (IC) and intersystem crossing to T_1 (ISC):

$$k_{\text{Md}}^{\text{S}} = k_{\text{F}} + k_{\text{IC}} + k_{\text{ISC}} \quad 4.03$$

For T_1 , k_{Md} is expressed as the sum of the rate constants of intersystem crossing to the ground state (ISC') and phosphorescence emission (P):

$$k_{\text{Md}}^{\text{T}} = k'_{\text{ISC}} + k_{\text{P}} \quad 4.04$$

Calculated values of the parameters involved in equations 4.01 and 4.02 are reported in Table 10. Due to the limits of the calculations or measurements of all the mentioned rate constants, some simplifications have been done. In the case of **DCA** we assumed $k_{\text{Md}}^{\text{S}} = k_{\text{F}}$, considering IC negligible and the extremely low yield of triplet formation by ISC. On the contrary, for **1-4** ISC is favored relative to fluorescence and $k_{\text{Md}}^{\text{S}} > k_{\text{F}}$ (IC is again considered negligible relative to the other component of equation 4.03). However, the calculations have been carried out assuming $k_{\text{Md}}^{\text{S}} = k_{\text{F}}$: the values of $P_{\text{O}_2}^{\text{S}}$ obtained and reported in Table 10 are thus maximum values. In the case of triplet excited states in the contrary the approximation of $k_{\text{Md}}^{\text{T}} = k'_{\text{ISC}}$ is actually valid, since no phosphorescence emission has been detected (see below).

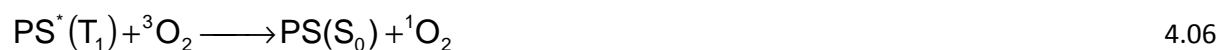
Table 10 Measured quantum yields of $^1\text{O}_2$ production (Φ_{Δ} , direct method), rate constants of fluorescence emission (k_{F} , Ar-saturated solutions), rate constant of S_1 quenching by O_2 ($k_{\text{O}_2}^{\text{S}}$), fractions of S_1 states quenched by O_2 ($P_{\text{O}_2}^{\text{S}}$), fractions of T_1 states quenched by O_2 ($P_{\text{O}_2}^{\text{T}}$), quantum yields of triplet (T_1) formation (Φ_{T}) and fractions of T_1 states quenched by O_2 yielding $^1\text{O}_2$ (f_{Δ}^{T}) for **1-4** and **DCA** in ACN. Values from Tables 3, 4 and 7.

^{a)} $\tau_{\text{F}} = 1/k_{\text{F}}$ in Ar-saturated solutions.

PS	Φ_{Δ}	$k_{\text{F}} / 10^8 \text{ s}^{-1\text{a}}$	$k_{\text{q},\text{O}_2}^{\text{S}} / 10^9 \text{ M}^{-1} \text{ s}^{-1}$	$P_{\text{O}_2}^{\text{S}}$	$P_{\text{O}_2}^{\text{T}}$	$\frac{\Phi_{\Delta}^{\text{T}} f_{\Delta}^{\text{T}}}{(=\Phi_{\Delta} / P_{\text{O}_2}^{\text{T}})}$	Φ_{T}	f_{Δ}^{T}
DCA ¹⁷⁸	0.30	0.61 ± 0.04	10 ± 1	0.28 ± 0.02	-	-	$0.02\text{-}0.04$ ⁴²	-
1	0.91	1.58 ± 0.05	5.00 ± 0.04	0.07 ± 0.01	0.97 ± 0.04	0.94	0.85	1.1
2	0.95	2.00 ± 0.06	4.60 ± 0.05	0.05 ± 0.01	0.95 ± 0.04	1.00	0.88	1.1
3	0.65	1.79 ± 0.08	12.00 ± 0.08	0.14 ± 0.02	0.96 ± 0.04	0.68	0.85	0.8
4	0.82	1.75 ± 0.06	5.20 ± 0.04	0.06 ± 0.01	0.98 ± 0.04	0.84	0.84	1.0

It should be noted here that efficient $^1\text{O}_2$ production by energy transfer from the S_1 state of a PS to O_2 may only occur by simultaneous formation of the T_1 state of the PS (reaction 4.05), and therefore requires a S_1 - T_1 energy gap larger than the $^1\text{O}_2$ energy (94.2 kJ mol^{-1}).^{18,39,40} If reaction 4.05 does occur, an enhanced intersystem crossing S_1 - T_1 (**EISC**) should be observed for the PS in the presence of O_2 . Following reaction 4.05, more $^1\text{O}_2$ may be produced by energy transfer from the T_1 state of the PS to O_2 (reaction 4.06), implying a theoretical limiting value of Φ_{Δ} of 2 if both subsequent energy transfer reactions are 100% efficient (equation 4.01).





There is a general agreement that ${}^1\text{O}_2$ is produced by energy transfer from the S_1 state of **DCA** to O_2 (reaction 4.05),^{32,39,40,287,293} the energy gap between the S_1 and T_1 states being large enough (approx. 105 kJ mol^{-1}).³⁷ Considering reactions 4.05 and 4.06, the efficiency of T_1 production by EISC ($f_{\text{T}}^{\text{O}_2}$) is equal to the quantum yield of singlet oxygen production from the S_1 state, that is:

$$f_{\text{T}}^{\text{O}_2} = \Phi_{\Delta}^{\text{S}} = P_{\text{O}_2}^{\text{S}} f_{\Delta}^{\text{S}} \quad 4.07$$

For **DCA**, assuming that Φ_{T} in de-oxygenated solutions (≤ 0.04 , Table 10)^{42,43,290} is negligible compared to the triplet excited state formed by EISC ($\Phi_{\text{T}} \ll f_{\text{T}}^{\text{O}_2}$), equation 4.01 may be rewritten as:

$$\Phi_{\Delta} = \Phi_{\Delta}^{\text{S}} + \Phi_{\Delta}^{\text{T}} = P_{\text{O}_2}^{\text{S}} f_{\Delta}^{\text{S}} + f_{\text{T}}^{\text{O}_2} P_{\text{O}_2}^{\text{T}} f_{\Delta}^{\text{T}} = P_{\text{O}_2}^{\text{S}} f_{\Delta}^{\text{S}} (1 + P_{\text{O}_2}^{\text{T}} f_{\Delta}^{\text{T}}) \quad 4.08$$

If the quenching of the T_1 state by oxygen is 100% efficient and yields exclusively ${}^1\text{O}_2$, $P_{\text{O}_2}^{\text{T}} f_{\Delta}^{\text{T}}$ reaches the higher limiting value of 1 and $\Phi_{\Delta}^{\text{S}} (= P_{\text{O}_2}^{\text{S}} f_{\Delta}^{\text{S}})$ is equal to $\Phi_{\Delta} / 2$. Such a 50% fraction represents the *minimum* contribution of Φ_{Δ}^{S} to the total Φ_{Δ} . Taking into account the value of Φ_{Δ} we determined experimentally for **DCA** (0.30) and the $P_{\text{O}_2}^{\text{S}}$ value of 0.28 (calculated from the rate constants k_{F} and $k_{\text{q},\text{O}_2}^{\text{S}}$ reported by Kikuchi *et al.*,¹⁷⁸ Table 10), we obtain:

$$f_{\Delta}^{\text{S}} (1 + P_{\text{O}_2}^{\text{T}} f_{\Delta}^{\text{T}}) \approx 1 \quad 4.09$$

Considering equation 4.09, if we assume again that the quenching of the T_1 state by oxygen is 100% efficient and it yields exclusively ${}^1\text{O}_2$ (*i.e.* $P_{\text{O}_2}^{\text{T}} f_{\Delta}^{\text{T}} = 1$), a minimum value of 0.5 is calculated for f_{Δ}^{S} . To summarize, in the presence of **DCA** as a photosensitizer, singlet oxygen production from the PS singlet excited state (S_1) has a 50% minimum contribution to the overall ${}^1\text{O}_2$ generation; moreover, at least the 50% of the singlet excited state of **DCA** quenched by ground state oxygen yields ${}^1\text{O}_2$. The fraction of singlet oxygen which is not generated by energy transfer from the S_1 state of **DCA**, is produced from the triplet excited state (T_1) populated by enhanced intersystem crossing.

In the case of **1** and its derivatives, results were drastically different. Quenching of the S_1 state of **1** by O_2 is poorly efficient in air equilibrated solutions, with a value of $k_{\text{q},\text{O}_2}^{\text{S}} [\text{O}_2]$ ($\approx 1.2 \times 10^7 \text{ s}^{-1}$) more than an order of magnitude smaller than the rate constant of the monomolecular deactivation of S_1 ($k_{\text{Md}}^{\text{S}} > k_{\text{F}} \approx 1.6 \times 10^8 \text{ s}^{-1}$, Table 10). Similar values were found for compounds **2-4**. The maximum $P_{\text{O}_2}^{\text{S}}$ value deriving from these photophysical conditions is approx. 0.07 (for compound **1**, Table 10). In contrast, quenching of the T_1 state is almost quantitative under the same experimental conditions ($P_{\text{O}_2}^{\text{T}}$ of approx. 0.97, Table 10). Similar results were obtained for **2-4**, with $P_{\text{O}_2}^{\text{T}}$ values of 0.95, 0.96 and 0.98, respectively. Moreover, the absorbance of T_1 did not increase with $[\text{O}_2]$ for **1-4** (see Figures 23 and 25), indicating the absence of an oxygen-enhanced intersystem crossing. Therefore, it can be concluded that ${}^1\text{O}_2$ production occurs exclusively from the T_1 state of these PSs. Knowing the values of Φ_{Δ} and $P_{\text{O}_2}^{\text{T}}$ (Table 10), and considering $\Phi_{\Delta}^{\text{S}} = 0$, the products $\Phi_{\text{T}} f_{\Delta}^{\text{T}}$ may be evaluated from equation 4.01 (Table 10). Attempts to estimate Φ_{T} values by laser flash photolysis were unfortunately unsuccessful: the energy transfer to anthracene and to rubrene was by far not quantitative (between 0.05 and 0.17) and the partial saturation method^{288,289} significantly underestimated Φ_{T} . However,

assuming the quantum yield of S_1 internal conversion negligible, the sum of Φ_F and Φ_T can be considered equal to 1. The quantum yield of triplet formation can thus be expressed as:

$$\Phi_T = 1 - \Phi_F \quad 4.10$$

and estimated values of f_{Δ}^T may be obtained (Table 10) from:

$$f_{\Delta}^T = \frac{\Phi_{\Delta}}{\Phi_T P_{O_2}^T} \quad 4.11$$

Within experimental error, values of f_{Δ}^T , fraction of T_1 states quenched by oxygen and yielding 1O_2 , are unity for **1**, **2** and **4**, and therefore, energy transfer leading to the production of 1O_2 is the only pathway of T_1 quenching by O_2 in ACN for these compounds. In the case of **3** $f_{\Delta}^T \approx 0.8$: this smaller value compared to the other compounds is directly related to the lower Φ_{Δ} measured for **3** (0.65) and, as pointed out above, traces of impurities acting as 1O_2 quenchers might explain this result.

As f_{Δ}^T is equal to the ratio of the rate constants of energy transfer from T_1 to O_2 (k_{ET}) and the second order rate constant of T_1 quenching by O_2 (k_{q,O_2}^T),

$$f_{\Delta}^T = \frac{k_{ET}}{k_{q,O_2}^T} \quad 4.12$$

k_{q,O_2}^T represents the experimental value of k_{ET} when f_{Δ}^T is equal to 1. Quenching of T_1 excited states by oxygen in fluid solutions occurs *via* a collisional mechanism, and spin-statistical factors for the encounter complex predict that the limiting value of k_{ET} should be equal to one-ninth of the diffusion controlled rate constant (k_{diff}).^{295,296}

$$k_{ET} = \frac{1}{9} k_{diff} \quad 4.13$$

The diffusion-controlled rate constant when oxygen is one of the reaction partners has been evaluated to be approx. $1.9 \times 10^{10} \text{ M}^{-1} \text{ s}^{-1}$ in ACN.³⁷ Hence, k_{ET} values obtained for **1-4** ($(1.5-2.3) \times 10^9 \text{ M}^{-1} \text{ s}^{-1}$, Table 4, considering $k_{ET} = k_{q,O_2}^T$) are close to the predicted value of $k_{diff}/9$ (*ca.* $2.1 \times 10^9 \text{ M}^{-1} \text{ s}^{-1}$).

In summary, the generation of 1O_2 by **DCA** occurs from the PS singlet excited state with a minimum contribution of 50% and from the triplet excited state formed by EISC in the presence of O_2 . In contrast, for compounds **1-4**, the efficiency of triplet formation by ISC from the S_1 to the T_1 state is close to unity and 1O_2 is produced exclusively by energy transfer from T_1 . Two hypotheses may be proposed to explain these differences: i) the energetic difference between the S_1 and T_1 states is less than the required 94.2 kJ mol^{-1} and ii) the extent of spin-orbit coupling is higher in the case of **1-4** favoring the formation of the T_1 state compared to **DCA**.

Low temperature phosphorescence measurements were carried out on compound **1** in frozen ethanol: unfortunately such experiments were unsuccessful for the determination of the T_1 state energies of **1-4**. However, the energies of the singlet and triplet excited states of **DCA** and **1** in polar and non-polar solvents, as well as in vacuum, were estimated by theoretical calculations (Figures 29 and 30). The procedure for TDDFT optimization of the structure of **DCA** and **1** at the DFT level was

carried out with the B3LYP functional and the 6-31G* basis using Gaussian09 package. This optimization has been carried out in vacuum as well as in heptane and ethanol using the PCM model.²⁹⁷ From the optimized structures, Time-Dependent Density Functional Theory (TDDFT) calculations have been performed at the B3LYP/6-31G* level in vacuum and in PCM model of heptane and ethanol in order to determine both singlet and triplet electronic excited states of **DCA** and **1**. The S_1 - T_1 energy differences ($\Delta E_{S_1-T_1}$) estimated for **DCA** are 123, 125 and 131 kJ mol⁻¹, respectively in ethanol, heptane and vacuum. Much lower values ($\Delta E_{S_1-T_1}$ = 89, 91 and 97 kJ mol⁻¹, respectively for ethanol, heptane and vacuum) were found in the case of **1**. Such values are similar to (in vacuum) or smaller than the ¹O₂ energy gap (94.2 kJ mol⁻¹), supporting the hypothesis that the $\Delta E_{S_1-T_1}$ differences are responsible for the different mechanisms involved in the ¹O₂ production by **DCA** and **1**. Moreover, in the case of **1**, the quasi-resonance of the T₃ state with S₁ is noteworthy (Figures 29 and 30) and may explain its intrinsically efficient intersystem crossing, and therefore the relatively low fluorescence quantum yield and the high quantum yield of ¹O₂ production.

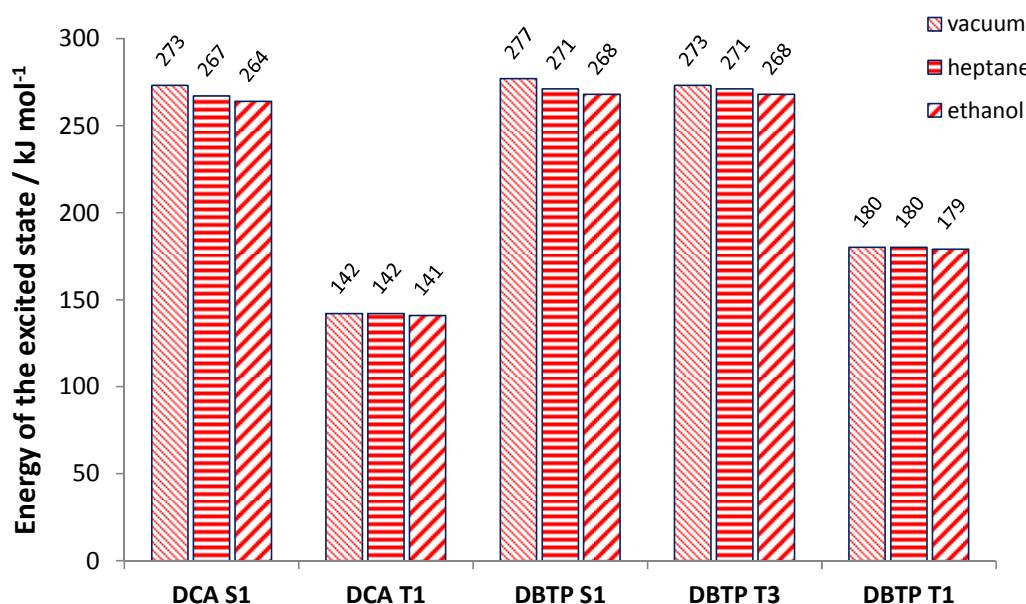


Figure 29 Energy levels of the S₁ and T₁ states of **DCA** and of the S₁, T₃ and T₁ states of **1** in vacuum, heptane and ethanol.

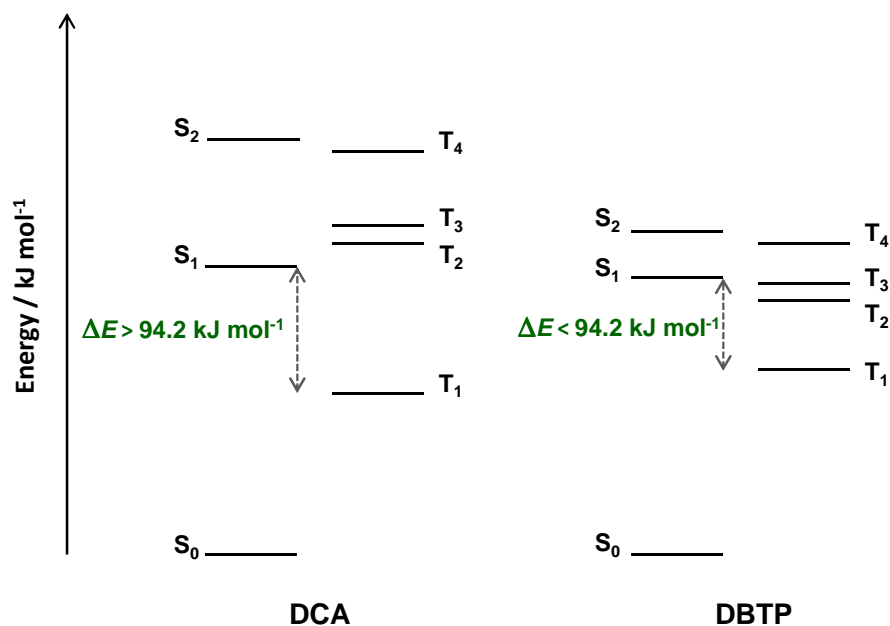


Figure 30 Complete representation of the energy levels of the ground and excited states of **DCA** and **1** in heptane. The difference between the S₁ and T₁ states is higher than 94.2 kJ mol⁻¹ only for **DCA**.

5.0 ELECTRON TRANSFER REACTIONS

As presented in the Introduction, many PSs can both produce singlet oxygen by energy transfer and oxidize organic substrates by ELT. In such cases, depending on the redox properties of PS and substrate, electron transfer reactions may compete with ¹O₂ mediated oxidation. **DCA** is known for its capability of reacting by photoinduced electron transfer reactions^{41,147} and in order to compare its photoreactivity with those of the other PSs, by taking into account all the possible pathways, the reduction potentials of **1-4** and **DCA** in ACN were determined by cyclic voltammetry (CV). The voltammograms of all the compounds, except **2**, were characterized by a one-electron reversible peak, indicative of the reversible reduction of PS to the radical anion PS^{•-}. For compound **2** an irreversible one-electron peak was observed. Values of reduction potentials were found to be -0.82 V/SCE for **DCA** (consistent with an already reported values)²⁰⁵ and to vary between -0.86 and -0.92 V/SCE for compounds **1**, **3** and **4** (Table 11). The slight difference between **DCA** and **DBTP** derivatives can be assigned to the electron-donor character of the two additional benzyl groups. Therefore, all the PSs investigated can be involved in exergonic photoinduced electron transfer processes from electron donor with oxidation potentials lower than approx. 2.1 V/SCE. This limit value could be calculated from the free energy changes (ΔG / kJ mol⁻¹, Table 11) approximated by the Rehm-Weller equation (equation 1.15).

Table 11 Reduction potentials ($E_{(PS/PS^{\bullet-})}$) of **DCA**, **1**, **3**, **4** and free energy changes (ΔG) involved in the ELT reaction from Et_3N as an electron donor to the S_1 state of the PSs; Stern-Volmer constants (K_{SV,Et_3N}^S) and rate constants of fluorescence quenching by Et_3N (k_{q,Et_3N}^S); free energy changes ($\Delta G_{O_2^{\bullet-}}$) involved in the formation of superoxide radical anion by ELT from $PS^{\bullet-}$ as an electron donor. Solvent: ACN at room temperature.

PS	$E_{(PS/PS^{\bullet-})} / V/SCE$	$\Delta G / kJ mol^{-1}$	$K_{SV,Et_3N}^S / M^{-1}$	$k_{q,Et_3N}^S / 10^{10} M^{-1} s^{-1}$	$\Delta G_{O_2^{\bullet-}} / kJ mol^{-1}$
DCA	-0.82	-95.4	293 ± 15	2.3 ± 0.2	-32.8
1	-0.92	-94.5	101 ± 5	1.9 ± 0.2	-27.0
3	-0.86	-100.2	95 ± 5	2.0 ± 0.2	-29.9
4	-0.89	-97.3	80 ± 5	1.6 ± 0.2	-23.1

As a model electron-donating compound, triethylamine ($E_{(D/D^{\bullet+})} = 1.15$ V vs SCE, ACN) was selected. In Table 11 the free energy changes relative to the photoinduced generation of the PS radical anion and the radical cation of Et_3N , calculated by using equation 1.15, are reported. The reaction is highly exergonic for all PSs. In addition, the reactivity of triethylamine towards the singlet excited states of the PSs was analyzed by measuring the corresponding fluorescence quenching.

The fluorescence intensity of compounds **1-4** has been monitored as a function of the concentration of Et_3N in the solution. By plotting the ratio of the fluorescence intensity and the fluorescence intensity in the absence of the quencher vs the concentration of Q it is possible to determine both K_{SV}^S (Stern-Volmer constant) and k_q^S , following equation 4.14:

$$\frac{I_F^0}{I_F} = 1 + \frac{k_q^S [Q]}{k_F} \quad 4.14$$

where k_q^S is the rate constant of quenching by Q (Et_3N in our case), k_F is the rate constant of fluorescence emission ($= 1/\tau_F$, equation 3.11), $[Q]$ is the quencher concentration, I_F and I_F^0 are the intensity of fluorescence emission in the presence and in the absence of the quencher, respectively. Equation 4.14 is only valid if the fluorophore absorbance at the excitation wavelength is the same whatever the concentration of the quencher, and if all the experimental parameters don't change within a series of measurements. The slope of the plot is equal to the Stern-Volmer coefficient, that is:

$$K_{SV}^S = \frac{k_q^S}{k_F} \quad 4.15$$

From the results obtained with this quenching analysis it emerged that the S_1 states of compounds **1-4** and **DCA** are very efficiently quenched by triethylamine (data in Table 11),²⁰⁵ indicating a very fast formation of $PS^{\bullet-}$ and $Et_3N^{\bullet+}$. The Stern-Volmer constants, as well as the rate constants of singlet excited state quenching, are of the same order of magnitude for compounds **1**, **3** and **4**. Compound **2** reacts in its ground state with amines to yield the carboxylate and the corresponding ammonium cation, and the radical anion cannot be formed. For **1**, **3** and **4**, the values of the quenching rate

constant k_{q,Et_3N}^S are close to those of a diffusion-controlled process, in agreement with the corresponding large ΔG (Table 11). With the exception of **2**, all the PSs in their singlet excited state S_1 can react with suitable electron donors, generating thus radical pairs able to induce ELT cascade reactions. In the presence of such substrates the ELT pathway should be taken into account as a photochemical mechanism alternative to singlet oxygen production. Moreover, all the photoinduced PS radical anions (formed by ELT in the presence of suitable donors) have reduction potentials negative enough to reduce ground state oxygen to the superoxide radical anion ($E_{(O_2/O_2^{\cdot-})} = -0.58$ V vs. SCE in ACN, equation 1.16).^{16,17} The free energy changes corresponding to the redox reaction between the PS radical anions and oxygen (equation 1.04), to yield the PS in the ground state and superoxide radical anion are reported in Table 11: for all the PSs this reaction is exergonic, with values of $\Delta G_{O_2^{\cdot-}}$ in a quite narrow range, between -23.0 and -33.0 kJ mol⁻¹ (for **DCA** and **1**, respectively). This assertion is in agreement with the observation that complete oxygen elimination was necessary to obtain reversible electrochemical peaks. Therefore, production of the superoxide anion, in competition with singlet oxygen, should be taken into account in the photosensitized oxidation of substrates with adequate oxidation potentials (< approx. 2.1 V vs SCE).

6.0 CONCLUSIONS

From the results presented in this chapter, it emerges that the functionalization of **DBTP** by either a carboxylic or an amide function has no strong effects on the spectroscopic properties of the chromophore. Absorption and emission spectra remain almost identical for all compounds, as well as fluorescence lifetimes and fluorescence quantum yields. Also, the triplet excited state has been confirmed for all compounds as the only transient species formed upon irradiation. All the spectroscopic properties of these compounds vary in very narrow ranges. The quantum yields of singlet oxygen production are much higher for compounds **1-4** (between 0.65 and 0.95) than for **DCA** (0.30) under the same conditions. Noteworthy, for compounds **1** and **2**, Φ_Δ was found very close to that of perinaphthenone. The detailed spectroscopic characterization we carried out allowed a fine analysis of the photosensitization mechanisms involved with **DBTP**-dyes and **DCA**. We showed that, contrary to **DCA**, for which intersystem crossing is highly disadvantaged, **DBTP** and its derivatives populate very efficiently the triplet excited state (quantum yield of triplet formation between 0.84 and 0.88). Deactivation of the triplet state of **1-4** by O_2 results in a quantitative energy transfer to yield 1O_2 . In the case of **DCA**, singlet oxygen is mainly produced from the singlet excited state of the PS, with a smaller contribution corresponding to the PS triplet excited state formed by enhanced intersystem crossing. Our results stress that the two additional aromatic cycles on the cyanoanthracene core have a much greater influence on the photosensitizing properties than the substituents on the **DBTP** structure. The greatest difference that could be highlighted in the series corresponded to compound **2**, which presented a rate constant of singlet oxygen quenching by the PS one order of magnitude larger than the other **DBTP** derivatives. This difference probably arises from a higher charge transfer character in the collision complex formed between 1O_2 and the PS ground state. It should be noted that, besides singlet oxygen production, compounds **1**, **3** and **4** in their excited state can abstract electrons from suitable electron-donating substrates. This process may provide another pathway for photooxidation processes, competing with 1O_2 mediated oxygenation. Again, only for compound **2** the results deviated from the other PSs of the series: the

electrochemically induced one-electron reduction carried out to obtain the radical anion resulted in a totally irreversible reaction. Probably the redox reaction resulted in the degradation of the dye, preventing any further use of the PS. Since it cannot photosensitize ELT reactions, compound **2** represents a good PS for singlet oxygen generation in ACN solutions: if used in the good concentration to minimize $^1\text{O}_2$ quenching by the PS it can be really efficient, stable under irradiation and selective. If **2** is considered as a starting compound for grafting **DBTP**, in reverse, all these considerations become trivial, since once grafted (or modified to produce other derivatives such as compounds **3** and **4** or similar) compound **2** loses the COOH group, which is responsible of these differences relative to the other compounds of the series. As a consequence of grafting, the carboxylic group is converted to, for instance, an amide function. The latter, as it has been shown in this chapter, has no significant effect on the overall photosensitizing process.

In summary, compounds **1-4** show several interesting characteristics:

- ~ their overall photophysical properties do not significantly change with chemical functionalization, opening the route for the development of different derivatives, adapted to various applications
- ~ they are stable under irradiation
- ~ they absorb in the visible and solar light could be used for their activation
- ~ they have high quantum yields of singlet oxygen production
- ~ except for **1**, they could be easily grafted on inert supports (*e.g.* silica or polystyrene), thanks to chemical modifications.

Therefore, these compounds are very good candidates for the preparation of visible-light photo-active materials that could be useful for photochemical applications at gas-solid and liquid-solid interfaces in different fields. The applications are however limited due to their absorption close the UV region of the spectrum: compounds **1-4** could not be used for applications in medicinal chemistry for PDT. They represent on the contrary perfect candidates for applications in fine chemistry and depollution/bactericidal processes, due to their high resistance under irradiation.

5 Phenothiazines: photophysical characterization in solution

Phenothiazines (PTZs) represent a very interesting class of molecules, with suitable properties for several widespread applications. Methylene blue (**MB**⁺) is probably the most well-known commercially available PZT photosensitizer: its photophysical behavior has been studied in detail, it efficiently produces singlet oxygen (quantum yields of singlet oxygen production, Φ_{Δ} , between 0.37 and 0.70),³¹ it is non-toxic and it absorbs light at 650 nm, which makes it suitable for photodynamic inactivation (PDI) of viruses and bacteria in blood fractions, notably for plasma sterilization, and for photodynamic therapy (PDT).^{62–65,128,129,139,142} Many PZT derivatives can be readily prepared to tune the photosensitizing properties of the dye. Among other phenothiazines, methylene violet (**MV**) and new methylene blue (**NMB**⁺), which have been studied during the last 15 years for potential applications in biology, showed interesting preliminary results. Relative to **MB**⁺, **NMB**⁺ has a higher Φ_{Δ} (1.35 taking **MB**⁺ as a reference) and, being more lipophilic, it has an enhanced intracellular PDT activity.^{63,187} **NMB**⁺ is non-toxic in the dark and it presents a good activity against highly drug-resistant organisms.^{190,191,206} **NMB**⁺ has been embedded in several polymeric matrices for ¹O₂ production.⁶⁴ **MV** can form singlet oxygen by energy transfer with relatively high efficiency ($\Phi_{\Delta} = 0.7$ in buffered solution, relative to **MB**⁺)¹²⁸ and it has a particular affinity towards DNA which makes it a good PS for photodynamic therapy.^{192,193} Some graftable **MV** derivatives have been prepared, and enhanced singlet oxygen production was achieved by adding iodine atoms on its structure.^{128,194} The spectroscopic properties of **MV**, partially presented by Otsuki and Taguchi in 1996,¹⁹⁵ seem to strongly depend on the solvent.

Good PSs of the PZT family could easily find applications: synthesis and functionalization of methylene blue derivatives, aimed at the development of photosensitizing materials, can be easily carried out. For such applications, a deep knowledge of their photochemical and photophysical properties, and of the effects that different media could have, is necessary. Fundamentals on their photophysics missing, we studied in detail the spectroscopic behavior (UV-Vis and fluorescence spectroscopy) of **MV** and **NMB**⁺, relative to rose bengal (**RB**, Φ_{Δ} between 0.68 and 0.95)^{31,67,196} and methylene blue. Their transient species were detected and analyzed (relative to the parent compound **MB**⁺) and their efficiency of ¹O₂ generation was compared under identical conditions. All these analyses were carried out in different solvents to investigate any solvatochromic effect on the overall photophysics of these dyes. **MV** showed a particular sensitivity towards the solvent and its properties have been analyzed in more detail to point out possible influences in its reactivity.

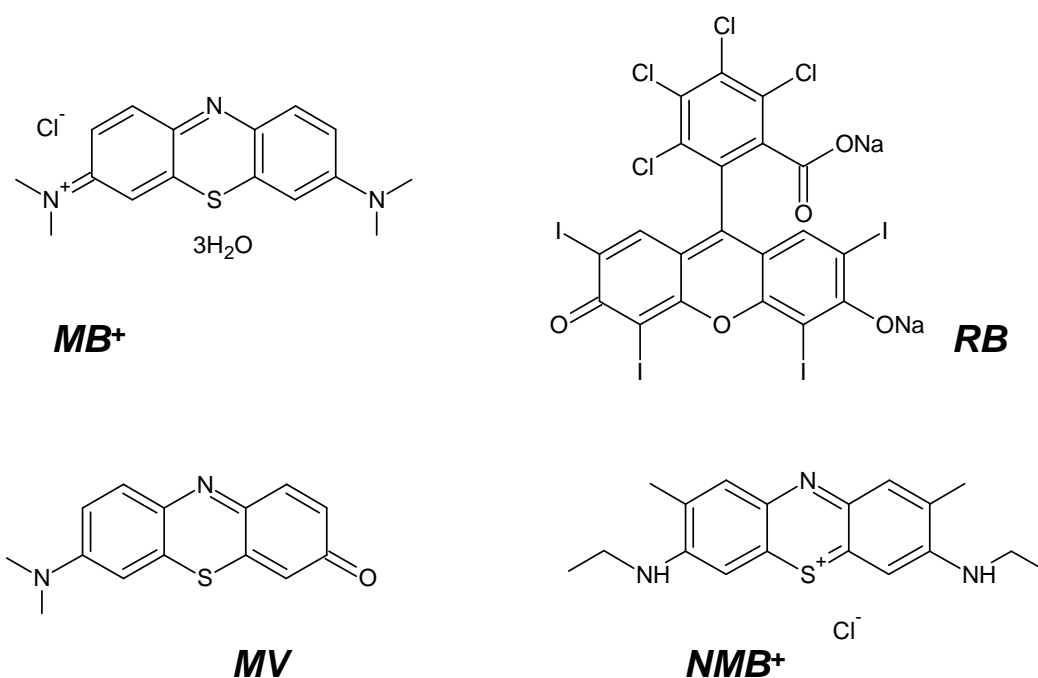


Chart 11 Chemical structure of methylene blue (**MB⁺**), rose bengal (**RB**), methylene violet (**MV**) and new methylene blue (**NMB⁺**).

1.0 UV-VIS AND FLUORESCENCE SPECTROSCOPY

1.1 **NMB⁺** and **MV**

The absorption spectra in MeOH and ACN of the two PSs under study and of the two reference dyes are reported in Figures 31 and 32. As far as **NMB⁺** is concerned no significant influence of the solvent on the position of the absorption bands is noticed, with a shift of approx. 3 nm of the maximum around 630 nm. On the contrary, the solvent effect on the molar absorption coefficient is remarkable: ϵ_{\max} in MeOH is almost double of that in ACN (Table 12). The shoulder positioned at approx. 500 nm which is more intense in ACN than in MeOH, relatively to the maximum of absorption at 630 nm, is probably due to the presence of an impurity which is more soluble in aprotic solvents. The absorption spectrum and the molar absorption coefficient of **NMB⁺** in MeOH and ACN are similar to those of **MB⁺**, as could be expected from the similar structures.

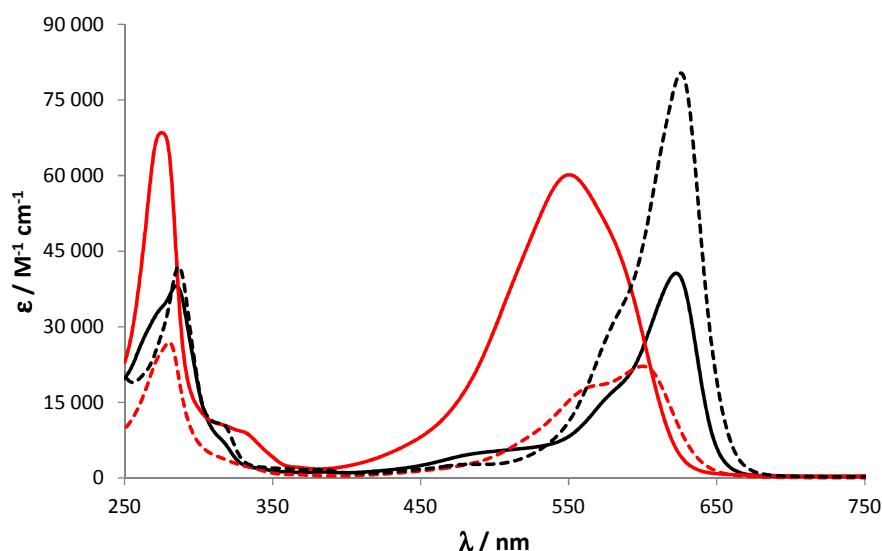


Figure 31 UV-Vis electronic spectra of **MV** (red) and **NMB⁺** (black) in ACN (solid lines) and MeOH (dashed lines).

For **MV** the shape of the spectrum, the position of the bands and the molar extinction coefficient change significantly from ACN to MeOH. In ACN the spectrum is characterized by a large unstructured band with a maximum at approx. 550 nm; in MeOH the band is more structured with a maximum at approx. 600 nm and shows a shoulder at approx. 565 nm. Relative to ACN, in MeOH the molar absorption coefficient is reduced by approx. a third at the absorption maximum. The absorption spectrum in MeOH for **MV** is close to the spectra recorded for **MB⁺** and **NMB⁺**, suggesting the presence of different absorbing species, depending on the solvent. Strong solvatochromic effects depending on the solvent have already been reported: **MV** absorbs at approx. 550 nm and 600 nm in non-polar and polar solvents, respectively, and it is considered responsible of the absorption band at approx. 500 nm observed after treating **MB⁺** with alkalis in toluene.^{60,298–300} According to these striking preliminary observations, the spectroscopic behavior of **MV** has been studied in detail (see below).

In Figure 33 the fluorescence emission spectra of **NMB⁺** and **MV** in both MeOH and ACN are reported and compared to those of **RB** and **MB⁺**. The emission spectrum of **NMB⁺** is slightly sensitive to the solvent: the maximum shifts from 642 to 653 nm from ACN to MeOH. In Figure 34, the rather unstructured excitation and emission bands of **NMB⁺** can be observed in both solvents. As far as the excitation spectra are concerned, they coincide with the absorption spectra reported above and no visible differences with the solvent are noticed.

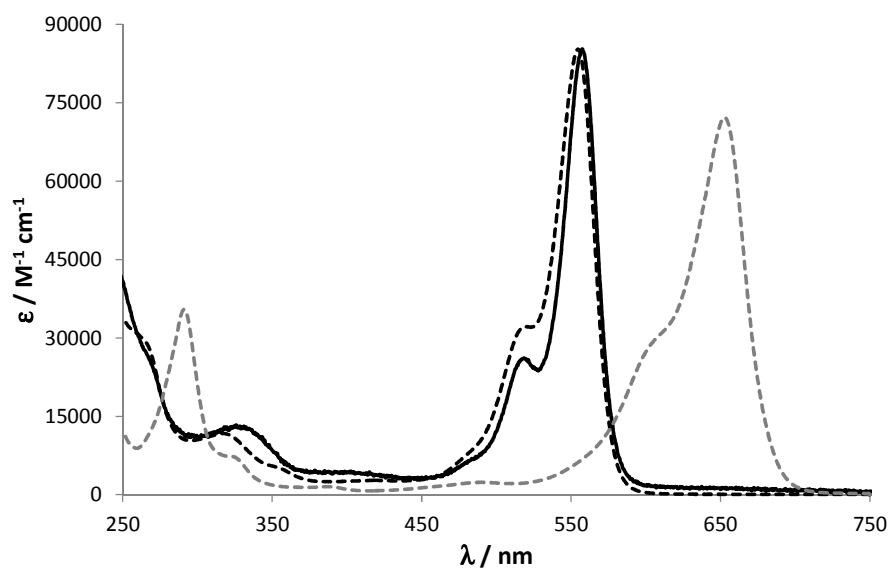


Figure 32 UV-Vis electronic spectra of RB (black) and MB^+ (grey) in ACN (solid lines) and MeOH (dashed lines).

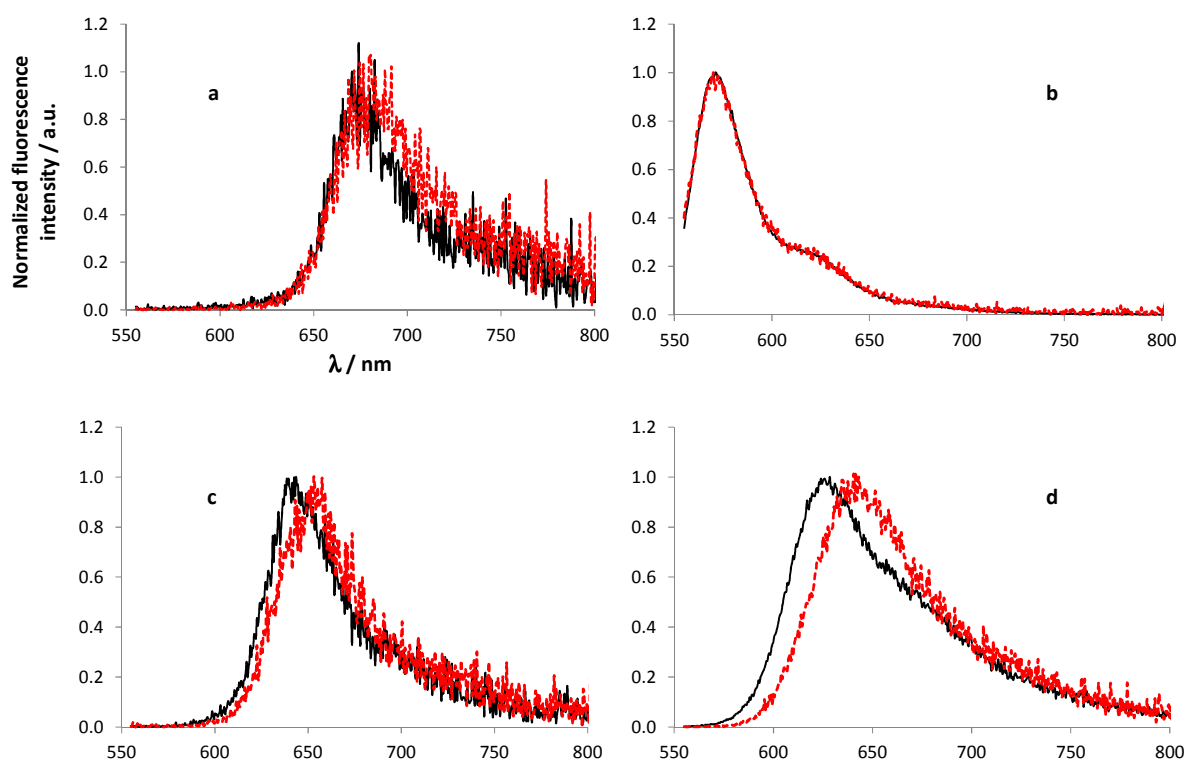


Figure 33 Fluorescence emission ($\lambda_{\text{ex}} = 550 \text{ nm}$) spectra of MB^+ (a), RB (b), NMB^+ (c) and MV (d) in ACN (black solid lines) and MeOH (red dashed lines). Air-equilibrated solutions at room temperature.

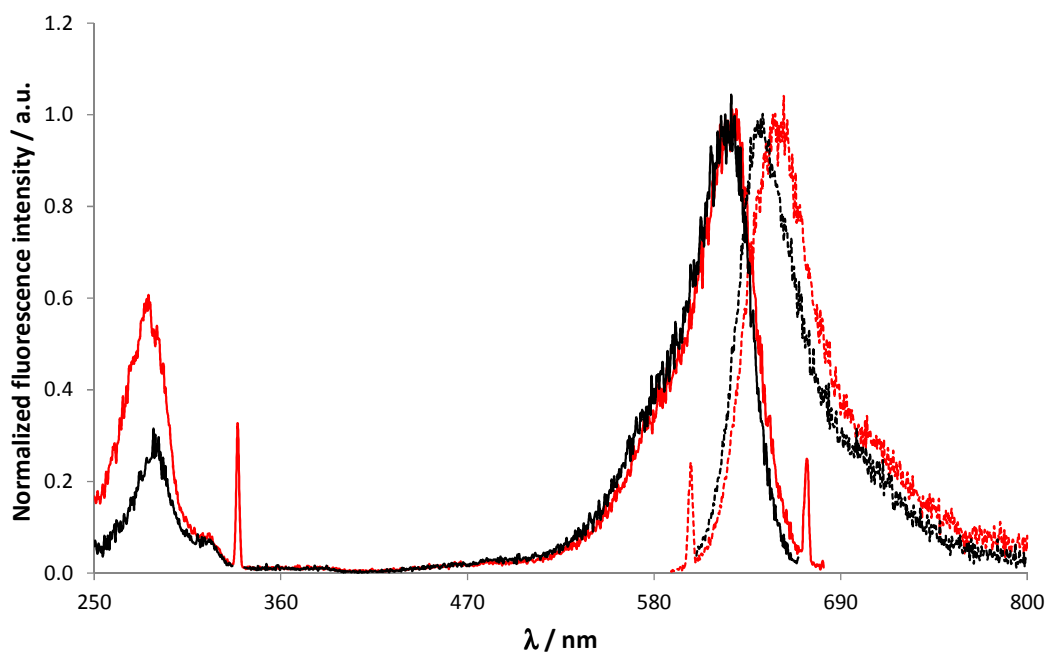


Figure 34 Fluorescence excitation ($\lambda_{em} = 670$ nm) and emission ($\lambda_{ex} = 600$ nm) spectra of NMB⁺ in MeOH (red) and ACN (black).

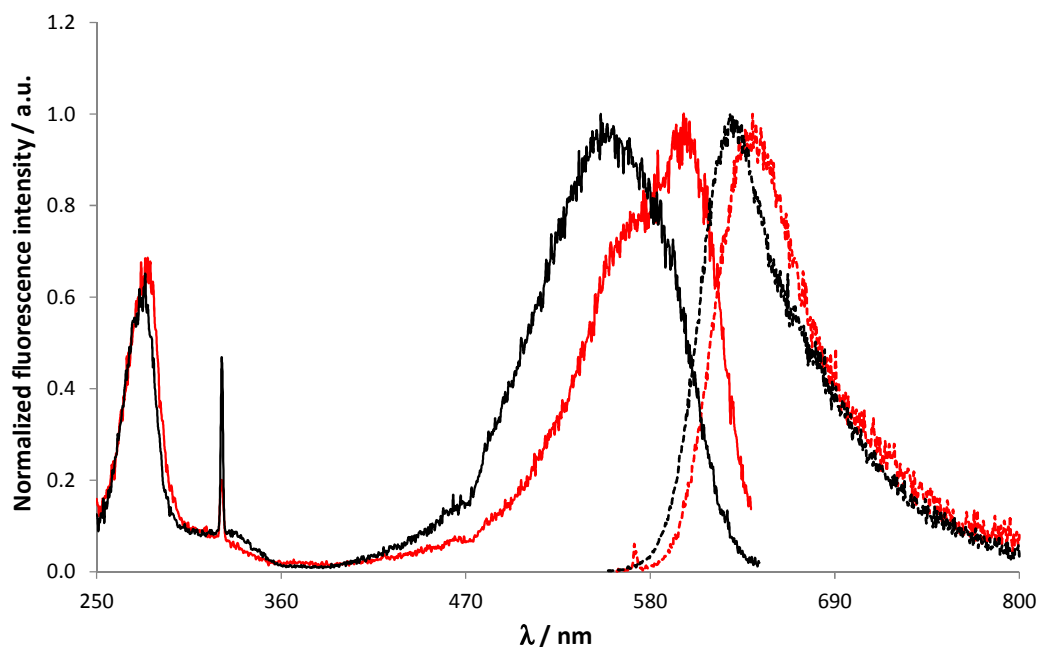


Figure 35 Fluorescence excitation ($\lambda_{em} = 650$ nm) and emission ($\lambda_{ex} = 550$ nm) spectra of MV in MeOH (red) and ACN (black).

For **MV** (Figure 35), the solvatochromic effects are more important. Relative to MeOH, the emission band recorded in ACN is larger and 15 nm blue-shifted. The excitation spectra are also different and correspond to the absorption bands observed in ACN (broad, λ_{\max} 550 nm) and MeOH (structured narrower band, λ_{\max} 600 nm). The Stokes shift is larger in acetonitrile (approx. 70 nm) than in methanol (approx. 40 nm). The photophysical behavior of **MV** may be assigned to the presence of two absorbing species, respectively yielding two fluorescent excited states.

The fluorescence quantum yields and lifetimes of the four PSs in ACN and MeOH are reported in Table 12. For the Φ_F calculations (equation 3.09), **MB⁺** in MeOH was selected as a reference ($\Phi_F = 0.03$).²⁴³ Except for **RB** in ACN ($\Phi_F = 0.20$), all the PSs showed Φ_F lower than 0.1. For **MB⁺** and **NMB⁺** the values are in a very narrow range, between 0.03 and 0.05, with slight differences induced by the solvent. Dramatic differences depending on the solvent emerged on the contrary for **RB** and **MV**: in ACN their quantum yields of fluorescence are respectively five and three times higher than in MeOH. Fluorescence lifetimes were very short in both ACN and MeOH: very rapid intersystem crossing from the singlet to the triplet excited state can account for this behavior.⁵⁹ In MeOH, τ_F is shorter than 700 ps for all PSs; in ACN values are slightly higher, notably for **MV**, which shows a fluorescence lifetime three times higher (1.49 vs 0.50 ns) in the latter solvent. For **MB⁺** we recorded slightly higher τ_F in ACN than in MeOH, while in the case of **NMB⁺** the difference is almost negligible.

Table 12 Wavelengths of absorption maximum (λ_{\max}), molar extinction coefficients at the absorption maximum (ϵ_{\max}), wavelengths of fluorescence emission maximum ($\lambda_{\max,em}$), fluorescence quantum yields (Φ_F) and fluorescence lifetimes (τ_F) in MeOH, ACN and the ratio of the values measured in MeOH and in ACN (only for Φ_F and τ_F) for the four PSs under study. Air-equilibrated solutions at room temperature.

^{a)} Errors: approx. 10%.

		RB	MB⁺	NMB⁺	MV
$\lambda_{\max} / \text{nm}$	<i>MeOH</i>	555	654	625	600
	<i>ACN</i>	557	655	622	549
$\epsilon_{\max} / \text{M}^{-1} \text{cm}^{-1\text{a}}$	<i>MeOH</i>	85250	72100	72000	21600
	<i>ACN</i>	85000	-	40600	60100
$\lambda_{\max,em} / \text{nm}$	<i>MeOH</i>	571	670	642	642
	<i>ACN</i>	571	670	653	628
Φ_F	<i>MeOH</i>	0.04 ± 0.01	0.03 ²⁴³	0.04 ± 0.01	0.03 ± 0.01
	<i>ACN</i>	0.20 ± 0.02	0.05 ± 0.01	0.04 ± 0.01	0.09 ± 0.01
	<i>MeOH:ACN</i>	0.2	0.60	1.00	0.33
τ_F / ns	<i>MeOH</i>	0.44 ¹⁹⁶	0.60 ± 0.05	0.70 ± 0.06	0.50 ± 0.05
	<i>ACN</i>	-	1.01 ± 0.10	0.86 ± 0.06	1.49 ± 0.10
	<i>MeOH:ACN</i>	-	0.59	0.81	0.34

Except for **MV**, the spectroscopic properties of these PSs do not seem strongly influenced by the solvent. All the dyes, once the singlet excited state reached, undergo intersystem crossing very efficiently.

1.2 MV solvatochromism

Relative to the other phenothiazine dyes, the spectroscopic properties of **MV** appeared peculiar. The solvatochromism effect on its absorption and fluorescence properties was striking and analyzed in more detail. Moreover, the effects induced by the addition of acids on the absorption spectra of **MV** were considered. Quantum chemical calculations, carried out by Patrice Bordat, has been used as a support to confirm the hypothesis proposed on the basis of spectroscopic experimental data.

1.2.1 UV-Vis spectroscopy in different solvents

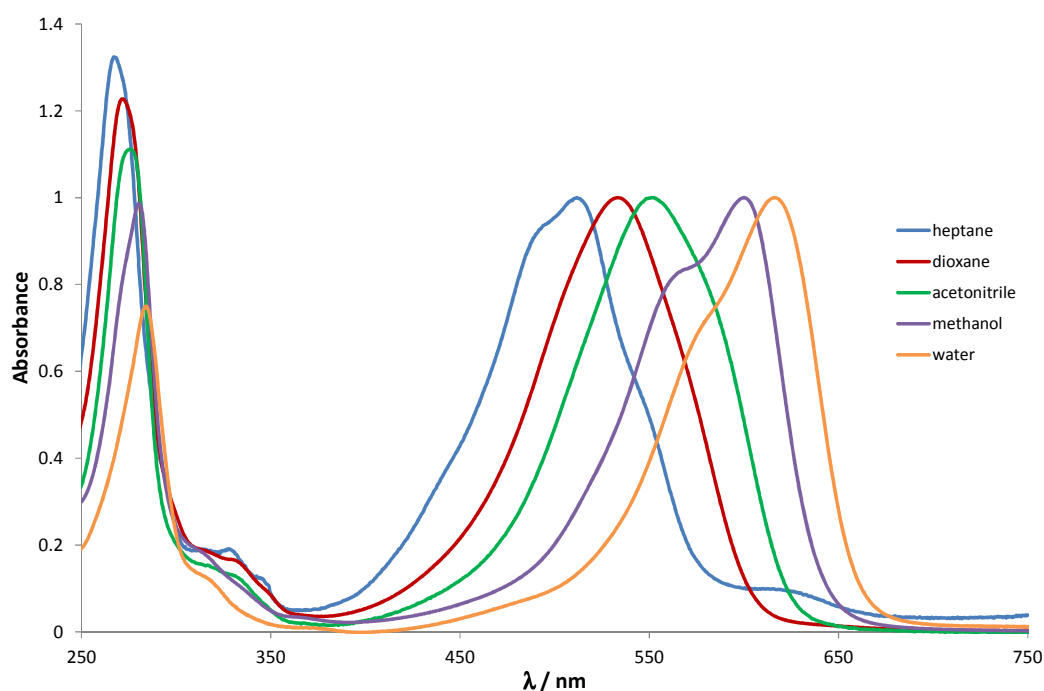


Figure 36 Normalized absorption spectra of **MV** in various solvents: *n*-heptane (blue line), dioxane (red line), acetonitrile (green line), methanol (purple line) and water (orange line). Air-equilibrated solutions at room temperature ($\ell = 1$ cm, quartz cells).

In Figure 36 the absorption spectra of **MV** in various solvents (*n*-heptane, dioxane, acetonitrile, methanol, water) are reported. The wavelengths of the UV maxima are between 270 nm (*n*-heptane) and 286 nm (water) and the band intensities, relative to the normalized absorption band in the visible region, also decrease from *n*-heptane to water. In the visible the differences are much more important (Figure 37). In *n*-heptane the absorption band is quite structured, with a maximum at 512

nm. A shoulder at higher wavelengths is also present: it could arise from impurities soluble only in non-polar solvents or from the formation of dimers, due to the low solubility of the dye in non-polar solvents. In polar solvents, *i.e.* triethylamine, dioxane and acetonitrile, we find the broad absorption band already described (for ACN). The position of λ_{max} depends on the solvent: between Et₃N and ACN the shift is approx. 26 nm. The absorption band in DMF (λ_{max} at 558 nm), similar to the one observed in dioxane or ACN, has a shoulder at higher wavelengths, approx. 585 nm, which could represent the beginning of the red-shifted absorption band noticed in slightly protic solvents such as MeOH and EtOH. In MeOH (Figure 36), as reported in the previous paragraph, a first shoulder at approx. 575 nm is followed by a more intense maximum at 600 nm. In water, the absorption band is even more red-shifted: λ_{max} is at 616 nm (Figure 37). A shift in the position of the absorption maximum of more than 100 nm passing from *n*-heptane to water was thus observed.

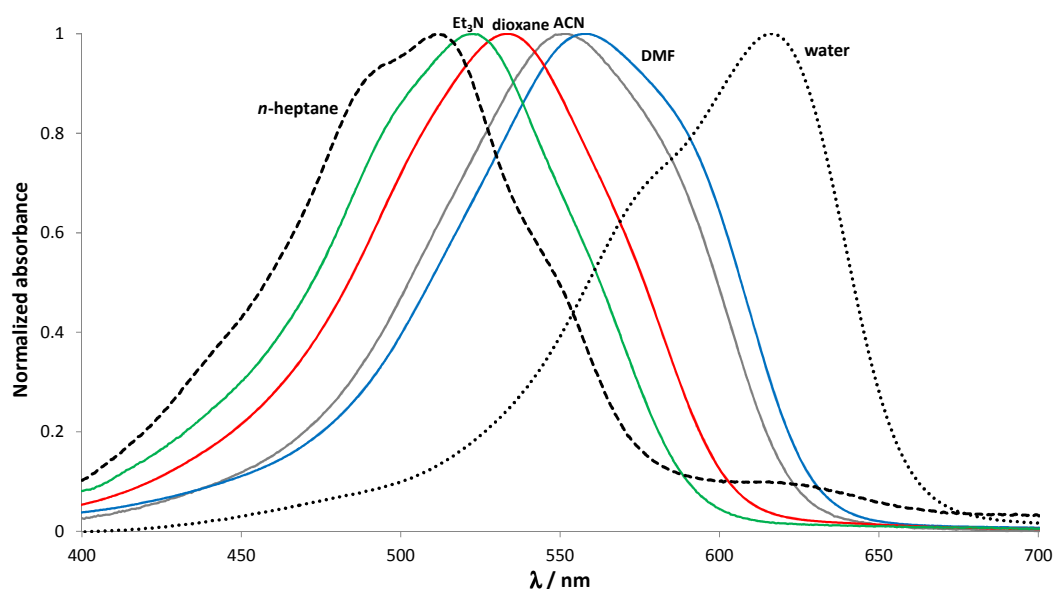
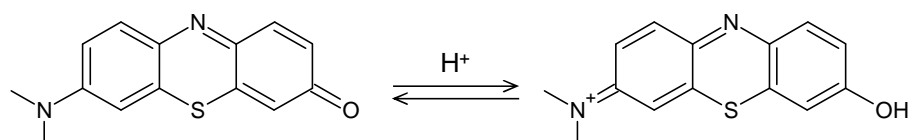


Figure 37 Normalized absorption spectra (400-700 nm range) of MV in various solvents: *n*-heptane (black dashed line), triethylamine (green line), dioxane (red line), ACN (grey line), dimethylformamide (blue line) and water (black dotted line). Air-equilibrated solutions at room temperature ($\ell = 1$ cm, quartz cells).

Table 13 Wavelengths of absorption maximum (λ_{\max}) and corresponding energy of the singlet excited state (E_s) for **MV** in several solvents; properties of the solvents: hydrogen bond donation ability (α), hydrogen bond acceptance (β), polarity/polarizability coefficient (π^*), Dimroth-Reichardt's polarity ($E_T(30)$), Dimroth-Reichardt's normalized polarity (E_T^N , see equation 5.02) and sum of all the mentioned parameters (XYZ, see equation 5.01). Values taken from:³⁰¹.

	λ_{\max} / nm	E_s / kJ mol ⁻¹	α	β	π^*	$E_T(30)$	E_T^N	XYZ
<i>n</i>-heptane	512	232	0	0	-0.08	31.1	0.01	-0.07
Et₃N	523	229	0	0.71	0.14	32.1	0.04	0.89
CCl₄	524	228	0	0.10	0.28	32.4	0.05	0.43
Et₂O	528	227	0	0.47	0.27	34.5	0.12	0.86
toluene	531	225	0	0.11	0.54	33.9	0.10	0.75
dioxane	533	225	0	0.37	0.55	36.0	0.16	1.08
AcEt	535	223	0	0.45	0.55	38.1	0.23	1.23
THF	539	222	0	0.35	0.58	37.4	0.21	1.14
acetone	546	219	0.08	0.43	0.71	42.2	0.35	1.57
ACN	549	218	0.19	0.40	0.75	45.6	0.46	1.80
CH₂Cl₂	550	218	0.13	0.10	0.82	40.7	0.31	1.36
CHCl₃	552	217	0.20	0.10	0.58	39.1	0.26	1.14
pyridine	556	215	0	0.64	0.87	40.5	0.30	1.81
DMF	558	214	0	0.69	0.88	43.7	0.40	1.97
DMSO	578	207	0	0.76	1.00	45.1	0.44	2.20
EtOH	597	200	0.86	0.75	0.54	54.0	0.72	2.87
MeOH	600	199	0.98	0.66	0.60	60.0	0.90	3.14
H₂O	616	194	1.17	0.47	1.09	63.1	1.00	3.73

Otsuki and Taguchi¹⁹⁵ found a correlation between λ_{\max} and the polarity/polarizability parameter (π^*) of the solvent: they suggested thus the presence of two absorbing species, identified as two rotational conformers of **MV**, non-twisted (low π^*) and twisted (high π^*). Such a rotation would occur around the C-N bond of the dimethylamino group. In addition, a third absorbing state of **MV** would derive from the protonation on the carbonyl group in acidic media (Scheme 17).



Scheme 17 Protonation of the carbonyl group of **MV** in the presence of acids yielding **MV-OH**.

In Table 13 the wavelengths of the absorption maxima in several solvents are reported, together with the corresponding singlet excited state energy and some solvent characteristics necessary for the understanding of these particular features of **MV** in solution. The correlation between the λ_{\max} of **MV** and the solvents' properties depends on the parameters of the solvent taken into account. If we consider the only polarity/polarizability parameter (π^*) we could identify two different species: all the tested solvents follow the same linear correlation, except for protic solvents (ethanol, methanol and water) (Figure 38). Our result seems thus consistent with those reported in the literature.¹⁹⁵

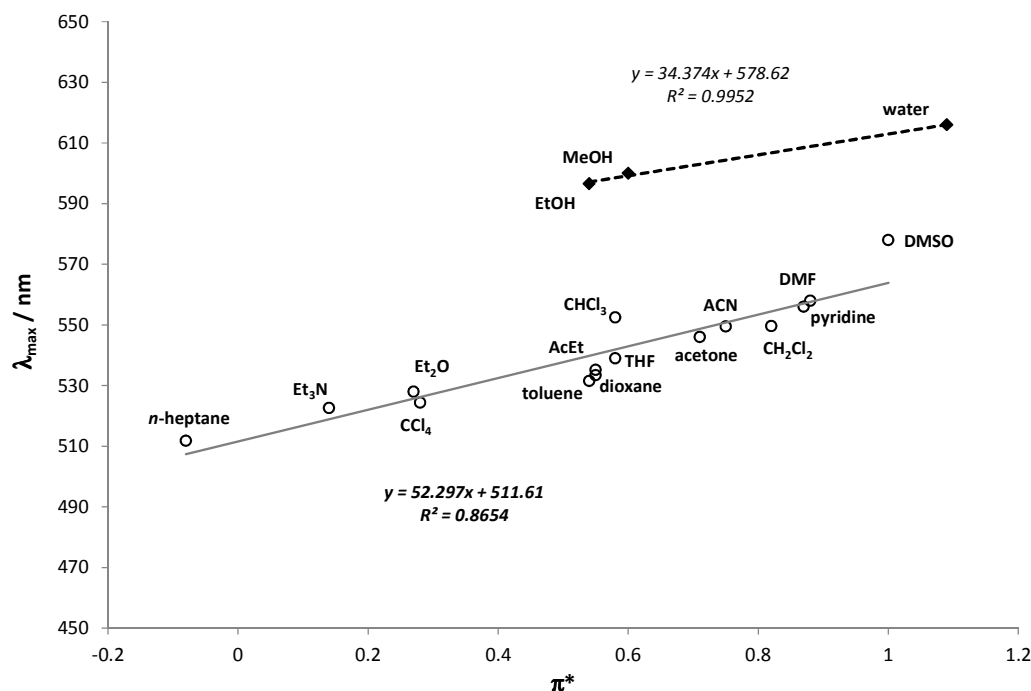


Figure 38 Variation of the absorption maximum wavelength of **MV** as a function of the polarity/polarizability parameter (π^*) of the solvent; different correlations were found for aprotic (grey solid line, grey empty circles) and protic (black dashed line, black diamonds) solvents.

We also studied the variation of the absorption maximum wavelength as a function of other parameters: hydrogen bond donation ability (α), hydrogen bond acceptance (β), polarity (considering the Dimroth-Reichardt's scale, $E_T(30)$)^{302,303} and a global parameter (XYZ) calculated as the sum of all the previously considered ones, following the theory developed by Kamlet and Taft.^{301,304–308}

$$XYZ = a\alpha + b\beta + s\pi^* + \dots \quad 5.01$$

where a , b and s are solvent-independent coefficients. To be applied to this model, polarity values $E_T(30)$ had to be normalized:³⁰¹

$$E_T^N = \frac{E_T(30) - 30.7}{32.4} \quad 5.02$$

where 30.7 is the $E_T(30)$ value of TMS (tetramethyl silane) and 32.4 represents the difference between water and TMS (63.1-30.7). The calculation of the overall function XYZ is however difficult, owing to the determination of the above-reported coefficients, and should not be taken into account in this case.

All the possible correlations (λ_{\max} vs α , β , E_T^N , XYZ) are reported in Figures 39-42.

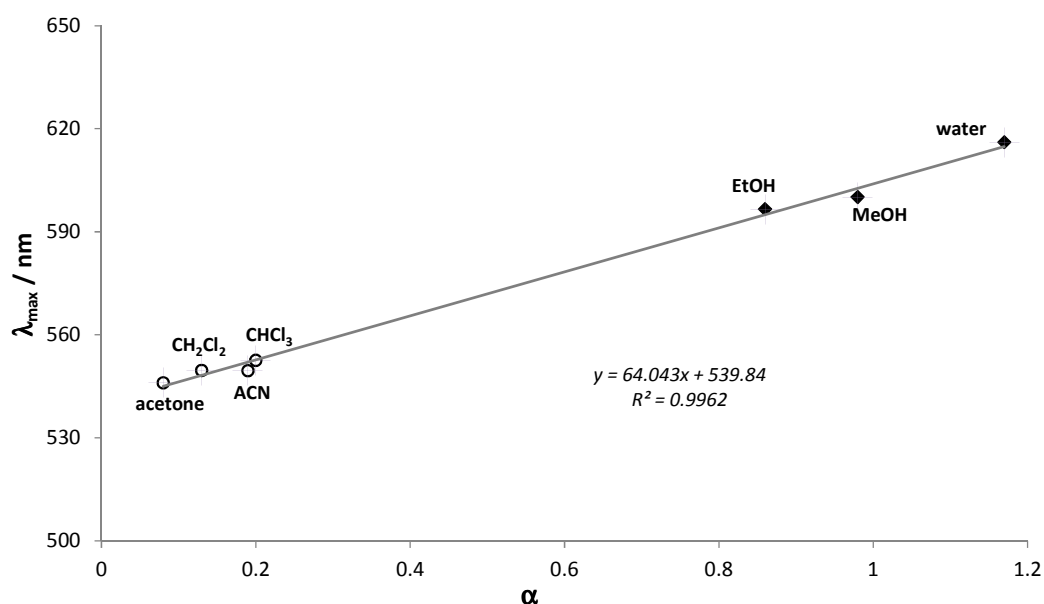


Figure 39 Variation of the absorption maximum wavelength of MV as a function of the hydrogen bond donation ability (α) of the solvent.

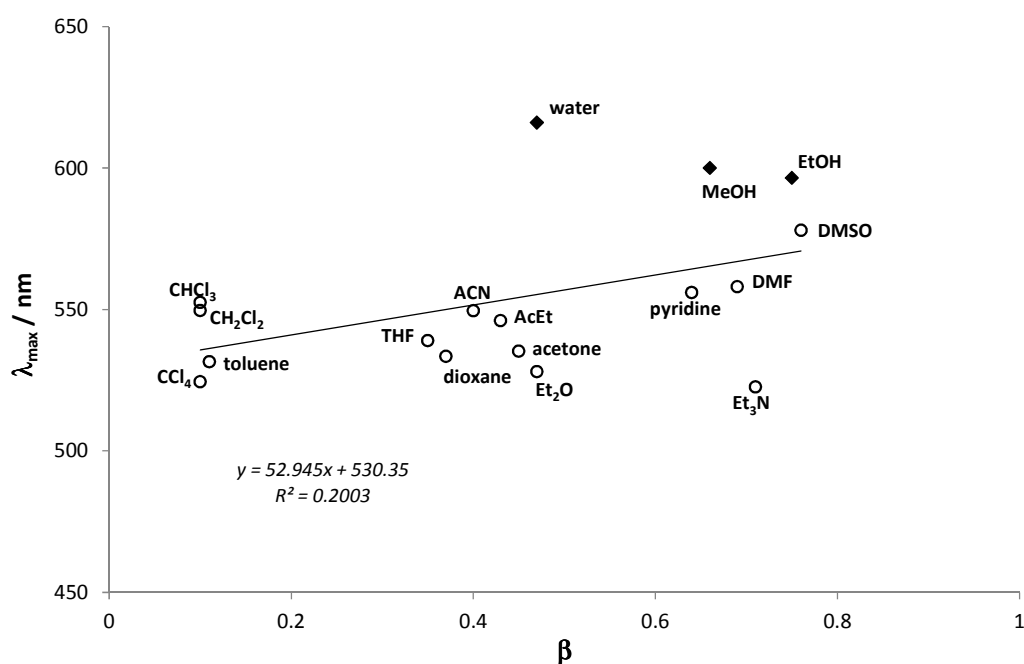


Figure 40 Variation of the absorption maximum wavelength of MV as a function of the hydrogen bond acceptance (β) of the solvent.

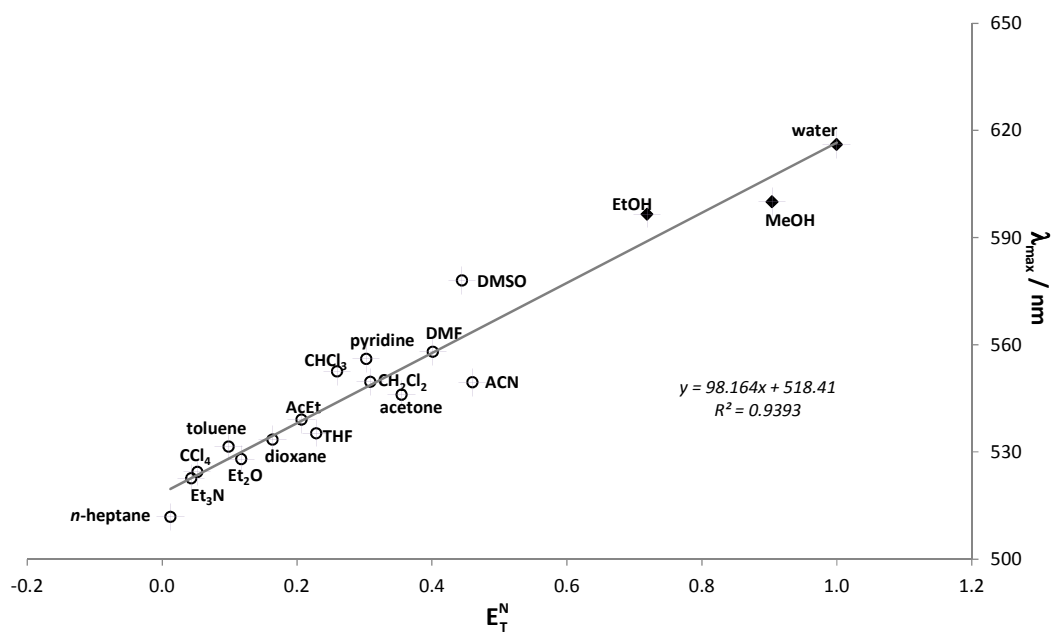


Figure 41 Variation of the absorption maximum wavelength of MV as a function of the normalized Dimroth-Reichardt's polarity (E_T^N) of the solvent; a unique correlation was found for aprotic (grey empty circles) and protic (black diamonds) solvents.

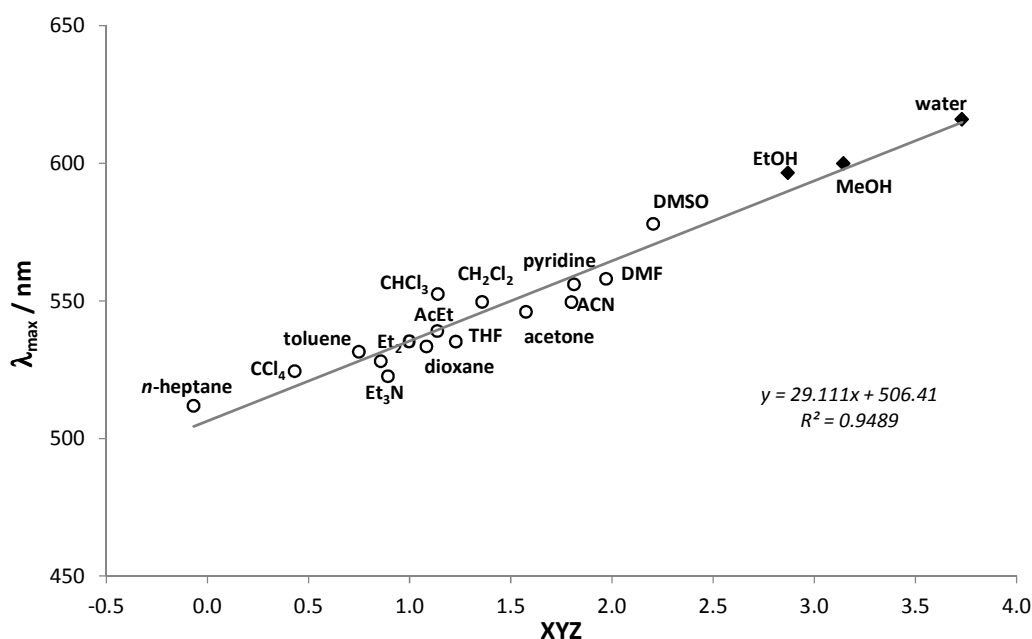


Figure 42 Variation of the absorption maximum wavelength of **MV** as a function of the global parameter (XYZ) of the solvent; a unique correlation was found for aprotic (grey empty circles) and protic (black diamonds) solvents. The determination of the XYZ factor was carried out by considering all the coefficients equal to 1.

For many of the tested solvents α being 0, the linear correlation obtained plotting λ_{\max} as a function of the H-bonding donor character of the solvent (Figure 39) is senseless. Alternatively, the plot of λ_{\max} against the H-bonding acceptance (β) of the solvents, gives the randomly dispersed data reported in Figure 40. The dependency of λ_{\max} on the polarity/polarizability factor (Figure 38) allowed the distinction between protic and non-protic solvents, for both of which linear correlations were found. By reporting λ_{\max} vs the solvent polarity following the Dimroth-Reichardt's scale, a linear plot with a very good correlation factor is obtained (Figure 41); a similar result is obtained by plotting λ_{\max} against the XYZ global factor (Figure 42). Although the relationship between λ_{\max} and the π^* of the solvent cannot be completely neglected, it seems that π^* is overwhelmed by the E_T^N parameter.

1.2.2 Effect of acidity

As already reported (Scheme 17), **MV** is very sensitive to acidic environments. We monitored the variations of the absorption spectrum of **MV** induced by adding small volumes of methanesulfonic acid ($\text{CH}_3\text{SO}_3\text{H}$) to chloroform (CHCl_3) or acetonitrile (ACN) solutions. The case of CHCl_3 is reported in Figure 43. Evidently two reactions take place, the second one occurring at acid concentrations higher than 1 mM (Figure 43, inset). The presence of two species during the first reaction is confirmed by the presence of five isosbestic points. Once the approximated 1 mM concentration of $\text{CH}_3\text{SO}_3\text{H}$ is reached (*i.e.* approx. 20 times more concentrated than **MV**), the second species appears, inducing a decrease of the red-shifted band (formed by the first additions of acid) and the formation of a shoulder at 500 nm. It seems that in CHCl_3 , **MV** undergoes protonation on the carbonyl group

(roughly as for an acid catalyzed enolization) and then, at higher acid concentrations (≥ 1 mM), a second protonation, probably on one of the two nitrogen atoms of the dye takes place.

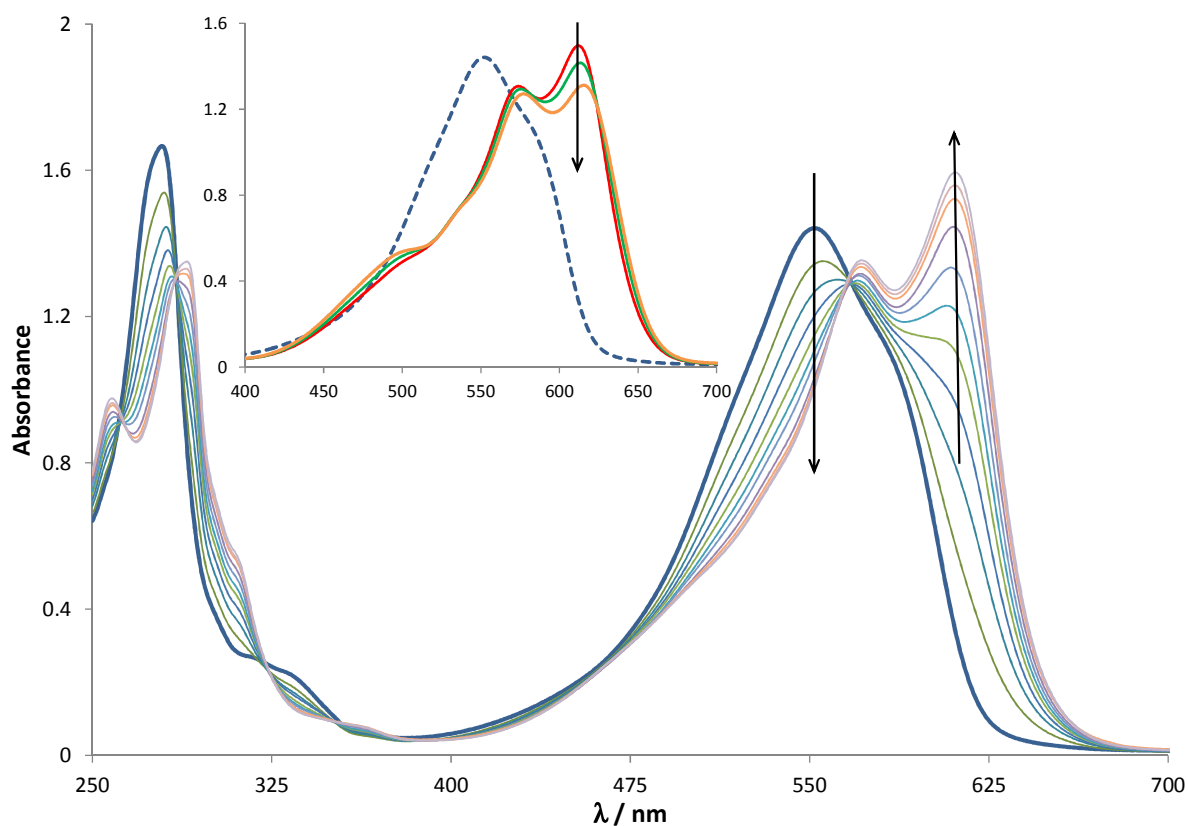


Figure 43 Evolution of the absorption spectrum of **MV** in CHCl_3 for subsequent additions of $\text{CH}_3\text{SO}_3\text{H}$ (2.0×10^{-6} to 5.0×10^{-4} M) ($l = 1$ cm, quartz cells, room temperature). Inset: evolution of the absorption spectrum at higher concentrations of $\text{CH}_3\text{SO}_3\text{H}$ (1.0×10^{-3} to 2.0×10^{-2} M).

In Figure 44 the absorption spectra of **MV** in ACN at different concentration of $\text{CH}_3\text{SO}_3\text{H}$ (1.3×10^{-8} M to 1.4×10^{-5} M) are reported. From this graph it emerges that also in ACN **MV** is very sensitive to small amounts of acid: the first modifications in the spectral band are noticed starting from a $2.5 \mu\text{M}$ concentration of $\text{CH}_3\text{SO}_3\text{H}$. Contrary to chloroform, the five superimposed spectra corresponding to the last five additions of acid (saturation of the spectroscopic signal) suggest that only one protonated species is formed in these experimental conditions; nevertheless, the highest concentration of acid reached for this experiment was much lower than 1 mM (limiting concentration for obtaining the possible di-protonated form in CHCl_3). After the addition of a suitable amount of triethylamine (Et_3N , enough to neutralize the amount of added acid) the absorption spectrum is exactly the same as in neutral ACN: no irreversible chemical reactions take place under these experimental conditions and the solvatochromic effect on **MV** is completely due to the presence of H^+ ions in solution.

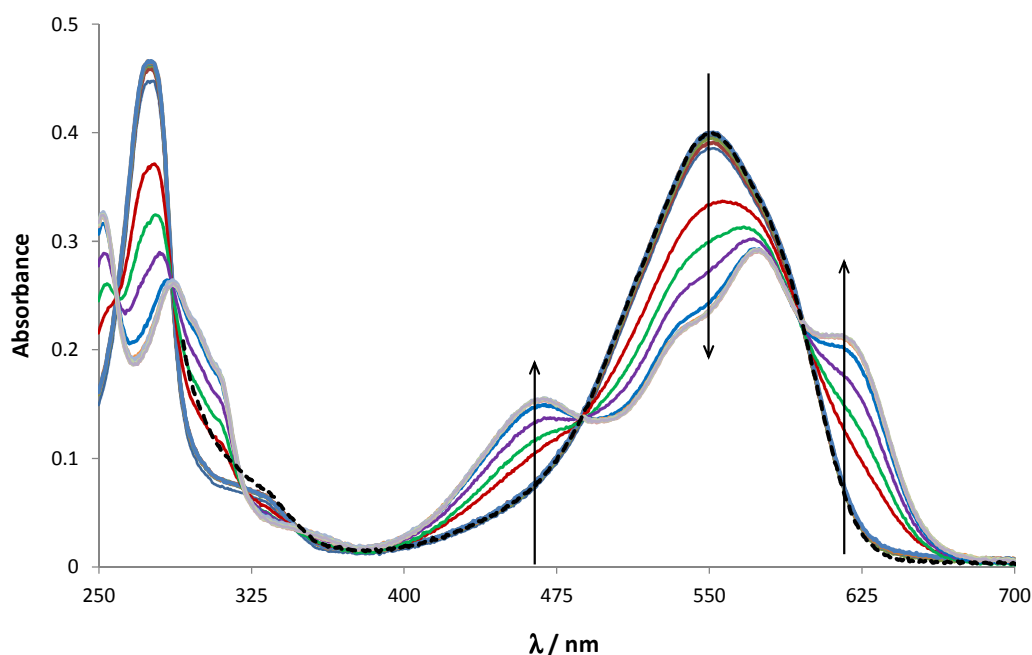


Figure 44 Evolution of the absorption spectrum of **MV** in ACN for subsequent additions of $\text{CH}_3\text{SO}_3\text{H}$ (1.3×10^{-8} to 1.4×10^{-5} M) ($l = 1$ cm, quartz cells, room temperature).

The acid-dependent solvatochromism of **MV** in ACN has been analyzed also by means of fluorescence spectroscopy (Figure 45): increasing amounts of $\text{CH}_3\text{SO}_3\text{H}$ induce a strong decrease of the fluorescence emission intensity and an important bathochromic shift of the band (Figure 45). Consistently to the absorption spectra, the addition of a base (Et_3N) neutralizes the H^+ present in the solution and the final spectrum is completely superimposable to the one recorded before any acid addition. The presence of two different species in ACN and acidified ACN is confirmed by considering fluorescence lifetimes and quantum yields in the two media: the protonated species has a τ_f of 0.35 ± 0.05 ns (against 1.49 ns in ACN) and a Φ_f of 0.01 (vs 0.09 in ACN).

According to Otsuki and Taguchi,¹⁹⁵ two reactions are provoked by the addition of acids to **MV** solutions: at low concentrations of acid, consistently to what observed in high π^* solvents, the twisted conformer is formed, while at higher $[\text{H}^+]$ the carbonyl group is protonated. It seems however more probable that the bathochromically shifted absorption and emission bands observed in slightly protic solvents, relative to polar solvents and somewhat different from the spectra obtained in acidified solutions, suggest that in alcohols and water both uncharged **MV** and its protonated derivative are present: the spectra probably result from the superimposition of the spectra of those two species.

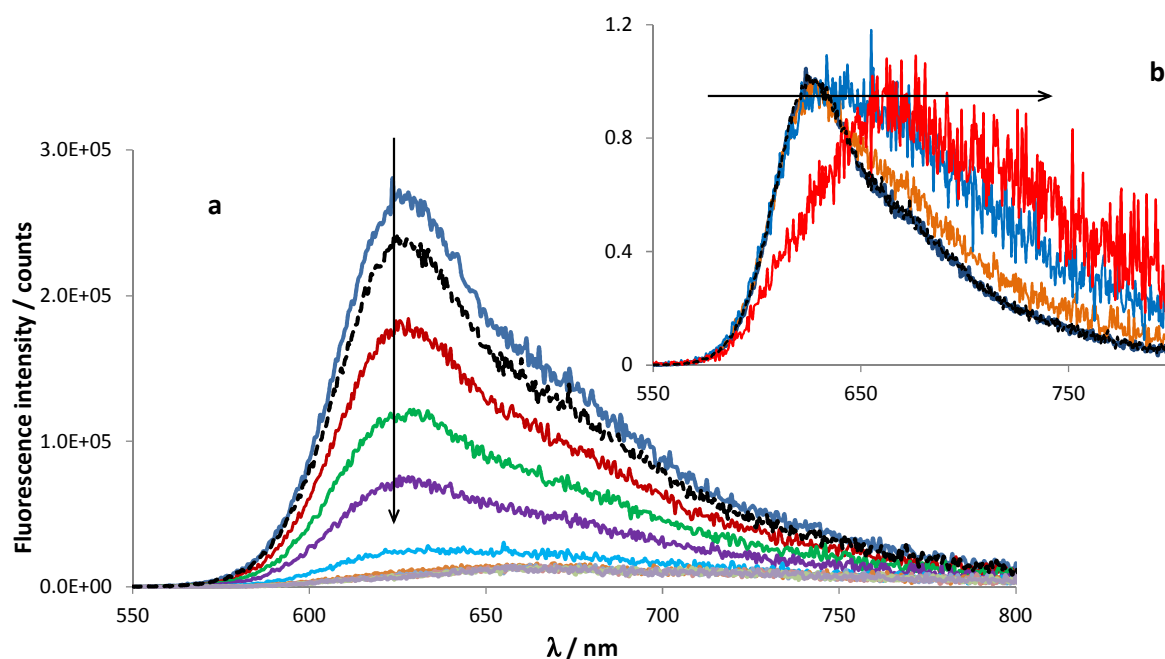


Figure 45 Evolution of the fluorescence emission spectrum ($\lambda_{\text{ex}} = 550 \text{ nm}$) of **MV** in ACN for subsequent additions of $\text{CH}_3\text{SO}_3\text{H}$ (1.3×10^{-8} to $1.4 \times 10^{-5} \text{ M}$). The decrease of fluorescence intensity (a) is pointed out by the arrow; black dashed line: spectrum recorded after addition of Et_3N to neutralize the acid. (b): normalized fluorescence emission spectra at different concentration of $\text{CH}_3\text{SO}_3\text{H}$: the arrow points out the red-shift provoked by acidification of the medium; the black dashed line (addition of Et_3N) shows the reversibility of the process.

1.2.3 Quantum chemical calculations

Quantum chemical calculation have been carried out in order to determine the stable forms (protonated and uncharged) of **MV** in different media and to identify the corresponding main electronic transitions. The aim was to find a correlation between the experimental and the theoretical data, to confirm our hypothesis on the protonation of **MV** in protic solvents. The procedure for geometrical optimization of the structure of **MV** and its protonated forms at the DFT level was carried out with the B3LYP functional and the 6-31G(d) basis using Gaussian09 package. The same calculations were carried out at a more detailed level using the CAM-B3LYP and WB97XD functionals and the 6-311++G(3df,3pd) and AUG-CC-pVTZ basis. The results did not seem to depend on the calculations parameters. Thus, for the TDDFT calculations carried out in order to determine the main electronic transitions of **MV** and its protonated form, the first functional and basis were used. The determination of the electrostatic potential and the polarizability of both the ground and the excited states was necessary to study the solvatochromism of these species.

Structural optimizations of all the possible protonated forms of **MV** were carried out in vacuum and dimethylsulfoxide (DMSO). In both these media the form protonated in position 1 is the most stable (in agreement with literature data),^{60,195} followed by the forms protonated in positions 2 and 3, respectively (Figure 46). We also noticed that the forms protonated in 2 and 3 are much more stable in solution than in vacuum, relative to the form protonated in 1. The uncharged and the 1-

protonated (named **MV-OH** in the following) forms of **MV** are more stabilized in DMSO, relative to vacuum, by approx. 5.7 and 37.6 kcal mol⁻¹, respectively.

The electronic transitions (UV-Vis absorption and fluorescence emission) of **MV** and **MV-OH** have been calculated in vacuum, acetonitrile and acidified (CH₃SO₃H) acetonitrile, as well as in methanol. In Table 14 the transition wavelengths calculated for these media are reported and compared to those measured experimentally. Only the first allowed transitions with non-negligible oscillator strength were taken into account.

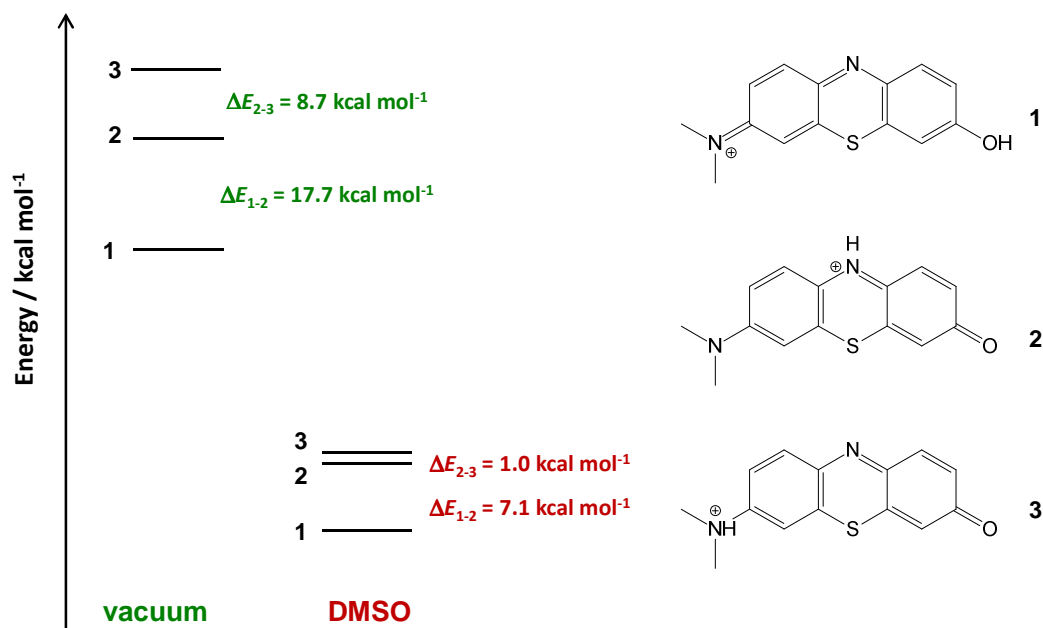


Figure 46 Relative energy levels of the three protonated forms of **MV** in vacuum and DMSO; the numbers refer to the position of the protonation, as indicated in the chemical structures reported.

Table 14 Wavelengths of the first allowed electronic transition (absorption, *abs* and fluorescence emission, *em*) calculated for **MV** and **MV-OH** in vacuum, ACN, acidified ACN and MeOH; Values are compared to those experimentally measured (*exp*).

^{a)} Wavelength of the absorption maximum measured in *n*-heptane.

PS	vacuum		ACN		ACN + CH ₃ SO ₃ H		MeOH	
	$\lambda_{max,abs}$	$\lambda_{max,em}$	$\lambda_{max,abs}$	$\lambda_{max,em}$	$\lambda_{max,abs}$	$\lambda_{max,em}$	$\lambda_{max,abs}$	$\lambda_{max,em}$
MV	508	508	545	619			588	634
MV-OH	532	532			622	676	604	649
MV exp	512 ^{a)}		549	628	620	675	600	642

Concerning the values of λ_{max} in ACN and acidified ACN the calculated and the experimental results are in very good agreement. This confirms that in ACN, by adding H^+ **MV** is protonated on the carbonyl moiety of the dye (**MV-OH**). Noteworthy, the calculated absorption maximum in vacuum and the value measured in *n*-heptane were also very close: this would mean that in non-polar solvents **MV** is similar as in vacuum. In MeOH, experimental values differ from those calculated for both **MV** and **MV-OH**. We could calculate that the experimental absorption and emission signals in MeOH ensue from the superimposition of the two bands of **MV** and **MV-OH**. From the wavelengths of the electronic transitions, the relative contributions to the absorption spectrum recorded in MeOH were estimated at approx. 70% and 30% for **MV** and **MV-OH**, respectively, and for the emission spectrum **MV** and **MV-OH** percentages were calculated to be approx. 59% and 41%, respectively.

Thus, the absorbing species identified by Otsuki and Taguchi¹⁹⁵ as the twisted conformer in solvent with high π^* values, can actually be assigned to the presence of both **MV** and its protonated form **MV-OH**. To confirm our conclusion, additional calculations were carried out in order to determine the feasibility of a rotation around the dimethylamino group. From our results the presence of a rotational isomer (90° rotation around the C-N bond) can be excluded (Figure 47):

- The energetic barrier between the 0° and the 90° conformers was estimated at approx. 14 kcal mol⁻¹ (12 kcal mol⁻¹ by taking into account the nuclei's relaxation) and 17 kcal mol⁻¹ for **MV** in vacuum and in MeOH, respectively
- The 90° conformation represents an energetic maximum
- In MeOH, relative to vacuum, the 0° conformer is more stabilized than the 90° one
- No significant electronic transitions (absorption) of the 90° conformer in vacuum at wavelengths higher than 406 nm were calculated, while the supposed isomer would present an absorption band at approx. 600 nm
- The C-N bond length in **MV** is 1.37 Å, similar to values typical of sp² C=N bonds (1.34 Å in pyridine, 1.37 Å in pyrrole): the C-N bond has thus a partial sp² character and it participates to the overall conjugation of **MV**.

All these arguments are consistent with the above-reported experimental and theoretical results and exclude the presence of two rotational conformers of the dye. **MV** is highly sensitive to the polarity of the medium: only one species is present in aprotic solvents (both non-polar and polar) and its absorption and fluorescence spectra significantly change depending on solvent. Moreover, in slightly protic solvents (water, alcohols) or acidified solutions, the PS is protonated to the **MV-OH** form. At very high $[\text{H}^+]$, a second protonation reaction can occur, probably on the nitrogen atom included in the polycyclic phenothiazine structure (position 2).

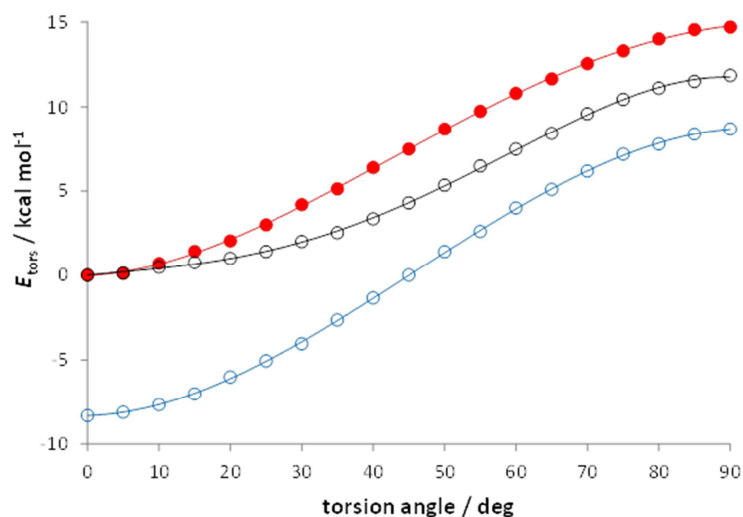


Figure 47 Relative strain energy as a function of the torsion angle of the C-N bond in position 3, for MV in vacuum (red), in vacuum considering nuclei's relaxation (black) and in MeOH (blue).

2.0 DETECTION OF THE TRANSIENT SPECIES

The transient absorption spectra of the phenothiazine dyes studied in this work are reported in Figures 48-50. In all cases, ground state photobleaching prevented the exact determination of the transient absorption maxima; the transient species could however be identified and analyzed.

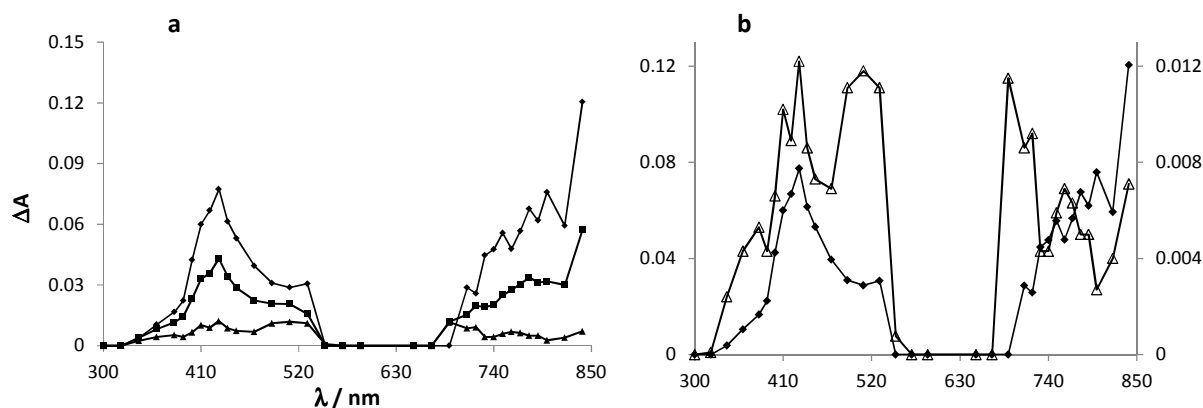


Figure 48 Transient absorption spectrum obtained by laser flash photolysis of MB^+ in ACN (2×10^{-5} M). Time-evolution (50 ns, diamonds, 250 ns, squares, and 1 μs , triangles, after the laser pulse end) of the transient spectrum in air-equilibrated ACN (a); detail of the spectrum obtained 1 μs (empty triangles, grey line, secondary axis) after the laser pulse in air-equilibrated ACN, compared to the one obtained at the laser pulse end (b).

The transient absorption spectra reported in Figure 48 for MB^+ in ACN are very similar to those reported by Kamat and Lichtin in the same solvent.^{309,310} The triplet excited state shows an apparent absorption maximum at 430 and a broad band centered at approx. 780 nm; the maximum in the

near-IR (870 nm)³¹⁰ is out of the detection limits of our experimental apparatus but the signal significantly increasing after 850 nm suggests the presence of such a band. The maximum at 520 nm is ascribed to the superimposition of the triplet band and that, weaker, derived from prompt production of the radical dication $\text{MB}^{\bullet 2+}$ by photoejection of an electron (equation 5.03).^{310,311}



Another transient species is observed after disappearance of both triplet MB^+ and $\text{MB}^{\bullet 2+}$. Electron photoejection from MB^+ to yield the semioxidized form $\text{MB}^{\bullet 2+}$ and subsequent rearrangement between ground state MB^+ and the solvated electron, yielding the semireduced form of the dye (MB^\bullet), as suggested by Kikuchi et al.,^{310,311} could explain the absorption spectrum obtained in ACN 1 μs after the laser pulse (Figure 48b). Under our experimental conditions no absorption of the protonated form of semireduced methylene blue ($\text{MBH}^{\bullet +}$) is observed at high wavelengths (namely 880 nm), owing to lack of water traces in ACN. From our experimental data it emerges that the triplet excited state is the main transient species formed upon laser irradiation of MB^+ in ACN solution. The measured lifetime of MB^+ triplet excited state, 12.5 μs in Ar-saturated solution, is perfectly consistent with the value reported by Kamat and Lichtin.³¹⁰

The transient absorption spectra recorded for NMB^+ in both MeOH and ACN (Figure 49a) are very similar to those of MB^+ . The triplet excited state can be assigned to the maximum at 420 (MeOH) or 430 (ACN) and to the broad band at approx. 760 nm, while the component at $\lambda > 850$ nm could not be entirely recorded. Prompt formation of the radical dication ($\text{NMB}^{\bullet 2+}$) would account for the weak shoulder at 510 nm. In Ar-saturated ACN, 6 μs after the laser pulse, the absorption band in the blue region is 10-20 nm hypsochromically shifted, relative to the triplet spectrum, and a small band at 520 nm appears (Figure 49b): we can confirm, as for MB^+ , the formation of NMB^\bullet (420 nm) and $\text{NMB}^{\bullet 2+}$ (520 nm). In O_2 -free ACN, τ_T for NMB^+ is 3.7 μs (4.8 in MeOH), *i.e.* significantly shorter than the 12.5 μs lifetime of MB^+ triplet state.

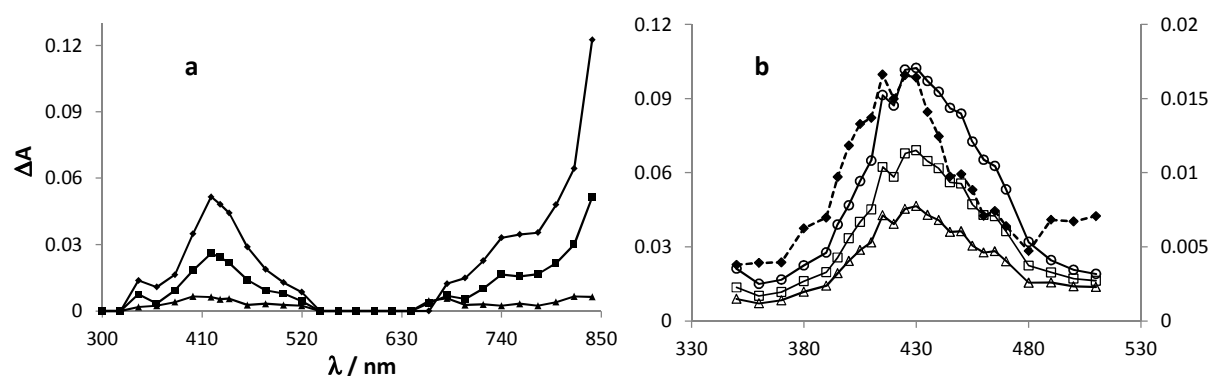


Figure 49 Transient absorption spectrum obtained by laser flash photolysis of NMB^+ in ACN (1.3×10^{-4} M). Time-evolution (50 ns, diamonds, 250 ns, squares, and 1 μs , triangles, after the laser pulse end) of the transient spectrum in air-equilibrated ACN (a); spectrum obtained 6 μs (diamonds, black dashed line, secondary axis) after the laser pulse in Ar-saturated ACN, compared to those obtained 140 ns (empty grey circles), 1 μs (empty grey squares) and 2 μs (empty grey triangles) after the laser pulse (b).

In air-equilibrated ACN the transient absorption spectrum of **MV** recorded after the laser pulse (Figure 50) presents a first maximum at 420 nm, preceded by a shoulder at approx. 400 nm, and followed by a large band between 600 and 820 nm. In ACN the band at approx. 420 nm and the band in the red region can be assigned to **MV** triplet excited state, similarly to the other PSs. In the spectrum recorded in aerated ACN 1 μ s after irradiation, *i.e.* after the complete disappearance of the triplet excited state, a first maximum at 380 nm is followed by two more intense maxima at 470 and 700 nm. As clearly seen within the wavelength window 490-520 nm (Figure 50a), in aerated conditions, the species absorbing at 470 nm is generated from the triplet excited state of **MV**: similarly to **MB⁺** and **NMB⁺**, such a signal can be assigned to the semioxidized (**MV^{•+}**) form of **MV**, while the band at 380 nm likely corresponds to semireduced **MV** (**MV^{•-}**). In air-equilibrated MeOH the blue part of the transient absorption spectrum is sharper than in ACN: the position of the maximum doesn't shift but the shoulder at 400 nm disappears. The broad band in the red is slightly more structured but similar to the one recorded in ACN: these slight differences are due to the presence of both **MV** and **MV-OH**. In MeOH, the triplet lifetime (5.9 μ s) is approx. 30% shorter than that measured in ACN (8.3 μ s).

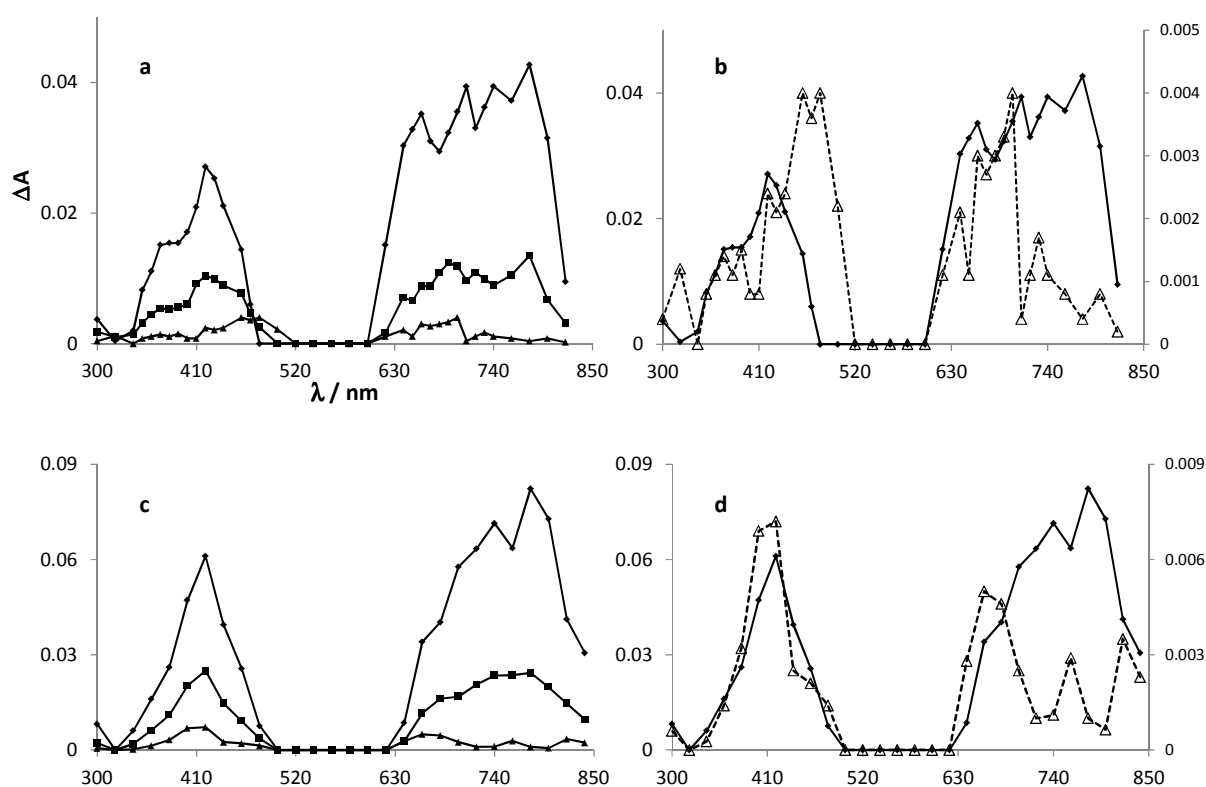


Figure 50 Time-evolution (50 ns, diamonds, 250 ns, squares, and 1 μ s, triangles, after the laser pulse end) of the transient spectrum obtained by laser flash photolysis of **MV** in air-equilibrated ACN (a, 5×10^{-6} M) and MeOH (c, 2.5×10^{-5} M). Spectra obtained 50 ns (diamonds, solid lines) and 1 μ s (empty triangles, dashed lines, secondary axis) after the laser pulse in air-equilibrated ACN (b) and MeOH (d).

The rate constants of triplet excited state deactivation in Ar-saturated, air-equilibrated and O₂-saturated solutions (Figure 51), as well as the second-order rate constant of deactivation by molecular oxygen (k_{q,O_2}^T) are reported in Table 15. The shorter lifetime of **NMB**⁺ and **MV**, relative to **MB**⁺, may be due to a more efficient intersystem crossing from the triplet excited state to the ground state of the PS. Moreover, for **MV** in MeOH, triplet state quenching by O₂ seems slightly favored than in ACN, while for **NMB**⁺ the difference induced by the solvent is negligible. In this series of measurements, **MV** triplet excited state quenching by O₂ is approx. twice more efficient relative to **MB**⁺ and **NMB**⁺; values of k_{q,O_2}^T are rather similar for the latter.

To summarize, the transient absorption spectra of the relatively unknown PSs **MV** and **NMB**⁺ appeared very close to those obtained for **MB**⁺, which could be consistently compared to literature data. For all the PSs, the triplet excited state could be identified as the main transient species. Unfortunately, the presence of different transient species absorbing in the same spectral regions (especially in the red) and the ground state photobleaching prevented the precise and complete interpretation of the transient absorption spectrum. Although slight variations of the triplet lifetime and of its reactivity towards molecular oxygen could be pointed out, all data were in the same order of magnitude. All PSs are efficiently quenched by oxygen and good quantum yields of singlet oxygen productions could be expected.

Table 15 Rate constants of triplet decay (k_d) in Ar-saturated, air-equilibrated and O₂-saturated solutions, rate constants of triplet quenching by O₂ (k_{q,O_2}^T), triplet lifetimes (τ_T) in Ar-saturated solutions. Data for **MB**⁺, **NMB**⁺ and **MV** in ACN and MeOH.

PS		k_d			$k_{q,O_2}^T / 10^9 \text{ M}^{-1} \text{ s}^{-1}$	$\tau_T / \mu\text{s}$
		Ar / 10^5 s^{-1}	Air / 10^6 s^{-1}	O ₂ / 10^7 s^{-1}		
MB ⁺	ACN	0.8 ± 0.1	3.6 ± 0.4	1.8 ± 0.3	1.85 ± 0.10	12.5 ± 0.3
NMB ⁺	ACN	2.7 ± 0.3	2.7 ± 0.3	1.5 ± 0.2	1.66 ± 0.20	3.7 ± 0.2
	MeOH	2.1 ± 0.3	4.0 ± 0.3	2.0 ± 0.3	1.72 ± 0.20	4.8 ± 0.2
MV	ACN	1.2 ± 0.2	5.1 ± 0.4	2.5 ± 0.3	2.26 ± 0.30	8.3 ± 0.2
	MeOH	1.7 ± 0.2	5.2 ± 0.4	2.6 ± 0.3	2.90 ± 0.30	5.9 ± 0.2

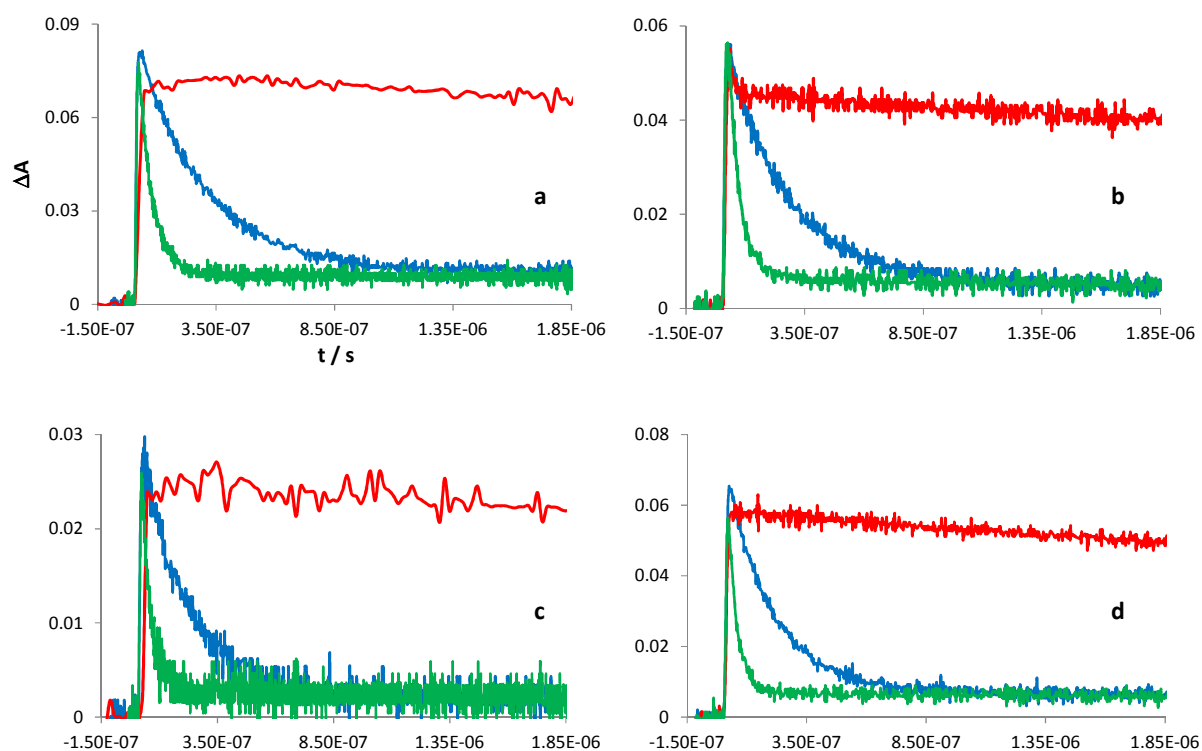


Figure 51 Decays of the transient absorption of MB^+ in ACN (a), NMB^+ in MeOH (b), MV in ACN (c) and MeOH (d) in Ar-saturated (red), air-equilibrated (blue) and oxygen-saturated (green) solutions.

3.0 SINGLET OXYGEN PRODUCTION

Quantum yields of 1O_2 production (Φ_Δ) and rate constants of 1O_2 total quenching (k_t^{PS}) of the investigated PSs in ACN and CD_3OD (deuterated methanol) were determined by monitoring the 1O_2 near-IR phosphorescence emission, upon continuous irradiation, using perinaphthenone (**PN**) or rose bengal (**RB**) as references (R), following the procedure previously described. Measurements in deuterated methanol were carried out to put in evidence any solvent effect. **RB** could be used as a reference only in CD_3OD ($\Phi_\Delta = 0.76$).^{31,196,289,312} Since its Φ_Δ in ACN was measured between 0.54 and 0.83,^{31,313,314} **PN** had to be used as a reference in this solvent ($\Phi_\Delta = 1$),⁴⁵⁻⁴⁷ taking care of corrections for the different irradiation wavelengths (equation 3.35). Singlet oxygen lifetime in CD_3OD and MeOH is $270^{32,315}$ and $3 \mu s$,³² respectively: the use of deuterated methanol was necessary to significantly detect 1O_2 phosphorescence (equation 3.16).

The ratio of 1O_2 signals (S_e) for R and PS was analyzed as a function of the PS concentration, in order to determine the quantum yields of 1O_2 production and k_t^{PS} in the range of concentrations used for this work (Table 16). In all cases, except for **RB** and for **MV** in ACN, a significant variation of the signal intensity as a function of the PS concentration was observed (Figure 52 and Tables 16 and 17): singlet oxygen quenching by the PS was not negligible and the use of equation 3.27 gave only apparent Φ_Δ . Values of Φ_Δ and k_t^{PS} were thus estimated from the intercept and the slope of the linear plot of $[(S_e^R/S_e^{PS})(P_a^{PS}/P_a^R)]$ vs $[PS]$ (Figure 52, equation 3.25). In the two cases where quenching by the PS was

negligible under our experimental conditions, limiting values of k_t^{PS} could be estimated from the maximum concentrations used.

Table 16 Quantum yields of singlet oxygen production (Φ_Δ) and rate constant of 1O_2 total quenching by the PS (k_t^{PS}) for **RB**, **MB⁺**, **NMB⁺** and **MV** in ACN and CD₃OD. **RB** and **PN** were used as reference PSs in CD₃OD and ACN, respectively. In brackets the Φ_Δ values measured by detection with a probe (rubrene).

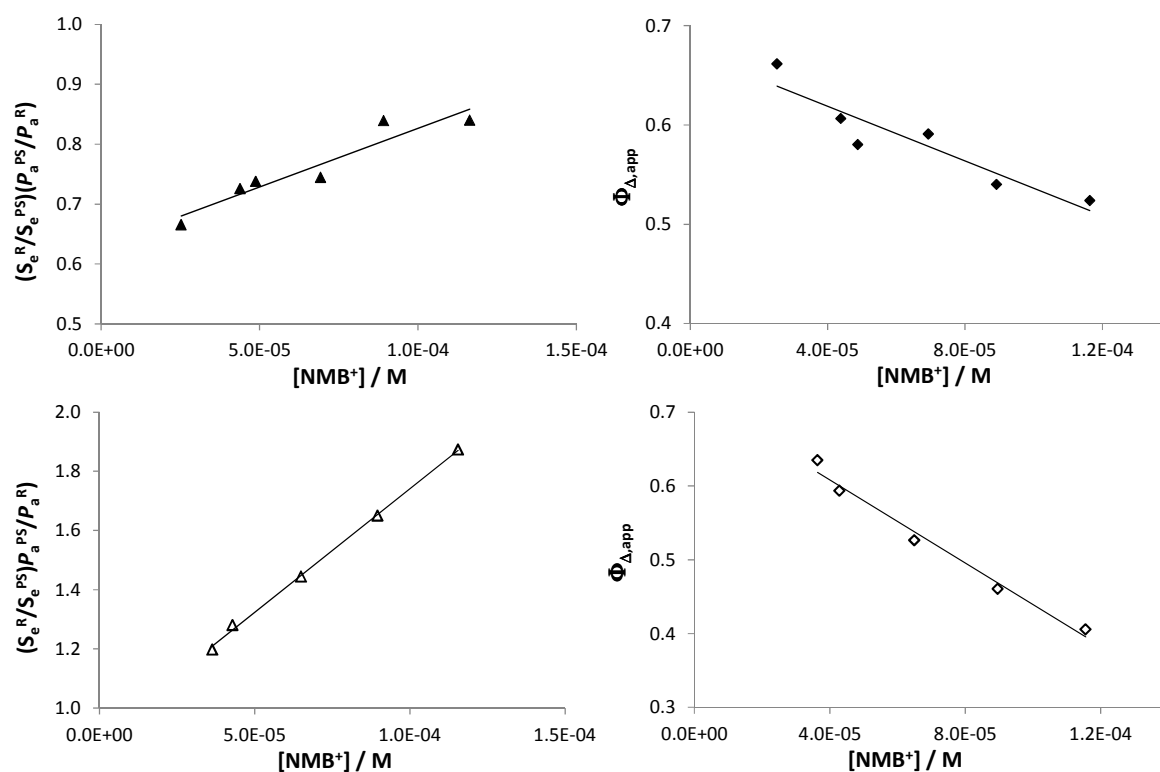
PS	Φ_Δ		$k_t^{PS} / 10^7 \text{ M}^{-1} \text{ s}^{-1}$	
	ACN	CD ₃ OD	ACN	CD ₃ OD
RB	0.42 ± 0.03	0.76 ± 0.04 ^{31,196,289}	≤ 9.0 ± 0.5	-
MB⁺	0.58 ± 0.04	0.52 ± 0.04	4.9 ± 0.4	0.60 ± 0.1
NMB⁺	0.66 ± 0.04 (0.65 ± 0.04)	0.82 ± 0.04	4.4 ± 0.4	3.4 ± 0.4
MV	0.60 ± 0.04 (0.59 ± 0.04)	0.73 ± 0.04	≤ 9.3 ± 0.7	16 ± 1

In both solvents, all the PSs present good photosensitizing properties for 1O_2 production, with Φ_Δ values higher than 0.50 with the exception of **RB** in ACN. Except for **MB⁺**, the quantum yields of singlet oxygen production are higher in CD₃OD than in ACN. For **MB⁺**, though values of Φ_Δ are rather similar in the two solvents, k_t^{PS} is approx. ten times lower in CD₃OD than in ACN. Our results for **MB⁺** are in perfect agreement with those already reported: Φ_Δ between 0.44²⁰⁶ and 0.50^{59,82} in methanol and approx. 0.52 in ACN.³¹ Lower Φ_Δ for **MB⁺** may be assigned to dye dimerization (at [**MB⁺**] > 10⁻⁵ M);⁵⁹ given that dimerization is favored in aqueous solutions relative to organic solvents, this could also explain the slightly less efficient 1O_2 production in CD₃OD than in ACN. A lower Φ_Δ for **MB⁺** relative to **NMB⁺** and **MV** is consistent with the less efficient quenching of the triplet excited state by O₂ (Table 15).

NMB⁺ has a much higher Φ_Δ in CD₃OD than in ACN, even though both values are significantly high; on the contrary, the sensitivity of k_t^{PS} on the solvent is negligible. By using equation 3.27, values of apparent Φ_Δ at given PS concentrations could be calculated (Figure 52 and Table 17) In ACN, for [**NMB⁺**] ≤ 2.5 × 10⁻⁵ M, Φ_Δ doesn't vary with the concentration of PS and 1O_2 quenching by the PS is negligible: the condition of $k_t^{PS}[\text{PS}] \leq 0.1k_d$ is satisfied. It is worth saying here that for all the indirect measurements of 1O_2 using rubrene as a probe, the concentration of **NMB⁺** was lower than the limiting value of 2.5 × 10⁻⁵ M: a quantum yield of 0.66 was always obtained under those experimental conditions. To our knowledge, no absolute Φ_Δ values have been measured until now for **NMB⁺**; all values were reported to be higher than 1, relative to **MB⁺**. We can confirm the higher efficiency of singlet oxygen generation, relative to **MB⁺**: 1.35 in buffered aqueous solutions,^{63,64} 1.6 in CD₃OD and 1.1 in ACN.

Table 17 Variation of the apparent quantum yields of singlet oxygen production with the concentration of NMB^+ in air-equilibrated CD_3OD and ACN at room temperature.

$[\text{NMB}^+]_{\text{CD}_3\text{OD}} / 10^{-5} \text{ M}$	$\Phi_{\Delta, \text{app}, \text{CD}_3\text{OD}}$	$[\text{NMB}^+]_{\text{ACN}} / 10^{-5} \text{ M}$	$\Phi_{\Delta, \text{app}, \text{ACN}}$
11.6	0.41 ± 0.03	11.6	0.52 ± 0.03
9.0	0.46 ± 0.03	8.9	0.54 ± 0.03
6.5	0.53 ± 0.04	6.9	0.59 ± 0.04
4.3	0.59 ± 0.04	4.9	0.58 ± 0.04
3.6	0.63 ± 0.04	4.4	0.61 ± 0.04
		2.5	0.66 ± 0.04

**Figure 52** Variation of the emission signals (normalized to the reference $^1\text{O}_2$ signal (PN, top and RB, bottom) and corrected for different photon flux absorbed by the PSs) for NMB^+ as a function of $[\text{NMB}^+]$ (triangles); variation of the apparent Φ_{Δ} of NMB^+ as a function of its concentration (diamonds). Air-equilibrated ACN (full symbols) and CD_3OD (empty symbols), at room temperature.

As far as the quantum yield of singlet oxygen production is concerned, the same trend as NMB^+ is followed by MV (Table 16): its Φ_{Δ} is higher in CD_3OD than in ACN (0.73 vs 0.60). On the contrary, the rate constant of $^1\text{O}_2$ quenching by the PS is higher in deuterated methanol. The higher Φ_{Δ} in CD_3OD relative to ACN is consistent with the higher rate constant of triplet excited state quenching by

oxygen ($2.90 \times 10^9 \text{ M}^{-1} \text{ s}^{-1}$ vs $2.26 \times 10^9 \text{ M}^{-1} \text{ s}^{-1}$ for ACN, Table 15). Probably **MV-OH** increases the charge transfer character in the collision complexes formed between ground state oxygen and the triplet excited state of the PS ($^1\text{O}_2$ generation) and between singlet oxygen and the PS ($^1\text{O}_2$ quenching). Hence, relative to the sole **MV** species (ACN), **MV-OH** contributes to more efficient singlet oxygen production and quenching. A similar behavior was observed for **DBTP-COOH**, probably due to the presence of the carboxylic group. Until now **MV** has been studied as a singlet oxygen producer only in biological (aqueous buffered) media: its Φ_{Δ} was reported to be approx. 0.70,^{128,194} taking **MB⁺** as a reference ($\Phi_{\Delta} = 1$). Our results differ from this trend: while in ACN the quantum yields of $^1\text{O}_2$ production of **MB⁺** and **MV** are similar, in CD_3OD **MV** is 40% more efficient than its parent compounds (0.73 against 0.52). The sensitivity of **MV/MV-OH** towards the polarity of the solvent and the acidity of the medium could explain these variations with the medium.

All the PSs tested for this work can efficiently produce singlet oxygen by absorption of visible light. The quantum yields we measured are higher than 0.52 and 0.58 in CD_3OD and ACN, respectively. The best PS in the series reported here is **NMB⁺**, followed by **MV** and **MB⁺**. The reference sensitizer **RB**, on the contrary, has a quite low Φ_{Δ} in ACN (0.42)³¹² which could be due to aggregation phenomena in this solvent; in methanol its quantum yield is stable and very high (0.76).

4.0 REACTIVITY OF MV IN SOLUTION

In order to determine any solvent effect on the stability of **MV** under irradiation its photobleaching was studied in dioxane, acetonitrile and methanol. Since sulfides are very sensitive to $^1\text{O}_2$, forming sulfoxides and sulfones, the photoreactivity of **MV** towards dibutylsulfide (DBS) was also studied in the three solvents, to highlight the influence of the solvent on the photosensitizing properties of the dye. The results are reported in Figures 53-55.

In the absence of DBS, in dioxane and ACN the absorption of **MV** decreases as long as irradiation takes place: the spectral shape doesn't vary during irradiation, even though the PS is efficiently consumed. On the contrary, in MeOH **MV** could be let under irradiation for more than three hours without any significant bleaching effect. The estimated values of quantum yields of bleaching ($\phi_{\text{bleaching}}$) in the three solvents are reported in Table 18. Relative to MeOH, the photodegradation of **MV** is 20 and 65 times more efficient in ACN and dioxane, respectively. As pointed out before, in methanol both **MV** and **MV-OH** are present, which could explain a better stability under irradiation. Moreover, the photobleaching extent is linearly correlated to the Reichardt's polarity of the solvents (E_T^N),³⁰³ as for the spectroscopic properties previously treated in this chapter (Figure 56). Apparently, **MV** stability depends on the polarity of the solvent: for applications, polar media are thus more convenient for increasing its durability.

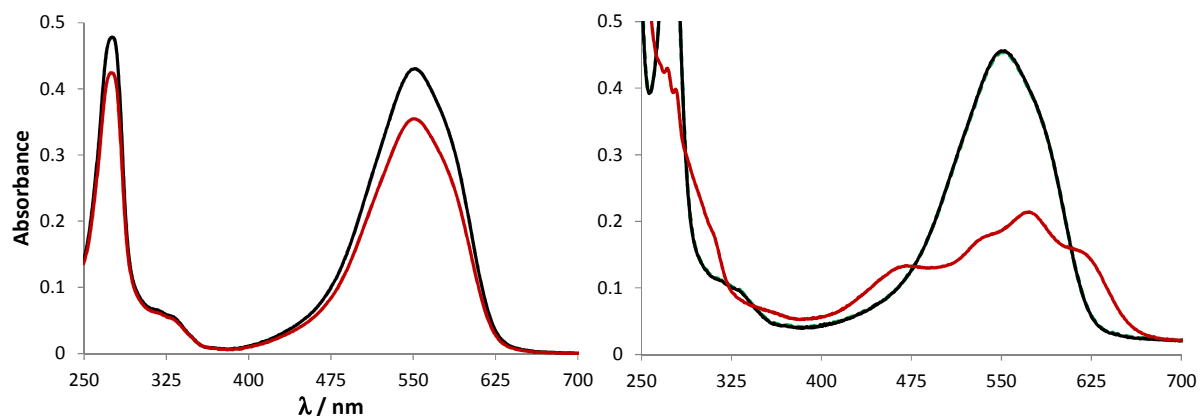


Figure 53 Absorption spectra of MV in ACN before (black lines) and after irradiation (red lines), in the absence (left) and in the presence (right) of DBS. Initial MV concentration: 7.5×10^{-6} M. Irradiation: 90 minutes (left) and 60 minutes (right), white light, $P_a = 5.1 \times 10^{-6}$ Einsteins $L^{-1} s^{-1}$. The spectrum recorded after addition of DBS in the dark (green line) is totally superimposed to the one recorded before the addition.

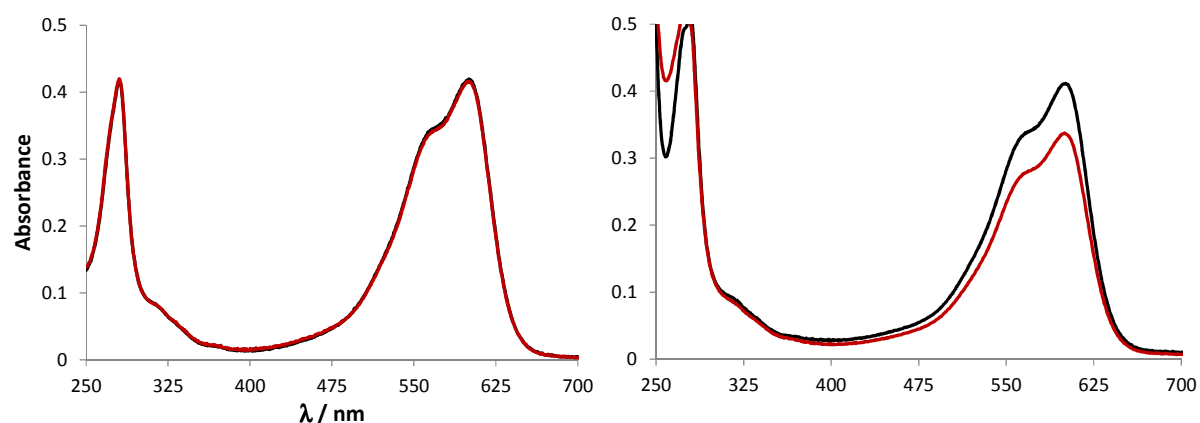


Figure 54 Absorption spectra of MV in MeOH before (black lines) and after irradiation (red lines), in the absence (left) and in the presence (right) of DBS. Initial MV concentration: 1.8×10^{-5} M. Irradiation: 200 minutes, white light, $P_a = 4.2 \times 10^{-6}$ Einsteins $L^{-1} s^{-1}$.

The dye photobleached more efficiently in the presence than in the absence of sulfide (Table 18, Figures 53-55). The extent of photobleaching was always linearly proportional to the solvent polarity (Figure 56), and the photostability of **MV** was higher in more polar solvents, independently on the presence of other reactants. Nonetheless, the increase of photobleaching induced by the presence of sulfides was much more important in MeOH: apparently, the influence of adding DBS to irradiated **MV** solutions is relatively more important in protic solvents. Probably, an interaction in the excited state between PS and reactant make the dye more prone to degradation. Supplementary tests would be necessary for a complete understanding of this phenomenon.

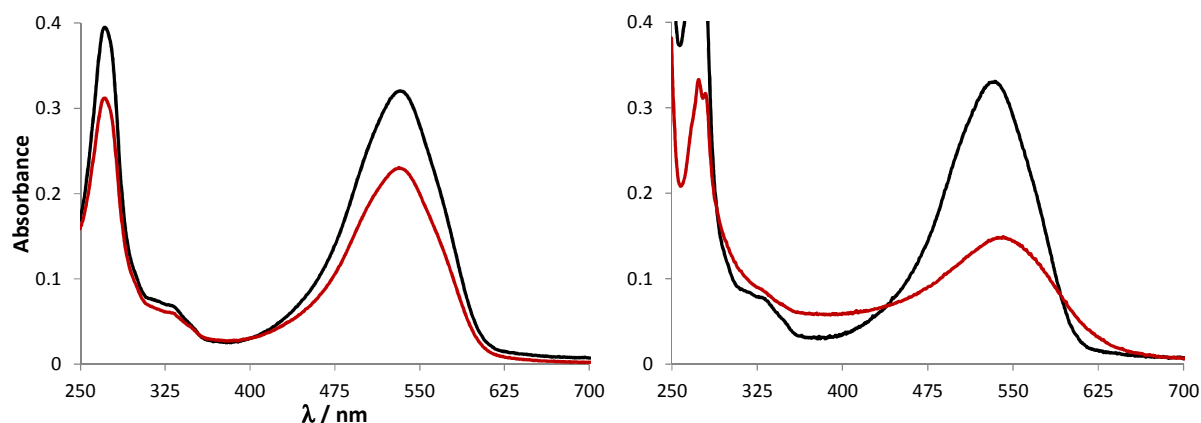


Figure 55 Absorption spectra of **MV** in dioxane before (black lines) and after irradiation (red lines), in the absence (left) and in the presence (right) of DBS. Initial **MV** concentration: 6.0×10^{-6} M. Irradiation: 40 minutes (left) and 20 minutes (right), white light, $P_a = 4.6 \times 10^{-6}$ Einsteins $L^{-1} s^{-1}$.

Table 18 Quantum yields of bleaching ($\phi_{\text{bleaching}}$) of **MV** in MeOH, ACN, dioxane, both in the absence and in the presence of DBS; ratio of the quantum yields of bleaching calculated in the presence and in the absence of dibutyl sulfide.

solvent	$\phi_{\text{bleaching}} / 10^{-5} \text{ mol}_{\text{MV}} \text{ Einsteins}^{-1}$	$\frac{\phi_{\text{bleaching, DBS}}}{\phi_{\text{bleaching}}}$
MeOH	0.26 ± 0.03	25
MeOH + DBS	6.4 ± 0.8	
ACN	5.5 ± 0.8	5
ACN + DBS	27.0 ± 2.0	
dioxane	17.0 ± 2.0	4
dioxane + DBS	67.0 ± 4.0	

In the presence of DBS in irradiated ACN and dioxane solutions, an evolution of the absorption spectrum of **MV** occurs. Notably, in ACN we finally obtain an absorption spectrum very similar to the one measured after acidification (Figure 44). In dioxane, although the spectrum is not as structured as in ACN, it is however possible to recognize an increase of absorbance at approx. 620 and 450 nm. The signal at 620 nm has been assigned to the first electronic transition of the protonated form **MV-OH**, formed in acidic media. By adding a suitable amount of a base (Et_3N), we noticed the total reversibility of this spectral variation, confirming that by irradiating **MV** in ACN (or dioxane) in the presence of DBS, a non-negligible amount of acid was formed. We already mentioned that in ACN the formation of the absorption band at 620 nm is noticed at very low $[\text{H}^+]$ (approx. 5.0×10^{-6} M). The ^1H NMR analysis of the reaction products showed however the sole presence of the sulfoxide (DBSO) and the sulfone (DBSO₂), in a 50/50 ratio, deriving from singlet oxygen addition to the sulfide. In ACN,

the estimated concentration of acid formed during the reaction would thus be between 5.0×10^{-6} M and the detection limits of NMR spectroscopy ($\approx 2\%$ M, *i.e.* approx. $(2.0 - 4.0) \times 10^{-5}$ M). Analyzing the absorption spectra recorded in the three solvents, a combined effect of photobleaching and **MV-OH** formation deriving from the formation of an acid can explain our experimental results. In dioxane (Figure 57), after the formation of **MV-OH**, photobleaching is almost complete and the absorption band within 450-620 nm disappears. In MeOH no variation of the spectral shape is noticed: it seems that thanks to the presence of **MV-OH** the absorption spectrum is somehow less sensitive to the formation of acid.

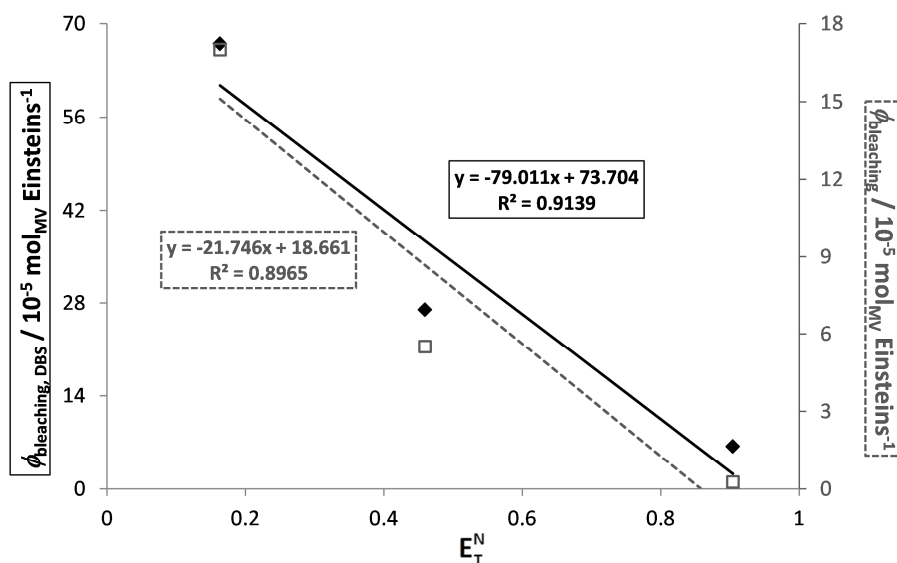
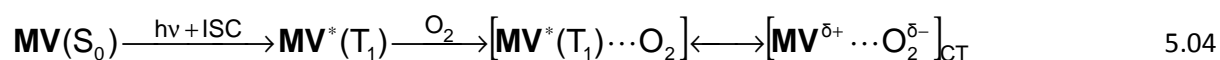


Figure 56 Variation of the quantum yield of photobleaching of **MV** in dioxane, acetonitrile and methanol in the absence (secondary axis, empty grey squares, grey dashed lines) and in the presence (black diamonds, black solid lines) of DBS as a function of the normalized Dimroth-Reichardt's polarity of the solvent.

In the dark, the addition of DBS doesn't have any influence on the absorption spectrum of **MV**: in Figure 53b the spectrum recorded after adding DBS in the dark is reported and is completely superimposed to the initial one, recorded before the addition. Moreover, tests carried out after N_2 bubbling in ACN solutions showed simply the photobleaching of **MV**, without the formation of acids. This behavior seems thus strictly photochemical and related to the presence of oxygen in solution.

Where does this acid come from? What mechanism could occur in addition to singlet oxygen production? A recent paper by Manju *et al.*³¹² can give some clues for a possible explanation. Studying the photosensitizing properties of 10-methylphenothiazine, besides 1O_2 formation, Manju *et al.*³¹² pointed out an electron transfer (ELT) reaction between the triplet excited state of the PS and O_2 (from the charge-transfer complex), yielding the formation of the PS radical cation and superoxide radical anion. In our case thus, in addition to the mechanism of singlet oxygen formation (equation 5.05), the charge transfer complex $[MV^{\delta+} \cdots O_2^{\delta-}]$ (CT, equation 5.04) formed between excited **MV** and O_2 could also evolve towards the formation of the radical cation of the PS (which was detected by laser flash photolysis, Figure 50) and superoxide radical anion (equation 5.06). Once formed, MV^{*+}

could react with DBS (Bu_2S in the reactions below) to yield $\text{DBS}^{*\bullet}$ and the PS in its ground state (reaction 5.07). Depending on the corresponding electrochemical properties, a first electron transfer reaction between the PS and the substrate could alternatively lead to the formation of $\text{DBS}^{*\bullet}$ and $\text{MV}^{\bullet-}$ (reaction 5.08); $\text{MV}^{\bullet-}$ could then produce superoxide radical anion through another ELT reaction (reaction 5.09). In both cases, a radical chain reaction between $\text{O}_2^{\bullet-}$ and $\text{DBS}^{*\bullet}$, involving H-abstraction from the sulfide, could lead thus to the formation of hydroperoxy radicals and H^+ ions (reactions 5.10 and 5.11, reactions 1.05 and 1.07 in the Introduction). The semi-dehydrogenated radical of DBS ($\text{Bu}_2(-\text{H})\text{S}^{\bullet}$), in the presence of oxygen, could also evolve towards the formation of the corresponding sulfonic acid and sulfuric acid (equation 5.12). These hypothetical pathways could lead to the acidification of the medium, responsible of the spectral variations of MV in ACN and dioxane. Considered the much higher concentration of DBS relative to MV , it is possible that even at the side-process scale (since DBSO and DBSO_2 are the sole detected oxidation products), these radical chain reactions produce enough H^+ to justify the spectral changes observed. Many further photochemical and electrochemical tests would be necessary for a detailed understanding of this mechanism; such a study would be very interesting as a perspective for the continuation of this work.



Sulfides are particular reactants, since they can react *via* both singlet oxygen addition and electron transfer reactions.^{23,41} Considering for example rubrene, which selectively reacts with ${}^1\text{O}_2$ without undergoing any ELT reaction, the absorption spectrum of MV doesn't evolve after rubrene oxygenation (Figure 58). The reaction has been carried out under the same experimental conditions as for DBS: after complete consumption of the probe, we observed an absorption spectrum perfectly superimposable to that recorded in the absence of rubrene.

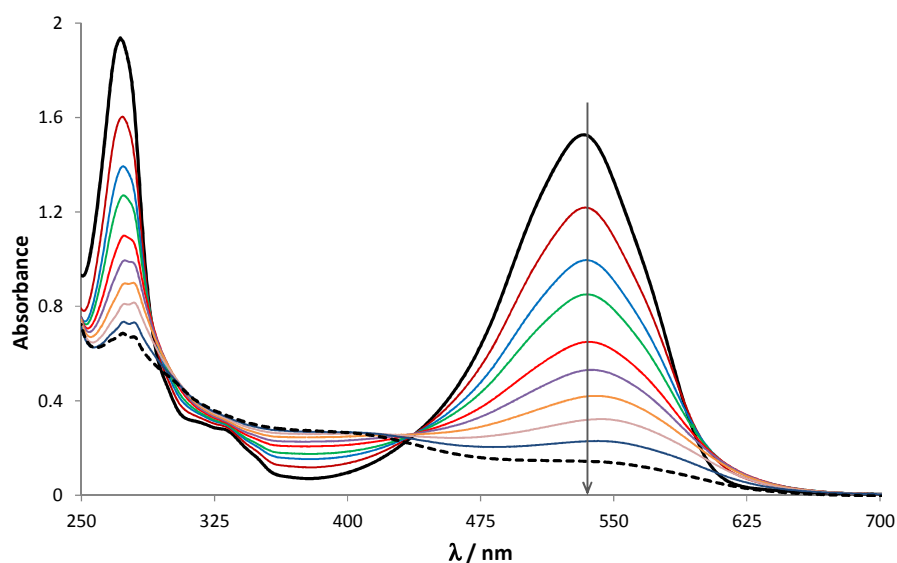


Figure 57 Evolution of the absorption spectrum of MV in dioxane as a function of irradiation time, in the presence of DBS ($\ell = 1$ cm, quartz cells). Initial MV concentration: 2.6×10^{-5} M. Irradiation: white light, 170 minutes. The decrease of absorbance is pointed out by the arrow from $t = 0$ (black line) to $t = 170$ min (black dashed line).

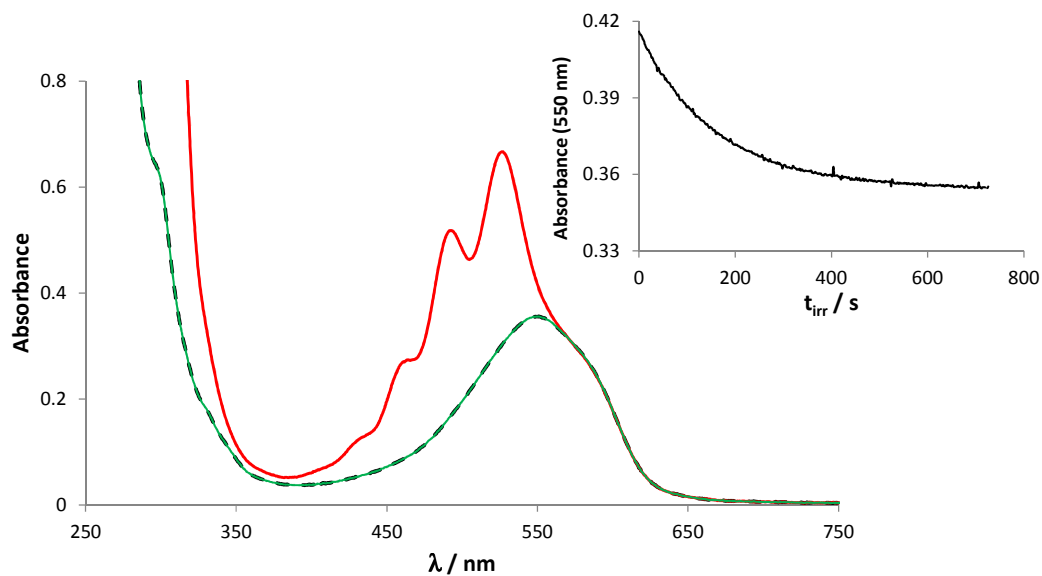


Figure 58 Evolution of the absorption spectrum of MV in ACN, irradiated in the presence of rubrene; MV spectrum before adding rubrene (green line), spectrum of MV+rubrene before irradiation (red line), MV spectrum after complete rubrene consumption (12 minutes irradiation, dashed black line) ($\ell = 1$ cm, quartz cells). Initial MV concentration: 6.0×10^{-6} M. Irradiation: white light, 12 minutes. Inset: variation of absorbance at 550 nm during irradiation.

5.0 CONCLUSIONS

New methylene blue (**NMB**⁺) and methylene violet (**MV**) have been described in previous works as very good candidates for photosensitization applications in PDT and PDI: they can efficiently generate ¹O₂ in biological media and they showed very good bactericidal and anticancer activities. With our results, we went further in their photophysical characterization with accurate determination of their singlet oxygen production.

The absorption and fluorescence spectra of **NMB**⁺ and **MB**⁺, as well as their transient species are rather similar. In the case of **MB**⁺, dimerization processes, can account for the slight red-shift of its absorption spectrum and for the lower Φ_{Δ} (increase of approx. 50% in the efficiency of singlet oxygen production for **NMB**⁺). **NMB**⁺ represents thus a very good option among methylene blue derivatives for applications in photodynamic therapy: it is commercially available, easily prepared and modified, it is non-toxic in the dark and it is really efficient as far as singlet oxygen generation is concerned.

MV, although it can efficiently produce ¹O₂, showed a very high sensitivity towards the polarity of the medium, which must be seriously taken into account. The absorption maximum can shift by more than 100 nm, depending on the solvent. Significant solvatochromism was also noticed on its fluorescence properties and on the transient species; singlet oxygen production also varied depending on the solvent (approx. 20% from ACN to MeOH). Detailed studies on the spectroscopic properties of **MV** in the presence of acidic media highlighted the presence of two forms of **MV**: in non-polar and polar solvents **MV** is the dominant species (with λ_{max} depending on the solvent polarity), whereas in protic media **MV-OH** is formed. The relative amount of this protonated form varies depending on the concentration of H⁺, influencing the photophysical properties of the dye and its ¹O₂ production. In MeOH, where the presence of **MV-OH** has been estimated around 35%, the triplet excited state is more efficiently quenched by O₂ and, consequently, the dye produces singlet oxygen more efficiently than in ACN. Besides, the presence of **MV-OH** contributes to a higher ¹O₂ quenching: for the best use of this PS, the evaluation of the effect that the medium can have on its photosensitizing properties is essential. By studying the photostability of **MV** under irradiation, in the absence and in the presence of sulfides, we concluded that besides ¹O₂ production other side-reactions were possible. We highlighted the formation of H⁺ during the irradiation of ACN or dioxane solutions of **MV** in the presence of dibutylsulfide. The amount of acid formed by this side-pathway, even though low, was efficiently detected by its influence on the absorption and fluorescence spectra of **MV**. Thanks to this peculiar reactivity, **MV** could act as PS and mechanism probe in the same time: acids, eventually formed by photoinduced radical chain reactions, could be detected by checking the absorption spectrum of **MV** during irradiation, and mechanisms other than ¹O₂ formation could be pointed out. Even though further experiments must be carried out to completely understand the mechanisms involved in these reactions, a more detailed comprehension of these phenomena could lead to important improvements as far as the applications of **MV** are concerned.

MV and **NMB**⁺ are very good singlet oxygen producers and, thanks to their large and intense absorption spectra in the red, are very good candidates for applications in PDT and other biomedical fields, such as blood disinfection. In addition, chemical functionalization on phenothiazine derivatives has been successfully and relatively easily achieved, making these PSs suitable for derivatization aimed at improving their photosensitizing properties or at grafting purposes.

6 Organic photocatalysts immobilized on transparent silica monoliths: reactivity at the gas-solid interface

As presented in the introductory chapters, several supports and grafting methods have been developed to conceive photoactive materials for widespread applications in photooxidation processes. The interaction of the PS with the supporting matrix may influence its photophysical properties. However, although extensive analyses of the PSs photophysics in highly scattering media is possible,^{316,317} the monitoring of their transient species is more scarce.^{82,318} Singlet oxygen quantum yields could be determined by detection of $^1\text{O}_2$ emission at 1270 nm for PSs supporting materials only *in suspensions*.^{82,319,320}

Transparent highly-porous silica monoliths can host PSs and can be used as solvent-free microreactors for photochemical applications at the gas-solid interface.^{116,321} Many are the advantages of utilizing these bulk materials: transparency optimizes light harvest by the PS,^{319,320} high porosity and specific surface area give these matrices important adsorption properties (for both the reactants and the products),³²² sol-gel syntheses are easily put to use, silica is inert and easily modified during the preparation steps,^{228,323–325} many PSs can be grafted on functionalized materials.¹⁴⁸ As already published, silica monoliths doped with cyanoanthracenes (**DCA** and **DBTP**) can efficiently produce singlet oxygen and oxidize sulfides.¹¹⁷

The results presented in this chapter are aimed at investigating the photophysical properties of several PSs included or grafted in silica monoliths with respect to their properties in solution, through the analysis of their absorption/emission and transient spectra, of their quantum yields of singlet oxygen production and of their photooxidation properties against dimethylsulfide (DMS).^{71,147} Thanks to the transparency and the free-standing shape of the monoliths, the complete spectroscopic characterization of the silica-embedded dyes was carried out directly at the gas-solid interface without any suspension in a solvent. The influence of the silica network, the nature of the dye and the adsorption/grafting link between the dye and silica was investigated. All the PSs, whose properties in solution have been presented in the previous chapters (**DBTP** derivatives, **DCA**, **MV**, **NMB**⁺ and reference sensitizers **MB**⁺,⁶⁰ **RB**³²⁶ and **PN**⁴⁷), were encapsulated in silica matrices, their photophysical properties were analyzed and compared to the corresponding soluble counterparts. Moreover, the **DBTP** derivative **6** (3-[*N*'-(triethoxysilyl)propyl-*N*'-hexylurea]carboxamido-9,14-dicyanobenzo[*b*]triphenylene) has been grafted onto silica: the effect of grafting, relative to simple inclusion of the dye inside the silica structure, was studied. The effects of PS concentration, gaseous atmosphere, humidity and hydrophobicity on the production of $^1\text{O}_2$ were analyzed.

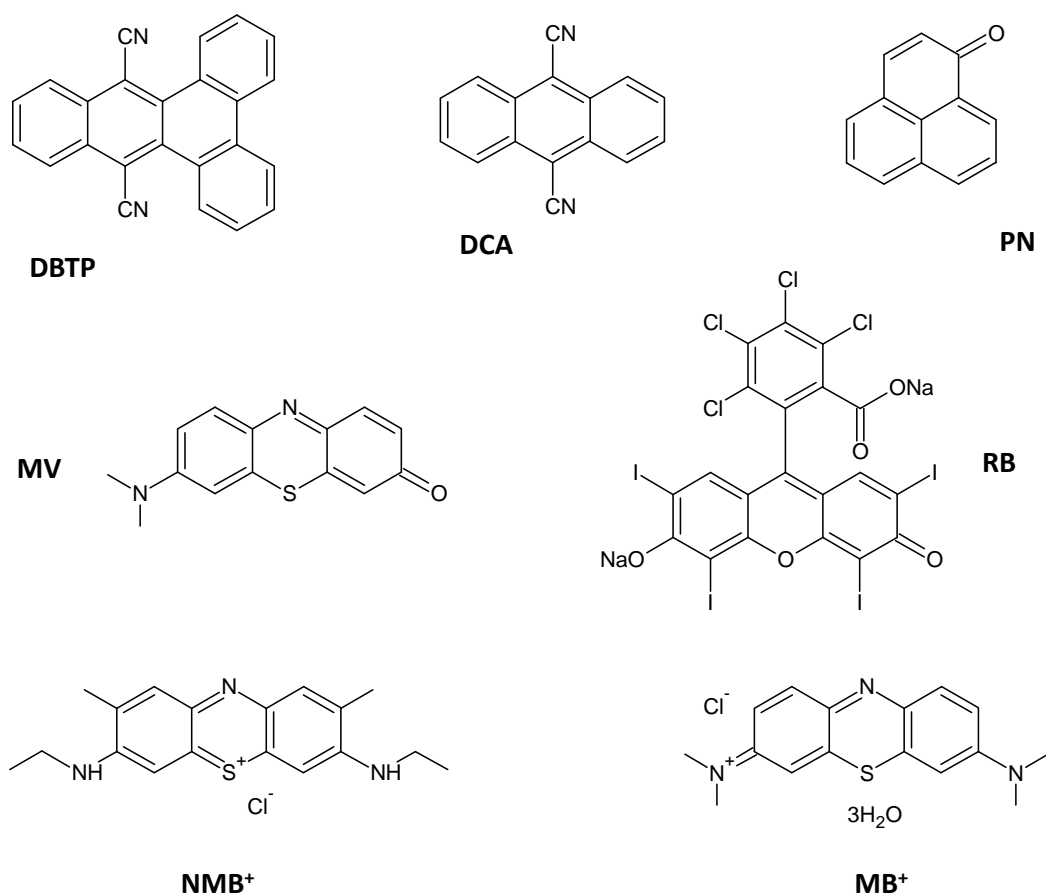


Chart 12 PSs encapsulated in silica monoliths.

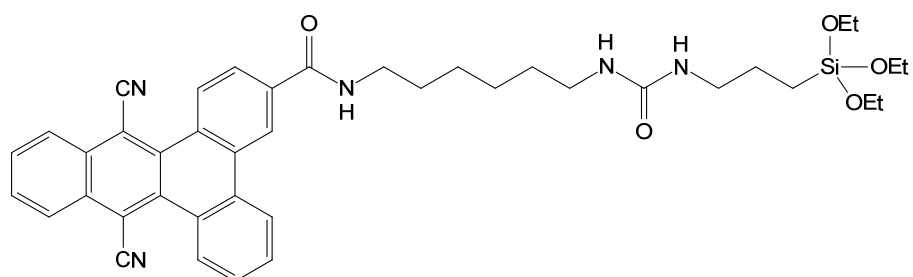


Chart 13 Compound 6, the DBTP derivative grafted onto silica monoliths.

1.0 SYNTHESSES

1.1 Synthesis of compound 6

Compound 5 was prepared from 4 following usual conditions for Boc-deprotection reactions (Scheme 10, Chapter 3).²¹⁷ The addition of trifluoroacetic acid (TFA) breaks the carbamate linker, forming an ammonium salt between the amino-derivative of **DBTP** and the acid. The 4-TFA salt is neutralized by

the addition of KOH, yielding the amino derivative **5**. The reaction can be easily followed by TLC, but for the poor solubility of **5** and its affinity towards glass flasks any NMR characterization was impossible. Compound **6** was obtained by a one-pot condensation of 3-(triethoxysilyl)propylisocyanate (TEOS-NCO) with the amino moiety of **5** (Scheme 10, Chapter 3) under strictly anhydrous conditions to avoid polycondensation reactions of the triethoxysilyl-derivative. The reaction between primary amines and isocyanates is very efficient and leaves no by-product: completion was reached after some hours under stirring at room temperature. The freshly prepared ACN solution containing **6** was then directly added to the solution for monoliths synthesis.

1.2 Synthesis of silica monolith and structural characterization

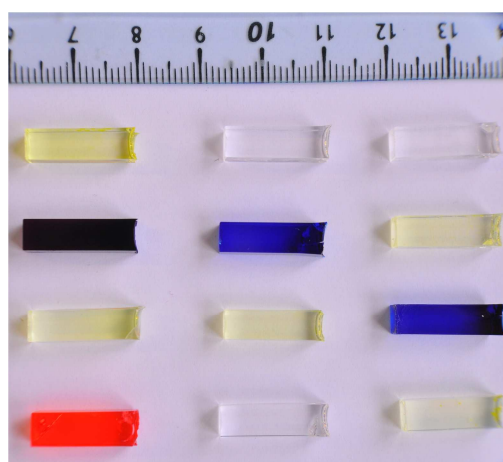


Figure 59 Some silica monoliths (series 2). From the left top: **SG0-ACN-DBTP**, **SG0-OC 2.5% OC**, **SG0**, **SG0-MV**, **SG0-MB⁺**, **SG0-DBTP**, **SG0-PN**, **SG0-OC-DBTP 1% OC**, **SG0-NMB⁺**, **SG0-RB**, **SG0-ACN**, **SG0-DCA**.

Several kinds of transparent silica monoliths were prepared following the procedures described in Chapter 3 (Materials and Methods):

- **SG0**: silica monoliths prepared under conventional hydrolysis of TMOS (tetramethyl orthosilicate) in MeOH. PSs included: **DBTP**, **DCA**, **PN**, **RB**, **MB⁺**, **NMB⁺**, **MV**.
- **SG0-OC**: silica monoliths prepared under conventional hydrolysis of TMOS in MeOH containing various molar percentages of octyl groups (from octyl-trimethoxysilane, TMOS-OC). PS included: **DBTP**.
- **SG0-ACN**: transparent silica monoliths prepared under conventional hydrolysis of TMOS in MeOH/ACN (1/1 molar ratio) mixture as a solvent. PSs included: **DBTP**, **MV**.
- **SG0-NCO** monoliths: silica monoliths prepared under conventional hydrolysis of TMOS in MeOH containing various molar percentages of isocyanate (NCO) groups (from TEOS-NCO).
- **SG0-SO₃H**: silica monoliths prepared under conventional hydrolysis of TMOS in MeOH containing various molar percentages of sulfonic acid groups (from the oxidation of TMOS-SH). PSs included: **MV**, **NMB⁺**.

- **SG1-NCO-DBTP**: silica monoliths prepared under conventional hydrolysis of TMOS in MeOH containing various molar percentages of isocyanate groups. Various amounts of compound **5** were added to the initial sol to react with TMOS-NCO.
- **SG2-ACN-DBTP**: silica monoliths prepared under conventional hydrolysis of TMOS in MeOH/ACN mixture. Various amounts of compound **6** were added to the initial sol (grafting).

Silica monoliths were characterized by N₂ adsorption-desorption isotherms (Table 19). All the monoliths have a very high specific surface area (> 500 m² g⁻¹), and were mainly microporous, but with a non-negligible percentage of mesopores (14%-42% of the total surface area).

As a general remark concerning **SGO** materials, we noticed a certain degree of non-reproducibility in different synthesis batches. In Table 19 monoliths have been divided in different series, corresponding to as many syntheses: it can be noticed how the structural characteristics change from one batch to another, even though all materials present high surface area and porosity. The surface area varies between 565 and 685 m² g⁻¹ while the percentage of mesopores varies between 14% and 42% (similar differences concerning the area and the volumes of mesopores); on the contrary, the pore size is not significantly dependent on the series. As a consequence, variations in the photochemical activity of these materials could be expected. Another peculiarity which should be stressed here is the dramatic effect of the photooxidation tests on the structure of **SGO** monoliths: apparently, as a consequence of the use for the photooxidation of DMS, the microporous structure collapses, and the calculated percentage of mesopores increases by 33%-68% in series 3 and 1, respectively, and of 365% in series 2. Such a behavior is not totally unexpected since the monoliths, during the PO tests, undergo really important mechanical stresses: they are dried under vacuum and they are subjected to the strain due to the air flux for approx. one week. The **SGO** monoliths doped with the different PSs were optically transparent (Figure 59) with a macroscopically uniform distribution of the dye. At the end of the aging step, approx. the 20% of the weight of the materials was due to adsorbed water (Table 19), which could be eliminated after 4 to 5 hours treatment under primary vacuum at 80°C.

To decrease the hydrophilic character of **SGO** monoliths,²²⁸⁻²³⁰ different amounts of TMOS-OC (2→5%, **SGO-OC**) were added to the initial sols. The octyl substituent accelerates the rate of hydrolysis by stabilizing the positive charge formed on the Si atom. As expected, in the final **SGO-OC** adsorbed water (Table 19, Figure 59) decreased from 20% (**SGO** monoliths) to approx. 12% of the total mass. Their specific surface area was maintained over 555 m² g⁻¹ with a maximum (640 m² g⁻¹) for the **SGO-OC 2%**: though differences occurred depending on the series, they were less significant than in the case of **SGO** monoliths. Moreover, the microporous/mesoporous ratio and the mesopores characteristics did not show any significant dependence on the OC percentage.

The 50/50 molar mixture of methanol and acetonitrile was used for two reasons: to increase the PS amount in **SGO-DBTP** monoliths since **DBTP** is more soluble in the mixture of the two solvents, and to better compare encapsulated (**SGO-ACN**) and grafted (**SG2-ACN**) **DBTP**. ACN is a polar non-protic solvent: if a mixture of ACN and MeOH is used in sol-gel syntheses, the hydrolysis rate is mainly controlled by MeOH (which creates H-bonding with the alkoxide). In addition, the two solvents have similar polarities (in terms of relative static permittivity, ϵ_r):²³¹ the migration of the dye during the synthesis and its final distribution inside the monolith should not strongly vary using MeOH or MeOH+ACN. As expected, the structure of **SGO** and **SGO-ACN** monoliths was macroscopically similar

(Figure 59), but the addition of ACN made the specific surface area and the mesoporous percentage increase from 605 to 730 m² g⁻¹ and from 22 to 30%, respectively (series 1). In series 2, the surface area of **SG0-ACN** monoliths was similar to that of **SG0** monoliths, while the same increase of the mesopores percentage was noticed. The variations between different synthetic batches also involved this class of materials. **MV** was also encapsulated in **SG0-ACN** monoliths, in order to detect any variations in its spectroscopic properties in the supported phase: due to its sensitivity to the environment **MV** could be used to point out possible variations in the polarity of silica due to the addition of ACN as a solvent.

SG2-ACN-DBTP monoliths (Figure 60a) were prepared starting from freshly prepared **6**. The one-pot condensation between the NH₂ group of **5** and the silyl-isocyanate derivative was chosen to prevent the formation of by-products²³⁵⁻²³⁸ and to avoid post-grafting steps which could endanger the structural stability of the material. A strict stoichiometry control was necessary to avoid the presence of free NCO functions in the sol: while usually disfavored, NCO hydrolysis can occur under the sol-gel conditions (high temperature, high water concentration) and prevent the formation of a transparent and compact structure (see below). Under our conditions, **SG2-ACN-DBTP** monoliths were transparent and macroscopically similar to their **SG0** counterparts, with a higher mesoporous character (38 %) for a significant specific surface area (660 m² g⁻¹), though slightly more fragile: it can thus be concluded that it is possible to graft **DBTP**-derivatives to silica without the formation of any by-product and without jeopardizing the optical and structural properties of the monoliths.

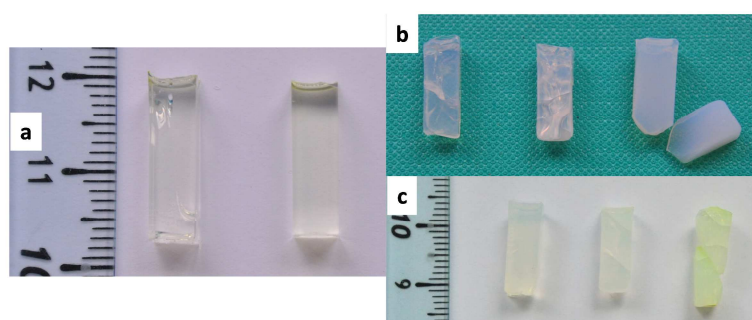


Figure 60 a): **SG2-ACN-DBTP** (left) vs **SG0-ACN-DBTP** (right); b): **SG1** monoliths at various concentrations of NCO and **5**; c): **SG0-NCO** monoliths at different amounts of NCO.

SG0-NCO blank monoliths (Figure 60b) were also prepared, aimed at post-grafting reactions between the NCO groups in silica and the amino derivative of **DBTP**, **5**, without the formation of side-products. The materials were however very fragile and not transparent. Probably because of the exothermic hydrolysis of NCO in the presence of water and methanol in the operative conditions for the preparation of monoliths, the condensation reactions were too fast for the formation of a well-structured matrix. As reported in Table 19, the **SG0-NCO** monoliths presented low surface area and high percentage of mesopores. Due to the unsuccessful preparation of this type of material, neither attempts of post-grafting, nor spectroscopic characterizations, nor photoactivity tests were carried out. Similar results were obtained for **SG1-NCO-DBTP** monoliths (Figure 60c): following this procedure, the amino derivative **5** should react with the NCO groups in the sol (grafting *in situ*). Nevertheless, also in this case the hydrolysis of NCO induced a structural collapse.

Table 19 Structural analysis of silica monoliths. Surface area (B.E.T. method), percentage, area, volume and diameter of mesopores (calculated by B.J.H. method), water percentage (weight) measured by sample weighing before and after drying under vacuum at 80 °C (in brackets values relative to TG-MS analyses). PO = after photooxidation tests. Errors for structural data: approx. 10%.

^{a)} Estimated by the ratio between A_{pores} and S_{BET} .

series	monolith	$S_{\text{BET}} \text{ m}^2 \text{ g}^{-1}$	% mesopores ^{a)}	$A_{\text{pores}} \text{ m}^2 \text{ g}^{-1}$	$V_{\text{pores}} \text{ cm}^3 \text{ g}^{-1}$	$\phi_{\text{pores}} / \text{Å}$	H ₂ O %
1	SG0-ACN-DBTP	730	30	222	0.176	33	16 (20)
	SG2-ACN-DBTP	660	38	252	0.228	37	15 (18)
	SG0-OC 5%	555	23	131	0.140	47	13 (11)
	SG0-OC 2%	640	23	146	0.103	29	12
	SG0	605	22	135	0.108	34	18
	SG0 PO	594	37	223	0.184	35	-
2	SG0-OC 2.5%	558	21	119	0.105	38	13 (11)
	SG0-ACN	560	38	210	0.130	25	22
	SG0	565	14	81	0.060	29	20
	SG0 PO	503	65	329	0.360	44	-
	SG0-SO ₃ H	12	41	5	0.004	30	10
	SG0-NCO	69	64	44	0.041	37	14 (12)
3	SG0	685	42	287	0.251	36	21
	SG0 PO	340	56	190	0.127	27	-

Another explorative synthesis was carried out to prepare some monoliths functionalized with sulfonic acids (**SG0-SO₃H**). These syntheses were aimed at preparing negatively charged monoliths in order to include cationic dyes by means of ionic interactions. These monoliths were very fragile but also extremely transparent. The sulfonic acid groups were obtained by H₂O₂-mediated oxidation of mercapto groups in the initial sol: such an exothermic reaction was probably responsible of the fragility of the monoliths. To prevent this consequence, the synthesis was performed in an ice bath, without however obtaining better results. **MV** and **NMB⁺** were anyway encapsulated in these materials and some spectroscopic and photochemical characterizations were carried out, thanks to the high transparency of the materials. No other synthetic attempts were carried out to create the sulfonate salts from the sulfonic acids for testing the above-mentioned ionic interactions with the positively charged dyes. The reaction route selected for preparing these monoliths is known to be highly exothermic and structured materials were only obtained in surfactant-mediated syntheses. The structural characteristics of **SG0-SO₃H** monoliths (Table 19) are surely related to these synthetic parameters: this type of silica was barely porous, characterized by a surface area of 12 m² g⁻¹ and by a high percentage of mesopores.

In general, many PSs could be easily encapsulated in highly transparent highly porous silica monoliths; the distribution of the dyes was macroscopically uniform in all materials, except particular cases listed below. The final materials were thus suitable for both the spectroscopic characterizations of the supported dyes and for their use as microreactors for the degradation of pollutants at the gas-solid interface. The modifications of the synthetic procedures had the expected consequences: the addition of octyl groups made the monoliths less hydrophilic and essentially microporous,²²¹ the use of acetonitrile as a solvent did not significantly change the final materials, except for slightly higher mesoporosity and surface area,²²¹ sulfonic acids gave to silica an extreme transparency.²³² The addition of NCO groups to silica, following our procedure, provoked dramatic effects, causing the collapse of the porous structure, and fragile non-transparent monoliths were obtained. Probably, this procedure to include NCO functions in silica can be adopted for the preparation of powders for which transparency is not required. Grafting of **DBTP** was successfully achieved without jeopardizing the structural properties obtained for the corresponding **SGO** materials. Unfortunately, we noticed some structural variations between monoliths synthesized in different batches: even slightly different conditions can influence the final result. The parameter that could more probably have caused such differences is the mixing time: depending on the amount of prepared monoliths (considering thus the time needed for pouring the sol in the disposable cuvettes) the initial sol might have been mixed for variable times (even though always around 2 minutes).

1.2.1 Monoliths' shortcomings

Some of the synthesized monoliths were visibly non-uniform. The main example concerns **SGO-RB**, materials which presented a more intensely colored layer at the top of the monolith, evidence that this dye is more soluble in the solvent than in silica (Figure 61a). Such a behavior has been also noticed for other monoliths but usually when the concentration of the dye was very high. In other samples, the concentration of the PS was so high that it was expelled from the silica matrix during the synthesis: in these examples it is possible to notice the presence of colored agglomerates, either at the most external surface of the monolith (Figure 61b) or adsorbed on the internal surface of the cuvettes used as mold for the synthesis (Figure 61c). This occurred for **DCA** and **DBTP**: cyanoanthracene derivatives are rather insoluble in most of the solvents compatible with the sol-gel synthesis. To prevent this effect we successfully undertook the **SGO-ACN** synthesis: the resulting monoliths were macroscopically equal to the **SGO** ones and, at even higher concentration of **DBTP**, the presence of agglomerates was not noticed. As already described, the presence of free NCO groups in the initial sol probably initiates parasite reactions (notably the hydrolysis of the isocyanate functions) which completely jeopardize, even at low NCO percentages, the transparency and the rigidity of the samples (Figure 60b-c). For this reason all the attempts carried out in order to obtain **SGO-NCO** and **SG1-NCO-DBTP** materials were unsuccessful and the corresponding monoliths were not taken into account for all the characterizations.

Many monoliths presented differences at a microscopic scale. For spectroscopic characterizations and for application tests the whole bulk is concerned: such differences in the structure and/or dye distribution may counterbalance each other without influencing the overall properties of the monoliths. A detailed work is being carried out within the group for a detailed analysis of these

materials by fluorescence microscopy and all these non-uniformities are being highlighted; such an analysis is however out of the scope of this work.

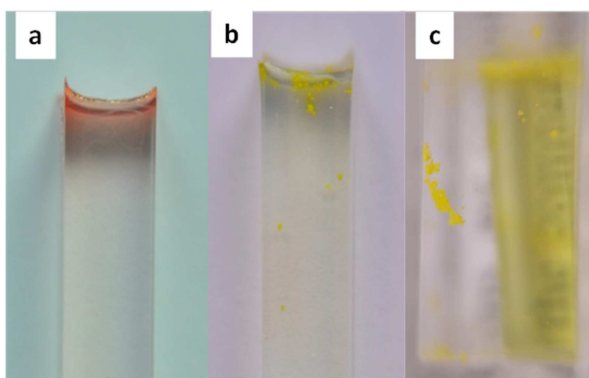


Figure 61 Drag off effect for RB in a diluted sample (**SG0**, a); dye expulsion from the matrix in concentrated **SG0** samples: the case of **DCA** (b, agglomerates at the monolith's external surface), and **DBTP** (c, agglomerates on the cuvette's surface).

2.0 SPECTROSCOPIC CHARACTERIZATION

2.1 UV-Vis and DRUV-Vis spectroscopy

The transparent silica monoliths could be analyzed by transmission UV-Vis spectroscopy since silica absorption was strictly limited to the UV ($\lambda < 300$ nm, dotted line in Figure 62) or by diffuse reflectance UV-Visible (DRUV) spectroscopy for the fragile or cracked samples (Figure 63). The values of the absorption maxima together with the corresponding molar extinction coefficient of the supported dyes were compared to data relative to methanol solutions (Table 20). The molar extinction coefficients were of the same order of magnitude as those reported for MeOH, except for **DBTP** for which 40% variations were observed depending on the silica structure. Relative to MeOH, the shifts in the spectra of **DBTP** are within the range 5-10 nm, depending on the matrix.^{60,63,205} For the other **SG0** materials the shifts relative to MeOH were also negligible (less than 11 nm).

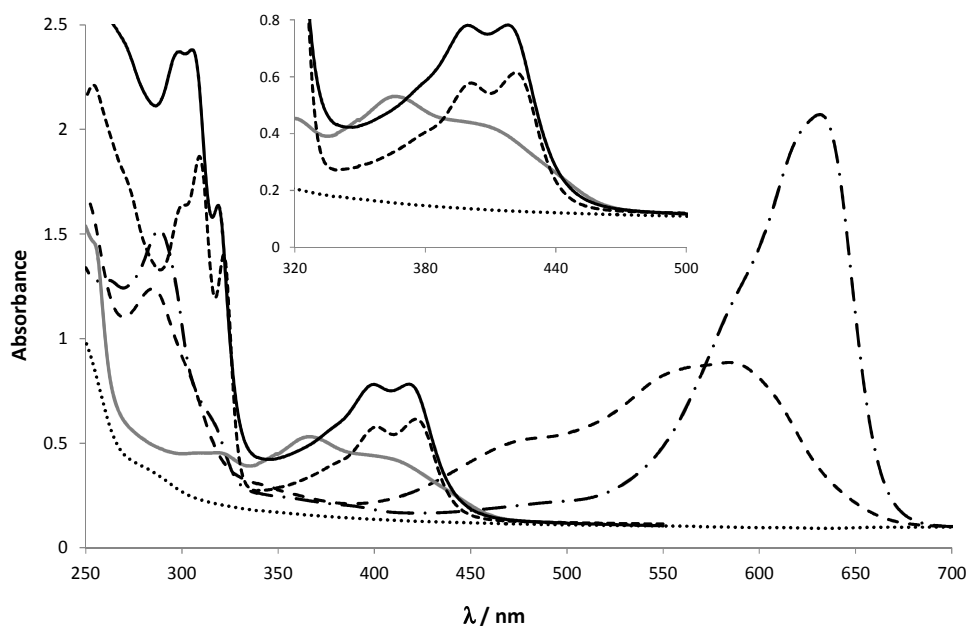


Figure 62 Transmission UV-Vis spectra of some PSs in silica monoliths. **SG0-NMB⁺** (dashed-dotted line), **SG0-MV** (long dashed line), **SG0-ACN-DBTP** (black solid line), **SG0-OC-DBTP** (dashed line), **SG0-PN** (grey solid line) and blank silica sample (dotted line) ($\ell = 0.5$ cm, monoliths). Inset: region between 330 and 500 nm.

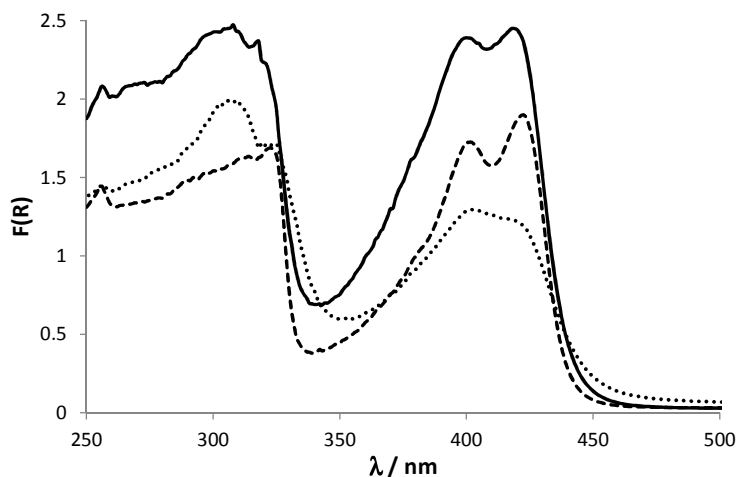


Figure 63 DRUV-Vis spectra of **DBTP**-derived silica materials. **SG0-ACN-DBTP** (solid line), **SG0-OC-DBTP** (dashed line), **SG2-ACN-DBTP** (dotted line).

Except for **MV**, the supported PSs absorption spectra were very similar to those collected in polar solvents: silica monoliths demonstrated to be suitable supports for the spectroscopic characterization of supported dyes. For some samples, due to their fragility, the use of DRUV-Vis was necessary to record absorption spectra. In Figure 63 the DRUV spectra of some **DBTP**-supporting samples are reported. The influence of grafting is clearly visible: the band centered at approx. 420

nm doesn't shift relative to the other samples but is much less structured than for included **DBTP**. Nonetheless, its absorption band is clearly recognizable, and the sample transparency is evident. The slight difference could derive from both the substituent on **DBTP** and the different matrix.

Table 20 Spectroscopic characterization of dye-doped **SG**-materials: maximum absorption wavelengths for the θ - θ transition (λ_{\max}), molar extinction coefficients at λ_{\max} (ϵ_{\max}), maximum wavelengths of fluorescence emission ($\lambda_{\max,em}$) and fluorescence lifetimes (τ_F); in brackets the corresponding values for PSs in MeOH (or in other solvents if specified).

^{a)} Calculated from the PS amount and its absorbance in the monolith. A volume of 0.44 cm³ (mL) was considered to calculate the PS molar concentration. Uncertainty: approx. 10%.

^{b)} Estimated from DRUV spectra.

monolith	λ_{\max} / nm ($\lambda_{\max,MeOH}$)	ϵ_{\max} / M ⁻¹ cm ^{-1a)} ($\epsilon_{\max,MeOH}$)	$\lambda_{\max,em}$ / nm ($\lambda_{\max,MeOH}$)	τ_F / ns (τ_F , solution)
SG0-RB	550 (555)	43 000 (85 000)	563 (570)	-
SG0-MB⁺	650 (655)	- (72 000)	-	τ_1 0.6 (90%) τ_2 1.4 (10%) (0.6, air)
SG0-NMB⁺	635 (628)	60 000 (73 000)	644 (649)	τ_1 0.7 (0.7, air)
SG0-DCA	426 (423)	7 000 (10 800)	434 (436)	τ_1 5.6 (74%) τ_2 12.2 (26%) (12.7 ACN, air) (7.6 ACN, O ₂)
SG0-PN	370 (363)	9 600 (10 200)	-	-
SG0-DBTP	420 (415)	5 000 (9500)	508 (493)	-
SG0-OC-DBTP 2%	425	7 550	502	-
SG0-ACN-DBTP	421	5 600	500	τ_1 2.1 (79%) τ_2 7.2 (21%) (5.4, air) (3.2, O ₂)
SG2-ACN-DBTP	424 ^{b)}	4 500 ^{b)}	470	τ_1 1.9 (78%) τ_2 8.0 (22%) (5.4, air) (3.2, O ₂)

2.2 Fluorescence spectroscopy

Except for the too concentrated **SG0-MB⁺** and non-fluorescent **SG0-PN**, fluorescence excitation and emission spectra were recorded for all the samples. The emission spectrum of **DBTP**, as previously described for solutions, is particularly dependent on both the medium (solvent) and the substituent. In a given solvent, for differently functionalized **DBTP** derivatives **1-4**, a bathochromic shift, inversely proportional to the polarity of the substituent, was observed (Chapter 4). Relative to **DBTP** (encapsulated), compound **6** is more polar, due to the presence of the linker groups: such a different

polarity explains the bathochromic shift of the emission maximum in **SG0-ACN-DBTP** relative to **SG2-ACN-DBTP** monoliths (approx. 30 nm, Table 20 and Figure 64). Fluorescence emission of **DBTP** is thus primarily dependent on the chemical modification carried out on the dye, whereas the effect of the medium (**SG0** vs **SG0-ACN**) seems to be negligible. Thanks to the extremely high quantum yield of fluorescence of **DCA**, it was possible to record very clean and resolved fluorescence spectra, which are very similar to those in MeOH (Figure 65).

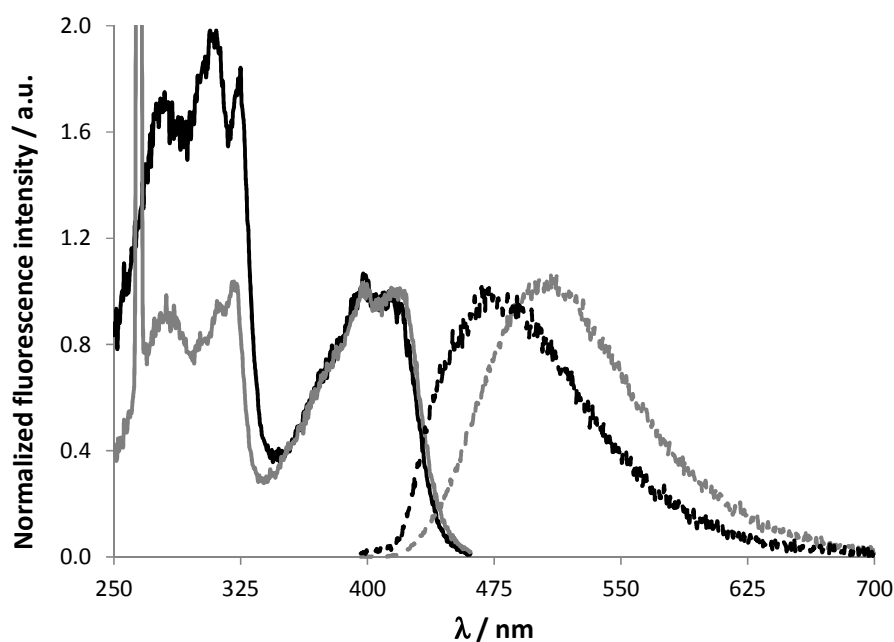


Figure 64 Fluorescence excitation ($\lambda_{em} = 470$ nm, solid lines) and emission ($\lambda_{ex} = 385$ nm, dashed lines) spectra of **DBTP**-derived silica materials: **SG0-ACN-DBTP** (grey) and **SG2-ACN-DBTP** (black).

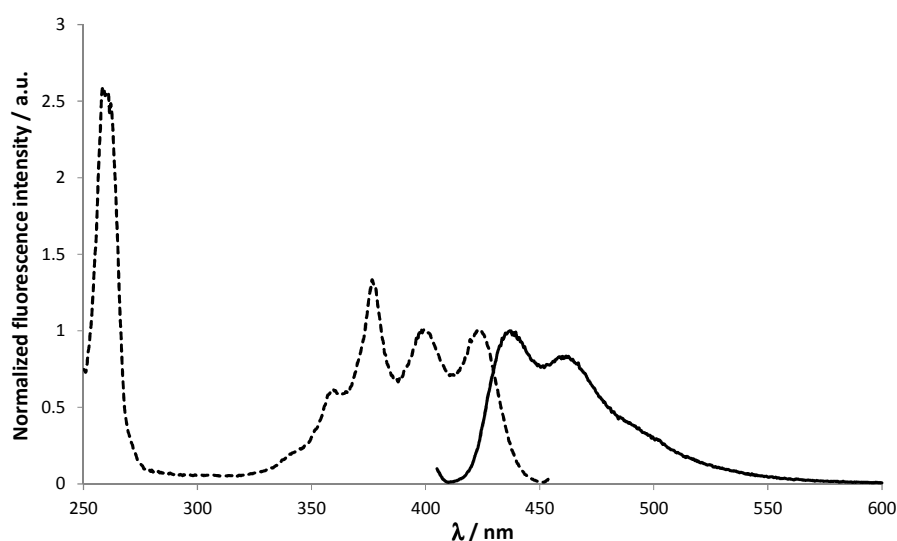


Figure 65 Fluorescence excitation ($\lambda_{em} = 460$ nm, dashed line) and emission ($\lambda_{ex} = 400$ nm, solid line) spectra of **SG0-DCA**.

Even though slightly less defined, the excitation-emission spectra of **SGO-NMB⁺** are very similar to those recorded in solutions (5 nm shift in the emission spectrum). In Figure 66 the spectra corresponding to three differently concentrated monoliths are reported: the fluorescence signal intensity for the three samples is linearly proportional to the dye concentration.

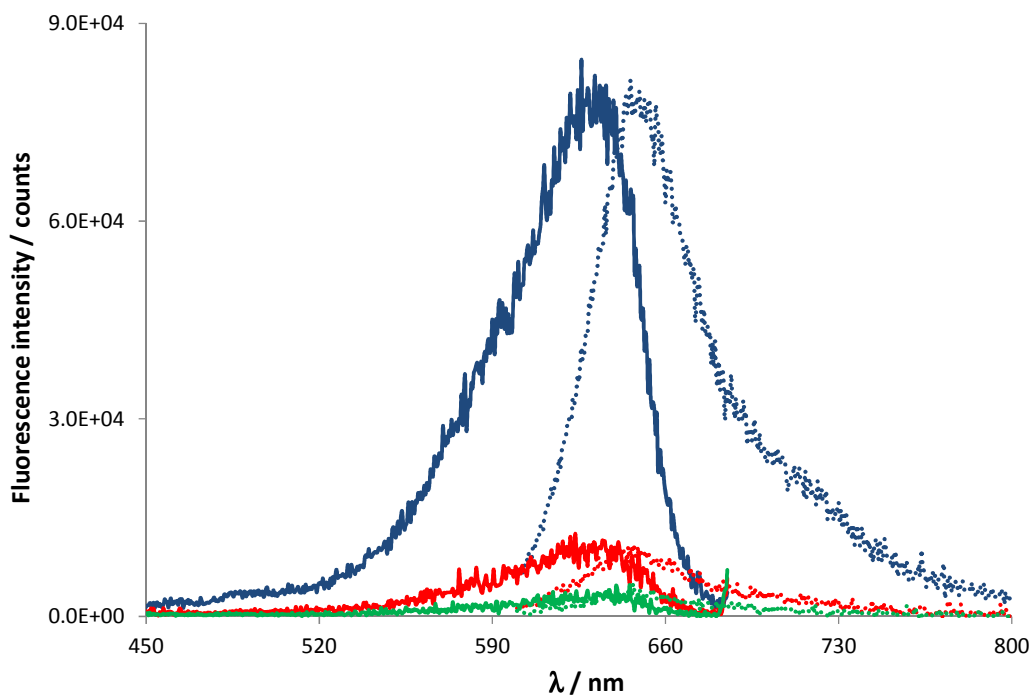


Figure 66 Fluorescence excitation ($\lambda_{em} = 690$ nm, solid lines) and emission ($\lambda_{ex} = 590$ nm, dotted lines) spectra of differently concentrated **SGO-NMB⁺** monoliths: the intensity of the fluorescence signals increases linearly with the PS concentration.

The fluorescence lifetimes of the silica-encapsulated PSs are listed in Table 20: for **MB⁺** and **NMB⁺**, very short lifetimes were found, in contrast with **DBTP** and mainly with **DCA**. For **SGO-MB⁺**, our bi-exponential fluorescence decay (0.6 (90 %) and 1.4 (10 %) ns) is consistent with previous data reported by Wetzler *et al.* for Nafion-supported **MB⁺** (0.2 (89 %) and 1.7 (11 %) ns).⁸² Moreover, these data are consistent with the fluorescence lifetimes we measured in MeOH (0.60 ns) and ACN (1.01 ns) and with those reported for **MB⁺** in water (0.37 (91 %) and 0.82 (9%) ns).³²⁷ As in solution, the singlet excited state of **MB⁺** is rapidly deactivated by intersystem crossing; traces of solvent in silica probably contributes to such short lifetimes. The monoexponential fluorescence decay of supported **NMB⁺** (0.70 ns) is consistent with the value measured for **SGO-MB⁺** and with the τ_F measured in ACN (0.86 ns) and MeOH (0.70 ns). Biexponential fluorescence decays were observed with **DCA**- and **DBTP**- monoliths. For **SGO-DCA** the longer (12.2 (26 %) ns) and the shorter (5.6 (74 %) ns) lifetimes recalled the values obtained respectively in air-equilibrated (12.7 ns) and in oxygen-saturated (7.6 ns) ACN,²⁰⁵ as if the main fraction of **DCA** was forced in pores together with higher concentrations of oxygen and water, which could efficiently quench its singlet excited state. Similarly, for **SGO-ACN-DBTP** and **SG2-ACN-DBTP** monoliths (2.1 (79 %) and 7.2 (21 %) ns, and 1.9 (78 %) and 8.0 (22 %) respectively), a good agreement was found between the shorter lifetime component and the values in oxygenated solutions (1.3 and 3.2 ns in chloroform and methanol respectively), while the longer component was closer to the values in air-equilibrated solutions (between 2.4 and 5.4 ns).

The similarity between the values recorded for **SG0** and **SG2** monoliths demonstrates that grafting has not a dramatic influence on the photophysical properties of the dye. Except for **DCA**, all the samples showed an additional very short lifetime (60 to 300 ps, not reported in Table 20). Bi- and tri-exponential decays with very short lifetimes were already observed with silica supported photosensitizers and were attributed to light diffraction^{328,329} or to the presence of hydrogen bonds between silica and the dye.³³⁰ The first assumption should more probably account for our results. Fluorescence quantum yields could not be calculated due to the absence of a reference in such a solid host.

2.3 Spectroscopic behavior of silica-embedded MV

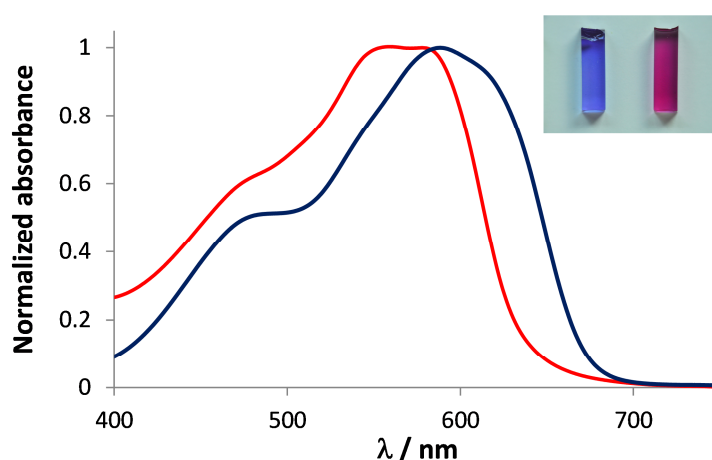


Figure 67 UV-Vis spectra of **SG0-ACN-MV** (blue, left in the picture) and **SG0-MV** (red, right in the picture) ($l = 0.5$ cm, monoliths).

For **SG0-MV** (Figures 62 and 67) the broad absorption band seems to be formed by the superimposition of absorption signals recorded in ACN and in alcoholic solution, giving the large maximum between 560 and 585 nm. Probably, **MV** in silica is partially segregated in more protic sites, which induce the formation of **MV-OH** together with **MV**. More protic sites can derive from higher concentrations of acidic OH groups (silanols).³³¹ The addition of ACN during the monoliths' synthesis (**SG0-ACN**) caused an enlargement of the absorption band in the monolith towards higher wavelengths, while at lower wavelengths the band coincides with that recorded for **SG0** materials. In the picture reported in Figure 67, the different color of the two materials is clearly visible to the naked eye. Such a bathochromic shift can be due to the formation of aggregates during the initial steps of the synthesis (Figure 67). The solvent effect in the initial sol could influence the distribution of the dye and the dye/dye-dye/silica interactions (both **MV** and **MV-OH** must be considered) responsible of the spectroscopic behavior observed in the final materials. The molar extinction coefficients estimated for **MV** in silica are closer to those calculated for MeOH or acidified ACN, further suggesting the presence of both forms of **MV** (see Table 21).

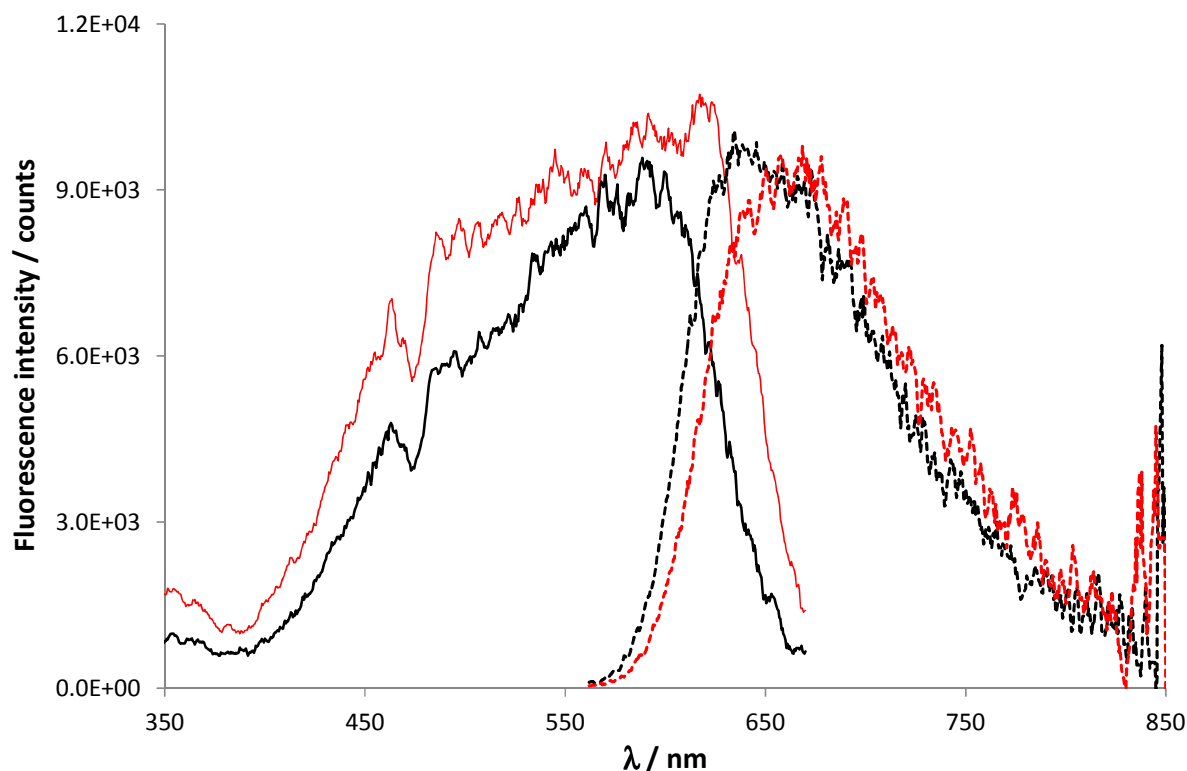


Figure 68 Fluorescence excitation ($\lambda_{em} = 675$ nm, solid lines) and emission ($\lambda_{ex} = 555$ nm, dashed lines) spectra of **MV**-derived silica materials: **SG0-MV** (red) and **SG0-ACN-MV** (black).

The influence of the silica host material can be also noticed in the fluorescence spectra of supported **MV** (Figure 68). In Table 21 the main spectroscopic parameters of **MV** in different media are summarized, in order to globally analyze the spectroscopic properties of this dye. The variation in the position of the fluorescence bands in different media most probably derives from the presence of differently acidic sites which affect the spectroscopic behavior of **MV**. Silica (**SG0**) appears to be more “protic” than MeOH (solution): consistently to the model developed in the previous chapter, both the excitation and emission spectra are red-shifted relative to the solution and the λ_{max} values are similar to those observed for acidified ACN solutions. It is known that silanols are more acidic than their corresponding alcohols,³³¹ which could explain this behavior. The use of a mixture of ACN and MeOH as a solvent for the sol-gel synthesis apparently makes silica less acidic than in the case of conventional preparation: the fluorescence spectra are more similar to those obtained in methanol solutions and blue-shifted relative to **SG0** monoliths, *i.e.* the fluorescence spectrum arises from the presence of both **MV** and **MV-OH**, in a ratio close to the one calculated for methanol. Moreover, the emission spectrum recorded with **SG0-ACN-MV** presents a shoulder at approx. 665 nm, coincident with the maximum recorded for **SG0-MV**: it emerges thus that in **SG0-ACN** monoliths the dye is located in two differently acidic sites. Hence, silica can be considered as an acidic medium; in addition to the effect on porosity and surface area, modifications in the synthesis can also influence the acid-base character of the material. During the generation of the silica structure, different sites can be formed, characterized by different acidity.

The data concerning the absorption spectra deviate from this analysis: probably some artefacts deriving from the presence of agglomerates induce an apparent hypsochromic shift (relative to

acidified ACN and even to MeOH) of the absorption bands recorded with the monoliths (Table 21). Moreover, from our results we can deduce that the aggregates (probably dimers, which can be easily formed with many PZT dyes)⁵⁹ which induce a significant enlargement of the absorption band towards higher wavelengths in **SGO-ACN** materials, are not fluorescent: the absorption and excitation spectra do not coincide.

Table 21 Spectroscopic parameters of **MV** in various solvents and silica monoliths: absorption, fluorescence excitation-emission maximum wavelengths (λ_{\max}), absorption extinction coefficients (ϵ_{\max}) and fluorescence lifetimes (τ_F).

^{a)} Uncertainty: 10%.

^{b)} Estimated from the analysis of the effect of adding $\text{CH}_3\text{SO}_3\text{H}$ to ACN.

medium	$\lambda_{\max} / \text{nm}$			$\epsilon_{\max} / \text{M}^{-1} \text{cm}^{-1\text{a}}$	τ_F / ns
	absorption	excitation	emission		
MeOH	600	600	642	21600	0.50 ± 0.05
ACN	549	552	628	60100	1.49 ± 0.10
ACN + $\text{CH}_3\text{SO}_3\text{H}$	620	616	666	33000 ^{b)}	0.35 ± 0.05
SGO	585	613	666	39900	0.70 ± 0.07
SGO-ACN	595	585	637	32800	0.90 ± 0.07

The **MV** fluorescence signal decayed mono-exponentially, with lifetimes of 0.70 and 0.90 ns, for **SGO** and **SGO-ACN**, respectively, similar to the values measured for **MV** in MeOH (0.50 ns) and ACN (1.49 ns). It thus seems that silica induces slightly longer lifetime for the “singlet” excited state of **MV**. In addition, a higher τ_F for **SGO-ACN-MV** than for **SGO-MV** was expected on the basis of the above-mentioned lower acidity of the former: we already observed that in solutions increasing acidity decreased fluorescence lifetimes.

3.0 ANALYSIS OF THE TRANSIENT SPECIES

The transient species of the PSs were studied directly inside the monoliths by nanosecond laser flash photolysis and characterized by their absorption spectra as well as their lifetimes (Table 22). Unfortunately, as for solutions, ground state photobleaching prevented the exact determination of the absorption maxima for all the PSs.

The transient absorption spectra recorded for **SGO-DCA** and **SGO-PN**, reported in Figure 69, are perfectly consistent with those reported in the literature for solutions. The absorption spectrum of **PN** shows three apparent maxima at 340, 400 and 490 nm, all of which have been assigned to the triplet excited state: no other transient species are formed upon irradiation.⁵¹ The transient absorption spectra of **DCA**, though hardly detectable in the absence of heavy atoms in order to enhance ISC, could be easily obtained.^{42,43} The absorption maximum should be positioned between the apparent maxima at 390 and 470 nm: consistently, Olea *et al.*⁴² reported a triplet-triplet

absorption spectrum with maxima at 415 and 445 nm, followed by a shoulder at 530 nm. Since good agreement with the results in solutions is obtained, transparent silica monoliths can actually be used as suitable host materials for the photophysical characterization of supported-dyes.

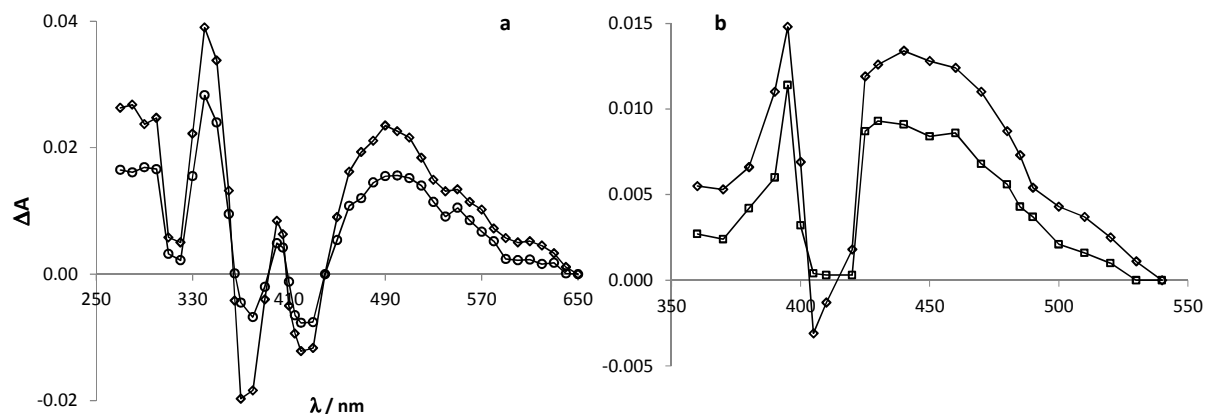


Figure 69 Time-evolution of the transient spectrum obtained by laser flash photolysis of a) **SG0-PN** (80 ns, diamonds, and 1 μ s, circles, after the laser pulse) and b) **SG0-DCA** (60 ns, diamonds, and 100 ns, squares, after the laser pulse).

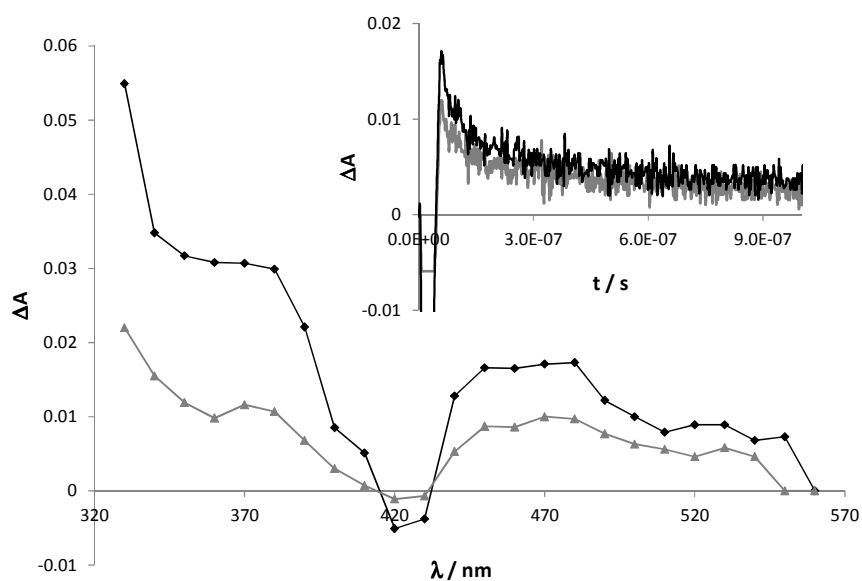


Figure 70 Time-evolution (50 ns, black squares, and 250 ns, grey triangles, after the laser pulse end) of the transient spectrum obtained by laser flash photolysis of **SG0-DBTP**. Inset: transient decays after irradiation of **SG0-DBTP** (grey) and **SG0-ACN-DBTP** (black); signals monitored at 470 nm.

The transient absorption spectra of **DBTP**, in both **SG0** and **SG0-ACN** materials were very similar to those obtained for ACN solutions (Figures 20 and 22, Chapter 4), with apparent maxima at approx.

370 and 470 nm (Figure 70). As reported above, no transient species other than the triplet excited state could be detected for the entire **DBTP** family, even though the formation of the radical anion should be possible. Notwithstanding the solid matrix, the triplet excited state is always the unique transient species detected by laser flash photolysis. Moreover, despite the different structures of **SGO** and **SGO-ACN** matrices (Figure 70), the same spectrum was obtained with the two materials. The photophysics of **DBTP** is confirmed to be very stable and barely influenced by the medium. The linear dependence of the transient absorbance on both the laser pulse energy (5-28 mJ) and the PS concentration confirms the monophotonic formation of the transient species and the absence of dimeric species in the ground state.

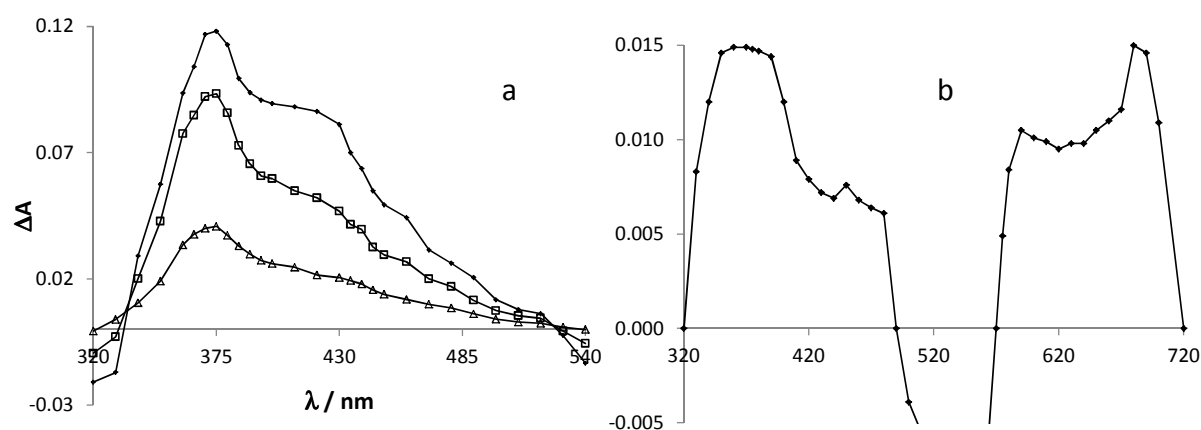


Figure 71 a) time-evolution of the transient spectrum obtained by laser flash photolysis of **SGO-MB⁺** (monitored at 70 ns, diamonds, 1 μ s, squares, and 7 μ s, triangles, after the laser pulse end) and b) transient absorption spectrum of **SGO-RB** recorded at the laser pulse end.

The detection of the transient species of **RB** in silica monoliths was only partially successful. The transient decays were too noisy to acquire the corresponding rate constants and the absorbance was below the detection limit: only the absorption spectrum at the laser pulse's end could be obtained (Figure 71b). It is characterized by a maximum at 370 nm followed by two other apparent maxima at higher wavelengths (590 and 680 nm). Our result is, in this case, scarcely consistent with literature data. Murasecco-Suardi *et al.*²⁸⁹ reported an absorption maximum at 470 nm, Grajcar *et al.*³³² at 820 nm, Ketsle *et al.*³³³ reported two maxima at 450 and 620 nm, Shimizu *et al.*³³⁴ observed an absorption maximum at 1070 nm. Unfortunately, our data are not precise enough to go further in this analysis, even more difficult due to the discrepancies of the already published data.

For **SGO-MB⁺** (Figure 71a) it was possible to identify the triplet excited state, with two maxima at 370 and 420 nm. The band at 370 nm is actually composed by the triplet absorption and that of another transient with slightly longer lifetime which could not be precisely assigned. To our knowledge, no transient species has been reported to absorb around 370 nm. The triplet-triplet absorption spectrum recorded for **SGO-MB⁺** is significantly blue-shifted (approx. 50 nm) relative to those recorded in ACN and MeOH (Figure 48, Chapter 5): the matrix effect is clearly important and every precise assignment is difficult. Wetzler *et al.* monitored the supposed triplet excited state produced

upon irradiation of Nafion[®]-supported **MB**⁺ at 420 and 870 nm, but unfortunately they did not report the absorption spectrum.⁸²

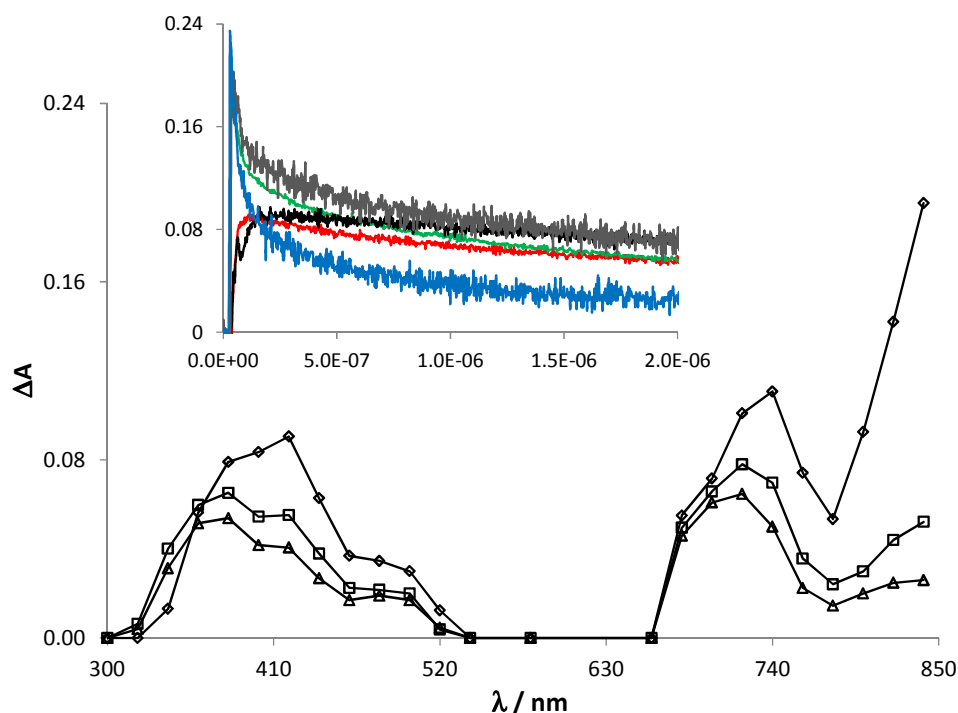


Figure 72 Time-evolution (65 ns, diamonds, 250 ns, squares, and 1 μ s, triangles, after the laser pulse end) of the transient spectrum obtained by laser flash photolysis of **SG0-NMB**⁺. Inset: transient decays at different wavelengths: 340 nm (red), 420 nm (green), 680 nm (black), 740 nm (grey) and 840 nm (blue).

The transient absorption spectrum of **SG0-NMB**⁺ is reported in Figure 72. It is very close to the one obtained with **SG0-MB**⁺ materials, showing a maximum at 420 nm, followed by a shoulder at approx. 500 nm and, in the red part of the spectrum, a maximum at 740 nm. Several species appeared at different wavelengths, as showed in the inset of Figure 72. It should be pointed out that a very short signal (< 100 ns) attributed to scattering phenomena, due to silica, is observed and is similar to that accounted for the very short fluorescence lifetimes. A species mainly absorbing at 720 nm could not be identified, while the triplet excited state has been assigned to the main signal in the blue part of the spectrum, with a maximum at 380 nm followed by two shoulders at 420 and 480 nm. Probably, as for **SG0-MB**⁺, two superimposed transient absorption bands form this signal. Also in this case the effects of the solid matrix induce a shift of the triplet-triplet absorption spectrum by approx. 40 nm towards the UV (Figure 49, Chapter 5). Considering the relative position of the bands, it is possible that such a T-T absorption band is partially due to the photoejection of one electron, creating the semireduced (**NMB**^{*}) and the semioxidized (**NMB**^{*2+}) forms of the dye, respectively absorbing at 360 and 500 nm. However, this possibility is just hypothetically devised: further tests should be carried out to fully interpret this transient absorption spectrum. Despite the important shift in the absorption spectrum, for **SG0-NMB**⁺ as for **NMB**⁺ in solution, the triplet excited state is the main transient species formed upon irradiation.

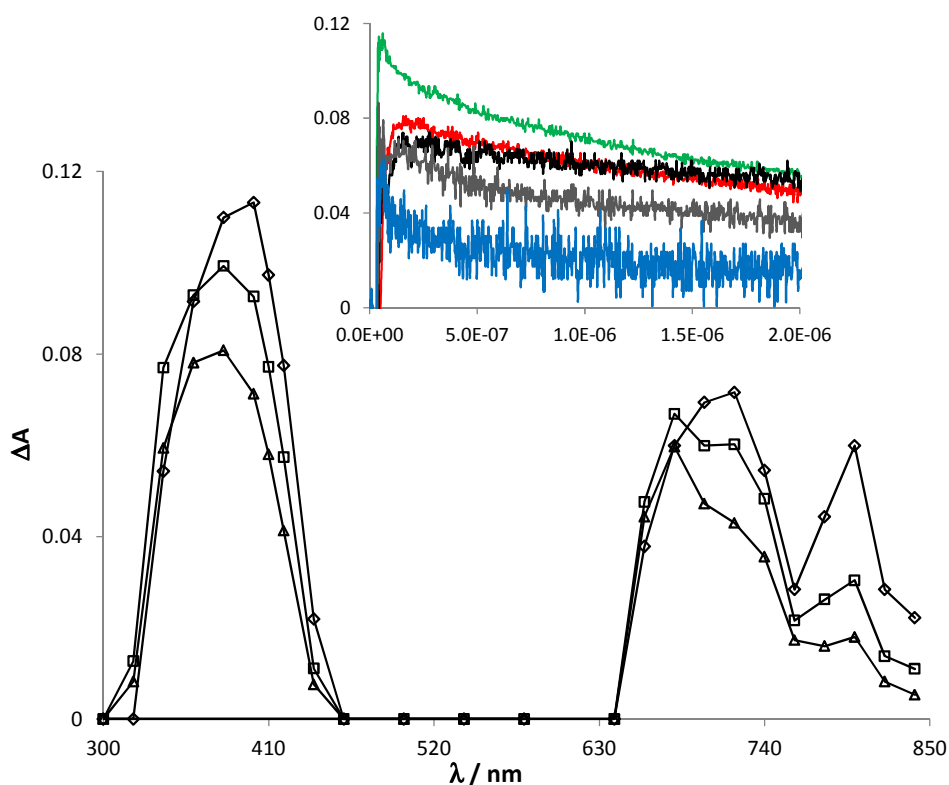


Figure 73 Time-evolution (65 ns, diamonds, 250 ns, squares, and 1 μ s, triangles, after the laser pulse end) of the transient spectrum obtained by laser flash photolysis of **SG0-MV**. Inset: transient decays at different wavelengths: 340 nm (red), 400 nm (green), 680 nm (black), 720 nm (grey) and 800 nm (blue).

The transient absorption spectrum of **SG0-MV** reported in Figure 73 can be analyzed similarly to **SG0-NMB⁺** material. A first very short-living species absorbs at 400, 720 and 800 nm; within all these wavelengths similar decays were obtained. Two other species are more likely present, as it can be noticed from the different lifetimes measured at different wavelengths. The triplet state is mainly responsible of the absorption band in the blue, with a maximum at 380 nm. Such a spectrum is similar to that recorded in MeOH (Figure 50, Chapter 5), even though blue-shifted by approx. 40 nm, as noticed for the other phenothiazine dyes. The broad band between 640 and 850 nm is, as for **MV** in solutions, difficultly assigned to precise species: it probably arises from the triplet excited state and other species which could not be identified. The similarities with the spectrum in MeOH suggest the presence of both **MV** and **MV-OH** in silica monoliths, confirming our previous assumptions.

All the measured τ_T , as well as the rate constants of transient decay, are reported in Table 22. The triplet lifetime measured with **SG0-PN** monolith (3.4 μ s) is much longer if compared to values obtained for aerated solutions, between 230 and 470 ns depending on the solvent,⁴⁵ but shorter than the values measured in de-aerated solutions (approx. 40 μ s).^{46,51} Except for **DBTP**, similar results were obtained for the other PSs. For **SG0-MB⁺** we obtained a triplet lifetime of 4.5 μ s, against the 12.5 and 0.28 μ s lifetimes measured in Ar-saturated and air-equilibrated ACN, respectively. Our results are consistent with those of Wetzler *et al.*,⁸² who reported triplet lifetimes of 19 and < 1 μ s for dry and wet Nafion[®]-supported **MB⁺**. **NMB⁺** in monoliths presented a triplet lifetime of 3.1 μ s,

which is very close to the values recorded for Ar-saturated ACN (3.7 μs) and MeOH (4.8 μs); for **MV** the 2.6 μs lifetime is closer to those measured in de-aerated ACN (8.3 μs) and MeOH (5.9 μs) than to air-equilibrated solutions (approx. 200 ns). All these values suggest that inside the matrix there is enough oxygen to quench the triplet excited state of the PSs but less than in air-equilibrated organic solvents. In addition, it is possible that the matrix plays a stabilization effect on the transient state by decreasing the collisions between the excited molecules and the environment (liquid solvent vs silica). It should be considered that to longer triplet lifetimes corresponds a higher probability of triplet quenching by oxygen to generate $^1\text{O}_2$. Thus, with these materials an efficient singlet oxygen production could be expected. Contrary to what observed for all the above-mentioned PSs, the triplet lifetime of supported **DBTP** (approx. 300 ns) was roughly the same as in air-equilibrated ACN. This PS is probably more sensitive than the others to small amounts of water or oxygen which can be included in the monolith. Alternatively, such a reduced lifetime can be ascribed to triplet deactivation by the host, as for porphyrins intercalated in layered doubled hydroxides.³³⁵

Table 22 Rate constants of transient decay (k_d) at different monitoring wavelengths, triplet excited state lifetimes measured for several silica monoliths and triplet excited state lifetimes in ACN (air-equilibrated and Ar-saturated solutions) and MeOH.

monolith	λ / nm	k_d / s^{-1}	τ_T / μs	τ_T / μs (ACN)	
				air	Ar
SG0-DBTP	470	$(3.3 \pm 0.3) \times 10^6$	0.30 ± 0.04	0.25-0.30	5.0-8.3
SG0-ACN-DBTP	470	$(3.3 \pm 0.3) \times 10^6$	0.30 ± 0.04		
SG0-PN	490	$(2.9 \pm 0.2) \times 10^5$	3.4 ± 0.3	0.23 ⁴⁵	-
SG0-DCA	470	$(5.1 \pm 0.5) \times 10^5$	2.0 ± 0.3	-	-
SG0-MB⁺	420	$(2.2 \pm 0.4) \times 10^5$	4.5 ± 0.4	0.28	12.5
SG0-NMB⁺	380	$(3.2 \pm 0.4) \times 10^5$	3.1 ± 0.3	0.37	3.7
	720	$(1.1 \pm 0.1) \times 10^6$		(0.25, MeOH)	(4.8, MeOH)
SG0-MV	380	$(3.9 \pm 0.4) \times 10^5$	2.6 ± 0.3	0.20	8.3
	720	$(1.0 \pm 0.1) \times 10^6$		(0.19, MeOH)	(4.8, MeOH)

4.0 SINGLET OXYGEN DETECTION

4.1 Singlet oxygen lifetime

Singlet oxygen lifetimes (τ_{Δ}) in the monoliths were determined by time resolved $^1\text{O}_2$ phosphorescence detection. Singlet oxygen phosphorescence decay traces observed for the series of **SG0-PN**, **SG0-DBTP** and **SG0-RB** monoliths could be fitted with a single exponential function from which τ_{Δ} values were derived (equation 3.29, Table 23). The measured τ_{Δ} in **SG0-DBTP**, **SG0-PN**, **SG0-DCA** and **SG2-ACN-DBTP** monoliths was in the range 18-21.5 μs , slightly lower than the values previously published, between 22 and 25 μs (values confirmed by new measurements).¹¹⁶ The measured τ_{Δ} for **SG0-RB** was slightly lower (15 μs) but, in contrast to the other cases, **RB** was not homogeneously distributed in the monolith.

Table 23 Values of $^1\text{O}_2$ lifetimes (τ_{Δ}) derived from monoexponential decays in the case of **PN**, **DCA**, **DBTP** and **RB** monoliths (a) and from biexponential decays in the case of **SG0-MV** and **SG0-NMB⁺** (b).

a)	Monolith	$\tau_{\Delta} / \mu\text{s}$	b)	monolith	$\tau_{\Delta,1} / \mu\text{s}$	$A_1 / \%$	$\tau_{\Delta,2} / \mu\text{s}$	$A_2 / \%$
	SG0-PN	20.0 ± 1.0		SG0-MV	16.0 ± 1.0	96	107 ± 30	4
	SG0-DCA	21.5 ± 0.8		SG0-NMB⁺	14.0 ± 1.0	95	136 ± 28	5
	SG0-DBTP	18.0 ± 1.0						
	SG2-ACN-DBTP	19.0 ± 1.0						
	SG0-RB	15.0 ± 1.0						

Decay traces observed for **SG0-MV** and **SG0-NMB⁺** could only be fitted with a bi-exponential function. Lifetimes $\tau_{\Delta,1}$ and $\tau_{\Delta,2}$ were derived from equation 3.30 (Table 23). The contribution of the decay with the longest lifetime (above 100 μs) was however weak ($\leq 5\%$). Two hypotheses may be proposed for explaining the apparent $^1\text{O}_2$ biexponential decay: i) the PSs may locate in two different sites with different properties for $^1\text{O}_2$ deactivation, and rate of $^1\text{O}_2$ exchange between these two sites is much slower than $^1\text{O}_2$ decay in each site; ii) electron transfer from the PS triplet excited state to molecular oxygen could occur in parallel with energy transfer and recombination of the radical ions pair (PS^{*+} and $\text{O}_2^{\bullet-}$) might produce $^1\text{O}_2$; in this case the apparently longer lived $^1\text{O}_2$ emission would be in fact delayed $^1\text{O}_2$ production. Control experiments carried out in ACN solution confirmed however that such a behavior was specific for the silica matrix: it is more probable that the bi-exponential decays are due to the presence of different sites for $^1\text{O}_2$ generation with different quenching effects. Moreover, we could point out the presence of different sites in silica analyzing the spectroscopic properties of **MV**. Because of the low contribution of the latter signal, discrimination between these two (or other) hypotheses was however not possible. It may be noticed that the most significant short lifetime component is smaller (14-16 μs) in the case of the phenothiazine dyes **MV** and **NMB⁺** than in the case of **PN** and **DBTP** (18-20 μs). This difference could possibly be assigned to the significant singlet oxygen quenching by the PS in the presence of **MV** and **NMB⁺**. It is worth noticing

here the negligible effect of grafting on τ_{Δ} : the differences between **SG0** and **SG2** monoliths (in the case of **DBTP**) are within the experimental errors.

4.2 Singlet oxygen production and quantum yields

The quantum yields of $^1\text{O}_2$ production (Φ_{Δ}) by the PSs inside the monoliths were determined by measuring the $^1\text{O}_2$ luminescence signals (S_e) at various PS concentrations for **SG0-ACN-DBTP**, **SG2-ACN-DBTP**, **SG0-MV**, **SG0-NMB[†]**, **SG0-RB** and **SG0-PN** monoliths. **PN** was chosen as a reference for applying the procedure previously described. Relative to the measurements in solution, in this case the quantum yields of singlet oxygen production cannot be considered absolute, since Φ_{Δ} is not known for silica-supported **PN**. The photon flux absorbed by the PS (α_{PS}) was calculated subtracting to the total measured absorbance at the irradiation wavelength that of a blank silica monolith. The relationship between S_e and α_{PS} , equation 6.01, is directly obtained from equations 3.14 and 3.16.

$$S_e = KP_0 \alpha_{\text{PS}} \tau_{\Delta} \Phi_{\Delta} = b \alpha_{\text{PS}} \quad 6.01$$

Table 24 Slopes (b) of the variation of the $^1\text{O}_2$ emission intensity (S_e) as a function of the photon flux absorbed by the PS (α_{PS}) (equation 6.01), quantum yields of $^1\text{O}_2$ production relative to **PN** ($\Phi_{\Delta, \text{rel}}$).

^{a)} Measurements on 6-years old monoliths (data published in ref¹¹⁷).

^{b)} Φ_{Δ} measured for **DBTP** derivatives **4**, to differentiate from just included **DBTP** (**1**).

monolith	b	$\Phi_{\Delta, \text{rel}}$ (τ_{Δ} variable)	$\Phi_{\Delta, \text{rel}}$ (τ_{Δ} average = 19 μs)	$\Phi_{\Delta, \text{ACN}}$ ($\Phi_{\Delta, \text{MeOH}}$)
SG0-PN	4.7 ± 0.3	1	1	1
SG0-DCA ^{a)}	-		$(1.02 \pm 0.08)^{117}$	0.30
SG0-DBTP ^{a)}	-		$(0.89 \pm 0.05)^{117}$	0.91
SG0-ACN-DBTP	4.4 ± 0.3	1.00 ± 0.08	0.9 ± 0.08	0.91
SG2-ACN-DBTP	2.7 ± 0.1	0.63 ± 0.08	0.6 ± 0.08	$0.82^{\text{b)}$
SG0-MV	3.5 ± 0.2	1.30 ± 0.07	1.0 ± 0.07	0.60 (0.73)
SG0-NMB[†]	2.1 ± 0.1	0.70 ± 0.06	0.6 ± 0.06	0.66 (0.82)
SG0-RB	2.2 ± 0.1	0.80 ± 0.09	0.6 ± 0.09	0.42 (0.76)

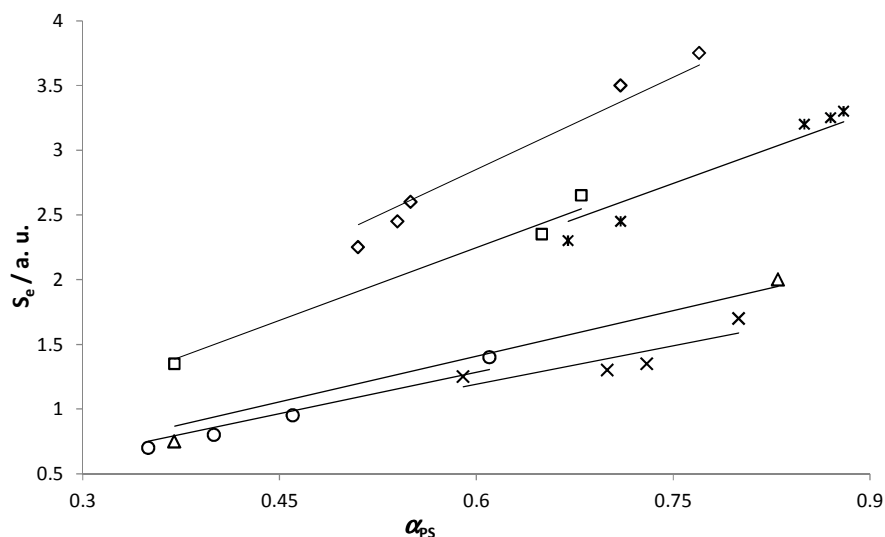


Figure 74 Variation of the $^1\text{O}_2$ phosphorescence signal as a function of the photon flux absorbed by the PS for **SG0-ACN-DBTP** (squares), **SG2-ACN-DBTP** (triangles), **SG0-PN** (diamonds), **SG0-MV** (stars), **SG0-NMB⁺** (crosses) and **SG0-RB** (circles). Point zero is taken into account for all the linear fits.

The linearity of these plots (Figure 74) attested that, in the range of concentrations used in this work, the Beer-Lambert law was valid (diluted samples, absence of aggregation phenomena).^{4,286} Moreover, this linear relationship showed that quenching of $^1\text{O}_2$ by the sensitizer itself could be neglected ($k_t^{\text{PS}}[\text{PS}] \ll k_d$). The ratio of the b values obtained for each PS and the reference sensitizer allowed the determination of relative quantum yields of $^1\text{O}_2$ production ($\Phi_{\Delta,\text{rel}}$) using equation 3.27. Values of b and $\Phi_{\Delta,\text{rel}}$ for the different sensitizers are listed in Table 24. Different quantum yield values are obtained considering either an average $^1\text{O}_2$ lifetime (= 19 μs) or the τ_{Δ} measured for the monolith under analysis; the highest differences were obtained with **MV**, **NMB⁺** and **RB SG0** monoliths. In the previous paragraph we assigned the dependence of τ_{Δ} to the quenching of singlet oxygen by the PS: such an explanation is evidently incorrect on the score of the linear relationship, observed for all the tested monoliths, between the intensity of the $^1\text{O}_2$ phosphorescence signal and the photon flux absorbed by the PS. It is thus possible that the different singlet oxygen lifetimes derive not from the PS but from optical artefacts due to the matrix. In fact, if the optical properties of the monolith changes, the K factor present in equation 6.01 cannot be considered constant and should be taken into account for precise calculations. Its determination being impossible, the average lifetime, calculated on the basis of all the measurements carried out by time-resolved detection, was used for the determination of the relative quantum yields of singlet oxygen production. Calculations carried out with the latter τ_{Δ} value should be considered more correct.

Noticeably, silica supported **PN**, **DCA**, **DBTP** and **MV (SG0)** showed high and very similar quantum yields of singlet oxygen production, whereas **RB** and **NMB⁺** were less efficient, with relative quantum yields of 0.6 vs 1.0 for the other dyes. It is also worth noticing that grafting of **DBTP** results in a lower singlet oxygen production. In solution, for compound **4** (Chapter 4, Table 8) we measured a slightly lower Φ_{Δ} relative to **DBTP** (0.91 for **1** and 0.82 for **4**): the grafting procedure was started from compound **4** and the substituent may be responsible of the lower efficiency of $^1\text{O}_2$ generation.

Similarly to solution, the substituent on the **DBTP** skeleton (difference between **SG0** and **SG2** materials) influences the fluorescence emission spectrum of the chromophore and its Φ_{Δ} .

Relative to ACN, Φ_{Δ} in monoliths significantly increased from 0.3 to 1.0 for **DCA** and from 0.6 (or 0.73 for MeOH) to 1.0 for **MV** (Table 24). For **SG0-NMB⁺** the quantum yield of $^1\text{O}_2$ production is 25% lower than in MeOH, but similar to that measured in ACN. **SG0-RB** showed a higher Φ_{Δ} than in ACN, even though lower than in MeOH. In general, all the silica supported PSs can efficiently produce singlet oxygen, even though with some samples the quantum yields slightly decrease relative to **PN**. However, considering the arbitrary scale of the $\Phi_{\Delta,rel}$ of silica-supported PSs, due to the optical characteristics of the media, an exact comparison silica/solution is rather approximate.

We also investigated the effect of the PS concentration in the monoliths on $^1\text{O}_2$ production at relatively high absorbances. We tested a **SG0-PN** monolith whose absorbance at the irradiation wavelength was $\gg 2$. The $^1\text{O}_2$ signal recorded for this monolith in ambient air was very weak (≈ 0.2 a.u., Figure 75a). As a result of the high **PN** concentration, the penetration depth of the incident radiation inside this monolith was limited to a very thin layer. In this layer, due to the high density of **PN** triplet excited state, triplet-triplet annihilation efficiently competed with quenching of the **PN** triplet excited state by O_2 to produce $^1\text{O}_2$.¹⁴³ In agreement with this hypothesis, after submitting the monolith to an O_2 flow (about 3 L min^{-1}) during 60 minutes, the $^1\text{O}_2$ signal rose significantly (≈ 1.3 a.u.) and then decreased and stabilized (≈ 0.7 a.u.) after about 10 min (Figure 75b). This result suggested that equilibration of O_2 with outside air in the monolith was faster close to the monolith's external surface than in the core.

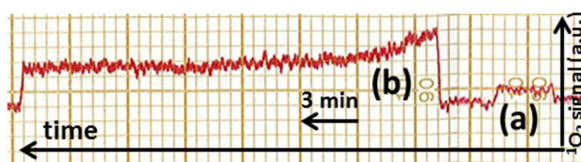


Figure 75 Intensity of the $^1\text{O}_2$ emission signal as a function of time for an **SG0-PN** monolith with an absorbance $\gg 2$ at 367 nm: (a) in ambient air; (b) after injection of O_2 in a flow cell during 60 min.

To determine the effect of gas exchange on singlet oxygen production, the monoliths were submitted to different gas environments and the effects on the intensity of $^1\text{O}_2$ phosphorescence were monitored. For this analysis we used **SG0-PN** materials with an absorbance of 0.5 at the irradiation wavelength. In a first step, in order to remove the ambient air at the gas-solid interface, Argon was let flow for approx. 30 minutes above a monolith positioned on the optical bench for $^1\text{O}_2$ measurements (*in-situ*). No significant change in the intensity of $^1\text{O}_2$ emission signals was noticed (Figure 76a). Afterwards, the same monolith was placed in a cell in which a flow of Ar ($\approx 3 \text{ L min}^{-1}$) was circulated during 30 minutes (degassing *ex-situ*): this treatment visibly forced the gas inside the matrix and a significant decrease (approx. 40 %) of $^1\text{O}_2$ production was observed (Figure 76b). This observation suggested that $^1\text{O}_2$ was mainly produced inside the monolith and not at the external solid-gas interface. This result could be expected since the total surface area of a monolith (whose weight is approx. 0.5 g) is higher than $27 \times 10^7 \text{ mm}^2$, versus the 75 mm^2 of the external surface.

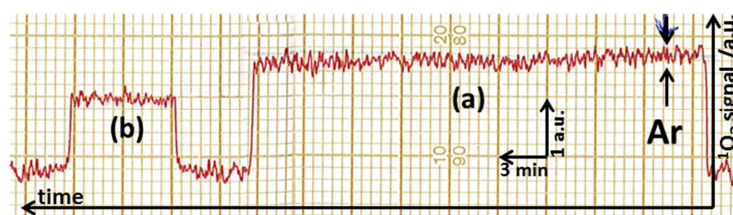


Figure 76 Intensity of the $^1\text{O}_2$ signal as a function of time recorded for **SG0-PN** after: (a) Ar introduced *in-situ* above the monolith for approx. 30 minutes (the arrow shows the start of Ar injection); (b) injection of Ar in a flow cell during 30 min before the measurement.

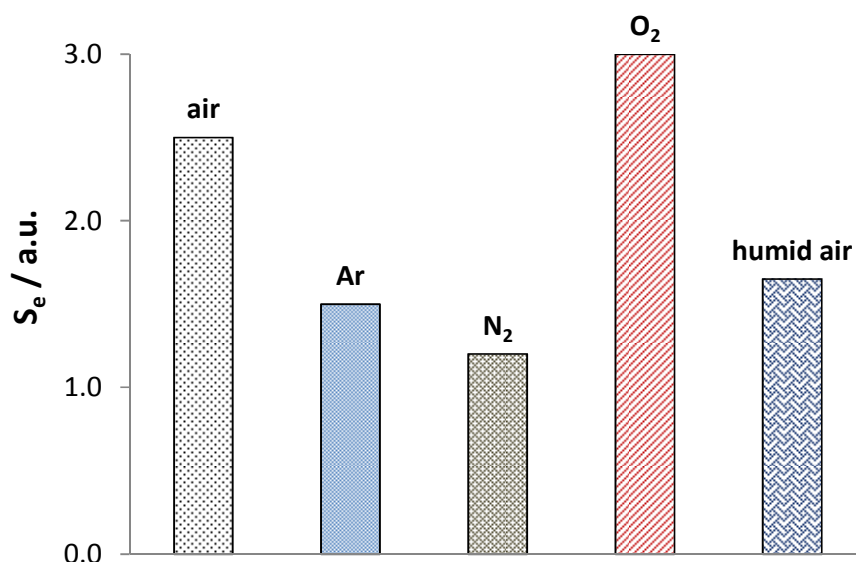


Figure 77 Singlet oxygen emission signals as a function of the added gas in the flow cell during 30 minutes prior to the measurement of the phosphorescence signal (successive experiments on a **SG0-PN** material).

In a second step, we investigated the effect of maintaining the monolith in different gaseous environments on its subsequent efficiency of $^1\text{O}_2$ production. An **SG0-PN** sample was submitted during 30 minutes successively to a flow of about 3 L min^{-1} of N_2 , O_2 and humid air. From these experiments, square signals were obtained showing that the production of $^1\text{O}_2$ was stable once the monolith was outside the flow cell and that gas exchange was negligible during the measurement time (5 minutes, Figure 76). N_2 led to a decrease of the $^1\text{O}_2$ emission signal by a factor of 2.3, larger than in the case of Ar (1.7), whereas O_2 led to a signal increase by a factor of 1.2 (Figure 77). N_2 seemed to be more efficient than Ar in removing O_2 from the microporous structure. The positive effect of an increased concentration of oxygen in the monoliths on $^1\text{O}_2$ production (Figure 77) may be explained by the increase of the probability of energy transfer from the triplet excited state of the PS to ground state oxygen, compared to ambient air. Humidification resulted in a decrease of the $^1\text{O}_2$ signal by a factor of 1.4 compared to the air-equilibrated monolith (Figure 77). This observation was

consistent with the fact that the $^1\text{O}_2$ lifetime in H_2O (approx. $3 \mu\text{s}$) is shorter than in other solvents and silica.^{34,336} Moreover, the rate constant of $^1\text{O}_2$ emission (k_e) has also the smallest value in H_2O ^{254,255} and NIR radiation is efficiently absorbed by H_2O .

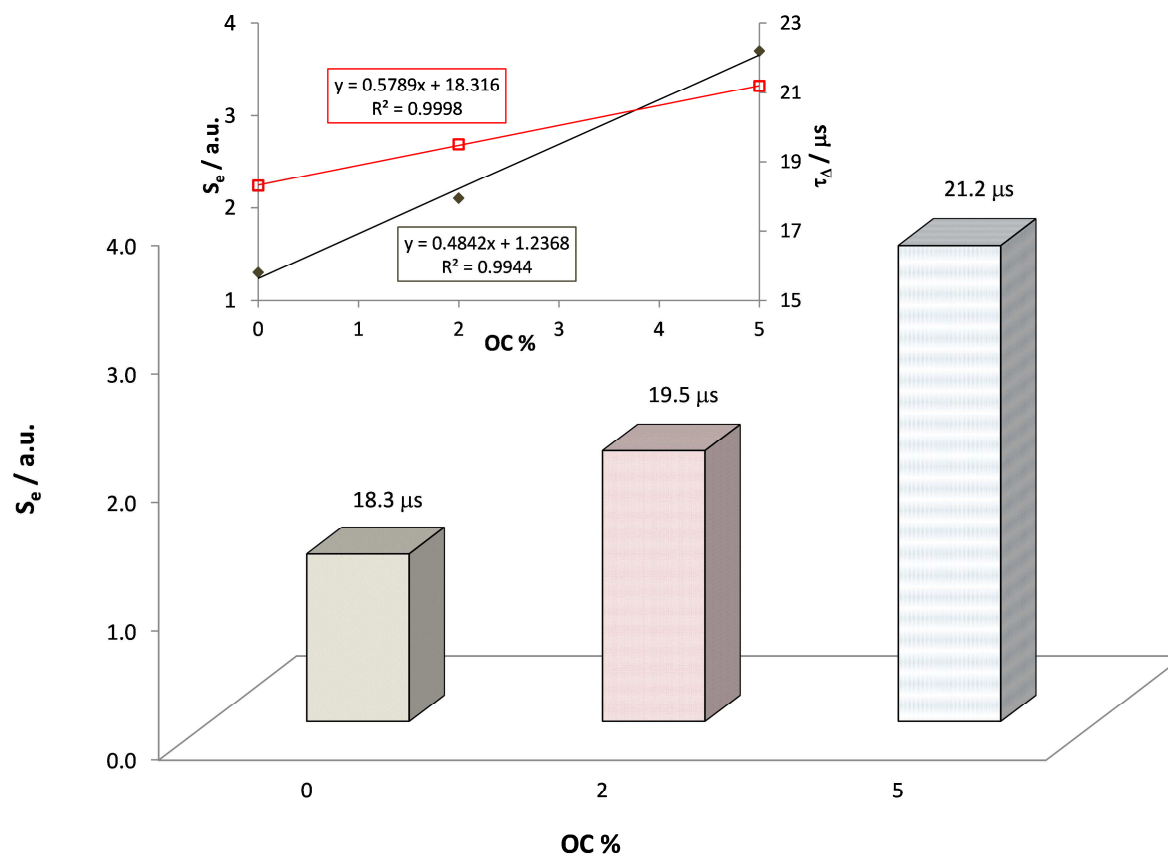


Figure 78 Intensity of the $^1\text{O}_2$ emission signal as a function of OC % in DBTP monoliths of the same absorbance ($A \approx 0.3$ at 367 nm) in ambient air. Inset: linear plot of the intensity of $^1\text{O}_2$ phosphorescence signal (diamonds, black) and singlet oxygen lifetime (empty squares, red, secondary axis) versus OC %.

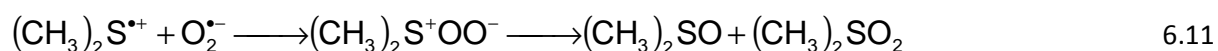
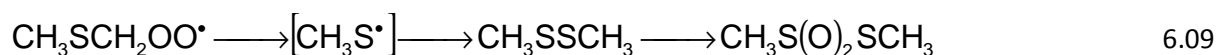
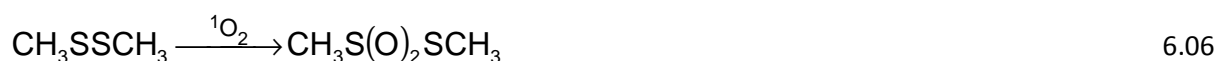
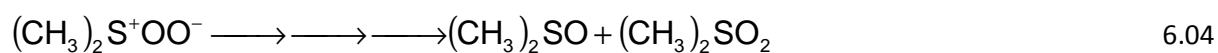
After observing the effect of moisture on the singlet oxygen production in monoliths, we were interested in measuring the effect of the hydrophobicity of the matrix on the efficiency of $^1\text{O}_2$ generation. To analyze this effect, two **SGO-OC-DBTP** monoliths of approximately the same absorbance ($A \approx 0.3$ at 367 nm) but containing different percentages of OC groups (2% and 5%) have been compared, relative to a **SGO-DBTP** sample. Figure 78 shows that the $^1\text{O}_2$ emission signal linearly increased with increasing TMOS-OC ratio. The $^1\text{O}_2$ lifetime in these three monoliths also increased linearly with OC %: $18.3 \mu\text{s}$, $19.5 \mu\text{s}$ and $21.2 \mu\text{s}$ respectively for 0, 2 and 5% of OC. The variation of signal intensity might reflect the efficiency of $^1\text{O}_2$ production. However, since the matrix has been modified by introducing TMOS-OC, the value of K (equation 6.01) could not be considered as constant anymore. Besides an increase of Φ_Δ , a signal intensity enhancement might also be due to: i) an increase of the value of k_e (rate constant of $^1\text{O}_2$ emission) as could be expected if the monolith becomes more hydrophobic;^{254,255} ii) a decrease in the refractive index of the monolith. Another possible explanation would be a decrease in the NIR absorption of the monolith in the wavelength

range of $^1\text{O}_2$ emission (1240-1300 nm) but in our case this was not consistent, since the transmittance spectra of the monoliths showed that NIR absorption slightly increased from 0% to 5% of OC. In summary, the significant increase of $^1\text{O}_2$ signal intensity with OC % (Figure 78) most probably reflected an increase of both k_e and Φ_Δ .

To summarize, for all the studied PSs, high singlet oxygen quantum yields (Φ_Δ 0.6-1.0) were determined directly at the gas-solid interface. Noticeably, despite its very short triplet lifetimes (0.3 μs), **SGO-DBTP** showed a high Φ_Δ , probably reflecting a highly efficient energy transfer to oxygen, already evidenced in solution and not significantly modified in silica. Singlet oxygen lifetime in the monoliths was between 15 and 21 μs , higher than in water (3 μs) and methanol (10 μs), and comparable to literature data for air-equilibrated polyurethane (17 μs),³³⁷ air-equilibrated Nafion® in MeOH (16 μs)⁸² and porphyrin-LDH-composites (32-55 μs).³³⁵ Steady-state singlet oxygen experiments with N_2 , O_2 or air also demonstrated the gaseous exchange inside silica and that $^1\text{O}_2$ is produced inside the cast materials and not at the external surface. In general, the influence of silica on the efficiency of singlet oxygen production of supported PSs is quite important. Moreover, the optical properties of the supports can account for the slight variations of τ_Δ , and thus of the corresponding relative Φ_Δ , measured with various samples. In the case of encapsulated and grafted **DBTP**, it seems that the substituent influences singlet oxygen production more than the host, since the differences noticed between **SGO** and **SG2** monoliths recalled those observed between compounds **1** (**DBTP**) and **4**.

5.0 PHOTOOXIDATION OF DMS AT THE GAS-SOLID INTERFACE

Since volatile DMS is very sensitive to singlet oxygen, we investigated the efficiency of the PSs containing monoliths for this solvent-free gas-solid reaction. The mechanism of the photosensitized oxidation of sulfides is well-known and described in detail in the literature.^{55,96,97,147,321,338} Two possible mechanisms can occur, following either energy transfer or electron transfer pathways. Following type II reactions, singlet oxygen, formed by ET from the triplet excited state of the PS (equation 6.02), add to the sulfide (equation 6.03) to yield the persulfoxide key intermediate. Such an intermediate evolves towards the corresponding sulfoxide and sulfone as main products (DMSO and DMSO_2 with DMS as reactant, equation 6.04). The persulfoxide can additionally undergo intramolecular H-abstraction, yielding a hydroperoxyl intermediate which, in the presence of another molecule of sulfide, can evolve to the formation of dimethyldisulfide (DMDS) as a side-product (equation 6.05). The latter can further react with $^1\text{O}_2$ to yield *S*-methyl methanethiosulfonate (MMTS, equation 6.06). Reactions 6.05 and 6.06 represent side-processes that yield the most commonly observed by-products. Alternatively, the PS and the sulfide can react via ELT (type I reaction) to give a radical pair formed by the radical cation of the sulfide and the radical anion of the PS (equation 6.07). Then, H-abstraction and O_2 -addition on $(\text{CH}_3)_2\text{S}^{+\cdot}$ (equation 6.08), followed by C-S bond cleavage and rearrangement (equation 6.09), yield DMDS and MMTS as main products. DMSO and DMSO_2 can be obtained as side-products from the formation *via* ELT of superoxide radical anion (equation 6.10) and its subsequent reaction with the sulfide radical cation, *via* the formation of the persulfoxide intermediate (equation 6.11). From the identification and quantification of the reaction products it is possible to pinpoint the main mechanism taking place.



For this study, a first adsorption step in the dark was carried out to saturate the silica monoliths with DMS. The saturation time varied between 22 hours for the monoliths with the lowest specific surface area and 56 hours for the more porous monoliths. We noticed different DMS saturation profiles between dried and H₂O-presaturated monoliths (Figure 79a), with a slightly longer equilibration time (56 hours) in the latter case, suggesting that the airflow gently dragged off the adsorbed water during this saturation step. These results imply that the highly porous monoliths are excellent adsorbents for DMS. In Figure 79b, a typical DMS concentration variation vs irradiation time is reported. The conversion and initial rates for each irradiation cycles are summarized in Table 25. A striking drop of DMS concentration to approx. 20 ppmv occurred as soon as the lamps were switched on, before beginning to slowly increase. No product other than DMS was detected in the gas phase all along the experiments. As soon as the lamps were switched off after 24 hours, the DMS concentration increased in two steps: very quickly to 150 ppmv, and slower in a second step to 200 ppmv, suggesting the presence of two adsorption sites. For **SGO-DBTP**, the initial consumption rate (v_0) was noticeably much higher for the second cycle than for the first one, contrary to all the other materials more prone to photobleaching (Table 25). It is worth noticing that the minimum DMS concentration reached at the beginning of the second irradiation cycle was always the same as the DMS concentration reached at the end of the first irradiation, as if the strong adsorption of the oxidation products (mainly DMSO and DMSO₂, see below) on silica limited the amount of DMS that could be adsorbed, conditioning thus the activity during the second cycles. When carrying out the experiment for a much longer time (several weeks), the products totally filled the monoliths pores, preventing further DMS photooxidation without precautionary products desorption.

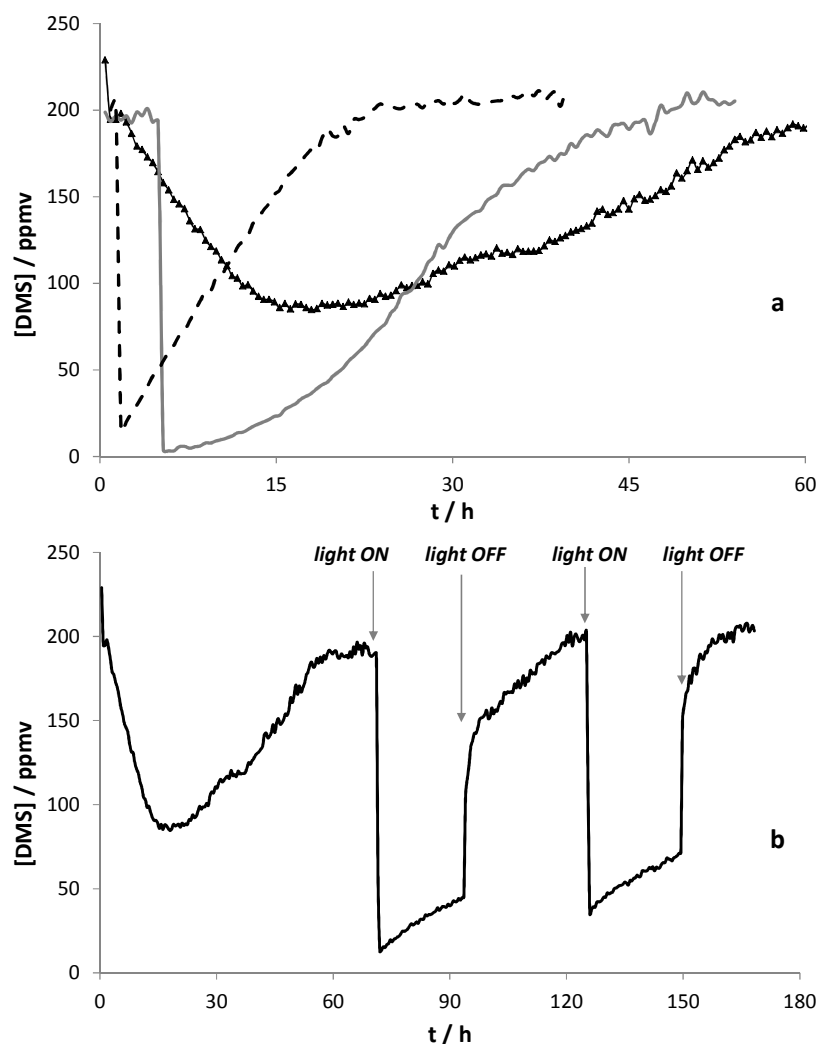


Figure 79 DMS concentration variation during photooxidation (PO) tests. (a) Saturation step in the dark: comparison between water-saturated **SG0-ACN-DBTP** (black, triangles), **SG0-ACN-DBTP** (grey line) and **SG0-RB** (dotted black line). (b) Profile throughout the PO test for a water-saturated **SG0-ACN-DBTP** monolith. Reaction conditions: 100 mL min^{-1} (air flow), 200 ppmv (DMS concentration), 420 nm (irradiation wavelength), room temperature.

A precise quantification of the products was difficult, but DMSO was identified as the main one, followed by DMSO_2 and traces of DMDS and MMTS (Figure 80). Since DMDS and MMTS were found in trace amounts, it can be concluded that the reaction mainly proceeded through singlet oxygen formation by energy transfer and its subsequent addition to DMS. Moreover, no obvious differences in the products distribution were noticed between the different materials, indicating that all the PSs followed the same photoreaction pathway.

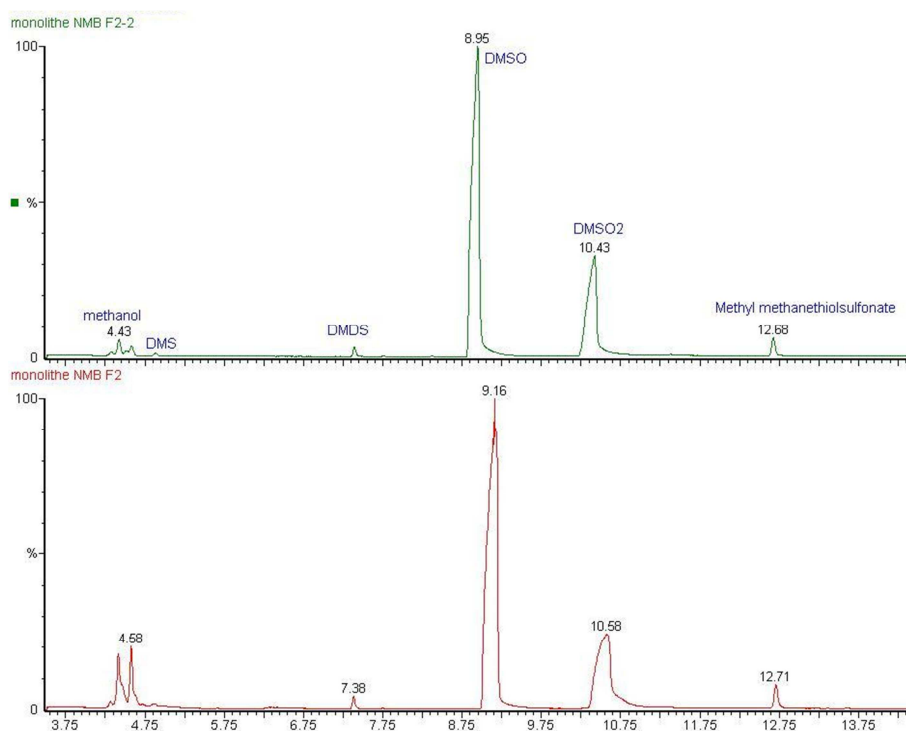


Figure 80 GC profiles obtained after thermodesorption of the PO products from a **SG0-NMB⁺** monolith (two subsequent desorptions); retention times of the products: MMTS (12.68 min), DMSO₂ (10.43 min), DMSO (8.95 min), DMDS (7.23 min).

All the supported PSs efficiently oxidized DMS under visible light irradiation (conversions 26-51% for the first irradiation cycle and 9-40 % for the second cycle, Table 25). Considering the more relevant conversion normalized by the photon flux absorbed by the PS, and, contrary to what expected from the data relative to singlet oxygen production (Table 24), for both irradiation cycles the most efficient materials were **SG0-DBTP**, **SG0-NMB⁺** and **SG0-RB** while the less efficient were **SG0-DCA** and **SG0-PN**. **DBTP** appeared to be the most bleaching resistant PS (< 30%), followed by **DCA** (40%) and **PN** (62%). The other PSs were not expected to be very resistant under such irradiating power and the bleaching percentages were very high (90% and 95% respectively for **NMB⁺/MV** and **RB**). Considering both conversion and bleaching percentages it emerged that the best material for the photosensitized oxidation of DMS was **SG0-DBTP**.

Table 25 PO activity of some **SGO** materials (series 3) for the sensitized oxidation of DMS: conversions (%) and initial rates are reported for both the first and the second cycles. The conversion values normalized by the absorbed photon flux are reported in brackets. Bleaching percentage (after 2×24 h irradiation) was estimated from DRUV spectra recorded before and after the two irradiation cycles.

^{a)} Irradiation at 420 nm, ^{b)} irradiation at 575 nm.

monolith	PS / mol g ⁻¹	P_a / mW cm ⁻²	conv ₁ / %	conv ₂ / %	$v_{0,1}$ / ppmV h ⁻¹	$v_{0,2}$ / ppmV h ⁻¹	bleaching / %
DBTP	1.6×10^{-7}	16.7 ^{a)}	51 (3.1)	40 (2.4)	-27	-120	27
DCA	9.4×10^{-8}	27.6 ^{a)}	26 (0.9)	11 (0.4)	-78	-25	40
PN	5.7×10^{-8}	33.6 ^{a)}	35 (1.0)	22 (0.7)	-40	-32	62
RB	2.6×10^{-7}	13.1 ^{b)}	42 (3.2)	19 (1.5)	-218	-140	95
MB⁺	4.7×10^{-7}	16.5 ^{b)}	27 (1.6)	17 (1.0)	-225	-28	65
NMB⁺	8.5×10^{-8}	15.1 ^{b)}	56 (3.7)	33 (2.2)	-430	-225	90
SO₃H-NMB⁺	2.7×10^{-7}	14.7 ^{b)}	41 (2.8)	23 (1.6)	-141	-147	78
MV	5.0×10^{-7}	16.2 ^{b)}	41 (2.5)	9 (0.6)	-195	-102	90
SO₃H-MV	5.7×10^{-7}	16.5 ^{b)}	34 (2.1)	22 (1.3)	-117	-125	38

SGO-SO₃H-NMB⁺ monoliths presented a slightly less efficient activity relative to that recorded for **SGO-NMB⁺**: the conversion normalized by the absorbed photons is 2.8, against 3.7 for conventional monoliths. The presence of sulfonic acids in the matrix had a different effect on **MV**: even though the activity was roughly similar, the dye showed a significantly higher resistance to photobleaching in **SGO-SO₃H** materials (38% versus 90%). This result is perfectly consistent with what observed in solution: in MeOH, where both **MV** and **MV-OH** are present, photobleaching was strongly lower than in ACN or dioxane. We suggested that the presence of the protonated form of the dye increases its overall stability under irradiation. Silica is a more acidic environment than alcohols and the presence of SO₃H groups represents a further increase of acidity: in these materials the **MV** must mainly be under the **MV-OH** form, which ensures a higher photoresistance. Only **DBTP** showed a higher photostability than **SGO-SO₃H-MV**. Considering the extremely low specific surface area of **SGO-SO₃H** monoliths and the high concentration of the PSs included, the photoreactions with these materials can be supposed to predominantly occur at the external surface of the monolith. Sulfonic acid functionalized silica is also known to act as a catalyst for the selective oxidation of sulfides to sulfoxides,³³⁹ which could explain the high activity observed with **SGO-SO₃H** materials despite their extremely low surface area, relative to **SGO** monoliths.

Given the high efficiency and stability of **SGO-DBTP**, we focused on the influence of silica modifications and of **DBTP** grafting on the photochemical activity. Two series of monoliths are reported in Table 26, corresponding to two different synthetic batches. In the first series, **SGO-ACN** materials were the most efficient and stable under irradiation. The effect of grafting (**SG2-ACN-DBTP**) on the photoactivity was negligible but surprisingly resulted in a lower stability under irradiation (Figure 81). Monolith saturation with water did not affect the photoactivity of the material (Figure

79). In the second series, the differences in the photooxidation activity were rather negligible, as well as the variations of surface area between the different samples reported. Moreover, the normalized conversions for these monoliths were close to those calculated for the monoliths of the first series characterized by lower (and similar) surface areas. It was easily outlined that, independently on the synthesis batch, the highest normalized conversions corresponded to the highest specific surface areas (normalized conversions of 1 and 2 for 555 and 730 m² g⁻¹ S_a respectively) while the influence of the micro/mesoporosity seemed less important. Silica functionalization with octyl groups decreased both the conversion (related to decreased S_a) and the photostability of the dye: for these oxidation conditions, it is thus not worthwhile increasing the hydrophobicity of the silica matrix. On the contrary, ACN as a co-solvent had a positive effect on the activity and PS stability under irradiation, probably related to an increase of the specific surface area. It seems from these results that for obtaining the best performing materials it is important to increase the surface area (> 650 m² g⁻¹) of the silica matrix; the percentages of micro and mesopores seems on the contrary negligible, as well as the hydrophobicity of the solid structure or the presence of adsorbed water.

Table 26 PO properties of some DBTP derived monoliths for the photooxidation of DMS, two series corresponding to as many synthesis batches. Initial conversion rate (v_0), conversion % and, in brackets, percentage conversion normalized by the photon flux absorbed by the PS, bleaching % (estimated from DRUV-Vis spectra). Specific surface areas and mesoporous percentage: see Table 20.

^{a)} water-saturated sample: approx. 100 mg of water were adsorbed (monolith initial weight: approx. 500 mg).

^{b)} Mass flow: 400 ppmv (200 ppmv for other entries).

series	monolith	PS / mol g ⁻¹	S _a / m ² g ⁻¹ (% mesopores)	P _a / mW cm ⁻²	v _{0,1} / ppmv h ⁻¹	conv ₁ / %	bleaching / %
1	SG0-OC 5%	9.2 × 10 ⁻⁸	555 (23)	41.5	-385	38 (0.9)	18
	SG0-ACN	2.0 × 10 ⁻⁷	730 (30)	43.4	-455	88 (2.0)	3
	SG0-ACN ^{a)}	2.0 × 10 ⁻⁷	730 (30)	43.4	-405	86 (2.0)	3
	SG2-ACN	5.0 × 10 ⁻⁷	660 (38)	40.7	-305	83 (2.0)	25
2	SG0-ACN	1.9 × 10 ⁻⁷	560 (38)	44.4	-255	46 (1.0)	8
	SG0-OC 1%	1.6 × 10 ⁻⁷	525 (10)	43.7	-220	43 (1.0)	33
	SG0 ^{b)}	2.0 × 10 ⁻⁷	565 (14)	43.6	-375	54 (1.2)	29

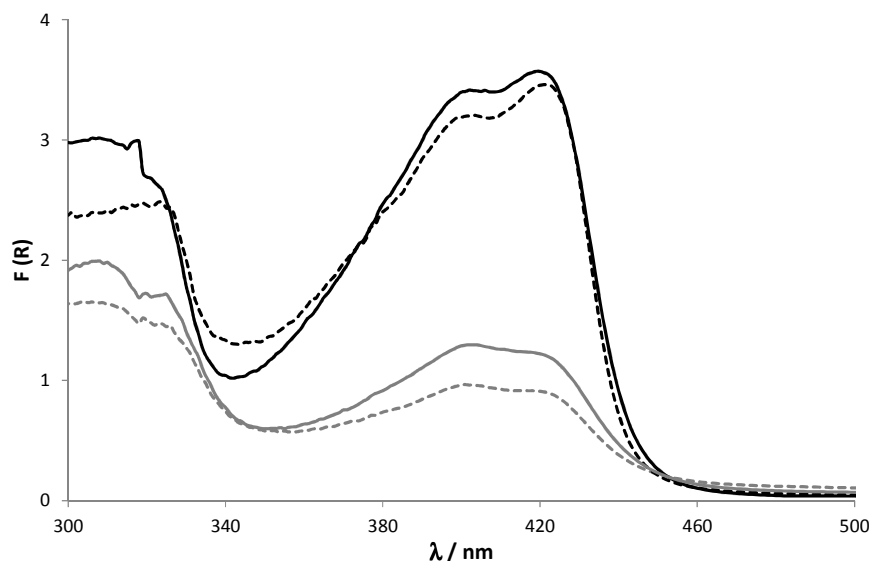


Figure 81 DRUV spectra of **SG0-ACN-DBTP** (black) and **SG2-ACN-DBTP** (grey) before (solid lines) and after (dashed lines) the PO tests for the evaluation the photobleaching extent.

It is thus concluded that the efficiency of DMS photooxidation is more related to the specific surface area of the matrix than to the singlet oxygen quantum yield of the sensitizer. The slow sensitivity of the singlet oxygen signal to a change from air to N_2 or O_2 illustrates the high porosity of the silica matrix and the long time required for oxygen to enter the whole monolith volume. The quenching of the triplet state by ground state oxygen (also located in the pores of the silica matrix) is highly efficient as shown by the significant singlet oxygen quantum yields. Taking into account the diffusion coefficient (D) of singlet oxygen in air ($0.18 \text{ cm}^2 \text{ cm}^{-1}$) and its measured lifetime (τ_Δ) in air (54 ms),²⁹² the diffusion length (d) of 1O_2 , calculated from equation 6.12, is 3.5 mm:

$$d = \sqrt{6D\tau_\Delta} \quad 6.12$$

The same calculation in silica gives a diffusion distance of $5 \cdot 10^{-3} \text{ nm}$ (with diffusion coefficient $D = 2.2 \cdot 10^{-15} \text{ cm}^2 \text{ s}^{-1}$ for SiO_2 coatings prepared by the sol-gel method³⁴⁰ and $\tau_\Delta = 20 \mu\text{s}$). These results mean that oxygen is able to diffuse only in the pores and that the quenching of the triplet state only occurs at the solid-gas interface. Once formed, singlet oxygen is free to diffuse across the silica pores, the diameter of which is much smaller than its diffusion length. If DMS is adsorbed and confined inside silica, singlet oxygen is able to readily add on it as soon as it is produced explaining the very fast decay of DMS adsorption as soon as the irradiation begins. This scheme also accounts for the decreased reaction rate when oxidation products such as DMSO and $DMSO_2$ are already adsorbed in the matrix, thus reducing DMS adsorption and oxygen diffusion. These observations could also explain the discrepancies observed between Φ_Δ and PO activity: possibly, slight variations in the porous structure of silica modify the accessibility of adsorbed DMS by 1O_2 . Different locations for the PS (and thus for singlet oxygen generation *via* ET) and the pollutant, entailing 1O_2 diffusion between the two sites, could condition the oxidation of DMS, in spite of an efficient singlet oxygen generation (*e.g.* the case of **SG0-DCA** which has the highest Φ_Δ and the lowest DMS conversion).

6.0 CONCLUSIONS

Embedded or grafted PSs are able to photogenerate long-lived $^1\text{O}_2$ molecules that react very efficiently with sulfides in a solvent-free process. These silica monoliths are also suitable for the easy acquisition of steady-state or time-resolved absorption/emission spectra directly in the solid samples, without use of any suspension.

High quality transient absorption spectra were obtained. A strong effect of the silica matrix was evidenced on the transient spectra of all the phenothiazine PSs: the triplet excited state absorption bands are shifted of at least 40 nm relative to the spectra recorded in solution. For the other dyes the triplet absorption spectra are similar to solution. The triplet lifetimes in silica appear much longer than in air-equilibrated solvents and in some cases close to the lifetimes measured in de-aerated solutions. Only for **DBTP**, the triplet lifetime is similar to aerated ACN solutions.

Triplet states are efficiently quenched by oxygen as shown by the high singlet oxygen quantum yields (Φ_{Δ} 0.6-1.0) determined directly at the gas-solid interface. It may thus be concluded that PS molecules included in the matrix are accessible to gaseous oxygen present in the silica network.

No obvious correlations between the production of singlet oxygen in silica monoliths and the corresponding photoactivity for DMS oxidation could be pointed out: the addition of hydrophobic octyl groups for example increases Φ_{Δ} while decreasing the photooxidation efficiency, together with a decreased specific surface area. It seems that in the experimental timescale of this work, the structural and porous properties of silica affect the photooxidation activity more than the efficiency of $^1\text{O}_2$ production by the PS itself. Such an influence could be related to singlet oxygen diffusion in the silica porous network. Nevertheless, from the analysis of the diffusion distance of oxygen inside the material, it is concluded that singlet oxygen, produced at the gas-solid interface, is free to diffuse inside the pores. For an efficient energy transfer to oxygen, the PS concentration inside silica has to be low enough to avoid triplet-triplet annihilation. In the presence of adsorbed water inside silica, singlet oxygen is efficiently quenched; nonetheless, under our experimental conditions for DMS photooxidation, water is dragged off the solid by the air flux and could not affect the photochemical activity. Transparent silica monoliths can act both as suitable supports for the characterization of the reactive species involved in the photochemical processes and as efficient microreactors for photosensitized oxidation reactions in a medium behaving like a "solid solution". The stability of the materials over time (6 years) is demonstrated. Among the various PSs tested, the three phenothiazine dyes, **MB**⁺, **NMB**⁺ and **MV** are very efficient but prone to photobleaching, while **DBTP** is more active and more resistant to photobleaching. Grafted **DBTP** also presents a high efficiency but with a slightly reduced resistance to bleaching. Consistently to what observed in solutions, **MV** results to be much more resistant to irradiation in more acidic silica than in conventional monoliths.

Fluorescence and transient decays, as well as $^1\text{O}_2$ production and DMS photooxidation, gave some evidences of the presence of different (or differently acidic) sites for the PS location inside silica; this heterogeneity could influence the photophysics of the dyes (e.g. **MV**) and the photoactivity of the materials.

7 Organic photocatalysts immobilized on silica powders: the photooxidation of α -terpinene at the gas-liquid interface

In the Introduction we focused on the interests and advantages of using photosensitizing materials, where PSs are covalently bound to inert supports, which can be used for many applications. Fundamental approaches are often necessary to point out the effect of grafting, the influence of the support and the different reaction pathways occurring with different PSs and substrates. In this chapter the results concerning the preparation and characterization, both spectroscopic and photochemical, of silica-immobilized organic photocatalysts (generally named PS-Si) are reported. Rose bengal (**RB**), anthraquinone-2-carboxylic acid (**AQ-COOH**) and **DBTP-COOH** were grafted on commercially available functionalized silica gels, following Scheme 11 (Chapter 3, Materials and Methods). The three PSs were chosen for their potential good activity and efficient singlet oxygen generation in solution: while **DBTP**, together with its derivatives, has been studied in detail in the first part of this work, **AQ** and **RB** are relatively well-known photosensitizers. Moreover, **RB** has been extensively used as a graftable reference dye for the development of photosensitizing materials. The preparation of these materials was carried out following efficient and rapidly achieved coupling reactions and the effect of the grafting on the spectroscopic properties of the dyes was analyzed. Their photochemical properties were tested for the photosensitized oxidation of α -terpinene (**α -t**), which easily adds singlet oxygen to yield ascaridole (**asc**, Introduction).^{341–343} Their reactivity was compared to that of the reference material **RB-ps**: polystyrene-supported rose bengal is a commercially available photosensitizing material frequently used as a reference for photochemical reactions with suspended photoactive powders.^{77,197,198} Moreover, the results obtained with the synthesized materials were analyzed in comparison with the reactivity of the same PSs in homogeneous solutions. The photooxygenation of **α -t** is usually considered as a model reaction for testing the photosensitizing properties of dyes and materials; nonetheless, striking results were obtained and we could outline different photochemical mechanisms depending on the PS.

other less soluble coupling agents represented a serious improvement to this technique.^{211,214,240} The elimination of unreacted dyes, especially for the relatively non-soluble **DBTP-COOH**, was more complicated: several Soxhlet extractions were necessary to eliminate all traces of unreacted dye. **RB-Si** was prepared according to the reported procedure of Tamagaki *et al.*⁹³ by reacting commercial Cl-Si with **RB** in DMF under reflux. In this case several Soxhlet extractions were also necessary to eliminate traces of unreacted **RB**. The amounts of reactants used for the preparation of each material are listed in Table 27, together with the amounts of grafted sensitizer and the grafting % (ratio of the grafted matrix functionalities and the totally available ones).

Table 27 Experimental details for the synthesis of PS-Si and characteristic IR bands.

^{a)} Functionalized silica: X = NH₂- (**DBTP-Si** and **AQ-Si**) and X = Cl- (**RB-Si**).

^{b)} PS loading calculated from TGA.

PS	PS / g (mmol)	X-Si ^{a)} / g (mmol-X)	PS-Si / mmol g ⁻¹	Grafting / %	IR (KBr) / cm ⁻¹
RB	0.80 (0.79)	4.0 (2.9)	0.19 (0.09) ^{b)}	26	1481 (C=C) 1643 (C=O)
DBTP-COOH	0.057 (0.15)	1.0 (1.4)	0.14 (0.30) ^{b)}	10	1541 (C=C) 1653 (C=O) 2216 (C≡N)
AQ-COOH	0.12 (0.50)	3.7 (3.7)	0.13 (0.34) ^{b)}	13	1540 (C=C) 1653 (C=O) 1678 (C=O)

The PS loading was determined by UV-Vis spectroscopic analysis of the washings and by TGA. The two methods gave different results but were in the same order of magnitude for the amount of grafted sensitizer (mmol g⁻¹). The values obtained from UV analysis, however, were closer to the expected ones (on the basis of the initial amount of sensitizer to be grafted). Consequently, these values were used for the calculation of the amount of sensitizer under the operating conditions for photooxidation experiments.

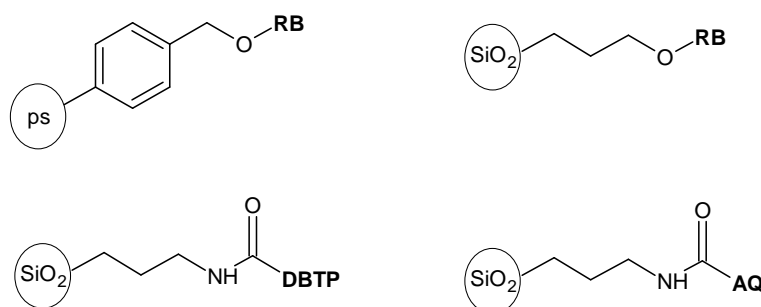


Chart 15 Schematic representation of the reference (**RB-ps**) and synthesized materials.

1.2 Spectroscopic characterization

The materials were characterized by Diffuse Reflectance Infrared Fourier Transform Spectroscopy (DRIFTS; Figure 83). **RB-Si** showed typical bands at approx. 1481 cm^{-1} and 1643 cm^{-1} , respectively, for $\nu(\text{C}=\text{C})$ and $\nu(\text{C}=\text{O})$ vibrations. The sharp and strong signal at approximately 1260 cm^{-1} , expected for an ether group in the final material, was covered by the strong and broad signal from Si-O and Si-CH₂ stretching vibrations found in the IR spectra of all starting (unbound) silica gels and all the samples. **DBTP-Si** showed typical bands at 1541 , 1653 and 2216 cm^{-1} , correlating to $\nu(\text{C}=\text{C})$, $\nu(\text{C}=\text{O})$ and $\nu(\text{C}\equiv\text{N})$ vibrations, respectively. In addition to the 1540 cm^{-1} $\nu(\text{C}=\text{C})$ vibration, **AQ-Si** showed two separate signals for C=O stretching (1653 and 1678 cm^{-1}), representing the amide linker and the quinone of the anthracene skeleton (Table 27). The amide bands (1653 cm^{-1}) resulting from the IR spectra of **DBTP-Si** and **AQ-Si** demonstrate that the grafting reaction between functionalized silica and the dye occurred.

Evidence of the actual grafting of **RB** onto silica emerged from the characterization by UV Diffuse Reflectance spectroscopy (DRUV), carried out on all solid samples (silica powders and solid unbound dyes). The DRUV spectrum of solid **RB** powder (Figure 84) showed a broad and unresolved band at about 610 nm compared to its UV-Vis spectrum in solution (Figure 86). The main peak at 555 nm observed in solution slightly shifted towards lower wavelengths and the low-intensity shoulder at 520 nm strongly increased with a hypsochromic shift of 20 nm. The DRUV spectrum of **RB-ps** (Figure 84) was similar to that of the pure powder, but slightly shifted towards higher wavelengths and characterized by a more intense peak at 560 nm. In contrast, the DRUV spectrum of **RB-Si** (Figure 84) revealed significant changes. The different colors of the silica- and polystyrene-supported **RB** are clearly visible to the naked eye (Figure 83a and 83b). According to the original paper by Tamagaki *et al.*,⁹³ the color and absorption intensity of **RB-Si** vary depending on the silica/**RB** ratio and hence on the amount of grafted dye. Compared to solid **RB** and commercial **RB-ps**, the spectrum of the orange **RB-Si** showed a significant blue-shift with a broad absorption maximum between 450-570 nm (Figure 84). Such a spectral variation demonstrates that, as a consequence of grafting, a significant change in the dye occurred, which can possibly have important effects on the photochemistry of the material. The DRUV spectra of **DBTP-COOH** (powder) and **DBTP-Si** showed a broad, unresolved absorption band between 450-380 nm (Figure 85), in contrast with the two well-resolved bands at 391 and 415 nm recorded in solutions.²⁰⁵ The DRUV spectra of **AQ-COOH** and **AQ-Si** were consistent with the absorption spectrum of **AQ-COOH** in solution with a very weak $n\rightarrow\pi^*$ absorption band extending to 450 nm (Figure 85).^{55,344} The absorption spectra of the unbound photosensitizers in methanol are shown for comparison in Figure 86.

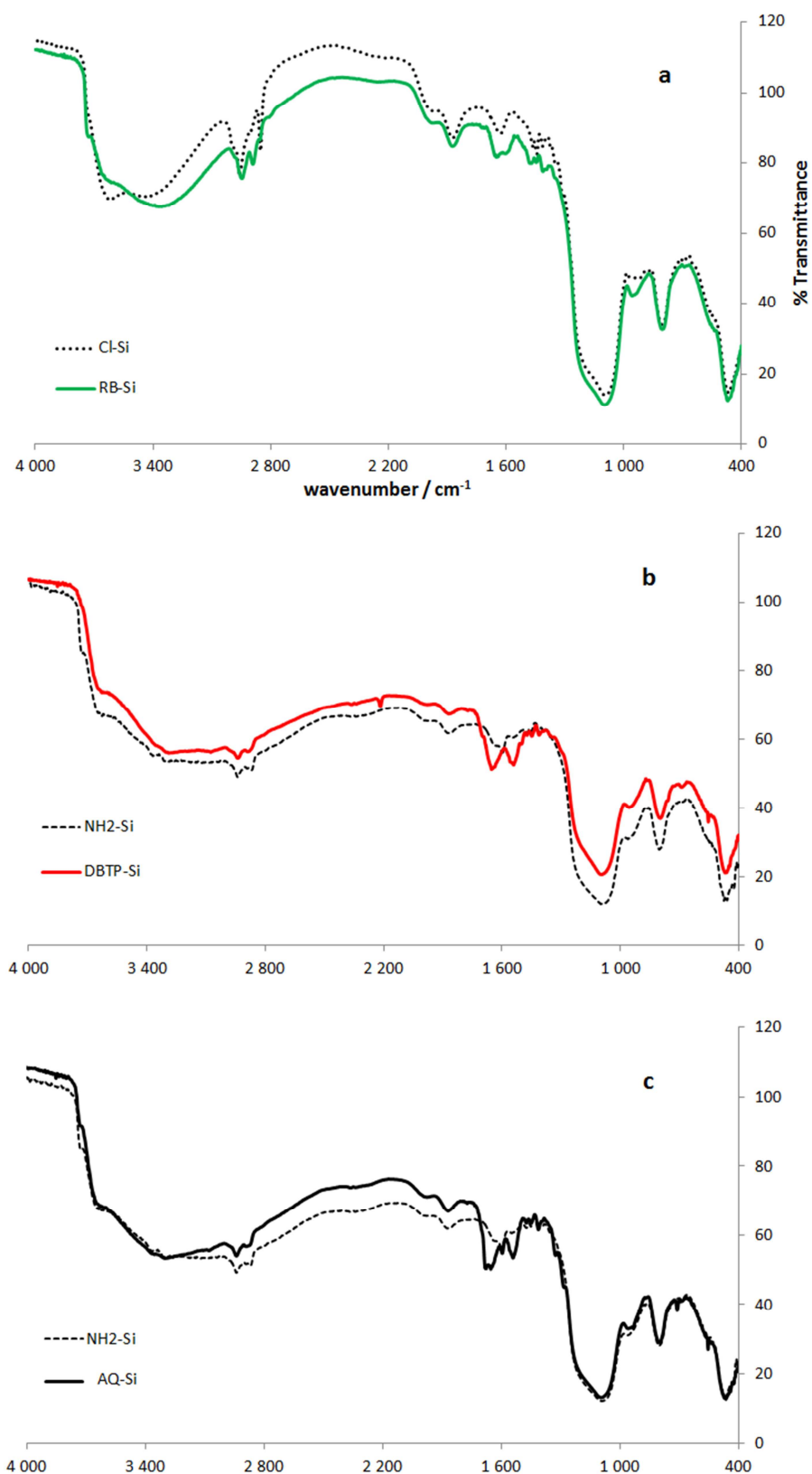


Figure 83 DRIFT spectra of the prepared materials: a) RB-Si, b) DBTP-Si and c) AQ-Si. The spectra are compared to those of the starting functionalized silica gels (dashed line for NH₂-Si and dotted line for Cl-Si).

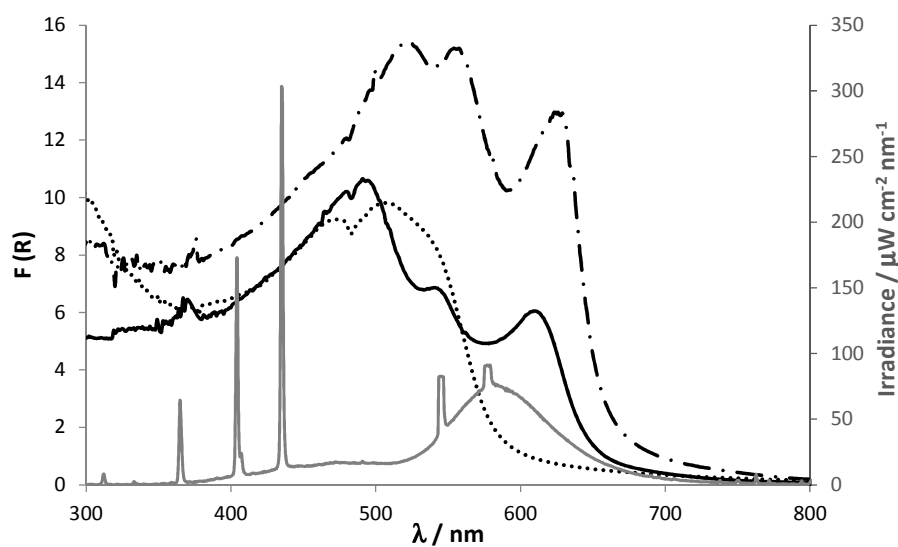


Figure 84 DRUV spectra of solid RB (solid line), RB-ps (dashed-dotted line) and RB-Si (dotted line) vs irradiance of 575 nm fluorescent tubes (grey, secondary axis).

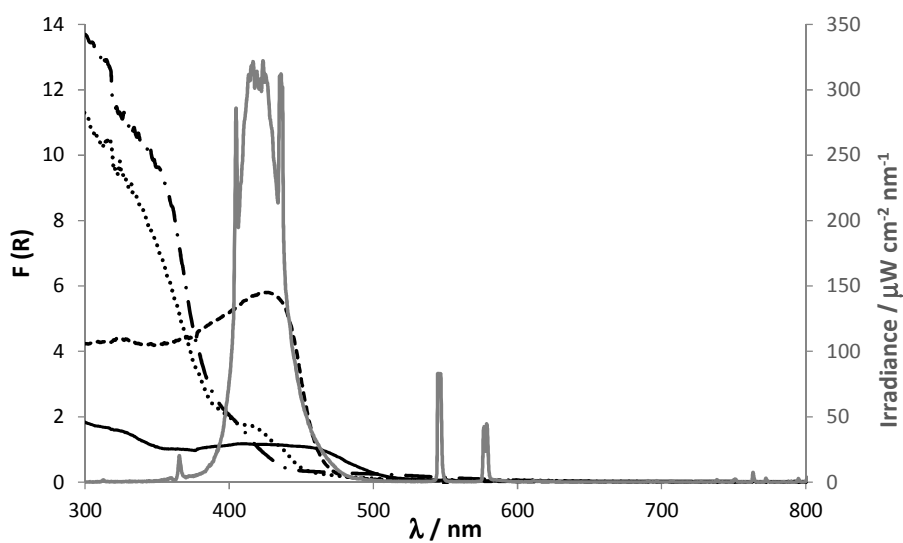


Figure 85 DRUV spectra of solid DBTP-COOH (solid line), DBTP-Si (dashed line), solid AQ-COOH (dotted line) and AQ-Si (dashed dotted line) vs irradiance of 419 nm fluorescent tubes (grey, secondary axis).

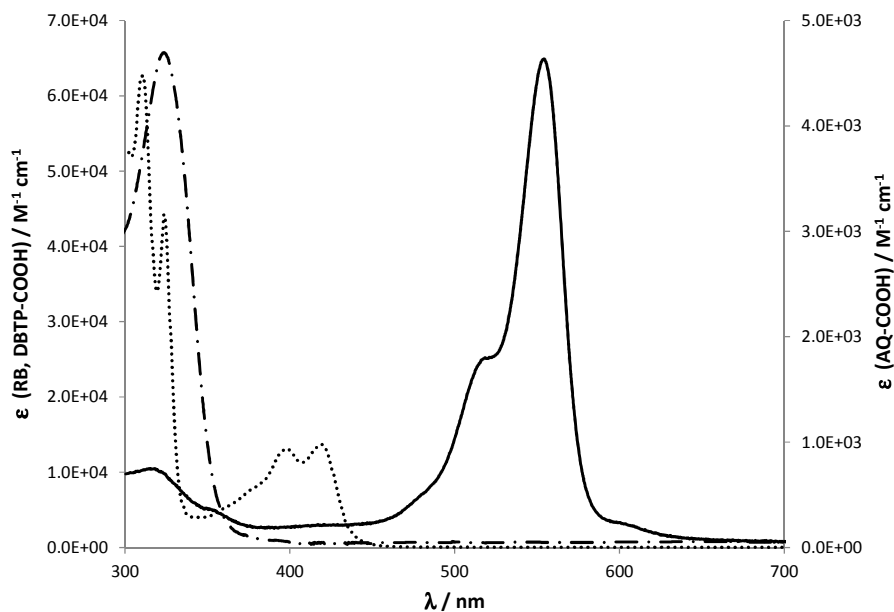


Figure 86 Absorption spectra of **RB** (solid line), **DBTP-COOH** (dotted line) and **AQ-COOH** (dashed-dotted line, secondary axis) in methanol at room temperature.

The spectrophotometric analysis of the synthesized materials confirmed that the peptide-coupling method used to graft **DBTP-COOH** and **AQ-COOH** did not influence the absorption properties of the immobilized dye relative to the pure powdered forms. The loss in fine structure relative to the solution spectra may be attributed to the high sensitizer loading on the solid support and thus to the formation of aggregates, as already observed for silica-supported porphyrins,³⁴⁵ phthalocyanines³⁴⁶ and methylene blue.⁹² The broad bands observed in the DRUV spectra of the solid-supported and the powder sensitizers could also be possibly explained by fluorescence artefacts due to the high concentration of the samples. The coupling agents (NHS and EDC) and their reaction products are water-soluble and were therefore easily removed together with the ungrafted sensitizer. Thus, the chosen coupling method represents a very efficient and simple way to graft carboxylic acid derived photosensitizers on commercially available silica-gels.

Compared to the commercially available **RB** on polystyrene (**RB-ps**) at similar dye loading, **RB** grafting on Cl-Si under our experimental conditions strongly altered the absorption spectrum of the PS. In this case, the formation of aggregates can be ruled out since this would correspond to a shift towards higher wavelengths.

2.0 DETERMINATION OF Φ_{Δ}

Before performing the photooxygenation experiments, the quantum yields of singlet oxygen production in ACN were determined for the soluble PSs using rubrene as singlet oxygen probe and **PN** as a reference sensitizer (Table 28).^{253,265} The indirect method involving $^1\text{O}_2$ chemical trapping by rubrene is described in the first chapters of this work. This procedure was adopted considering the good results previously achieved, perfectly consistent with those obtained by direct singlet oxygen

phosphorescence detection. Among the three tested PSs, **DBTP-COOH** showed the highest efficiency for $^1\text{O}_2$ production with quantum yield around unity (see Chapter 4). In contrast, **AQ-COOH**, as well as its non-functionalized parent compound **AQ**, have Φ_{Δ} about 25% lower than that of **DBTP-COOH**. Thus, all chosen sensitizers produce singlet oxygen very efficiently and selective photooxygenation of α -t to yield **asc** was expected. **RB**, as previously reported, has a lower Φ_{Δ} in ACN (determined by direct detection).

Table 28 Quantum yields of singlet oxygen production of **RB**, **DBTP-COOH**, **AQ** and **AQ-COOH** determined by chemical probing with rubrene (Reference PS: **PN**. Solvent: air-equilibrated ACN at room temperature).

^{a)} Determined by singlet oxygen phosphorescence detection.

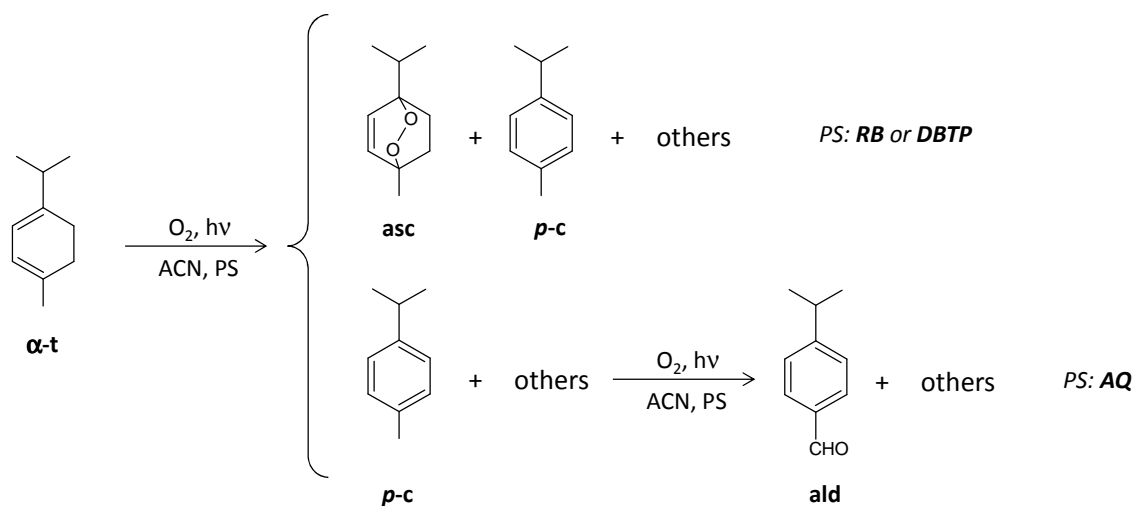
PS	Φ_{Δ}
RB	$0.42 \pm 0.03^{\text{a)}$
DBTP-COOH	1.03 ± 0.05
AQ-COOH	0.76 ± 0.04
AQ	0.74 ± 0.04

3.0 PHOTOOXIDATION REACTIONS

The synthesized materials were tested for the photooxidation of α -terpinene (α -t) in ACN as a model substrate, following the procedure described in detail in the Chapter 3. Irradiations were performed for 20-150 min (depending on the PS) until GC-MS monitoring showed complete conversion. Irradiation wavelengths were selected according to the absorption maxima of the photosensitizers (Figures 84 and 85). The conversion of α -t was followed by GC-MS analysis and by the drop in intensity of its UV band at 267 nm. Products and by-products were monitored by GC-MS to investigate their distribution and were identified by their MS spectra (reference spectra). Due to the large number of impurities and of by-products, a careful analysis of all the secondary compounds was necessary. The exact identification and quantification of these products was of primary importance for the correct study of the reaction mechanisms and kinetics. A special paragraph will be devoted to the identification, by mass and NMR spectroscopy, of the compounds corresponding to the several peaks emerging from the crude products chromatograms. As previously reported, because of the evaporation of the reaction products, NMR analysis could not be used to determine the composition of the crude product.¹⁵⁷ In case of the supported photosensitizers, subsequent UV-Vis spectroscopic analysis of the final reaction mixture excluded any leaching of the photosensitizer into the solvent.

3.1 Photosensitized oxidation of α -terpinene (α -t)

The mechanistic pathway of the photooxidation of α -t is represented in Scheme 18. The experimental results of the tests carried out with the prepared materials and with their homogeneous counterparts are reported in Table 29.^{341–343}

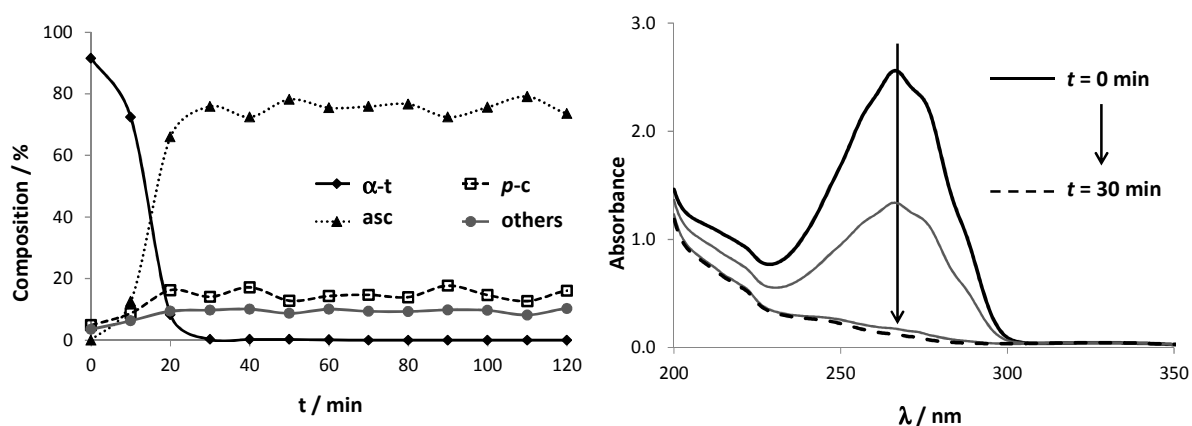


Scheme 18 Photosensitized oxidation of α -t.

A control irradiation for 2.5 h in the absence of any PS at 575 nm (entry 1) resulted in autooxidation to *p*-cymene (*p-c*) as the main product (39%). Other unidentified by-products (17%) mainly contained two compounds with molecular ions of 168 and 152 a.m.u. respectively. Autooxidation thus represents an important general pathway in the photooxidation of α -t and cannot be neglected.^{347,348} The addition of **RB** as a homogeneous sensitizer (entry 2) clearly accelerated the reaction rate with complete conversion of α -t after 30 min. Singlet oxygen addition to form **asc** became the dominant pathway and ascaridole was obtained in 78% yield, together with 14% of *p-c* and 8% of other products. Likewise, UV-Vis monitoring of the reaction showed a drop for the α -terpinene band after 30 min (Figure 87). The absorption band of **RB** underwent a slight bathochromic shift and decreased in intensity. These effects probably resulted from a combined effect of a change in the reaction medium polarity, caused by the formation of **asc** and *p-c*, and of photobleaching (Figure 88).^{207,208} Prolonged irradiation over 2 h did not cause any significant change in the product composition (Figure 87). Rose bengal thus prevented both further autooxidation of *p-c* and decomposition of **asc**.

Table 29 Experimental results for the photooxidation of α -t.a) Determined by GC analysis ($\pm 1\%$; initial composition: α -t = 93%, *p*-c = 4%, others = 3%).b) Including *i*-asc (see Figure 93 and Scheme 19).

entry	PS	PS / mg (mmol)	λ_{\max} / nm	t / min	composition / % ^{a)}				
					α -t	asc ^{b)}	<i>p</i> -c	ald	others
1	none	—	575	150	44	—	39	—	17
2	RB	30.8 (0.030)		30	—	78	14	—	8
3	RB-ps	30 (0.003)		110	—	77	13	—	10
4	RB-ps	150 (0.015)		50	—	81	13	—	6
5	RB-Si	200 (0.038)		150	9	50	27	—	14
6	none	—	419	150	72	—	22	—	6
7	DBTP-COOH	5.6 (0.015)		20	—	65	24	—	11
8	DBTP-COOH	11.2 (0.030)		20	—	55	34	—	11
9	DBTP-Si	20 (0.003)		90	—	75	18	—	7
10	DBTP-Si	100 (0.014)		30	—	82	13	—	5
11	AQ-COOH	7.6 (0.030)		40	—	1	64	8	27
12	AQ-Si	200 (0.030)		110	—	3	69	6	22
13	AQ-Si	500 (0.065)		80	—	4	70	10	16

**Figure 87** (left) GC monitoring of α -t, asc, *p*-c and others during the photooxidation of α -t in the presence of RB (entry 2). (right) UV monitoring: intervals of 10 minutes, until disappearance of the signal of α -t at 267 nm.

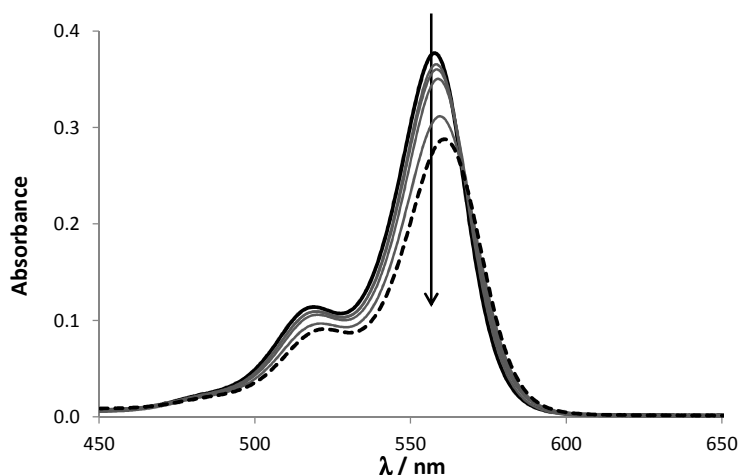


Figure 88 Evolution of the absorption spectrum of **RB** as a function of the irradiation time during the photooxidation of α -**t** (entry 2). The arrow shows the decrease of absorbance and slight bathochromic shift occurred during the two hours of irradiation.

In the presence of commercial **RB-ps** (entries 3 and 4), similar activity and selectivity were observed, although the reaction rate depended on the molar amount of the grafted PS. Using a low loading of **RB-ps** (entry 3), the reaction took 110 min to reach completion, while with a higher loading (entry 4), full consumption of α -**t** was reached after 50 min of irradiation, as confirmed by GC as well as UV-Vis monitoring. Photoactivity sharply decreased when **RB-Si** was employed (entry 5). After prolonged irradiation for 2.5 h, the conversion was still incomplete (91%) and selectivity for **asc** was low (50%) while **p-c** was obtained in 27%, more than twice the amount found with **RB-ps**. The amount of other by-products likewise increased. This poor activity and selectivity with **RB-Si** may be accounted for by:

- I. the poor overlap between the adsorption spectrum of **RB-Si** and the emission spectrum of the fluorescent tubes (Figure 84) compared to the much better overlap with the absorption spectrum of **RB-ps**,
- II. a structural change due to grafting, which could also explain the orange color of the material and its modified DRUV spectrum and/or
- III. the enhanced efficiency of **RB-ps** due to swelling of the organic PS-backbone in ACN, which may improve diffusion of both O_2 and α -**t** into the solid support.^{77,197,198}

Photosensitized oxidation with **DBTP**-derived sensitizers was carried out at 419 nm. In the absence of sensitizer (entry 6), autooxidation was slow and **p-c** was found in an amount of 22% after prolonged irradiation for 2.5 h, together with small amounts of other products (total of 6%). The autooxidation is thus slower at 419 nm than at 575 nm (entry 1). In the presence of soluble **DBTP-COOH** (entries 7 and 8, Figure 89), very fast conversions of α -**t** were achieved after 20 min. A further increase in **DBTP-COOH** concentration was not considered since the selectivity towards **asc** dropped (possibly due to its flocculation caused by its low solubility in ACN), while the amount of **p-c** increased from 24% to 34% (entry 8). **DBTP-COOH** nevertheless functions as an efficient singlet oxygen sensitizer that does not catalyze any follow-up reactions.

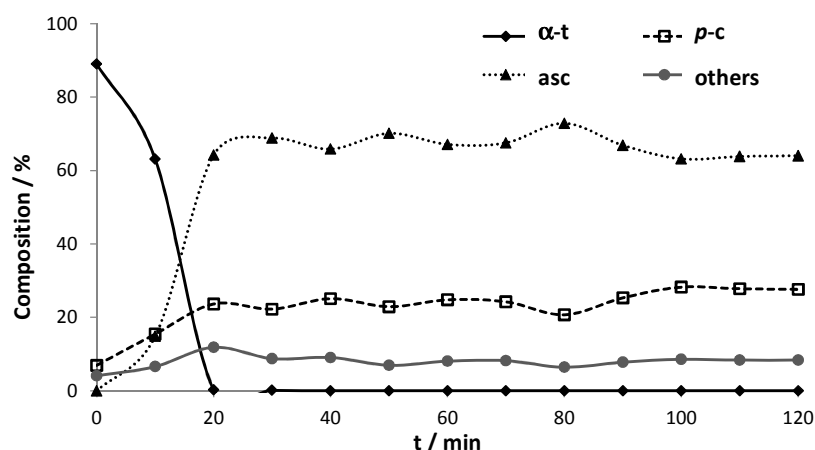


Figure 89 GC monitoring of α -t, asc, p-c and others during the photooxygenation of α -t in the presence of DBTP-COOH (entry 7).

In contrast, silica-supported **DBTP-COOH** (entries 9 and 10) showed by far the best performance and resulted in rapid photooxygenation and high selectivity towards **asc**. Reactivity improved with higher photocatalyst loading (entry 10) and complete conversion of α -t to **asc** (82%) was achieved after 30 min of irradiation, a result similar to the one obtained with **RB-ps** (entry 4). In addition, small amounts of **p-c** (13-18%) and of other by-products (5-7%) were formed. **DBTP-Si** reacted faster than **RB-ps** at a similar photosensitizer loading, while maintaining a similar selectivity. This effect may be due to the higher total irradiance of the 419 nm tubes, in combination with the higher Φ_{Δ} for **DBTP-COOH** (see below for kinetic analyses).

Due to the superior performance of **DBTP-Si**, a series of repeated experiments was conducted under standard conditions. As shown in Table 30, the recovered material performed equally well even after four consecutive runs and the desired product **asc** was obtained as main product (81-86%). Selectivity was likewise high and just 6-8% of *p*-cymene was formed. **DBTP-Si** therefore represents an efficient (even more than the reference material **RB-ps**), selective and reusable photosensitizing material for the catalytic photooxygenation of α -t by means of $^1\text{O}_2$ addition.

Table 30 Reuse experiment: experimental results for photooxygenations of α -t with DBTP-Si (irradiation times: 30 min). Initial loading: 50 mg of DBTP-Si. Approximately 5 mg lost for each recovery.

^{b)} Determined by GC analysis ($\pm 1\%$; initial composition: α -t = 93%, *p*-c = 4%, others = 3%).
^{c)} Including *i*-asc.

Run	composition / % ^{b)}			
	α -t	asc ^{c)}	<i>p</i> -c	others
1	1	86	6	7
2	1	81	8	10
3	1	82	7	10
4	1	83	8	8

In case of AQ-derived sensitizers (entries 11-13, Figure 90), also irradiated at 419 nm, the photoreaction proceeded rather unselectively and asc was only obtained in trace amounts (1-4%), in spite of the total conversion of α -t. The reaction thus follows a different mechanism. After complete consumption of α -t (after 40-110 min), *p*-cymene was identified as the main photoproduct (64-70%), together with smaller amounts of cuminaldehyde (**ald**, 6-10%) and other products (16-27%; Chart 16). Of these, eucalyptol (**euc**) and isocineole (*i*-cin) could be identified by their MS-spectra. The formation of **ald** was furthermore noticeable upon UV-Vis monitoring with the characteristic $\pi \rightarrow \pi^*$ transition at approximately 250 nm (Figure 90).³⁴⁹ At equal molar amounts of AQ-COOH (entry 11), the reaction rate for the disappearance of α -t appeared to be in the same order of magnitude as those of RB (entry 2) and DBTP-COOH (entry 8).

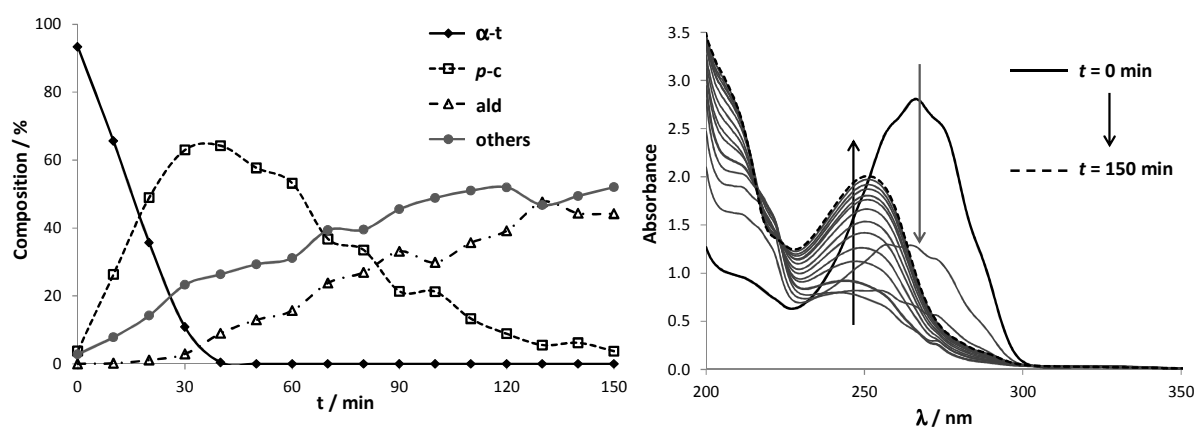


Figure 90 (left) GC monitoring of α -t, *p*-c, ald and others during the photooxygenation of α -t in the presence of AQ-COOH (entry 11). (right) UV monitoring: measuring intervals of 10 minutes (0→150 minutes), until disappearance of the signal of α -t at 267 nm (grey) and the formation of ald, absorbing with a maximum at 250 nm.

In contrast to the other sensitizers (Figures 87 and 89), the product composition further changed upon exhaustive irradiation of **AQ**-derived sensitizers and **p-c** was readily consumed, while the amounts of **ald** and other by-products increased (Figure 90). Among them, 4-isopropylbenzoic acid (**ac**) could be verified by MS (Figure 95) and NMR analysis, while GC-MS analysis, in comparison with library spectra, additionally suggested the presence of the isomeric benzylic alcohols **7-ol** and **8-ol** (Chart 16, Figure 95). An additional product with a molecular mass of 168 a.m.u. was detected (Chart 16), possibly the isomeric open chain aldehydes **op1** or **op2**.^{150,350,351}

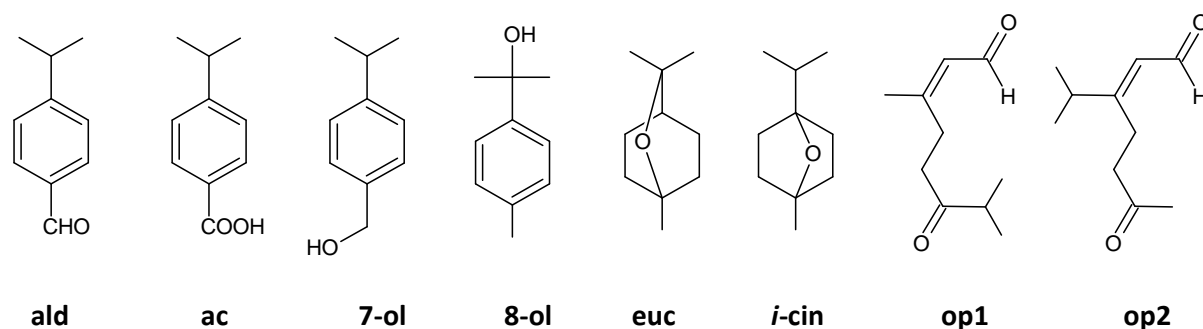
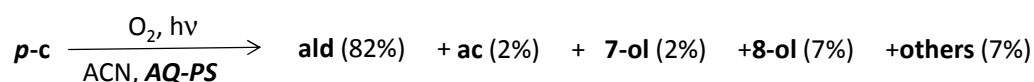


Chart 16 Identified secondary products obtained during the photooxidation of α -t in the presence of **AQ** photosensitizers: 4-isopropylbenzaldehyde (cuminaldehyde, **ald**), 4-isopropylbenzoic acid (**ac**), (4-isopropylbenzyl)methanol (*p*-cymene-7-ol, **7-ol**), 2-(4-methylphenyl)-2-propanol (*p*-cymene-8-ol, **8-ol**), 1,3,3-trimethyl-2-oxabicyclo[2.2.2]octane (eucalyptol, **euc**), 1-isopropyl-4-methyl-7-oxabicyclo[2.2.1]heptane (isocineole, **i-cin**), and possible open chain aldehydes (3,7-dimethyl-2-octenal-6-on, **op1**) and (3-isopropyl-2-heptenal-6-on, **op2**).

3.2 Photosensitized oxidation of *p*-cymene (*p*-c)

The accelerating effect of anthraquinone on the secondary photooxygenation of **p-c** was striking and was thus further investigated. When **p-c** was independently irradiated for 160 min in the presence of **AQ-COOH** it was readily consumed (Figure 91) and a variety of oxygenated compounds were formed (Chart 16 and Scheme 19). As previously observed, **ald** was generated as the main product and its amount constantly increased to 82% during the course of the irradiation. The benzylic alcohols **7-ol** and **8-ol** were likewise rapidly detected, of which *p*-cymene-7-ol (**7-ol**) was further oxidized to **ald** and **ac** upon extended irradiation. When considering the combined yields of **ald**, **ac** and **7-ol**, it may be concluded that oxidation preferentially took place on the methyl group.



Scheme 19 Photosensitized oxidation of *p*-c in the presence of **AQ**-sensitizers

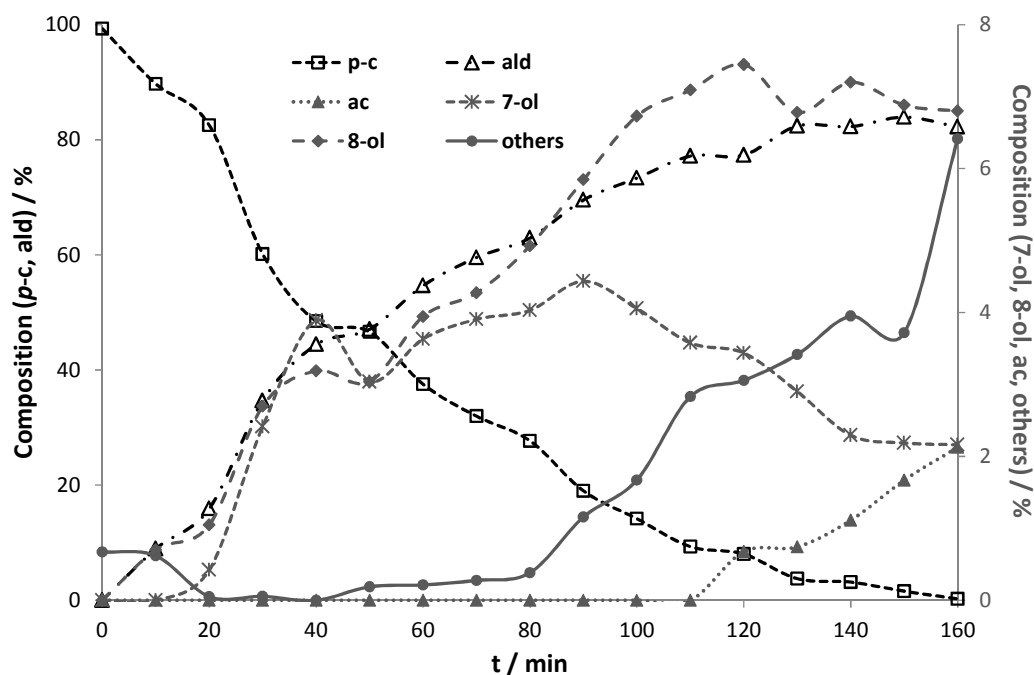


Figure 91 GC monitoring of *p-c* and *ald* (main axis), *ac*, *7-ol*, *8-ol* and *others* (secondary axis) during the photosensitized oxidation of *p-c* in the presence of AQ-COOH (homogeneous ACN solution, standard conditions).

3.3 Detection of the main products and by-products by ^1H NMR and MS spectroscopy

The main products (ascaridole, **asc**, *p*-cymene, ***p-c*** and cuminaldehyde, **ald**), identified by GC-MS analysis, were furthermore confirmed by ^1H NMR analysis in comparison with literature data.³⁵²

Ascaridole (**asc**), yellowish oil. R_f (SiO_2 ; cyclohexane:ethyl acetate=3:1): 0.61. ^1H NMR (400 MHz, CDCl_3) δ : 0.96 (6H, d, $J=6.9$ Hz, $2\times\text{CH}_3$), 1.34 (3H, s, CH_3), 1.49 (2H, m, CH_2), 1.89 (1H, sept, $J=6.9$ Hz, CH), 1.99 (2H, m, CH_2), 6.38 (1H, d, $J=8.5$ Hz, =CH), 6.46 (1H, d, $J=8.5$ Hz, =CH). ^{13}C NMR (100 MHz, CDCl_3) δ : 17.2, 17.3, 21.4, 25.6, 29.5, 32.1, 74.4, 79.8, 133.0, 136.4. MS (EI) m/z : 168 (M^+), 150, 139, 125, 107, 97, 95, 69, 55, 43. In agreement with literature data.³⁵²

p-Cymene (***p-c***), in mixture with **asc**. ^1H NMR (400 MHz, CDCl_3) δ : 1.25 (6H, d, $J=6.8$ Hz, $2\times\text{CH}_3$), 2.34 (3H, s, CH_3), 2.89 (1H, sept, $J=6.8$ Hz, CH), 7.14 (4H, m, H_{arom}). MS (EI) m/z : 134 (M^+), 119, 91, 77, 65, 57, 51, 41. In agreement with literature data.³⁵²

Cuminaldehyde (**ald**), from the crude reaction mixture. ^1H NMR (400 MHz, CDCl_3) δ : 1.28 (6H, d, $J=6.9$ Hz, $2\times\text{CH}_3$), 2.99 (1H, sept, $J=6.9$ Hz, CH), 7.39 (2H, d, $J=8.1$ Hz, H_{arom}), 7.82 (2H, d, $J=8.1$ Hz, H_{arom}), 9.96 (1H, s, CHO). MS (EI) m/z : 148 (M^+), 133, 119, 105, 91, 77, 61, 51, 41. In agreement with literature data.¹⁵⁷

4-isopropylbenzoic acid (**ac**), from the crude reaction mixture. ^1H NMR (400 MHz, CDCl_3) δ : 1.27 (6H, d, $J=6.8$ Hz, $2\times\text{CH}_3$), 2.91 (1H, sept, $J=6.8$ Hz, CH), 7.33 (2H, d, $J=8.2$ Hz, H_{arom}), 8.03 (2H, d, $J=8.2$ Hz, H_{arom}). MS (EI) m/z : 164 (M^+), 149, 145, 133, 115, 105, 91, 77, 65, 51, 43. In agreement with literature data.¹⁵⁷

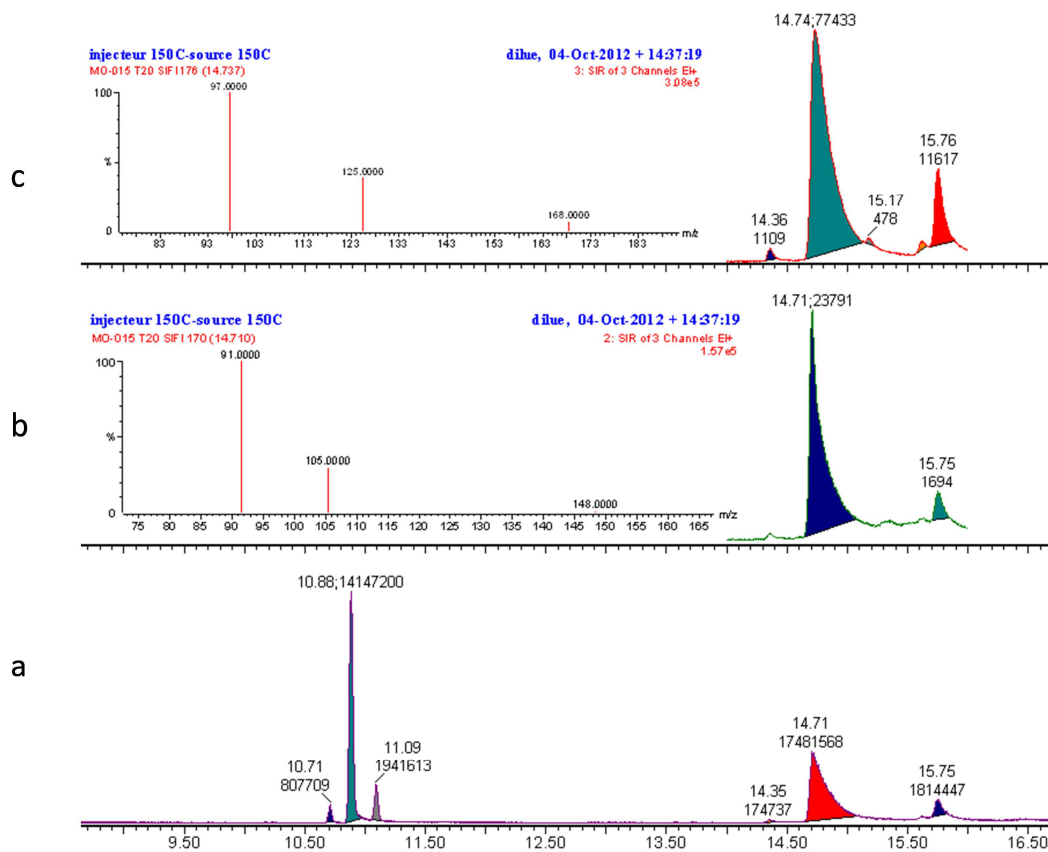
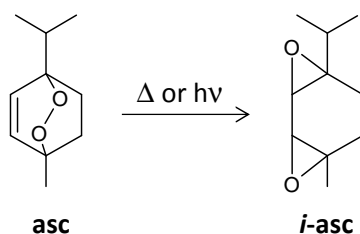


Figure 92 Chromatogram of the crude reaction mixture: the main product has a retention time of 14.71 minutes (a); SIFI analysis of the main product's peak, selecting the main m/z peaks of **asc** (c) and **ald** (b) to obtain the corresponding chromatographic signals.

Under the chosen GC conditions ascaridole (**asc**) and cuminaldehyde (**ald**) showed very similar retention times (rt). Simultaneous Collection of Full Scan and Selected Ion (SIFI) analysis was therefore performed to determine their relative percentages. For **asc**, ions at m/z 168, 125 and 97 were selected (Figure 92c). For **ald**, ions at m/z 148, 105 and 91 were selected (Figure 92b).



Scheme 20 Thermally/photochemically induced isomerization of ascaridole (**asc**) to isoascaridole (**i-asc**).

In almost all of the chromatograms, the peak of **asc** (rt 14.74 min) was accompanied by a much smaller peak (< 5%) at rt 15.75 min with an identical mass spectrum (Figure 93). This peak was attributed to isoascaridole (***i*-asc**, Scheme 20), a bisepoxide that is known to arise from either photochemical or thermal isomerization of **asc**.^{342,347,353–355} By changing the experimental conditions of the GC-MS analysis (*i.e.* reducing the injector temperature to 120°C), slightly lower amounts of ***i*-asc** were detected, implying that ***i*-asc** is formed predominantly photochemically and to a lesser extent by thermal conversion of **asc** in the GC injector. This assumption was confirmed by irradiation of pure ascaridole with visible light, confirming its slow isomerization (< 10% after 6 hours of irradiation) to ***i*-asc**. Since ***i*-asc** unambiguously arises from **asc**, their combined yields were given (Table 29).

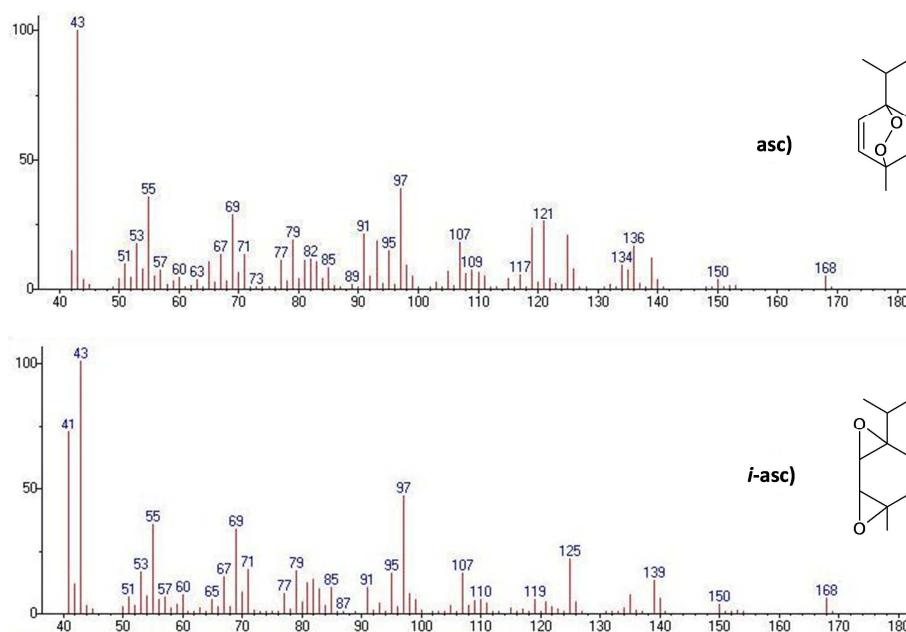


Figure 93 MS spectra of **asc** and ***i*-asc**.

Below, the evolution of the crude GC peaks as a function of irradiation time in the presence of **AQ**-derived sensitizers is reported in Figure 94: the large number and variety of side-products formed during the photochemical test is evident. Moreover, the consumption of **α -t** (rt 10.80) and the formation of ***p*-c** (rt 10.91) and **ald** (rt 14.74) as the main products are easily observed. In addition, the MS spectra of some of the above-cited products and side-products are reported (Figure 95).

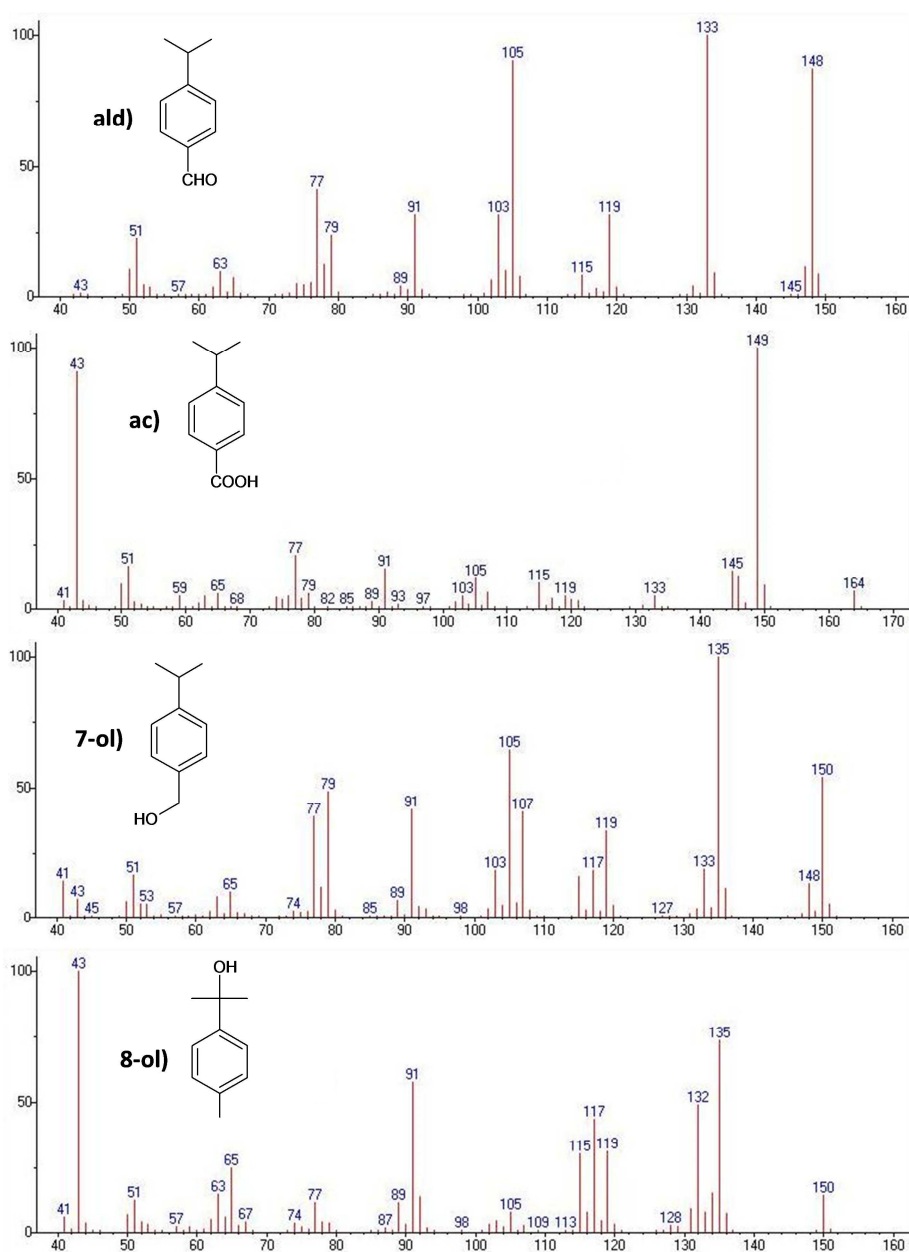


Figure 95 MS spectra and chemical structures of the main products of photooxygenation of *p*-c. ald) cuminaldehyde, ac) 4-isopropylbenzoic acid, 7-ol) *p*-cymene-7-ol, 8-ol) *p*-cymene-8-ol.

4.0 DISCUSSION OF THE MECHANISMS

Two different mechanistic schemes are deduced from our results. Soluble **DBTP** and **RB**, as well as **RB-ps** and **DBTP-Si** photosensitizers, efficiently produce singlet oxygen and lead selectively to ascaridole (including less than 5% of isosascaridole, directly from **asc**, Scheme 20) via [4+2] cycloaddition (*photooxygenation*).³⁵⁶ Besides, no significant changes in the product compositions were noticed upon prolonged irradiation. *p*-Cymene, commonly observed as a side-product from thermal dehydrogenation (autooxidation) with ground state oxygen (O_2),³⁵¹ was only observed in significant yields in the absence of sensitizer or with **RB-Si**. Other mechanistic pathways to ***p*-c**

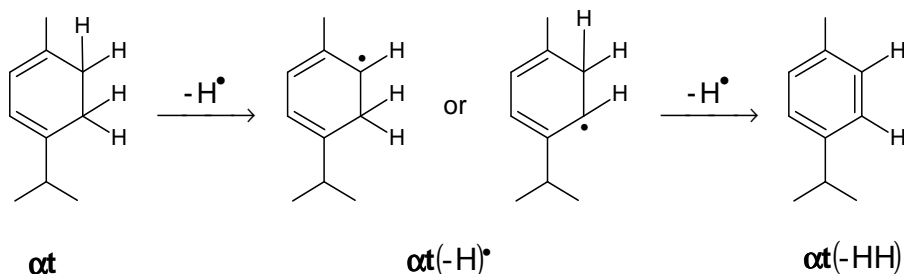
(electron transfer involving the PS,^{150,151} decomposition of ascaridole³⁵⁷ or thermal breakdown of hydroperoxide intermediates³⁵⁸) appear less likely under our conditions. For the discussion reported below, we considered the data relative to **DBTP** and **AQ** (instead of those of **DBTP-COOH** and **AQ-COOH**): in the case of **DBTP-COOH** no electrochemical data could be obtained due to the irreversible peaks observed in solution, and for anthraquinone, the influence of the COOH group should not be significant, as emerged from the values of Φ_{Δ} for the two compounds.

The mechanistic scenario that can explain the product distribution for the photooxidation of α -t in the presence of **AQ**-sensitizers is outlined in reactions 7.01-7.08 and mirrors the mechanism described by Chen and coworkers for perylene diimides or **DCA** as photosensitizers.^{150,359} Upon excitation and intersystem crossing (ISC) the triplet excited state of the photosensitizer is populated (equation 7.01). Subsequent electron-transfer (ELT) between the excited PS and α -t generates a radical-ion pair (equation 7.02), which undergoes further proton transfer to the corresponding radical pair (**AQ(H)** \cdot and α -t(-H) \cdot , equation 7.03). The resulting **AQ(H)** and α -t(-H) radicals react with molecular oxygen to form the hydroperoxyl radical, HOO \cdot (equations 7.04 and 7.05), and the dehydrogenation product α -t(-HH) (= *p-c*) (Scheme 21). HOO \cdot consequently undergoes hydrogen abstraction from α -t, forming hydrogen peroxide and regenerating the α -terpinene derived chain carrier radical (α -t(-H) \cdot , equation 7.06). Alternatively, the radical anion of anthraquinone can directly react with molecular oxygen to generate the superoxide radical anion, (equation 7.07), which itself reacts via proton transfer with the radical cation α -t \cdot^{+} to create the hydroperoxyl radical, HOO \cdot , and the chain carrier radical, α -t(-H) \cdot (equation 7.08). Likewise, the peroxidation of isomeric γ -terpinene has been shown to yield *p*-cymene as the only organic product in a radical reaction with HOO \cdot as a chain carrier.^{360,361} The preferred oxidation of the methyl group over the isopropyl group deduced from our results strongly suggested an electron-transfer rather than a free-radical pathway.^{347,348,362}



A similar mechanism has been recently proposed by Cui *et al.*¹⁸⁴ for the photooxidation of isopropanol with **AQ-COOH** as a sensitizer: direct H-transfer between the PS and the substrate generating a radical pair, O₂ addition on the substrate with formation of an unstable hydroperoxide derivative, deactivation by loss of H₂O₂ to yield the oxidized product.

The formation of **p-c**, **op2** and various by-products *via* the decomposition of ascaridole and unstable benzylic hydroperoxides has already been proposed by Karapire *et al.*¹⁵¹ Under our experimental conditions, though, the benzylic hydroperoxides^{92,93} could not be detected.



Scheme 21 H-abstraction and radical formation on α -t: photosensitized dehydrogenation yields **p-c**.

It follows from our results that, in the working conditions adopted here and contrary to what expected from the Φ_Δ values we measured, singlet oxygen formation is strongly disadvantaged with **AQ**; on the other hand, 1O_2 generation is confirmed to be very efficient with **RB** and **DBTP** sensitizers. From the Rehm-Weller equation (equation 1.15), electron-transfer from α -terpinene ($E_{(\alpha-t/\alpha-t^{\bullet+})}^0 = 1.60$ V vs SCE)³⁶³ to the excited PS (equation 7.02) should be exothermic for both singlet and triplet excited **AQ**, and strongly endothermic for **RB** (independently of the excited state); with **DBTP**, the ELT from α -t is highly exothermic to the singlet excited state and endothermic to the triplet excited state (Table 31). With **DBTP** thus, such a reaction could occur from the singlet excited state: nonetheless, as reported in the previous chapters, ISC for this class of compounds is very efficient, thanks to the quasi-resonance between the S_1 and the T_3 states, with subsequent very fast internal conversion to yield the T_1 state. Once this excited state populated, the energy gap is not sufficient for the ELT reaction with α -t to take place; on the contrary, the quenching of the triplet excited state of the PS by molecular oxygen is extremely efficient and quantitative. **DBTP** is at least as efficient as **RB** for singlet oxygen production, and no evidence of electron transfer could be pointed out, neither from a photophysical study nor from the products distribution after photochemical tests. With **AQ** electron- or H-transfer are possible and radical-chain mechanisms are favored on thermodynamic grounds: ΔH_f (reaction 7.05) = -31.9 kcal mol $^{-1}$ and ΔH_f (reaction 7.06) = -18.8 kcal mol $^{-1}$.¹⁵⁰ This result confirms previously reported reactivity of **AQ**-sensitizers with sulfides where high amounts of sulfonic and sulfuric acids were obtained and attributed to an electron transfer mechanism.⁵⁵ Anthraquinone is capable of producing singlet oxygen by energy transfer upon irradiation (Table 28).^{56,57} The question of additional anthraquinone sensitized superoxide radical anion formation, similarly to anthraquinone-2-sulfonate which is able to produce both 1O_2 ^{53,86} and $O_2^{\bullet-}$,^{56,57} was raised.^{16,17,55} This double reactivity should be possible: considering the redox potential of **AQ** and O_2 ($E_{AQ/AQ^{\bullet-}}^0 = -0.62$ V and $E_{O_2/O_2^{\bullet-}}^0 = -0.33$ V vs SHE in ACN respectively; equation 1.16) the free energy change corresponding to this ELT reaction is approx. -30.0 kJ mol $^{-1}$. The formation of superoxide radical anion from the photoproducted radical anion is highly favorable (Table 31) for all the PSs of this study.

Table 31 Calculated free energy for the electron transfer reactions from α -terpinene to the singlet or triplet excited states of the studied photosensitizers; free energy of the photosensitized ELT reaction from the PS radical anion to oxygen, yielding superoxide radical anion. Redox potentials are expressed vs SCE in ACN. ΔG values obtained from equation 1.15. Redox potential of α -t: $E_{(\alpha\text{-t}/\alpha\text{-t}^{\bullet+})}^0 = 1.60$ V vs SCE.³⁶³

PS	$E_{\text{PS/PS}^{\bullet-}}^0$ / V	$\Delta E_{00}(\text{S}_1)$ / kJ mol ⁻¹	$\Delta G(\text{S}_1)$ / kJ mol ⁻¹	$\Delta E_{00}(\text{T}_1)$ / kJ mol ⁻¹	$\Delta G(\text{T}_1)$ / kJ mol ⁻¹	$\Delta G(\text{PS}^{\bullet-} \rightarrow \text{O}_2^{\bullet-})$ / kJ mol ⁻¹
AQ	-0.86 ¹⁷	284	-52.6	261 ³⁷	-26.7	-30.0
RB	-1.20 ³⁶⁴	213	55.0	164	100.1	-60.7
DBTP	-0.92	288	-50.8	198	39.1	-33.7

5.0 KINETIC STUDIES

Selected reaction rate constants (k) for the photosensitized oxidation of α -t were determined by UV-Vis spectroscopy over the first 30 min of each experiment (Table 32) because in case of **AQ**-derived sensitizers, the formation of strongly absorbing secondary products (**ald**), impacted on the values for longer irradiation times. Under all experimental conditions, pseudo-zero order reactions were established. In addition, the reaction rates were of the same order of magnitude.

Nevertheless, the simple rate constant values (k) do not consider the different absorption properties of the three sensitizers. In particular, their molar absorption coefficients and the position of their absorption maxima relative to the emission spectra of the lamps differ significantly (Figures 84 and 85). Thus, approximate values of the rate constants normalized by the photon flux absorbed by the sensitizer (k_p) were calculated and were additionally compiled in Table 32. For the experiments in homogeneous solution the reactivity order was **AQ-COOH** > **DBTP-COOH** > **RB**; the same trend was found for the silica-supported sensitizers. Anthraquinone, both in solution and supported on silica was the most efficient photosensitizer, with rate constants at least one order of magnitude higher than for the other catalysts. **DBTP**, consistently to what observed in terms of quantum yields of singlet oxygen production, was at least 1.5 times more efficient than **RB**. Notably, k_p for **DBTP-Si** was only 20% lower than that for **DBTP-COOH** in homogeneous solution. In contrast, the drops in activity for silica-supported **RB** and **AQ-COOH** versus their soluble forms were significant with about 40% for **RB-Si** and 80% for **AQ-Si**, respectively. For **RB**-derived photosensitizers, the rate constants strongly depended on the support and **RB-ps** was found four times more efficient than **RB-Si**. In addition, the rate constant did not increase consistently to higher amounts of **RB-ps** (entries 3 and 4): this behavior may be caused by physical quenching of singlet oxygen by the solid sensitizer or by unfavorable absorption of light due to scattering and diffraction phenomena. For **RB**, silica was clearly not the most suitable support, while polystyrene was found advantageous for this reaction. As reported in Table 32, the same trend as for k_p was found considering the quantum yields of conversion of α -t (ϕ_{conv}), approximated by calculating the ratio of the converted molar amount of α -t and the photon flux absorbed by the sensitizer.

The k_p and ϕ_{conv} values suggest that the reaction rates and efficiencies depended on the mechanism. Compared to the **DBTP**- and **RB**-derived sensitizers, **AQ**-based materials have a much higher capability of photooxidizing α -terpinene: electron transfer induced oxidative cleavage yielding **p-c** as a main product (reactions 7.01-7.08) must thus be much faster than photooxygenation to **asc**. For the reactions involving $^1\text{O}_2$ generation by energy transfer and its cycloaddition to α -**t**, the **DBTP**-based materials were at least twice faster than their **RB**-derived counterparts, in line with what was expected from the respective values of Φ_{Δ} . In general, with supported photocatalysts the reaction efficiency decreased: this may be due to higher physical quenching of $^1\text{O}_2$ by the suspended solid.

Table 32 Kinetic constants for photosensitized conversion of α -**t** (k = kinetic constant directly calculated from the evolution of UV absorption signals; k_p = approximate values of kinetic constants normalized by the estimated photon flux absorbed by the PS (equation 3.37); ϕ_{conv} = approximate values of quantum yields of conversion of α -**t**).

^{a)} Entry numbers refer to Table 29.

entry ^{a)}	PS (mmol)	$k / 10^{-2} \text{ M min}^{-1}$	$k_p / 10^{-2} \text{ M Einstein}^{-1}$	$\phi_{\text{conv}} / 10^{-6} \text{ mol}_{\alpha\text{-t}} \text{ Einstein}^{-1}$
2	RB (0.030)	5.00 ± 1.00	7.0 ± 0.2	105 ± 5
3	RB-ps (0.003)	1.44 ± 0.03	3.8 ± 0.1	19 ± 2
4	RB-ps (0.015)	2.80 ± 0.03	4.4 ± 0.1	39 ± 3
5	RB-Si (0.038)	0.81 ± 0.02	1.1 ± 0.1	5 ± 1
7	DBTP-COOH (0.015)	5.75 ± 0.08	13.0 ± 0.2	170 ± 5
10	DBTP-Si (0.014)	4.10 ± 0.07	10.0 ± 0.2	120 ± 5
11	AQ-COOH (0.030)	6.70 ± 0.40	840 ± 40	6300 ± 100
12	AQ-Si (0.003)	1.30 ± 0.03	180 ± 4	880 ± 15

6.0 CONCLUSIONS

The reactivity and the efficiency of powdered silica-supported sensitizers, based on **DBTP-COOH**, **RB** and **AQ-COOH**, for the photooxidation of α -terpinene were analyzed. In ACN, a higher singlet oxygen quantum yield ($\Phi_{\Delta} = 1.03$) was measured for **DBTP-COOH** than for **RB** and **AQ-COOH** ($\Phi_{\Delta} = 0.42$ and 0.76, respectively). Although formation of ascaridole by singlet oxygen addition to α -**t** has been extensively studied, the fate of the by-products (followed by GC-MS and UV-Vis analysis) and of the reaction scheme appeared more complicated than expected and depended on the organic function of the immobilized photocatalyst.

With **DBTP** and **RB**-based sensitizers, ascaridole was efficiently obtained as the major product. On the other hand, **AQ**-based sensitizers favored selective photodehydrogenation to *p*-cymene followed by its oxidative cleavage upon exhaustive irradiation time. In this case, in agreement with previous

literature data, an electron transfer mechanism inducing a radical chain reaction to **p-c** and its oxidation products was proposed.

We could outline the importance of fundamental photophysical and photochemical studies for understanding the mechanisms involved in photooxidation processes: the PS, the support and the substrate can all play an important role. From our experimental results we could demonstrate that **AQ**-derived materials are efficient catalyst for photoinduced electron transfer reactions, in apparent contradiction with the efficient singlet oxygen production of the soluble PS: the reactivity scheme depends on the substrate, more precisely on the electrochemical properties of both the PS and the substrate. **DBTP-Si**, on the contrary, showed the highest efficiency and selectivity for ascaridole production: its activity was higher than that of the reference **RB**-based material (**RB-ps**) and it showed a very good reusability. As far as the photooxygenation of **α -t** in the presence of **DBTP**-derived sensitizers is concerned, the only possible mechanism involves the generation of singlet oxygen *via* ET and its subsequent addition to the diene. This newly developed material is thus really attractive for future applications in photooxygenation reactions.

All the prepared materials were obtained from commercial PSs or from easily available ones, following one-step grafting procedures which can guarantee the quantitative formation of covalent bonds between the dye and the support. The supports were also commercially available and chemically inert. These silica-supported environmentally-friendly photocatalysts are thus convenient for various applications which demand inexpensive, efficient, stable and reusable photosensitizing materials. Moreover, using functionalized silica gels as supports and the above-described grafting procedure, by suitable selection of the organic part of the catalyst, the reaction mechanisms and the achievement of particular oxidation products can be tuned. Thus, naturally available compounds can be selectively converted upon visible-light irradiation and with oxygen as the sole reactant to either endoperoxides or aromatic derivatives, all of them known as high-added value products. All these properties make these materials attractive for future green applications as immobilized photocatalyst in solar synthesis,^{124,164–166,365} waste treatment^{8,98,145,146,366,367} and microflow reactors.^{155,284,285,368–371}

General conclusions

This work was aimed at the study of the photophysical properties of several photosensitizers and at the development of photoactive materials for singlet oxygen ($^1\text{O}_2$) mediated oxidation reactions.

Three classes of sensitizers were studied:

- ~ Cyanoanthracene derivatives, originally conceived and synthesized, which were compared to 9,10-dicyanoanthracene (**DCA**). Starting from **DBTP** (9,14-dicyanobenzo[*b*]triphenylene), the graftable derivatives **2-6** were prepared and the effect of chemical functionalization on the photophysics of the dye was analyzed
- ~ Anthraquinone derivatives, which were mainly analyzed from an applicative point of view
- ~ Phenothiazine derivatives, methylene violet (**MV**) and new methylene blue (**NMB⁺**), which were compared to the well-known parent compound, methylene blue.

To study the effect of a host material on the photophysics of these visible-light absorbing dyes, transparent silica monoliths were prepared: the transparency and the free-standing shape of these materials allowed their use as microreactors for the photosensitized oxidation of sulfides at the gas-solid interface and for the characterization of the transient species directly on the supported PSs. Generally, the PSs were just inserted in the silica network, with the exception of **DBTP**, which was suitably modified for grafting purposes. In addition, some PSs were grafted to functionalized silica powders, used for photooxidation of α -terpinene at the gas-liquid interface.

The transient species of the PSs (in solution and in the supported phase) were studied and compared: the singlet and triplet excited states could be detected and analyzed. Singlet oxygen production was quantified by means of two complementary methods: direct detection of $^1\text{O}_2$ phosphorescence and chemical trapping by a selective probe. For the latter, an optical bench was set-up in the course of this work and the technique was validated by comparison with the results obtained with the direct method. This part of the work led to the determination, for all the PSs, of the photophysical pathways involved in photosensitization reactions.

By using the above-described materials in two photooxidation reactions, it was possible to point out the dependence of the reaction mechanism on both the PS and the substrate. In addition to singlet oxygen production electron transfer reactions can occur. Different mechanisms induce different products: the choice of the sensitizer must be appropriate for the photochemical process foreseen.

Fundamental studies for the precise identification of the reaction mechanisms represent an important step for the design and conception of photosensitizing materials which can be used in several application fields: fine chemistry, depollution, medical and biological phototreatments.

Concerning cyanoanthracenes, two fundamental aspects of their photophysics could be pointed out:

- ~ For all **DBTP** derivatives the triplet excited state is rapidly obtained by intersystem crossing and singlet oxygen generation is very efficient. Chemical functionalization doesn't influence the transient species significantly. The photophysical behavior of **DBTP** is not strongly modified by the insertion in silica; despite slightly lower $^1\text{O}_2$ production efficiency, the characteristics of grafted **DBTP** are similar to those of just encapsulated dye. **DBTP** showed a significant photochemical activity for the photooxidation of dimethylsulfide and α -terpinene: $^1\text{O}_2$ is the only reactive species formed with these sensitizers. Electron transfer reactions did not occur under our conditions.
- ~ The photophysics of **DBTP** derivatives significantly differs from that of **DCA**. For **DCA** singlet oxygen production predominantly occurs *via* energy transfer from the singlet excited state to ground state oxygen, while direct intersystem crossing to the triplet excited state is negligible. Such a particular behavior is due to the high energy gap between the triplet and the singlet excited states. For **DBTP** derivatives this mechanism is not observed: these PSs "classically" undergo intersystem crossing with efficiency close to unity and singlet oxygen generation occurs from the triplet excited state. Noticeably, the insertion of two additional benzyl rings on **DCA** leads to important variations on the properties of the sensitizer.

Anthraquinone was grafted to silica powders and used for the photooxidation of α -terpinene in acetonitrile. Though this PS can efficiently produce singlet oxygen ($\Phi_{\Delta} = 0.76$), the oxidation of the cyclic diene occurred *via* an electron transfer pathway yielding dehydrogenation products, further oxidized upon prolonged irradiation. Similar materials prepared with **DBTP** or rose bengal as PSs, on the contrary, produced $^1\text{O}_2$ as main reactive species and no electron transfer could be pointed out.

Phenothiazine derivatives, **MV** and **NMB**⁺, also showed good photosensitizing properties for singlet oxygen generation. In addition to the triplet excited states, semioxidized and semireduced radicals could be formed as transient species. Contrary to cyanonathracenes, phenothiazines can be very sensitive to the environment. For **MV** we observed a dramatic effect of the polarity of the medium; moreover, in acidic environments, a protonated form of the dye (**MV-OH**) is formed and becomes predominant depending on the concentration of H^+ , inducing further evolutions of the absorption spectrum. We could highlight the effects of the presence of two different forms on the ground and excited states of the PS and on the production of singlet oxygen, in both solutions (different solvents) and differently prepared silica monoliths. The stability under irradiation also depended on the presence of the protonated form. With the two phenothiazines the main photochemical reactivity implied singlet oxygen formation, but electron transfer reactions couldn't be excluded. By studying the photooxidation of dibutylsulfide in ACN, we detected traces of acids, evidenced by the solvatochromic effect on the PS absorption spectrum, deriving from photoinduced electron transfer side-reactions.

Generally, **DBTP** represents a very good candidate for the development of photosensitizing materials for depollution and fine chemistry: it absorbs visible light, it is relatively easily functionalized, it is barely sensitive to the environment, it is highly stable under UV-Vis irradiation and it is a very efficient singlet oxygen producer. Anthraquinone represents a suitable PS for electron transfer reactions in the same application fields: it is stable, easily available and graftable and, notwithstanding its low absorbance in the visible, its reactivity is surprisingly efficient. **MV** and **NMB**⁺

can be seriously considered for photodynamic therapy and photoinduced inactivation of viruses and bacteria: the two PSs are very efficient singlet oxygen producers, they are commercially available, easily produced and modified.

The work carried out during the last three years allows for very interesting further explorations:

- For the synthesis of compounds **3** and **4**, more efficient purification steps can be undertaken, mainly aimed at less consumption of solvents. Unfortunately, for all the synthesis, the low solubility of **DBTP** derivatives represented the main difficulty to face and the use of high amounts of solvents for the purification of the dyes was necessary (also for washing silica powders). Compound **4** already represents an important improvement relative to compound **3** but other steps forward should be possible.
- Further investigations concerning **MV**, whose properties showed peculiar fluctuations depending on the environment, are necessary. Some clues for the understanding of its particular behavior were pointed out but many questions are still unanswered. It would be interesting to analyze the photochemical reactivity and stability of **MV** in other media and for other reactions, and to set-up methods for the detection of reactive species other than singlet oxygen. More information will allow the precise identification of the reaction mechanisms taking place upon irradiation in the presence of dibutylsulfide in acetonitrile.
- Grafting procedures could be attempted to covalently bind the phenothiazine PSs to suitable supports. **NMB⁺** presents a grafting group which could be exploited, even though its reactivity is quite low; **MV** in its neutral form is not graftable but **MV-OH** is actually a species we could take advantage of, also considering its higher stability under irradiation.
- Since silica monoliths are good supports for the spectroscopic characterization of dyes, they can be used for other photosensitizers.
- Silica bearing functional groups other than those presented here could be used. Several differently functionalized silica gels are commercially available and could be envisaged for grafting photosensitizers. Moreover, the optimization of the synthesis of silica bearing sulfonic functionalities might lead to the insertion of photosensitizers *via* ionic interactions: this could also be done starting from silica powders bearing SO_3H groups.
- Hosting materials other than silica could be prepared. **DBTP** can be grafted on polystyrene resins: many organic and inorganic supports that can bear reactive functionalities can be used as supports for the preparation of photoactive materials.
- Testing the photosensitizing activity of the materials described in this work on biological media would perfectly insert in the research subject currently carried out in our group on the photocatalytic bactericidal activity of TiO_2 -derived materials. It would enlarge the future developments of photoactive materials for bacteria inactivation. In the case of **DBTP**-supporting materials, since we observed unique generation of singlet oxygen, it would be possible to focus on the reactivity of this ROS towards cellular specimens.

- The design of a flow reactor conceived for the use of supported photosensitizers could imply further technological evolutions of this subject: the oxidation of α -terpinene could be used as a model reaction for the optimization of such a device. With the development of an efficient reactor, many synthetic reactions could be performed under green conditions.

Acknowledgements

Evidently, such an extensive work is the outcome of several fruitful partnerships: without the support and the collaboration of the people involved in this project, our results would be less complete and well-interpreted.

I would like to thank Mohamed Sarakha and Claire Richard of the ICCF (Université Blaise Pascal – Clermont Ferrand), for welcoming me in their laboratory for the laser flash photolysis tests; their help in carrying out the experiments and, especially, in interpreting our results was extremely constant and deepened. I also gladly thank Esther Oliveros of the IMRCP (Université Paul Sabatier – Toulouse) for letting us apprehend the technique for direct singlet oxygen detection; her knowledge of singlet oxygen chemistry and of photochemistry in general was a substantial support for the interpretation of our results. I would like to thank also Michael Oelgemöller of the University of Townsville, for the tremendous and intense work he carried out in Pau for the α -terpinene photooxidation tests: his mastery of organic chemistry and photochemical techniques for fine chemicals was fundamental for the positive and interesting results obtained. He helped me in discovering the world of the applications of photosensitization in chemical synthesis. Thanks to these people photochemistry is a less mysterious universe...

Special thanks to Nathalie Costarramone and Mickaël Le Behec: they demonstrated that without the supports of *ingénieurs*, research would be extremely slower and less efficient. Thanks to Nathalie for all the hours she spent with earplugs trying to identify and analyze our products by GC-MS; and thanks to Mickaël for his constant, precise and detailed support for gas chromatography and radiant power measurements. Their management of the laboratory and of the equipment has always been very effective and their helpfulness a constant of our everyday working life.

Thanks to Patrice Bordat, who has always been helpful for carrying out theoretical calculations for supporting our sometimes unsteady results. I gladly thank Aurélien Trivella (Université Blaise Pascal, Clermont Ferrand) and Emmanuel Arzoumanian (Université Paul Sabatier, Toulouse) for the experiments they carried out for the detection of the transient species and singlet oxygen, respectively. Thanks to Cyril Cugnet and Abdel Khoukh for the electrochemical tests and the NMR spectra, respectively. I would like to thank some people that never balked at my demands of suggestions, advices, supports: Stéphane Labat for his deep mastery of organic synthesis, Hélène Paolacci for the constructive discussions concerning the sol-gel synthesis and Thierry Pigot, without forgetting all the above-mentioned colleagues.

I am aware of the fact that without the work carried out before my arrival, my PhD would have been much different: an overall acknowledgement for all the members, past or present, of our small group of photochemical reactivity: my predecessors Philippe, Christophe and Virginie, for their first ideas and advances (especially for the synthesis of materials and for the set-up for the gas-phase reactivity); Ross and Patrice for their impressive knowledge of spectroscopy; Thierry for his capability

of considering subjects in a global perspective, Mickaël and Nathalie for their technical advices and their overall capability of solving problems, of all matters.

I am extremely grateful of the time and energy my advisers spent during these last three years for me and my research work: without their constant help I would have groped in the dark. Sylvie Blanc and Sylvie Lacombe were always aware of what I was doing and they were exceptionally helpful for all the problems occurring: their presence has been a fundamental support for all the aspects of my life in Pau. I want to thank them for their supervision, but also for their respect towards me, my ideas and my advices: they always made me feel more like a coworker than like a student to manage and if I can consider my PhD as a personal work it is thanks to the liberty they gave me to build up my own trail in this field.

Last, but not least, I would like to particularly thank Xavier Allonas (LPIM, Laboratoire de Photochimie et d'Ingénierie Macromoléculaires, Ecole Nationale Supérieure de Chimie de Mulhouse, Université de Haute Alsace, Mulhouse) and Elena Selli (Dipartimento di Chimica Fisica ed Elettrochimica, Università degli Studi di Milano), the *rapporteurs* of this long and dense PhD thesis, for accepting the intense task of reviewing my work. I am sorry, I've always been long-winded...

I should also thank the MESR for funding my PhD thesis and ANR for financing the MEPHISTO project; thanks again to Sylvie for including me in this project, allowing me to travel and discover many other realities (Clermont, Toulouse etc.) and to present my results in various international and national meetings.

I would also like to thank E. S. for pushing me to accept this PhD position in Pau: her advice has been really important for my final decision and there is nothing, professionally speaking, that I can regret. Obviously, a perfect thesis and a perfect working environment are just utopias: life is a continuous compromise but I firmly believe to have accepted a good deal. It has been an immense pleasure to work with the people I briefly thanked here. Much more words should be written to completely express these feelings, but I think that the concerned people already know them. I am just happy to have shared the last three years of my life with these colleagues. I also hope to succeed in leaving them something authentic, in addition to this dense *manuscrit*.

SPECIAL THXs

Uno degli obiettivi principali di un dottorato è quello di non farsi intrappolare in quella strana dimensione dove le settimane scivolano via a una velocità spaventosa e si passa la maggior parte del tempo in laboratorio o in ufficio davanti al computer, tralasciando la vita privata e sociale. E se si trovano delle scappatoie è grazie a quelle persone i cui cammini si sono incrociati ai nostri, con cui si sono condivisi dei momenti importanti e veri. È d'obbligo quindi un ringraziamento generale a tutte quelle persone che hanno contribuito a riempire questi tre fugaci anni.

Un generalizzato grazie a tutti gli erasmus che hanno accompagnato i miei primi passi in terra paloise, tra serate, corsi di lingua e lunghi altri momenti d'internazionalità: grazie all'atmosfera creata con loro, gli inizi da dottorando in terra straniera sono stati spensierati e sereni.

Un grazie a Pierre, mio primo coloc e compagno di ufficio, che mi ha gentilmente introdotto alla cultura francese, agli usi e costumi di questo strano popolo...e a Vincent, grande compagno di serate e di conversazioni. Due dottori che mi sono sinceramente mancati in questi ultimi mesi...

Ringrazio tutti coloro che hanno partecipato alla mia vita di tutti i giorni all'IPREM, tutti i miei colleghi dottorandi, dottorati et al. Mi sono sempre lamentato dell'ipocrisia e della superficialità delle relazioni umane nella nostra équipe e non è certo adesso che cambierò opinione...tuttavia ho avuto la fortuna di incrociare dei colleghi con cui ho potuto instaurare delle relazioni solide e generose, fondate sul rispetto reciproco. Tra questi vorrei ringraziare Sylvie, sempre attenta ad accogliere con un sorriso i nuovi arrivati e sempre sensibile alle mie lamentele e ai miei problemini di tesi. E grazie a Kasia e Simon, gli altri due caratteriali del caso, con cui, tra le altre cose, ho potuto sfogarmi circa le abitudini della maggior parte dei colleghi. Benchè al di fuori dell'IPREM, vorrei ringraziare calorosamente Maïté, che si è sempre prodigata con un generoso sorriso a scaldare le riunioni e le serate in quel di Toulouse, per i suoi consigli e il suo appoggio in questi tre anni.

Vorrei ringraziare Alex, mia coinquilina per questo terzo anno, per le chiacchierate e per il gioioso equilibrio che siamo riusciti a creare in questo appartamento....e kouna, che in fin dei conti è stata un'ottima compagna di "coccole"...quanti peli però!

Ringrazio dal profondo del cuore tutti i miei amici italici che, malgrado la distanza che ci ha separati in questi anni, sono sempre riusciti a farsi sentire vicini e a mostrarsi come prima che partissi, senza dare importanza alla lontananza: ciò che è stato creato rimarrà, che ci si veda ogni giorno o ogni anno! Un grazie speciale quindi ai miei amici che condividono ormai la loro vita con la mia da anni e anni: che meraviglia partire e sapere che, indipendentemente da dove si sia e cosa si stia facendo, c'è un luogo che si potrà sempre chiamare "chez soi" e dove ci aspettano le persone che si possono veramente chiamare amici. Fa parte di questo piccolo universo del sentirsi a casa anche tutta la mia famiglia, che mi ha non solo amato e sostenuto qualunque cosa facessi, ma che si è data da fare per rendere la mia vita la più agevole possibile. Grazie di cuore, per questi ultimi tre anni e per tutti i precedenti.

Un enorme ringraziamento ai Pirenei e a questa verde terra di piogge e anatre; alcune delle tradizioni di questi luoghi (soprattutto culinarie, evidentemente!) mi hanno marcato in modo indelebile e cercherò di esportare un po' di questo spirito del sud-ouest là dove andrò...e grazie a Barbara e tutti gli altri "animali" della famiglia, per avermi accettato di cuore nella loro vita.

Un grazie particolare alla mia capa, Sylvie, che non solo è stata una direttrice formidabile, ma si è anche dimostrata una persona sensibile e aperta, che non mi ha mai guardato dall'alto in basso, che mi ha aiutato a prendere coscienza di me stesso e con cui abbiamo passato piacevolissimi momenti di lavoro e non, tra cui un paio di apéritifs dînatoires a dir poco luculliani...tutta colpa di Jean-Claude!

Infine un enorme grazie alle due persone con cui ho condiviso di più. Grazie a Mickaël, collega ideale e ormai grande amico, per gli scambi di idee che hanno continuamente accompagnato le nostre pause caffè e per le magnifiche serate passate in sua compagnia con Sarah ed Emilie; il mio ultimo anno di tesi sarebbe stato senz'altro disastrosamente noioso e monotono senza la sua compagnia! Senza il vino! È bello sapere di poter contare su qualcuno...e grazie a Sarah, che nonostante i difetti che può avere, ha avuto per due anni e mezzo (e spero avrà ancora a lungo), il magnifico pregio di sopportare i miei difetti. Senza contare il suo appoggio, gli incoraggiamenti e la fiducia che ha riposto in me; grazie a lei mi sono sentito importante, per la prima volta dopo tanto tempo; la sua presenza mi dato la voglia di diventare una persona migliore. Il suo contributo alla buona riuscita del mio lavoro e alla mia sanità mentale durante tutto il dottorato é incalcolabile.

Eccoci dunque, questo pezzo di vita termina e un altro comincerà ben presto, dove e come non si sa...verso l'infinito e oltre! Il mio ricordo sarà estremamente positivo: quello che ho imparato e acquisito in tre anni sarà un bagaglio estremamente importante che mi porterò appresso per molto tempo. Spero di lasciare qualcosa di buono alle persone che hanno lasciato qualcosa di buono in me. Mi riferisco al lavoro ma anche ai rapporti umani che si sono instaurati. Questa é la speranza...mal che vada avrò incentivato gli scambi culturali italo-francesi/franco-italiani!

L'altra speranza é che quanto costruito nel nostro gruppo non si perda una volta partite le "braccia"; già un po' di lassismo ha minato l'atmosfera che regnava agli inizi della mia tesi e ha abbassato il rendimento lavorativo. Spero che le cose non si degradino troppo in fretta, che le redini del gioco non vengano lasciate penzolare a terra mentre i cavalli proseguono alla cieca, che la buona volontà riprenda vigore per continuare a lavorare in modo concertato e piacevole. Mi piace pensare che le cose andranno avanti e non indietro, che potrò riguardare a Pau e ai miei compagni di lavoro come riferimenti per le mie prossime avventure. Per me, ma soprattutto per coloro che hanno speso tante energie per il bene collettivo e che continueranno a farlo, ne sono certo, negli anni a venire.

L'un des principaux objectifs d'un doctorat est de ne pas être pris au piège dans cette étrange dimension où les semaines se succèdent à une vitesse effrayante et où on passe la plupart du temps dans le laboratoire (bien sûr, pas tout seule) ou au bureau devant l'ordinateur, en négligeant la vie privée et sociale. Et s'il y a des échappatoires c'est grâce aux gens qu'on a croisés, avec qui on a partagé des moments véritablement importants. Il est donc nécessaire un grand remerciement à tous ceux qui ont aidé à remplir ces trois fugaces années.

Un remerciement général à tous les erasmus qui ont accompagné mes premiers pas en terre paloise, pendant les soirées, les cours de langues et les autres moments internationaux ; grâce à l'atmosphère créée avec eux, les premiers mois de ma vie en tant que doctorant en terre étrangère ont été sereins.

Merci à Pierre, mon premier coloc et collègue de bureau, qui m'a gentiment introduit à la culture française, aux habitudes et coutumes de ce peuple bizarre...et Vincent, grand compagnon de soirées et de conversations. Deux docteurs qui m'ont sincèrement manqué ces derniers mois...

Je remercie toutes les personnes qui ont participé à ma vie de tous les jours à l'IPREM, tous mes collègues doctorants, docteurs et al. Je me suis toujours plaint de l'hypocrisie et la superficialité des relations humaines dans notre équipe et ce n'est pas maintenant que je vais changer d'avis...mais j'ai aussi eu la chance de croiser des collègues avec lesquels des relations solide et généreuse, fondées sur le respect mutuel, se sont établies. Parmi eux, je tiens à remercier Sylvie, toujours prête à accueillir les nouveaux avec un sourire et toujours sensible à mes plaintes et mes petits soucis de thèse. Et merci à Kasia et Simon, les

deux autres caractéristiques de la situation, avec qui, entre autres choses, j'ai pu me défouler sur les habitudes de la plupart des collègues. Malgré extérieurement à la réalité de l'IPREM, merci à Maïte, qui s'est toujours prodiguée en souriant pour réchauffer l'atmosphère durant les réunions et les soirées à Toulouse, pour ses conseils et son soutien pendant ces trois ans.

Je tiens à remercier Alex, ma coloc pour la troisième année, pour les conversations et l'équilibre joyeux que nous avons créé dans cet appartement...et Kouna, qui finalement a été une excellente partenaire de « chouchoutement »...combien de poils par contre!

Je remercie du fond du cœur tous mes amis italiens qui, malgré la distance qui nous séparait, ont toujours réussi à se faire sentir proches et à se comporter comme avant que je parte, sans se soucier de la distance: ce qui a été créé restera, que l'on se voit tous les jours ou une fois par an! Un grand merci à mes amis qui ont partagé leurs vies avec la mienne pendant des nombreuses années : quelle merveille partir à l'étranger en sachant que, peu importe où on est et ce qu'on fait, il y a un endroit qu'on peut toujours appeler chez nous et où nous attendent des personnes qu'on peut vraiment appeler amis. Fait aussi partie de ce petit univers du chez soi, toute ma famille, qui ne m'a pas seulement aimé et soutenu, mais qui a toujours fait de grands efforts pour rendre ma vie aussi agréable que possible. Merci beaucoup, pour les trois dernières années et pour toutes les précédentes.

Un grand merci aux Pyrénées et à cette verte terre de pluie et canards; certaines traditions de cette région (surtout culinaire, évidemment!) m'ont marqué de façon indélébile, et j'essaierai d'exporter un peu de cet esprit du sud-ouest là où je serai...merci à Barbara et tous les autres « animaux » de la famille, de m'avoir chaleureusement accepté dans leur vie.

Un merci spécial à ma chef, Sylvie, qui non seulement a été une directrice formidable, mais qui s'est également démontrée être une personne sensible et ouverte, qui ne m'a jamais regardé vers le bas, qui m'a aidé à prendre conscience de moi-même et avec qui j'ai passé d'agréables moments de travail et non, compris quelques somptueux apéritifs dînatoires...c'est la faute de Jean-Claude!

Enfin un grand merci aux deux personnes avec qui j'ai partagé le plus. Merci à Mickaël, un collègue idéal et maintenant grand ami, pour l'échange d'idées qui a toujours accompagné nos pauses café et les magnifiques soirées passées en sa compagnie avec Sarah et Emilie ; ma thèse aurait sans doute été désastreusement terne et ennuyeuse sans sa compagnie! Sans parler du pinard! C'est bien de savoir qu'on peut compter sur quelqu'un...et merci à Sarah, qui malgré les défauts qu'elle peut avoir, a eu pendant deux ans et demi (et je l'espère, pour une longue période à suivre), la magnifique qualité de supporter les miens de défauts. Sans parler de son soutien, de l'encouragement et de la confiance qu'elle m'a donné ; grâce à elle je me suis senti important, pour la première fois depuis un long moment ; sa présence m'a donné l'envie de devenir une meilleure personne. Sa contribution à la réussite de mon travail et à ma santé mentale tout au long du doctorat est incalculable.

Nous voici donc, ce morceau de vie se termine et un autre commence bientôt, où et comment on ne sait pas...vers l'infini et au-delà! Mon souvenir sera extrêmement positif: ce que j'ai appris et acquis en trois ans sera un bagage très important que je porterai avec moi pendant un long moment. J'espère de laisser quelques choses de bon aux personnes qui ont laissé plein de choses positives en moi. Je me réfère au boulot, mais aussi aux relations humaines qui se sont créées. C'est mon espoir... au pire j'aurai contribué aux échanges culturels franco-italiens ou italo-français!

Un autre espoir est que tout ce qui a été construit au sein de notre groupe ne se détériore pas une fois les « bras » partis ; déjà un peu de laxisme a miné l'atmosphère qui régnait au début de ma thèse et baissé le rendement du travail. J'espère que les choses ne se dégradent pas trop vite, que les rênes qui mènent le jeu ne soient pas laissées pendre au sol pendant que les chevaux poursuivent à l'aveuglette, que la bonne

volonté reprenne force pour continuer à travailler de manière concertée et agréable. J'aime penser que les choses n'iront pas en arrière, que Pau et mes collègues de travail resteront une référence pour mes prochaines aventures. Pour moi, mais surtout pour ceux qui ont prodigué tant d'énergie pour le bien collectif et continueront de le faire, j'en suis sûr, les années à venir.

Bibliography

- (1) Wayne, R. P. *Principles and applications of photochemistry*; Oxford University Press, Incorporated: Oxford, 1988.
- (2) Hoffmann, R.; Woodward, R. B. *J. Am. Chem. Soc.* **1965**, *87*, 2046.
- (3) Gilbert, A.; Baggott, J. E. *Essentials of molecular photochemistry*; CRC Press, 1991.
- (4) Braslavsky, S. E. *Pure Appl. Chem.* **2007**, *79*, 293.
- (5) Braslavsky, S. E.; Braun, A. M.; Cassano, A. E.; Emeline, A. V.; Litter, M. I.; Palmisano, L.; Parmon, V. N.; Serpone, N. *Pure Appl. Chem.* **2011**, *83*, 931.
- (6) DeRosa, M. C.; Crutchley, R. J. *Coord. Chem. Rev.* **2002**, *233*, 351.
- (7) Lacombe, S.; Pigot, T. In *New materials for sensitized photo-oxygenation*; The Royal Society of Chemistry, 2010; Vol. 38.
- (8) Marin, M. L.; Santos-Juanes, L.; Arques, A.; Amat, A. M.; Miranda, M. A. *Chem. Rev.* **2012**, *112*, 1710.
- (9) Fukuzumi, S.; Ohkubo, K. *Chem. Sci.* **2013**, *4*, 561.
- (10) Liu, N.; Sun, G. *Ind. Eng. Chem. Res.* **2011**, *50*, 5326.
- (11) Silva, E. F. F.; Serpa, C.; Dąbrowski, J. M.; Monteiro, C. J. P.; Formosinho, S. J.; Stochel, G.; Urbanska, K.; Simões, S.; Pereira, M. M.; Arnaut, L. G. *Chem. Eur. J.* **2010**, *16*, 9273.
- (12) Sawyer, D. T. In *Oxygen Complexes and Oxygen Activation by Transition Metals*; Martell, A. E.; Sawyer, D. T., Eds.; Springer US, 1988; pp. 131–148.
- (13) Sawyer, D. T. *Oxygen Chemistry*; Oxford University Press: Oxford, 1991.
- (14) Sawyer, D. T.; Valentine, J. S. *Acc. Chem. Res.* **1981**, *14*, 393.
- (15) Rehm, D.; Weller, A. *Isr. J. Chem.* **1970**, 259.
- (16) Oppenländer, T. *Photochemical Purification of Water and Air*; Wiley-VCH, Weinheim, 2003.
- (17) Gollnick, K.; Held, S. *J. Photochem. Photobiol., A* **1993**, *70*, 135.
- (18) Herzberg, G. *Molecular spectra and molecular structure. Vol.1: Spectra of diatomic molecules*; Van Nostrand Reinhold: New York, 1950; Vol. 1.
- (19) Arnold, S. J.; Kubo, M.; Ogryzlo, E. A. In *Oxidation of Organic Compounds*; Advances in Chemistry; American Chemical Society, 1968; Vol. 77, pp. 133–142.
- (20) Merkel, P. B.; Kearns, D. R. *J. Am. Chem. Soc.* **1972**, *94*, 1029.
- (21) Long, C. A.; Kearns, D. R. *J. Am. Chem. Soc.* **1975**, *97*, 2018.
- (22) Foote, C. S.; Clennan, E. L. In *Active Oxygen in Chemistry*; Foote, C. S.; Valentine, J. S.; Greenberg, A.; Liebman, J. F., Eds.; Structure Energetics and Reactivity in Chemistry Series (SEARCH Series); Springer Netherlands, 1996; pp. 105–140.
- (23) Clennan, E. L. *Tetrahedron* **2000**, *56*, 9151.
- (24) Rawls, H. R.; Santen, P. J. V. *J. Am. Oil Chem. Soc.* **1970**, *47*, 121.
- (25) Adams, G. E.; Willson, R. L. *Trans. Faraday Soc.* **1969**, *65*, 2981.
- (26) Clennan, E. L.; Pace, A. *Tetrahedron* **2005**, *61*, 6665.
- (27) Kruk, I. *Environmental Toxicology and Chemistry of Oxigen Species*; Springer, 1998.
- (28) Hastings, J. W.; Wilson, T. *Photochem. Photobiol.* **1976**, *23*, 461.
- (29) Mazur, S.; Foote, C. S. *J. Am. Chem. Soc.* **1970**, *92*, 3225.
- (30) Rabek, J. F. *Photodegradation of polymers: physical characteristics and applications*; Springer, 1996.
- (31) Wilkinson, F.; Helman, W. P.; Ross, A. B. *J. Phys. Chem. Ref. Data* **1993**, *22*, 113.
- (32) Olea, A. F.; Wilkinson, F. *J. Phys. Chem.* **1995**, *99*, 4518.
- (33) Redmond, R. W.; Gamlin, J. N. *Photochem. Photobiol.* **1999**, *70*, 391.
- (34) Wilkinson, F.; Helman, W. P.; Ross, A. B. *J. Phys. Chem. Ref. Data* **1995**, *24*, 663.
- (35) Kavarnos, G. J.; Turro, N. J. *Chem. Rev.* **1986**, *86*, 401.
- (36) Kalsi, P. S. *Spectroscopy Of Organic Compounds*; New Age International, 2007.
- (37) Murov, S. L.; Hug, G. L.; Carmichael, I. *Handbook Of Photochemistry*; Second Edition.; Marcel Dekker Inc, New York, Basel, 1993.

- (38) Foote, C. S. *Tetrahedron* **1985**, *41*, 2221.
- (39) Dobrowolski, D. C.; Ogilby, P. R.; Foote, C. S. *J. Phys. Chem.* **1983**, *87*, 2261.
- (40) Kanner, R. C.; Foote, C. S. *J. Am. Chem. Soc.* **1992**, *114*, 678.
- (41) Lykakis, I. N.; Lestakis, S.; Orfanopoulos, M. *Tetrahedron Lett.* **2003**, *44*, 6247.
- (42) Olea, A. F.; Worrall, D. R.; Wilkinson, F.; Williams, S. L.; Abdel-Shafi, A. A. *Phys. Chem. Chem. Phys.* **2002**, *4*, 161.
- (43) Manring, L. E.; Gu, C. L.; Foote, C. S. *J. Phys. Chem.* **1983**, *87*, 40.
- (44) Wu, H.; Song, Q.; Ran, G.; Lu, X.; Xu, B. *TrAC, Trends Anal. Chem.* **2011**, *30*, 133.
- (45) Martí, C.; Jürgens, O.; Cuenca, O.; Casals, M.; Nonell, S. *J. Photochem. Photobiol., A* **1996**, *97*, 11.
- (46) Oliveros, E.; Suardi-Murasecco, P.; Aminian-Saghafi, T.; Braun, A. M.; Hansen, H.-J. *Helv. Chim. Acta* **1991**, *74*, 79.
- (47) Schmidt, R.; Tanielian, C.; Dunsbach, R.; Wolff, C. *J. Photochem. Photobiol., A* **1994**, *79*, 11.
- (48) Arnbjerg, J.; Paterson, M. J.; Nielsen, C. B.; Jørgensen, M.; Christiansen, O.; Ogilby, P. R. *J. Phys. Chem. A* **2007**, *111*, 5756.
- (49) Daza, M. C.; Doerr, M.; Salzmann, S.; Marian, C. M.; Thiel, W. *Phys. Chem. Chem. Phys.* **2009**, *11*, 1688.
- (50) Segado, M.; Reguero, M. *Phys. Chem. Chem. Phys.* **2011**, *13*, 4138.
- (51) Flors, C.; Nonell, S. *J. Photochem. Photobiol., A* **2004**, *163*, 9.
- (52) Baier, J.; Fuß, T.; Pöllmann, C.; Wiesmann, C.; Pindl, K.; Engl, R.; Baumer, D.; Maier, M.; Landthaler, M.; Bäuml, W. *J. Photochem. Photobiol., B* **2007**, *87*, 163.
- (53) Alegría, A. E.; Ferrer, A.; Santiago, G.; Sepúlveda, E.; Flores, W. *J. Photochem. Photobiol., A* **1999**, *127*, 57.
- (54) Shen, L.; Ji, H.-F.; Zhang, H.-Y. *J. Mol. Struct.: THEOCHEM* **2008**, *851*, 220.
- (55) Latour, V.; Pigot, T.; Simon, M.; Cardy, H.; Lacombe, S. *Photochem. Photobiol. Sci.* **2005**, *4*, 221.
- (56) Gutiérrez, I.; Bertolotti, S. G.; Biasutti, M. A.; Soltermann, A. T.; García, N. A. *Can. J. Chem.* **1997**, *75*, 423.
- (57) Maurino, V.; Borghesi, D.; Vione, D.; Minero, C. *Photochem. Photobiol. Sci.* **2008**, *7*, 321.
- (58) Saint-Cricq, P.; Pigot, T.; Blanc, S.; Lacombe, S. *J. Hazard. Mater.* **2012**, *211–212*, 266.
- (59) Chen, J.; Cesario, T. C.; Rentzepis, P. M. *Chem. Phys. Lett.* **2010**.
- (60) Mills, A.; Hazafy, D.; Parkinson, J.; Tuttle, T.; Hutchings, M. G. *Dyes Pigments* **2011**, *88*, 149.
- (61) Mills, A.; Hazafy, D.; Parkinson, J. A.; Tuttle, T.; Hutchings, M. G. *J. Phys. Chem. A* **2009**, *113*, 9575.
- (62) Wainwright, M. *Int. J. Antimicrob. Ag.* **2000**, *16*, 381.
- (63) Wainwright, M.; Giddens, R. M. *Dyes Pigments* **2003**, *57*, 245.
- (64) Wainwright, M.; Byrne, M. N.; Gattrell, M. A. *J. Photochem. Photobiol., B* **2006**, *84*, 227.
- (65) Wainwright, M.; Mohr, H.; Walker, W. H. *J. Photochem. Photobiol., B* **2007**, *86*, 45.
- (66) Aebisher, D.; Zamadar, M.; Mahendran, A.; Ghosh, G.; McEntee, C.; Greer, A. *Photochem. Photobiol.* **2010**, *86*, 890.
- (67) Stracke, F.; Heupel, M.; Thiel, E. *J. Photochem. Photobiol., A* **1999**, *126*, 51.
- (68) Wainwright, M. *J. Antimicrob. Chemother.* **2001**, *47*, 1.
- (69) Darwent, J. R.; Douglas, P.; Harriman, A.; Porter, G.; Richoux, M.-C. *Coord. Chem. Rev.* **1982**, *44*, 83.
- (70) Sanjuán, A.; Aguirre, G.; Alvaro, M.; García, H. *Appl. Catal., B* **1998**, *15*, 247.
- (71) Bonesi, S. M.; Carbonell, E.; Garcia, H.; Fagnoni, M.; Albin, A. *Appl. Catal., B* **2008**, *79*, 368.
- (72) Miranda, M. A.; Marín, M. L.; Amat, A. M.; Arques, A.; Seguí, S. *Appl. Catal., B* **2002**, *35*, 167.
- (73) Sanjuán, A.; Aguirre, G.; Alvaro, M.; García, H. *Water Res.* **2000**, *34*, 320.
- (74) Arbogast, J. W.; Foote, C. S. *J. Am. Chem. Soc.* **1991**, *113*, 8886.
- (75) Arbogast, J. W.; Darmanyan, A. P.; Foote, C. S.; Diederich, F. N.; Whetten, R. L.; Rubin, Y.; Alvarez, M. M.; Anz, S. *J. Phys. Chem.* **1991**, *95*, 11.
- (76) Bayarri, B.; Carbonell, E.; Gimenez, J.; Esplugas, S.; Garcia, H. *Chemosphere* **2008**, *72*, 67.
- (77) Paczkowski, J.; Neckers, D. C. *Macromolecules* **1985**, *18*, 1245.
- (78) Gottschalk, P.; Paczkowski, J.; Neckers, D. C. *J. Photochem.* **1986**, *35*, 277.
- (79) Perni, S.; Piccirillo, C.; Pratten, J.; Prokopovich, P.; Chrzanowski, W.; Parkin, I. P.; Wilson, M. *Biomaterials* **2009**, *30*, 89.
- (80) Naik, A. J. T.; Ismail, S.; Kay, C.; Wilson, M.; Parkin, I. P. *Mater. Chem. Phys.* **2011**, *129*, 446.
- (81) Shiraishi, Y.; Kimata, Y.; Koizumi, H.; Hirai, T. *Langmuir* **2008**, *24*, 9832.
- (82) Wetzler, D. E.; García-Fresnadillo, D.; Orellana, G. *Phys. Chem. Chem. Phys.* **2006**, *8*, 2249.
- (83) Zhu, J.; Sun, G. *J. Mater. Chem.* **2012**, *22*, 10581.
- (84) Ricciardi, L.; Puoci, F.; Cirillo, G.; Deda, M. L. *Dalton Trans.* **2012**, *41*, 10923.
- (85) Han, X.; Bourne, R. A.; Poliakov, M.; George, M. W. *Chem. Sci.* **2011**, *2*, 1059.

- (86) Liu, N.; Sun, G.; Zhu, J. *J. Mater. Chem.* **2011**, *21*, 15383.
- (87) Brewer, S. A.; Artiles, C. P.; Taylor, J. A.; Dennis, M. *Appl. Surf. Sci.* **2010**, *256*, 1908.
- (88) Jesenská, S.; Plíštil, L.; Kubát, P.; Lang, K.; Brožová, L.; Popelka, Š.; Szatmáry, L.; Mosinger, J. *J. Biomed. Mater. Res., Part A* **2011**, *99A*, 676.
- (89) Ringot, C.; Sol, V.; Barrière, M.; Saad, N.; Bressollier, P.; Granet, R.; Couleaud, P.; Frochot, C.; Krausz, P. *Biomacromolecules* **2011**, *12*, 1716.
- (90) Lee, S. J.; Koo, H.; Jeong, H.; Huh, M. S.; Choi, Y.; Jeong, S. Y.; Byun, Y.; Choi, K.; Kim, K.; Kwon, I. C. *J. Controlled Release* **2011**, *152*, 21.
- (91) Santos, D. T.; Albarelli, J. Q.; Joyce, K.; Oelgemöller, M. *J. Chem. Technol. Biotechnol.* **2009**, *84*, 1026.
- (92) Albitzer, E.; Alfaro, S.; Valenzuela, M. A. *Int. J. Photoen.* **2012**, *2012*, 1.
- (93) Tamagaki, S.; Liesner, C. E.; Neckers, D. C. *J. Org. Chem.* **1980**, *45*, 1573.
- (94) Miranda, M. A.; Amat, A. M.; Arques, A. *Catal. Today* **2002**, *76*, 113.
- (95) Murillo-Cremaes, N.; López-Periago, A. M.; Saurina, J.; Roig, A.; Domingo, C. *Green Chem.* **2010**, *12*, 2196.
- (96) Soggiu, N.; Cardy, H.; Habib Jiwan, J. L.; Leray, I.; Soumillion, J. P.; Lacombe, S. *J. Photochem. Photobiol., A* **1999**, *124*, 1.
- (97) Lacombe, S.; Cardy, H.; Simon, M.; Khoukh, A.; Soumillion, J. P.; Ayadim, M. *Photochem. Photobiol. Sci.* **2002**, *1*, 347.
- (98) Benabbou, A. K.; Guillard, C.; Pigeot-Rémy, S.; Cantau, C.; Pigot, T.; Lejeune, P.; Derriche, Z.; Lacombe, S. *J. Photochem. Photobiol., A* **2011**, *219*, 101.
- (99) Trytek, M.; Majdan, M.; Lipke, A.; Fiedurek, J. *J. Catal.* **2012**, *286*, 193.
- (100) Jia, X.; Jia, L. *Curr. Drug Metab.* **2012**, *13*, 1119.
- (101) Bachl, J.; Hohenleutner, A.; Dhar, B. B.; Cattivola, C.; Maitra, U.; König, B.; Díaz, D. D. *J. Mater. Chem. A* **2013**, *1*, 4577.
- (102) Horsa, S.; Perez, K.; Miksovska, J. *J. Photochem. Photobiol., A* **2011**, *221*, 84.
- (103) Amat, A. M.; Arques, A.; Bossmann, S. H.; Braun, A. M.; Miranda, M. A.; Vercher, R. F. *Catal. Today* **2005**, *101*, 383.
- (104) Kyriakopoulos, J.; Tzirakis, M. D.; Panagiotou, G. D.; Alberti, M. N.; Triantafyllidis, K. S.; Giannakaki, S.; Bourikas, K.; Kordulis, C.; Orfanopoulos, M.; Lycourghiotis, A. *Appl. Catal., B* **2012**, *117–118*, 36.
- (105) Madhavan, D.; Pitchumani, K. *Tetrahedron* **2001**, *57*, 8391.
- (106) Pigot, T.; Arbitre, T.; Martinez, H.; Lacombe, S. *Tetrahedron Lett.* **2004**, *45*, 4047.
- (107) Xiong, Z.; Xu, Y.; Zhu, L.; Zhao, J. *Langmuir* **2005**, *21*, 10602.
- (108) Manjón, F.; García-Fresnadillo, D.; Orellana, G. *Photochem. Photobiol. Sci.* **2009**, *8*, 926.
- (109) Manjón, F.; Santana-Magaña, M.; García-Fresnadillo, D.; Orellana, G. *Photochem. Photobiol. Sci.* **2010**, *9*, 838.
- (110) Ogawa, M.; Sohmiya, M.; Watase, Y. *Chem. Commun.* **2011**, *47*, 8602.
- (111) Afzal, S.; Daoud, W. A.; Langford, S. J. *J. Mater. Chem.* **2012**, *22*, 4083.
- (112) Rahal, R.; Le Behec, M.; Guyoneaud, R.; Pigot, T.; Paolacci, H.; Lacombe, S. *Catal. Today* **2009**, *209*, 134.
- (113) Saint-Cricq, P.; Pigot, T.; Nicole, L.; Sanchez, C.; Lacombe, S. *Chem. Commun.* **2009**, 5281.
- (114) Jain, B.; Uppal, A.; Gupta, P. K.; Das, K. *Photochem. Photobiol.* **2009**, *85*, 927.
- (115) Ribeiro, S.; Serra, A. C.; Rocha Gonsalves, A. M. d'A. *ChemCatChem* **2013**, *5*, 134.
- (116) Cantau, C.; Pigot, T.; Manoj, N.; Oliveros, E.; Lacombe, S. *ChemPhysChem* **2007**, *8*, 2344.
- (117) Lacombe, S.; Soumillion, J.-P.; El Kadib, A.; Pigot, T.; Blanc, S.; Brown, R.; Oliveros, E.; Cantau, C.; Saint-Cricq, P. *Langmuir* **2009**, *25*, 11168.
- (118) Coyle, E. E.; Joyce, K.; Nolan, K.; Oelgemöller, M. *Green Chem.* **2010**, *12*, 1544.
- (119) Gryglik, D.; Miller, J. S.; Ledakowicz, S. *Sol. Energy* **2004**, *77*, 615.
- (120) Trytek, M.; Lipke, A.; Majdan, M.; Pisarek, S.; Gryko, D. *Eur. J. Org. Chem.* **2013**, 1653.
- (121) Griesbeck, A. G.; Miranda, M. A.; Uhlig, J. *Photochem. Photobiol. Sci.* **2011**, *10*, 1431.
- (122) Silva, M.; Azenha, M. E.; Pereira, M. M.; Burrows, H. D.; Sarakha, M.; Forano, C.; Ribeiro, M. F.; Fernandes, A. *Appl. Catal., B* **2010**, *100*, 1.
- (123) Suchard, O.; Kane, R.; Roe, B. J.; Zimmermann, E.; Jung, C.; Waske, P. A.; Mattay, J.; Oelgemöller, M. *Tetrahedron* **2006**, *62*, 1467.
- (124) Oelgemöller, M.; Jung, C.; Mattay, J. *Pure Appl. Chem.* **2007**, *79*, 1939.
- (125) Gut, F.; Schiek, W.; Haefeli, W. E.; Walter-Sack, I.; Burhenne, J. *Eur. J. Pharm. Biopharm.* **2008**, *69*, 582.
- (126) Souza, M. I.; Jaques, Y. M.; de Andrade, G. P.; Ribeiro, A. O.; da Silva, E. R.; Fileti, E. E.; Ávila, É. de S.; Pinheiro, M. V. B.; Krambrock, K.; Alves, W. A. *J. Phys. Chem. B* **2013**, *117*, 2605.
- (127) Oberley, L. W.; Buettner, G. R. *Cancer Res.* **1979**, *39*, 1141.

- (128) Wainwright, M. *Photochem. Photobiol. Sci.* **2004**, *3*, 406.
- (129) Wainwright, M. *Chem. Soc. Rev.* **2002**, *31*, 128.
- (130) Nazarova, A.; Ignatova, A.; Feofanov, A.; Karmakova, T.; Pljutinskaya, A.; Mass, O.; Grin, M.; Yakubovskaya, R.; Mironov, A.; Maurizot, J.-C. *Photochem. Photobiol. Sci.* **2007**, *6*, 1184.
- (131) Spiller, W.; Kliesch, H.; Wöhrle, D.; Hackbarth, S.; Röder, B.; Schnurpfeil, G. *J. Porphyrins Phthalocyanines* **1998**, *2*, 145.
- (132) Hah, H. J.; Kim, G.; Lee, Y. E. ; Orringer, D. A.; Sagher, O.; Philbert, M. A.; Kopelman, R. *Macromol. Biosci.* **2011**, *11*, 90.
- (133) Goto, Y.; Sawada, H. *Colloid. Polym. Sci.* **2009**, *287*, 1317.
- (134) Harris, F.; Sayed, Z.; Hussain, S.; Phoenix, D. A. *Photodiagn. Photodyn.* **2004**, *1*, 231.
- (135) Tada, D. B.; Rossi, L. M.; Leite, C. A. P.; Itri, R.; Baptista, M. S. *J. Nanosci. Nanotechnol.* **2010**, *10*, 3100.
- (136) Mamaeva, V.; Sahlgren, C.; Lindén, M. *Adv. Drug Deliv. Rev.* **2013**, *65*, 689.
- (137) Sharman, W. M.; Allen, C. M.; van Lier, J. E. *Drug Discov. Today* **1999**, *4*, 507.
- (138) Mir, Y.; Houde, D.; Lier, J. E. *Photochem. Photobiol. Sci.* **2006**, *5*, 1024.
- (139) Rolim, J. P. M. L.; de-Melo, M. A. S.; Guedes, S. F.; Albuquerque-Filho, F. B.; de Souza, J. R.; Nogueira, N. A. P.; Zanin, I. C. J.; Rodrigues, L. K. A. *J. Photochem. Photobiol., B* **2012**, *106*, 40.
- (140) Rebeiz, C. A.; Reddy, K. N.; Nandihalli, U. B.; Velu, J. *Photochem. Photobiol.* **1990**, *52*, 1099.
- (141) Rebeiz, C. A.; Gut, L. J.; Lee, K.; Juvik, J. A.; Rebeiz, C. C.; Bouton, C. E.; Towers, G. H. N. *Crit. Rev. Plant Sci.* **1995**, *14*, 329.
- (142) Ben Amor, T.; Jori, G. *Insect Biochem. Molec.* **2000**, *30*, 915.
- (143) Bourdelande, J. L.; Font, J.; Marques, G.; Abdel-Shafi, A. A.; Wilkinson, F.; Worrall, D. R. *J. Photochem. Photobiol., A* **2001**, *138*, 65.
- (144) Masilela, N.; Kleyi, P.; Tshentu, Z.; Priniotakis, G.; Westbroek, P.; Nyokong, T. *Dyes Pigments* **2013**, *96*, 500.
- (145) Pepe, E.; Abbas, O.; Rebufa, C.; Simon, M.; Lacombe, S.; Julliard, M. *J. Photochem. Photobiol., A* **2005**, *170*, 143.
- (146) Gryglik, D.; Miller, J. S.; Ledakowicz, S. *J. Hazard. Mater.* **2007**, *146*, 502.
- (147) Baciocchi, E.; Del Giacco, T.; Elisei, F.; Gerini, M. F.; Guerra, M.; Lapi, A.; Liberali, P. *J. Am. Chem. Soc.* **2003**, *125*, 16444.
- (148) Gu, X.; Li, X.; Chai, Y.; Yang, Q.; Li, P.; Yao, Y. *Green Chem.* **2013**, *15*, 357.
- (149) Aprile, C.; Martín, R.; Alvaro, M.; Garcia, H.; Scaiano, J. C. *Chem. Mater.* **2009**, *21*, 884.
- (150) Chen, L.; Lucia, L. A.; Gaillard, E. R.; Whitten, D. G.; Icil, H.; Icli, S. *J. Phys. Chem. A* **1998**, *102*, 9095.
- (151) Karapire, C.; Kus, M.; Turkmen, G.; Trevithick-Sutton, C. C.; Foote, C. S.; Icli, S. *Sol. Energy* **2005**, *78*, 5.
- (152) Maurya, R. A.; Park, C. P.; Kim, D.-P. *Beilstein J. Org. Chem.* **2011**, *7*, 1158.
- (153) Shvydkiv, O.; Nolan, K.; Oelgemöller, M. *Beilstein J. Org. Chem.* **2011**, *7*, 1055.
- (154) Elvira, K. S.; Wootton, R. C. R.; Reis, N. M.; Mackley, M. R.; deMello, A. J. *ACS Sustainable Chem. Eng.* **2013**, *1*, 209.
- (155) Shvydkiv, O.; Limburg, C.; Nolan, K.; Oelgemöller, M. *J. Flow Chem.* **2012**, *2*, 52.
- (156) Yavorskyy, A.; Shvydkiv, O.; Nolan, K.; Hoffmann, N.; Oelgemöller, M. *Tetrahedron Lett.* **2011**, *52*, 278.
- (157) Yavorskyy, A.; Shvydkiv, O.; Limburg, C.; Nolan, K.; Delauré, Y. M. C.; Oelgemöller, M. *Green Chem.* **2012**, *14*, 888.
- (158) Ciamician, G. *Science* **1912**, *36*, 385.
- (159) Amat, A. M.; Arques, A.; Galindo, F.; Miranda, M. A.; Santos-Juanes, L.; Vercher, R. F.; Vicente, R. *Appl. Catal., B* **2007**, *73*, 220.
- (160) Blanco, J.; Malato, S.; Fernández-Ibañez, P.; Alarcón, D.; Gernjak, W.; Maldonado, M. I. *Renew. Sust. Energy Rev.* **2009**, *13*, 1437.
- (161) Vivar, M.; Skryabin, I.; Everett, V.; Blakers, A. *Sol. Energ. Mat. Sol. C.* **2010**, *94*, 1772.
- (162) Barlev, D.; Vidu, R.; Stroeve, P. *Sol. Energ. Mat. Sol. C.* **2011**, *95*, 2703.
- (163) Chekir, N.; Boukendakdji, H.; Igoud, S.; Taane, W. *Procedia Engineering* **2012**, *33*, 174.
- (164) Pohlmann, B.; Scharf, H.-D.; Jarolimek, U.; Mauermann, P. *Sol. Energy* **1997**, *61*, 159.
- (165) Hoffmann, N. *ChemSusChem* **2012**, *5*, 352.
- (166) Oelgemöller, M.; Jung, C.; Ortner, J.; Mattay, J.; Zimmermann, E. *Green Chem.* **2005**, *7*, 35.
- (167) Bazylńska, U.; Pietkiewicz, J.; Saczko, J.; Nattich-Rak, M.; Rossowska, J.; Garbiec, A.; Wilk, K. A. *Eur. J. Pharm. Sci.* **2012**, *47*, 406.
- (168) Miao, W.; Shim, G.; Lee, S.; Lee, S.; Choe, Y. S.; Oh, Y.-K. *Biomaterials* **2013**, *34*, 3402.
- (169) Kano, A.; Taniwaki, Y.; Nakamura, I.; Shimada, N.; Moriyama, K.; Maruyama, A. *J. Controlled Release* **2013**, *167*, 315.

- (170) Shvydkiv, O.; Yavorsky, A.; Tan, S. B.; Nolan, K.; Hoffmann, N.; Youssef, A.; Oelgemöller, M. *Photochem. Photobiol. Sci.* **2011**, *10*, 1399.
- (171) Ghosh, J. P.; Sui, R.; Langford, C. H.; Achari, G.; Berlinguette, C. P. *Water Res.* **2009**, *43*, 4499.
- (172) Vilhunen, S.; Rokhina, E.; Virkutyte, J. *J. Environ. Eng-ASCE* **2010**, *136*, 274.
- (173) Lawal, O. In *Imaging and Applied Optics Technical Papers*; OSA Technical Digest (online); Optical Society of America, 2012; p. AM3A.2.
- (174) Kim, H.; Kim, W.; Mackeyev, Y.; Lee, G.-S.; Kim, H.-J.; Tachikawa, T.; Hong, S.; Lee, S.; Kim, J.; Wilson, L. J.; Majima, T.; Alvarez, P. J. J.; Choi, W.; Lee, J. *Environ. Sci. Technol.* **2012**, *46*, 9606.
- (175) Parakh, P.; Gokulakrishnan, S.; Prakash, H. *Sep. Purif. Technol.* **2013**, *109*, 9.
- (176) US EPA Green Chemistry Program at EPA http://www.epa.gov/greenchemistry/pubs/epa_gc.html#goals (accessed Apr 10, 2013).
- (177) Leray, I.; Ayadim, M.; Ottermans, C.; Jiwan, J. L. H.; Soumillion, J. P. *J. Photochem. Photobiol., A* **2000**, *132*, 43.
- (178) Kikuchi, K.; Sato, C.; Watabe, M.; Ikeda, H.; Takahashi, Y.; Miyashi, T. *J. Am. Chem. Soc.* **1993**, *115*, 5180.
- (179) Breslin, D. T.; Fox, M. A. *J. Am. Chem. Soc.* **1993**, *115*, 11716.
- (180) Nonell, S.; Gonzales, M.; Trull, F. R. *Afinidad* **1993**, *448*, 445.
- (181) Nanclares, J.; Gil, J.; Rojano, B.; Saez, J.; Schneider, B.; Otálvaro, F. *Tetrahedron Lett.* **2008**, *49*, 3844.
- (182) Kuznetsova, N. A.; Kaliya, O. L.; Solodar', S. L. *J. Appl. Spectrosc.* **1985**, *43*, 901.
- (183) Rosquete, L. I.; Cabrera-Serra, M. G.; Piñero, J. E.; Martín-Rodríguez, P.; Fernández-Pérez, L.; Luis, J. G.; McNaughton-Smith, G.; Abad-Grillo, T. *Bioorgan. Med. Chem.* **2010**, *18*, 4530.
- (184) Cui, L.; Furuhashi, S.; Tachikawa, Y.; Tada, N.; Miura, T.; Itoh, A. *Tetrahedron Lett.* **2013**, *54*, 162.
- (185) Ragàs, X.; Dai, T.; Tegos, G. P.; Agut, M.; Nonell, S.; Hamblin, M. R. *Lasers Surg. Med.* **2010**, *42*, 384.
- (186) Ragàs, X.; He, X.; Agut, M.; Roxo-Rosa, M.; Gonsalves, A.; Serra, A.; Nonell, S. *Molecules* **2013**, *18*, 2712.
- (187) Brecher, G. *Am. J. Clin. Pathol.* **1949**, *19*, 895.
- (188) Jensen, W. N.; Montjar, M.; Heinle, E., Jr; Padilla, F.; Trakatellis, A. C. *Nouv. Rev. Fr. Hematol.* **1967**, *7*, 841.
- (189) Hussain, S.; Harris, F.; Phoenix, D. A. *FEMS Immunol. Med. Microbiol.* **2006**, *46*, 124.
- (190) Wagner, S. J.; Robinette, D.; Dodd, R. *Transfusion* **1993**, *33*, 713.
- (191) Skripchenko, A.; Robinette, D.; Wagner, S. J. *Photochem. Photobiol.* **1997**, *65*, 451.
- (192) Morrison, H.; Mohammad, T.; Kurukulasuriya, R. *Photochem. Photobiol.* **1997**, *66*, 245.
- (193) Mohammad, T.; Morrison, H. *J. Chromatogr. B* **1997**, *704*, 265.
- (194) Houghtaling, M. A.; Perera, R.; Owen, K. E.; Wagner, S.; Kuhn, R. J.; Morrison, H. *Photochem. Photobiol.* **2000**, *71*, 20.
- (195) Otsuki, S.; Taguchi, T. *B. Chem. Soc. Jpn.* **1996**, *69*, 2525.
- (196) Neckers, D. C. *J. Photochem. Photobiol., A* **1989**, *47*, 1.
- (197) Blossey, E. C.; Neckers, D. C.; Thayer, A. L.; Schaap, A. P. *J. Am. Chem. Soc.* **1973**, *95*, 5820.
- (198) Schaap, A. P.; Thayer, A. L.; Blossey, E. C.; Neckers, D. C. *J. Am. Chem. Soc.* **1975**, *97*, 3741.
- (199) Nilsson, R.; Kearns, D. R. *Photochem. Photobiol.* **1974**, *19*, 181.
- (200) Yan, Z.; Wei, W.; Xun, H.; Anguo, S. *Chem. Lett.* **2012**, *41*, 1500.
- (201) Burguete, M. I.; Galindo, F.; Gavara, R.; Luis, S. V.; Moreno, M.; Thomas, P.; Russell, D. A. *Photochem. Photobiol. Sci.* **2009**, *8*, 37.
- (202) Burguete, M. I.; Gavara, R.; Galindo, F.; Luis, S. V. *Catal. Comm.* **2010**, *11*, 1081.
- (203) Shiraishi, Y.; Suzuki, T.; Hirai, T. *New J. Chem.* **2010**, *34*, 714.
- (204) Moczek, L.; Nowakowska, M. *Biomacromolecules* **2007**, *8*, 433.
- (205) Blanc, S.; Pigot, T.; Cugnet, C.; Brown, R.; Lacombe, S. *Phys. Chem. Chem. Phys.* **2010**, *12*, 11280.
- (206) Wagner, S. J.; Skripchenko, A.; Robinette, D.; Foley, J. W.; Cincotta, L. *Photochem. Photobiol.* **1998**, *67*, 343.
- (207) Rauf, M. A.; Graham, J. P.; Bukallah, S. B.; Al-Saedi, M. A. S. *Spectrochim. Acta A* **2009**, *72*, 133.
- (208) Islam, S. D.-M.; Ito, O. *J. Photochem. Photobiol., A* **1999**, *123*, 53.
- (209) Albano, G.; Belser, P.; De Cola, L.; T. Gandolfi, M. *Chem. Commun.* **1999**, 1171.
- (210) Matschke, M.; Beckert, R. *Molecules* **2007**, *12*, 723.
- (211) Zhao, L.; Mullen, K. M.; Chmielewski, M. J.; Brown, A.; Bampos, N.; Beer, P. D.; Davis, J. J. *New J. Chem.* **2009**, *33*, 760.
- (212) Hooper, K. A.; Kohn, J. J. *Bioact. Compat. Polym.* **1995**, *10*, 327.
- (213) Berthelot, T.; Talbot, J.-C.; Lain, G.; Déleris, G.; Latxague, L. *J. Pept. Sci.* **2005**, *11*, 153.

- (214) Choithani, J.; Sethi, D.; Kumar, P.; Gupta, K. C. *Surf. Sci.* **2008**, *602*, 2389.
- (215) Yadav, V. K.; Ganesh Babu, K. J. *Org. Chem.* **2004**, *69*, 577.
- (216) Movassaghi, M.; Schmidt, M. A. *Org. Lett.* **2005**, *7*, 2453.
- (217) Shendage, D. M.; Fröhlich, R.; Haufe, G. *Org. Lett.* **2004**, *6*, 3675.
- (218) Schneider, R.; Schmitt, F.; Frochot, C.; Fort, Y.; Lourette, N.; Guillemin, F.; Müller, J.-F.; Barberi-Heyob, M. *Bioorgan. Med. Chem.* **2005**, *13*, 2799.
- (219) Van Berkel, S. S.; Dirks, A. (Ton) J.; Debets, M. F.; van Delft, F. L.; Cornelissen, J. J. L. M.; Nolte, R. J. M.; Rutjes, F. P. J. T. *ChemBioChem* **2007**, *8*, 1504.
- (220) Liu, W.; Hao, G.; Long, M. A.; Anthony, T.; Hsieh, J.-T.; Sun, X. *Angew. Chem. Int. Ed.* **2009**, *48*, 7346.
- (221) Brinker, C. J.; Scherer, G. W. *Sol-Gel Science: The Physics and Chemistry of Sol-Gel Processing*; Gulf Professional Publishing, 1990.
- (222) Smart, L. E.; Moore, E. A. *Solid State Chemistry: An Introduction, Third Edition*; CRC Press, 2005.
- (223) Buckley, A. M.; Greenblatt, M. J. *Chem. Educ.* **1994**, *71*, 599.
- (224) Smith, D. M.; Stein, D.; Anderson, J. M.; Ackerman, W. J. *Non-Cryst. Solids* **1995**, *186*, 104.
- (225) Yoldas, B. E. *J. Mater. Sci.* **1977**, *12*, 1203.
- (226) Anderson, C.; Bard, A. J. *J. Phys. Chem.* **1995**, *99*, 9882.
- (227) Baleizão, C.; Gigante, B.; Das, D.; Álvaro, M.; Garcia, H.; Corma, A. *J. Catal.* **2004**, *223*, 106.
- (228) Latthe, S. S.; Imai, H.; Ganesan, V.; Kappenstein, C.; Venkateswara Rao, A. *J. Sol-Gel Sci. Technol.* **2009**, *53*, 208.
- (229) Hegde, N. D.; Venkateswara Rao, A. *Appl. Surf. Sci.* **2006**, *253*, 1566.
- (230) Nogami, M.; Hotta, S.; Kugimiya, K.; Matsubara, H. *J. Sol-Gel Sci. Technol.* **2010**, *56*, 107.
- (231) Abboud, J.-L. M.; Notari, R. *Pure Appl. Chem.* **1999**, *71*, 645.
- (232) Margolese, D.; Melero, J. A.; Christiansen, S. C.; Chmelka, B. F.; Stucky, G. D. *Chem. Mater.* **2000**, *12*, 2448.
- (233) Melero, J. A.; van Grieken, R.; Morales, G. *Chem. Rev.* **2006**, *106*, 3790.
- (234) Supplit, R.; Sugawara, A.; Peterlik, H.; Kikuchi, R.; Okubo, T. *Eur. J. Inorg. Chem.* **2010**, *2010*, 3993.
- (235) Graffion, J.; Cattoën, X.; Wong Chi Man, M.; Fernandes, V. R.; André, P. S.; Ferreira, R. A. S.; Carlos, L. D. *Chem. Mater.* **2011**, *23*, 4773.
- (236) Chaker, J. A.; Santilli, C. V.; Pulcinelli, S. H.; Dahmouche, K.; Briois, V.; Judeinstein, P. *J. Mater. Chem.* **2007**, *17*, 744.
- (237) Benyahya, S.; Monnier, F.; Taillefer, M.; Man, M. W. C.; Bied, C.; Ouazzani, F. *Adv. Synth. Catal.* **2008**, *350*, 2205.
- (238) Molina, E. F.; Pulcinelli, S. H.; Santilli, C. V.; Briois, V. *J. Phys. Chem. B* **2012**, *116*, 7931.
- (239) Mahadik, S. A.; Kavale, M. S.; Mukherjee, S. K.; Rao, A. V. *Appl. Surf. Sci.* **2010**, *257*, 333.
- (240) Storgaard, M.; Dörwald, F. Z.; Peschke, B.; Tanner, D. *J. Org. Chem.* **2009**, *74*, 5032.
- (241) Kubelka, P. *Z. Tech. Phys.* **1931**, 539.
- (242) Kubelka, P.; Munk, F. *Z. Tech. Phys.* **1931**, 593.
- (243) Olmsted, J. *J. Phys. Chem.* **1979**, *83*, 2581.
- (244) Kuramochi, H.; Kobayashi, T.; Suzuki, T.; Ichimura, T. *J. Phys. Chem. B* **2010**, *114*, 8782.
- (245) McElroy, W. J. *J. Phys. Chem.* **1990**, *94*, 2435.
- (246) Brahmia, O.; Richard, C. *Photochem. Photobiol. Sci.* **2005**, *4*, 454.
- (247) Mark, G.; Schuchmann, M. N.; Schuchmann, H.-P.; Sonntag, C. von *J. Photochem. Photobiol., A* **1990**, *55*, 157.
- (248) Chin, K. K.; Chuang, S.-C.; Hernandez, B.; Selke, M.; Foote, C. S.; Garcia-Garibay, M. A. *The Journal of Physical Chemistry A* **2006**, *110*, 13662.
- (249) Bensasson, R.; Land, E. J. *Trans. Faraday Soc.* **1971**, *67*, 1904.
- (250) Braun, A. M.; Oliveros, E. *Pure Appl. Chem.* **1990**, *62*, 1467.
- (251) Aminian-Saghafi, T.; Nasini, G.; Caronna, T.; Braun, A. M.; Oliveros, E. *Helv. Chim. Acta* **1992**, *75*, 531.
- (252) Thomas, A. H.; Lorente, C.; Capparelli, A. L.; Martinez, C. G.; Braun, A. M.; Oliveros, E. *Photochem. Photobiol. Sci.* **2003**, *2*, 245.
- (253) Cabrerizo, F. M.; Laura Dántola, M.; Petroselli, G.; Capparelli, A. L.; Thomas, A. H.; Braun, A. M.; Lorente, C.; Oliveros, E. *Photochem. Photobiol.* **2007**, *83*, 526.
- (254) Scurlock, R. D.; Nonell, S.; Braslavsky, S. E.; Ogilby, P. R. *J. Phys. Chem.* **1995**, *99*, 3521.
- (255) Martinez, L. A.; Martínez, C. G.; Klopotek, B. B.; Lang, J.; Neuner, A.; Braun, A. M.; Oliveros, E. *J. Photochem. Photobiol., B* **2000**, *58*, 94.
- (256) Nonell, S.; Braslavsky, S. E. In *Methods in Enzymology*; Lester Packer, H. S., Ed.; Academic Press, 2000; Vol. 319, pp. 37–49.

- (257) Boneva, M.; Ivanov, S. K.; Oliveros, E.; Braun, A. M. *J. Photochem. Photobiol., A* **1992**, *68*, 343.
- (258) Gomes, A.; Fernandes, E.; Lima, J. L. F. C. *J. Biochem. Biophys. Methods* **2005**, *65*, 45.
- (259) Hideg, É. *Cent. Eur. J. Biol.* **2008**, *3*, 273.
- (260) Song, B.; Wang, G.; Tan, M.; Yuan, J. *J. Am. Chem. Soc.* **2006**, *128*, 13442.
- (261) Umezawa, N.; Tanaka, K.; Urano, Y.; Kikuchi, K.; Higuchi, T.; Nagano, T. *Angew. Chem. Int. Ed.* **1999**, *38*, 2899.
- (262) Tanaka, K.; Miura, T.; Umezawa, N.; Urano, Y.; Kikuchi, K.; Higuchi, T.; Nagano, T. *J. Am. Chem. Soc.* **2001**, *123*, 2530.
- (263) Naito, K.; Tachikawa, T.; Cui, S.-C.; Sugimoto, A.; Fujitsuka, M.; Majima, T. *J. Am. Chem. Soc.* **2006**, *128*, 16430.
- (264) Tan, M.; Song, B.; Wang, G.; Yuan, J. *Free Radical Biol. Med.* **2006**, *40*, 1644.
- (265) Günther, G.; Lemp, E.; Zanocco, A. L. *J. Photochem. Photobiol., A* **2002**, *151*, 1.
- (266) Petrenko, T.; Krylova, O.; Neese, F.; Sokolowski, M. *New J. Phys.* **2009**, *11*, 015001.
- (267) Nakazumi, H.; Shiozaki, H.; Kitao, T. *Chem. Lett.* **1989**, *18*, 1027.
- (268) Singh-Rachford, T. N.; Castellano, F. N. *J. Phys. Chem. A* **2008**, *112*, 3550.
- (269) Neumann, M.; Hild, M.; Brauer, H.-D. *Ber. Bunsen Phys. Chem.* **1998**, *102*, 999.
- (270) Stevens, B.; Algar, B. E. *J. Phys. Chem.* **1968**, *72*, 2582.
- (271) Stevens, B.; Perez, S. R.; Ors, J. A. *J. Am. Chem. Soc.* **1974**, *96*, 6846.
- (272) Monroe, B. M. *J. Phys. Chem.* **1977**, *81*, 1861.
- (273) Peters, G.; Rodgers, M. A. *J. Am. Chem. Soc.* **1981**, *103*, 6759.
- (274) Matsumoto, S.; Sugimoto, H.; Sawyer, D. T. *Chem. Res. Toxicol.* **1988**, *1*, 19.
- (275) Kim, J. Y.; Choi, D. S.; Jung, M. Y. *J. Agric. Food Chem.* **2003**, *51*, 3460.
- (276) Oh, Y. S.; Jang, E. S.; Bock, J. Y.; Yoon, S. H.; Jung, M. Y. *J. Food Sci.* **2006**, *71*, C260.
- (277) Lee, Y.; Choe, E. *J. Food Sci.* **2008**, *73*, C506.
- (278) Sels, B. F.; De Vos, D. E.; Grobet, P. J.; Pierard, F.; Kirsch-De Mesmaeker, F.; Jacobs, P. A. *J. Phys. Chem. B* **1999**, *103*, 11114.
- (279) Koylu, D.; Sarrafpour, S.; Zhang, J.; Ramjattan, S.; Panzer, M. J.; Iii, S. W. T. *Chem. Commun.* **2012**, *48*, 9489.
- (280) Hoijemberg, P. A.; Chemtob, A.; Croutxé-Barghorn, C.; Poly, J.; Braun, A. M. *Macromolecules* **2011**, *44*, 8727.
- (281) Benoit-Marquié, F.; Wilkenhöner, U.; Simon, V.; Braun, A. M.; Oliveros, E.; Maurette, M.-T. *J. Photochem. Photobiol., A* **2000**, *132*, 225.
- (282) McKelvey, J. M.; Hoelscher, H. E. *Anal. Chem.* **1957**, *29*, 123.
- (283) Cantau, C.; Pigot, T.; Brown, R.; Mocho, P.; Maurette, M. T.; Benoit-Marquié, F.; Lacombe, S. *Appl. Catal., B* **2006**, *65*, 77.
- (284) Carofiglio, T.; Donnola, P.; Maggini, M.; Rossetto, M.; Rossi, E. *Adv. Synth. Catal.* **2008**, *350*, 2815.
- (285) Jähnisch, K.; Dingerdissen, U. *Chem. Eng. Technol.* **2005**, *28*, 426.
- (286) Braun, A. M.; Maurette, M. T.; Oliveros, E. *Photochemical technology*; Wiley-VCH, Weinheim, 1991.
- (287) Kristiansen, M.; Scurlock, R. D.; Lu, K. K.; Ogilby, P. R. *J. Phys. Chem.* **1991**, *95*, 5190.
- (288) Carmichael, I.; Hug, G. L. *J. Phys. Chem. Ref. Data* **1986**, *15*, 1.
- (289) Murasecco-Suardi, P.; Gassmann, E.; Braun, A. M.; Oliveros, E. *Helv. Chim. Acta* **1987**, *70*, 1760.
- (290) Jensen, P.-G.; Arnbjerg, J.; Tolbod, L. P.; Toftegaard, R.; Ogilby, P. R. *J. Phys. Chem. A* **2009**, *113*, 9965.
- (291) Salice, P.; Arnbjerg, J.; Pedersen, B. W.; Toftegaard, R.; Beverina, L.; Pagani, G. A.; Ogilby, P. R. *J. Phys. Chem. A* **2010**, *114*, 2518.
- (292) Schweitzer, C.; Schmidt, R. *Chem. Rev.* **2003**, *103*, 1685.
- (293) Scurlock, R. D.; Ogilby, P. R. *J. Photochem. Photobiol., A* **1993**, *72*, 1.
- (294) Garcia-Fresnadillo, D.; Georgiadou, Y.; Orellana, G.; Braun, A. M.; Oliveros, E. *Helv. Chim. Acta* **1996**, *79*, 1222.
- (295) Gijzeman, O. L. J.; Kaufman, F.; Porter, G. *J. Chem. Soc., Faraday Trans. 2* **1973**, *69*, 708.
- (296) Garner, A.; Wilkinson, F. *Chem. Phys. Lett.* **1977**, *45*, 432.
- (297) Scalmani, G.; Assael, M. J. *J. Chem. Phys.* **2010**, *132*, 114110.
- (298) Epstein, L. F.; Karush, F.; Rabinowitch, E. *J. Opt. Soc. Am.* **1941**, *31*, 77.
- (299) Singhal, G. S.; Rabinowitch, E. *J. Phys. Chem.* **1967**, *71*, 3347.
- (300) Lee, C.; Sung, Y. W.; Park, J. W. *J. Phys. Chem. B* **1999**, *103*, 893.
- (301) Marcus, Y. *Chem. Soc. Rev.* **1993**, *22*, 409.
- (302) Dimroth, K.; Reichardt, C.; Siepmann, T.; Bohlmann, F. *Justus Liebigs Ann. Chem.* **1963**, *661*, 1.
- (303) Reichardt, C. *Angew. Chem. Int. Ed.* **1965**, *4*, 29.

- (304) Taft, R. W.; Kamlet, M. J. *J. Am. Chem. Soc.* **1976**, *98*, 2886.
- (305) Kamlet, M. J.; Taft, R. W. *J. Am. Chem. Soc.* **1976**, *98*, 377.
- (306) Kamlet, M. J.; Abboud, J. L.; Taft, R. W. *J. Am. Chem. Soc.* **1977**, *99*, 6027.
- (307) Kamlet, M. J.; Abboud, J. L. M.; Abraham, M. H.; Taft, R. W. *J. Org. Chem.* **1983**, *48*, 2877.
- (308) Kamlet, M. J.; Abboud, J. L. M.; Taft, R. W. In *Progress in Physical Organic Chemistry*; Taft, R. W., Ed.; John Wiley & Sons, Inc., 2007; pp. 485–630.
- (309) Kamat, P. V.; Lichtin, N. N. *J. Phys. Chem.* **1981**, *85*, 814.
- (310) Kamat, P. V.; Lichtin, N. N. *J. Phys. Chem.* **1981**, *85*, 3864.
- (311) Kikuchi, K.; Tamura, S.-I.; Iwanaga, C.; Kokubun, H.; Usui, Y. *Z. Phys. Chem.* **1977**, *106*, 17.
- (312) Manju, T.; Manoj, N.; Braun, A. M.; Oliveros, E. *Photochem. Photobiol. Sci.* **2012**, *11*, 1744.
- (313) Schmidt, R.; Afshari, E. *J. Phys. Chem.* **1990**, *94*, 4377.
- (314) Usui, Y.; Koike, H.; Kurimura, Y. *B. Chem. Soc. Jpn.* **1987**, *60*, 3373.
- (315) Tournaire, C.; Croux, S.; Maurette, M.-T.; Beck, I.; Hocquaux, M.; Braun, A. M.; Oliveros, E. *J. Photochem. Photobiol., B* **1993**, *19*, 205.
- (316) Amore, S.; Lagorio, M. G.; Dicalio, L. L.; San Román, E. *Prog. React. Kinet. Mech.* **2001**, *26*, 159.
- (317) Ma, D.; Kell, A. J.; Tan, S.; Jakubek, Z. J.; Simard, B. *J. Phys. Chem. C* **2009**, *113*, 15974.
- (318) Mosinger, J.; Lang, K.; Plíštil, L.; Jesenská, S.; Hostomský, J.; Zelinger, Z.; Kubát, P. *Langmuir* **2010**, *26*, 10050.
- (319) Guli, M.; Li, X.; Zhang, K.; Chi, Y. *J. Sol-Gel Sci. Technol.* **2010**, *54*, 329.
- (320) Adachi, I.; Tabata, M.; Kawai, H.; Sumiyoshi, T. *Nucl. Instrum. Methods Phys. Res., Sect. A* **2011**, *639*, 222.
- (321) Latour, V.; Pigot, T.; Mocho, P.; Blanc, S.; Lacombe, S. *Catal. Today* **2005**, *101*, 359.
- (322) Kumar, P.; Gulians, V. V. *Micropor. Mesopor. Mat.* **2010**, *132*, 1.
- (323) Gao, C.; Che, S. *Adv. Funct. Mater.* **2010**, *20*, 2750.
- (324) Gay, D. S. F.; Fernandes, T. H. M.; Amavisca, C. V.; Cardoso, N. F.; Benvenuti, E. V.; Costa, T. M. H.; Lima, E. C. *Desalination* **2010**, *258*, 128.
- (325) Fukaya, N.; Haga, H.; Tsuchimoto, T.; Onozawa, S.; Sakakura, T.; Yasuda, H. *J. Organomet. Chem.* **2010**, *695*, 2540.
- (326) Lamberts, J. J. M.; Neckers, D. C. *J. Am. Chem. Soc.* **1983**, *105*, 7465.
- (327) Dunn, D. A.; Lin, V. H.; Kochevar, I. E. *Photochem. Photobiol.* **1991**, *53*, 47.
- (328) Negrón-Encarnación, I.; Arce, R.; Jiménez, M. J. *Phys. Chem. A* **2005**, *109*, 787.
- (329) Gehlen, M. H.; Pereira, R. V.; Gallas, M. R.; Costa, T. M. H.; Stefani, V. *J. Photochem. Photobiol., A* **2006**, *181*, 147.
- (330) Ferreira, A. P. G.; Frederice, R.; Janssen, K. P. F.; Gehlen, M. H. *J. Lumin.* **2011**, *131*, 888.
- (331) Lickiss, P. D. In *Advances in Inorganic Chemistry*; A.G. Sykes, Ed.; Academic Press, 1995; Vol. 42, pp. 147–262.
- (332) Grajcar, L.; Ivanoff, N.; Delouis, J. F.; Faure, J. *J. Chim. Phys.* **1984**, *81*, 33.
- (333) Ketsle, G. A.; Levshin, L. V.; Sokolova, L. K. *Opt. Spectrosc.* **1979**, *47*, 494.
- (334) Shimizu, O.; Watanabe, J.; Naito, S.; Shibata, Y. *J. Phys. Chem. A* **2006**, *110*, 1735.
- (335) Lang, K.; Bezdička, P.; Bourdelande, J. L.; Hernando, J.; Jirka, I.; Káfuňková, E.; Kovanda, F.; Kubát, P.; Mosinger, J.; Wagnerová, D. M. *Chem. Mater.* **2007**, *19*, 3822.
- (336) Rodgers, M. A. J. *J. Am. Chem. Soc.* **1983**, *105*, 6201.
- (337) Jockusch, S.; Sivaguru, J.; Turro, N. J.; Ramamurthy, V. *Photochem. Photobiol. Sci.* **2005**, *4*, 403.
- (338) Clennan, E. L. *Acc. Chem. Res.* **2001**, *34*, 875.
- (339) Bahrami, K.; Khodaei, M. M.; Fattahpour, P. *Catal. Sci. Technol.* **2011**, *1*, 389.
- (340) García-Rodríguez, F.; Pérez-Robles, F.; Manzano-Ramírez, A.; Vorobiev, Y.; González-Hernández, J. *Solid State Commun.* **1999**, *111*, 717.
- (341) Spraul, M. H.; Nitz, S.; Drawert, F. *Tetrahedron* **1991**, *47*, 3037.
- (342) Schenck, G. O.; Kinkel, K. G.; Mertens, H.-J. *Justus Liebigs Ann. Chem.* **1953**, *584*, 125.
- (343) Schenck, G. O.; Ziegler, K. *Naturwissenschaften* **1944**, *32*, 157.
- (344) Cantau, C.; Larribau, S.; Pigot, T.; Simon, M.; Maurette, M. T.; Lacombe, S. *Catal. Today* **2007**, *122*, 27.
- (345) Dougherty, T. J.; Dougherty, T. J.; Gomer, C. J.; Jori, G.; Kessel, D.; Korbelik, M.; Moan, J.; Peng, Q. *J. Natl. Cancer Inst.* **1998**, *90*, 889.
- (346) Ishii, K.; Kikukawa, Y.; Shiine, M.; Kobayashi, N.; Tsuru, T.; Sakai, Y.; Sakoda, A. *Eur. J. Inorg. Chem.* **2008**, *2008*, 2975.
- (347) Kropf, H.; Wischer, D. *Tetrahedron Lett.* **1969**, *10*, 1751.
- (348) Serif, G. S.; Hunt, C. F.; Bourns, A. N. *Can. J. Chem.* **1953**, *31*, 1229.

- (349) Singh, A.; Singh, V. K.; Quraishi, M. A. *Int. J. Corr.* **2010**, *2010*, 1.
- (350) Karapire, C.; Kolancilar, H.; Oyman, Ü.; İcli, S. *J. Photochem. Photobiol., A* **2002**, *153*, 173.
- (351) Rudbäck, J.; Bergström, M. A.; Börje, A.; Nilsson, U.; Karlberg, A.-T. *Chem. Res. Toxicol.* **2012**, *25*, 713.
- (352) Ribeiro, S. M.; Serra, A. C.; Gonsalves, A. M. d'A R. *J. Mol. Catal. A: Chem.* **2010**, *326*, 121.
- (353) Martins, R. R. L.; Neves, M. G. P. M. S.; Silvestre, A. J. D.; Silva, A. M. S.; Cavaleiro, J. A. S. *J. Mol. Catal. A: Chem.* **1999**, *137*, 41.
- (354) Crivello, J. V.; Yang, B. *J. Polym. Sci., Part A: Polym. Chem.* **1995**, *33*, 1881.
- (355) Matush, R.; Schmidt, G. *Chem. Ztg.* **1990**, *114*, 382.
- (356) Maheshwari, K. K.; Mayo, P. de; Wiegand, D. *Can. J. Chem.* **1970**, *48*, 3265.
- (357) Jary, W. G.; Ganglberger, T.; Pöchlauer, P.; Falk, H. *Monatsh. Chem.* **2005**, *136*, 537.
- (358) Matusch, R.; Schmidt, G. *Angew. Chem.* **1988**, *100*, 729.
- (359) Alp, S.; Erten, Ş.; Karapire, C.; Köz, B.; Doroshenko, A. O.; İçli, S. *J. Photochem. Photobiol., A* **2000**, *135*, 103.
- (360) Foti, M. C.; Ingold, K. U. *J. Agric. Food Chem.* **2003**, *51*, 2758.
- (361) Sortino, S.; Petralia, S.; Foti, M. C. *New J. Chem.* **2003**, *27*, 1563.
- (362) Saito, I.; Tamoto, K.; Matsuura, T. *Tetrahedron Lett.* **1979**, *20*, 2889.
- (363) Salah, N. B.; Matoussi, F. *J. Electroanal. Chem.* **2005**, *583*, 1.
- (364) Zakrzewski, A.; Neckers, D. C. *Tetrahedron* **1987**, *43*, 4507.
- (365) Esser, P.; Pohlmann, B.; Scharf, H.-D. *Angew. Chem., Int. Ed.* **1994**, *33*, 2009.
- (366) Miller, J. S. *Water Res.* **2005**, *39*, 412.
- (367) Ryskova, L.; Buchta, V.; Slezak, R. *Cent. Eur. J. Biol.* **2010**, *5*, 400.
- (368) Park, C. P.; Maurya, R. A.; Lee, J. H.; Kim, D.-P. *Lab Chip* **2011**, *11*, 1941.
- (369) Wootton, R. C. R.; Fortt, R.; de Mello, A. J. *Org. Process Res. Dev.* **2002**, *6*, 187.
- (370) Lévesque, F.; Seeberger, P. H. *Angew. Chem., Int. Ed.* **2012**, *51*, 1706.
- (371) Lévesque, F.; Seeberger, P. H. *Org. Lett.* **2011**, *13*, 5008.